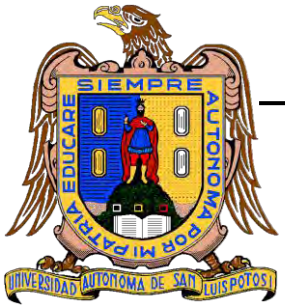

UNIVERSIDAD AUTÓNOMA DE SAN LUÍS POTOSÍ

Doctorado Institucional en Ingeniería y Ciencia de Materiales

Study on fabrication and lithium extraction properties of functionalized lithium ion-sieves

PARA OBTENER EL GRADO DE

DOCTOR EN INGENIERÍA Y CIENCIA DE MATERIALES

QUE PRESENTA

Lingjie Zhang

DIRECTORA

Dra. Mildred Quintana Ruiz

PATROCINADO POR SECIHTI Beca número 847199

San Luis Potosí, S.L.P. Junio de 2026

UNIVERSIDAD AUTÓNOMA DE SAN LUÍS POTOSÍ

Doctorado Institucional en Ingeniería y Ciencia de Materiales

Study on fabrication and lithium extraction properties of functionalized lithium ion-sieves

QUE PARA OBTENER EL GRADO DE

DOCTOR EN INGENIERÍA Y CIENCIA DE MATERIALES

QUE PRESENTA

Lingjie Zhang

DIRECTORA

Dra. Mildred Quintana Ruiz

Sinodales

Dra. Mildred Quintana Ruiz _____

Dr. José Adrián Martínez González _____

Dr. Hiram Joazet Ojeda Galván _____

Dra. Socorro Oros Ruiz _____

Dra. Selene Concepción Acosta Morales _____

San Luis Potosí, S.L.P. Junio de 2026

Acknowledgement

“What is given is not to be repaid, but to be cherished forever.”

This thesis begins with acknowledgments, expressing my deepest gratitude to my family, advisors, fellow students, and friends who provided invaluable assistance, support, and encouragement throughout my academic journey. Without their guidance and assistance, none of what follows in this thesis would have been possible. With this work, I humbly express my deepest gratitude.

Family are like sails, urging me forward. As the saying goes, *the foundation of all under heaven lies in the family*. After twenty-three years of learning, though I have achieved nothing of great worldly distinction, I have nonetheless completed my studies and reached this milestone. For this, I owe profound thanks to my grandparents, whose lifelong guidance and protection shaped my perseverance, resolve, and confidence. Through both words and deeds, they taught me gratitude and integrity, enabling me to remain true to my original aspirations, keeping my head down, pressing forward, and treading through snow toward the summit. My parents have labored tirelessly to raise me, yet my prolonged years away from home have left me unable to fully repay their devotion. I am deeply grateful to my father and mother for their care, encouragement, and unwavering trust, believing in every decision made by a once mischievous little boy. Their faith taught me to be courageous when necessary and resolute when there was no turning back. At twenty-one, I first learned to truly smile again, willing to share both dust and ashes. My heartfelt gratitude goes to Ms. Cai Yue, who has walked beside me for many years, through wind and rain alike. Your encouragement, comfort, companionship, and support have become a gentle spring breeze, nurturing all things in silence. You are my destination and my guiding star. In 2021, our shared journey began to unfold, willing to share both dust and ashes. My heartfelt gratitude goes to Ms. Cai Yue, who has walked beside me for many years, through wind and rain alike. Your encouragement, comfort, companionship, and support have become a gentle spring breeze, nurturing all things in silence. You are my destination and my guiding star. I also thank my relatives for their generous praise. I am keenly aware that I may not yet live up to such esteem, yet I hold it firmly in my heart as motivation to continue refining myself and moving forward.

Teachers are like lamps, illuminating my path. A teacher of knowledge is easy

to find; a teacher of character is rare. After twenty-three years of learning, I have come to understand this deeply. Entering the academic path midway and knocking late at the doors of Song's Group scholarship, I was fortunate to be accepted and guided by Professor Shaoxian Song and Professor Yunliang Zhao, who patiently instructed me despite my limitations and shared their knowledge without reservation. I am especially grateful to Professor Song for "leading me through the door." Though I encountered his guidance later than most, it was far better than never encountering it at all. Such recognition and mentorship are beyond words. I sincerely thank Professor Zhao for his comprehensive guidance, from study to life, from research to management, from conduct to character, allowing me to look back at myself four years ago with confidence and say proudly "I have grown, and I have become stronger". Your teaching philosophy of empowering students with enduring skills, your commitment to talent cultivation above all else, your willingness to endure solitude in research, and his never-give-up attitude toward life will remain enduring standards by which I measure myself. As the saying goes, *a teacher transmits the Way, imparts knowledge, and resolves doubts*, and here, this is most fully embodied. Science knows no borders, and kindred minds resonate across great distances. During my studies abroad in the West, I had the privilege of learning under Professor Mildred Quintana, whose guidance was like a lamp in a dark room. I am deeply grateful for her meticulous instruction and thoughtful care, which allowed me to study, research, and live with peace of mind far from home. Though my studies now conclude and parting is at hand, her mentorship will remain forever in my heart, awaiting a future reunion over shared celebration. I also extend sincere thanks to Professor Tingting Zhang, Professor Hiram Joazet Ojeda Galván, and Professor Selene Acosta, Professor José Adrián Martínez-González for their encouragement and guidance. Such kindness is impossible to fully repay.

Friends are like stars, accompanying me through long nights. My abilities are limited, yet learning is enriched not only by good advisors but also by good companions. I am profoundly grateful to my senior colleagues. Wen Tong, whose wisdom, steadiness, and clarity of thought consistently illuminated my confusion and revealed deeper insights, serving as a pillar of the research group; Licai Chen, diligent and generous, who never hesitated to share his knowledge and guide me through challenges, a true backbone of the team; Haoyu Bai, erudite and perceptive, who offered invaluable insight even without ever meeting in person, guiding me through moments of uncertainty. I thank my junior brother Zhenlei Wang, Shuaike Lv, Xiongrui Jiang,

Jianglin Yan, and my junior sister Yanhui Miao for their diligence, enthusiasm, and open-hearted academic exchange, always extending help whenever needed; Renbo Gao, who bore responsibilities without complaint and reminded me constantly of the virtue of diligence; Junior brother Xingwen Wang, Shutong Wang, Yupeng Sun, Xin Zhang, Jierui Wang, Bowen Kuang, Xianghao He, Yuting Feng and my junior sisters Jiaoyan Liu, Wenbo Wang, Ying Li, and Lianqiu Huang, all individuals of both integrity and industry, whose futures hold great promise. My close friend of the same cohort, Lei Hou, exemplifies moral clarity and sincerity. I also thank my fellow students of Mexico Wu Jie, Cui Zhang, Zijia Zhang, Weiquan Zhan, Yuan Yuan, Keqiang Zhou, Ning Wang, Yingxin Chen, Jianhui Zhu, and Yunjia Ling, each diligent and thoughtful, with paths ahead destined to bloom. The bonds among fellow students cannot be fully expressed in words. One journey of mountains and rivers, yet a lifetime of fortune, and the friendship will remain forever in my heart.

"One longs to buy osmanthus flowers and sail with wine once more, yet it no longer feels like the carefree days of youth." After years of study and the kindness of many, I now don the red doctoral gown, filled with gratitude and reflection. Looking back on the once desolate paths, and gazing forward toward drifting clouds and open waters, I step onward with calm resolve.

Finally, I gratefully acknowledge the financial support from the Secretariat of Science, Humanities, Technology, and Innovation (SECIHTI) of Mexico under Grant No. 847199.

Lingjie Zhang

Mexico

Resumen

Debido a su papel crucial en la transformación energética orientada a la descarbonización, el suministro sostenible de litio (Li) se ha vuelto cada vez más crítico. La extracción de Li a partir de salmueras prácticamente inagotables se está convirtiendo en una alternativa preferente para garantizar el desarrollo sostenible de los recursos de litio, lo que exige el desarrollo de tecnologías de extracción verdes, eficientes y altamente selectivas. Los iono-tamices de litio ofrecen soluciones prometedoras para la extracción selectiva de litio a partir de salmueras, en particular los hidróxidos dobles laminares de litio-aluminio (LiAl-LDHs), gracias a su estructura de cavidades octaédricas específicamente adaptadas para Li^+ y a su capacidad de desorción sin pérdidas por disolución. No obstante, aunque los LiAl-LDHs ya han sido utilizados en la extracción industrial de litio, persisten preocupaciones clave que limitan su aplicación a mayor escala.

En este trabajo, se sintetizan en primer lugar las relaciones estructura-rendimiento y los avances en la investigación de diversos iono-tamices, demostrando el alto grado de sofisticación y desarrollo alcanzado por los LiAl-LDHs. Posteriormente, al centrarse en los factores que influyen en el desempeño de los LiAl-LDHs para la extracción de Li, se resumen las principales limitaciones que restringen su desarrollo ulterior: i) baja capacidad de adsorción de Li^+; ii) el efecto de "envenenamiento por iones sulfato (SO_4^{2-})" en salmueras de tipo sulfato; y iii) la escasa viabilidad en salmueras de baja calidad. Con este objetivo, se desarrollan una serie de estrategias, que incluyen ingeniería de dopaje, control de las interacciones interlaminares, construcción de dominios multifuncionales y diseño molecular, para superar dichas limitaciones de los LiAl-LDHs. Como resultado, los LiAl-LDHs modificados exhiben capacidades de adsorción de Li^+ significativamente mejoradas, selectividades ultraltas hacia Li^+, excelentes propiedades de resistencia al envenenamiento por sulfato y una notable estabilidad en diversos tipos de salmueras, incluyendo salmueras de lagos salinos, salmueras de tipo sulfato y salmueras de baja calidad. Sobre la base de estas ventajas, finalmente se obtiene carbonato de litio (Li_2CO_3) de alta pureza (97.85 %) a partir de la salmuera empleando los LiAl-LDHs desarrollados. Esta tesis proporciona aportes teóricos y contribuciones técnicas para ampliar el aprovechamiento de recursos de salmuera accesibles con miras a una extracción sostenible de litio.

Palabras clave: Extracción de litio; Salmuera; Hidróxidos dobles laminares de litio-aluminio; Iono-tamiz; Adsorción; Modificación.

Abstract

Owing to the crucial role in energy transformation for decarbonization, sustainable lithium (Li) supply has become increasingly critical. Li extraction from abundant brines is becoming a preferred alternative to ensure the sustainable development of Li resources, which requires green, effective, and selective extraction techniques. Lithium ion-sieves offer promising solutions for selective lithium extraction from brines, especially lithium aluminum layered double hydroxides (LiAl-LDHs) due to their tailored Li^+ octahedral cavity structure and desorption without dissolution loss. While LiAl-LDHs have been used for industrial Li extraction, the crucial concerns remain regarding the wider applications.

Herein, the structure-performance relationships and research progress of various ion-sieves are first synthesized, demonstrating the sophistication and advancement of LiAl-LDHs. Further, by focusing on the influencing factors of LiAl-LDHs for Li extraction, the main limitations that restrict their further development were summarized: i) low Li^+ adsorption capacity; ii) 'sulfate ion (SO_4^{2-}) poisoning' effect in SO_4^{2-}-type brines; and iii) poor feasibility in low-quality brines. To this end, a series of strategies are developed, including doping engineering, steering interlayer interaction, constructing multiple functional domains, and molecular tailoring engineering, to overcome these concerns of LiAl-LDHs. Accordingly, the modified LiAl-LDHs exhibit significantly improved Li^+ adsorption capacities, high Li^+ selectivity, excellent anti-sulfate poisoning features and stabilities in various brines, involving salt lake brines, SO_4^{2-}-type brines, and low-quality brines. On the basis of these merits, high-purity (97.85%) Li_2CO_3 is finally produced from the brine using the as-obtained LiAl-LDHs. The thesis provides theoretical insights and technical contributions for expanding accessible brine resources towards sustainable Li extraction.

Keywords: Lithium extraction; Brine; Lithium aluminum layered double hydroxides; Ion-sieve; Adsorption; Modification

Extended Abstract

Driven by global electrification and decarbonization strategies, the market demand for lithium (Li) is skyrocketing. To enable the sustainable supply of Li, there is an urgent and timely need to extract and recover Li from various resources, especially abundant brines. The development of lithium adsorbents constructed from selective nano-ion sieves opens an advanced avenue for Li extraction from brines. Therein, lithium aluminum layered double hydroxides (LiAl-LDHs) have emerged as the most promising adsorbents for lithium extraction from brines. However, the wider application of LiAl-LDHs is challenging, the crucial concerns remain to be resolved.

Here, the structure-performance relationships and research progress of various ion-sieves are first synthesized, including LiAl-LDHs, lithium titanium oxide type lithium-ion sieves (LTO-LISs), lithium manganese oxide type lithium-ion sieves (LMO-LISs), ion-imprinted polymers (Li-IIPs) and ion-exchange resins. Taking the adsorption capacity, adsorption rate, selectivity, reusability, and cost into account, LiAl-LDHs present are the sophistication and advancement for industrial applications. Further, the main limitations that restrict the further development of LiAl-LDHs are summarized through revealing the influencing factors of Li extraction, namely, low Li^+ adsorption capacity, 'sulfate ion (SO_4^{2-}) poisoning' effect in SO_4^{2-}-type brines, and poor feasibility in low-quality brines.

To improve suboptimal Li^+ adsorption performance of LiAl-LDHs, a doping engineering strategy is developed to fabricate novel Zn^{2+}-doped LiAl-LDH (LiZnAl-LDH). Combining experiments and simulation calculations, it is revealed that the doping engineering endows LiZnAl-LDH with increased specific surface area, hydrophilic, surface attraction for Li^+, and oxygen vacancies, which increase the adsorption energy (E_{ad}) of Li^+ adsorption, while reduce Gibbs free energy (ΔG) of Li^+ insertion and energy barrier of Li^+ diffusion. Consequently, LiZnAl-LDH exhibits the remarkable higher Li^+ adsorption capacity (13.4 mg/g) and selectivity (separation factors of 213, 834, 171 for Li^+/K^+, Li^+/Na^+, Li^+/Mg^{2+}, respectively), as well as excellent reusability in the real brine compared to the pristine LiAl-LDH.

To impart an anti-sulfate poisoning feature to LiAl-LDHs, a steering interlayer interaction strategy by embedding portion of PO_4^{3-} into interlayers of LiAl-LDH beads (BLDH-P) is developed. Owing to the lower binding energy (E_b) and stronger diffusion energy barrier of SO_4^{2-} within interlayers, BLDH-P features the property of preventing

SO_4^{2-} intercalation, with the unchanged adsorption and desorption capacity in Lop Nor brine (the largest SO_4^{2-}-type brine in the world). BLDH-P also shows excellent Li extraction performance, as the results of enlarged interlayer spacing and selective electrostatic repulsion. The static and dynamic Li^+ uptake reaches 5.26 mg/g and 3.96 mg/g, with high separation factors of 39.84, 48.14, and 144.87 for Li^+/K^+, Li^+/Na^+, and Li^+/Mg^{2+}, respectively, superior to those of reported and commercialized LiAl-LDH.

To strengthen the anti-sulfate poisoning performance of LiAl-LDHs, an organic modification strategy is developed to construct multiple functional domains of LiAl-LDHs (LiAl-LDH/PAM) using polyacrylamide (PAM). Benefiting from the newly created multiple SO_4^{2-} repelling domains in the interface and interlayer of the LiAl-LDH/PAM, the energy barrier for SO_4^{2-} migration over interface and interlayer is significantly increased, which hinders the SO_4^{2-} intercalation during long-term Li cycling extraction. Accordingly, anti-sulfate poisoning properties exceed all previously reported LiAl-LDHs, where the adsorption capacity loss of the LiAl-LDH/PAM is less than 6% in ten cycle experiments in Lop Nor brine. Additionally, PAM enhances the affinity between the LiAl-LDHs and Li^+, resulting in the excellent Li^+ selectivity and the maximum adsorption capacity (13.25 mg/g).

To realize high-efficiency lithium recovery from diverse low-quality brines, a proof-of-concept polymer side-chain structure design (SCSD) strategy that delivers intralayer engineering of LiAl-LDHs (LiAl-LDH/PR) with functional polymers is developed. The results of simulations and experiments demonstrate that the SCSD strategy engineers LiAl-LDHs with a Li^+-enriched intralayer domain, which overcomes the diffusion-limited Li^+ uptake in low-quality brines. Notably, the local chemical microenvironment and spatial microstructure of LiAl-LDH/PR can be readily tuned through rational designs of side-chains of polymer to accommodate Li extraction from different brines. Consequently, LiAl-LDH/PR realizes an ultra-high recovery efficiency of 91.62% from real oilfield brine with ultra-low Li^+ concentration of 19.7 mg/L and a sustainable Li extraction and production of high-purity Li_2CO_3 from one of the largest low-quality brines in the world.

Contents

Index of Figures

Index of Tables

Chapter 1. Introduction

1.1. Justification

Lithium (Li), a critical energy metal and strategic resource, has been hailed as the "white oil" and "white gold" of the 21st century due to its huge economic success and crucial role in the energy transition, particularly in rechargeable lithium-ion batteries (LIBs) [1-4]. With the fast commercialization of LIBs, both lithium demand and price are skyrocketing. It is projected that the demand for Li is expected to grow at over 30% per annum by 2030 [5]. Unquestionably, cost-effective and sustainable extraction of lithium is imperative.

Currently, Li is mainly sourced from ores and brines, in which harvesting Li from the latter, typically salt lake brines, has aroused rising interest in the lithium industry due to the abundant reserves (tons of thousands of times more than ore reserves), environmentally friendly operation and cost-effectiveness compared to conventional ore mining [6-10]. As such, one important way to enable the sustainable supply of lithium is to develop a promising approach for lithium extraction from brines. Nevertheless, lithium in brines is normally accompanied by high concentrations of cations such as Mg^{2+}, Na^{+}, K^{+}, and Ca^{2+}. These cations, especially Mg^{2+}, possess similar properties to Li^{+} [11], causing challenges in lithium recovery from brines [12,13].

Recently, adsorption has served as a critical technique for selective lithium extraction from brines, in particular those with high Mg^{2+}/Li^{+} ratios, due to the advantages of the minimal pre-processing requirement of the brine, high lithium selectivity and recovery, additional concentration function, cost-effective and environment-friendly advantages [14-17]. Notably, the lithium recovery efficiency significantly depends on the lithium adsorbents. Despite numerous lithium adsorbents have been developed, lithium aluminum layered double hydroxides (LiAl-LDHs) are the only Li^{+} adsorbents for industrial application because of simple preparation and easy elution in water without dissolution loss [18-20]. Therefore, it is imperative to fabricate high-performance and robust-stability LiAl-LDHs for guaranteeing the sustainability of Li resources.

The structure of LiAl-LDHs is a two-dimensional structure formed by the insertion of Li^{+} into ordered octahedral voids in the $Al(OH)_3$ layer, and anions (usually Cl^{-}) and water molecules are also inserted into the interlayer synchronously to balance the

charge. Therefore, the chemical formula of Li/Al-LDHs can be described as $mLiCl{\cdot}2Al(OH)_3{\cdot}nH_2O$ ($0 < m < 1$) [21]. While LiAl-LDHs have been used as an industrial and commercial-scale adsorbent for lithium extraction, their more extensive applications are still limited, and crucial concerns remain: i) the low Li^+ adsorption capacity. According to the chemical formula, LiAl-LDHs have inherently limited Li^+ theoretical maximum adsorption capacity (~ 30 mg g^{-1}), while the practical adsorption capacity of LiAl-LDH (4 ~ 8 mg g^{-1}) is always far below the theoretical capacity [22,23]. It is worth noting that such limited extraction efficiency will further deteriorate in low-quality brines containing low Li^+ concentration, which significantly restrict the availability of lithium resource for conventional LiAl-LDHs. ii) LiAl-LDHs easily suffer from the 'sulfate ion (SO_4^{2-}) poisoning' effect in SO_4^{2-}-type brines. During the lithium extraction from sulfate-rich brines that are the second most significant type of brines in the world, SO_4^{2-} readily intercalates into the interlayer of LiAl-LDHs and strongly binds to Li^+, making desorption very challenging and gradually reducing Li^+ adsorption capacity [24,25]. Apparently, targeted design and innovation in LiAl-LDHs adsorbents aiming on efficient Li^+ adsorption and strong anti-sulfate intercalation is important for sustainable Li extraction from various brines.

1.2. Hypothesis

Considering the unique layered structures, LiAl-LDHs inherently feature tunable microstructures of the host layer and microenvironments of the guest interlayer. Therefore, the intralayer and interlayer modification are two obvious practicable routes for LiAl-LDHs to enhance lithium extraction and anti-sulfate ion poisoning performances. Previous studies have confirmed that the intralayer doping engineering is a simple yet effective strategy for improving physicochemical property of adsorbents, thereby facilitating adsorption [26]. By modulating dopants and levels of doping, adsorbents show a highly flexible tunability in terms of microstructures and affinity towards various ions [27], which offers promising pathways for enhancing the Li^+ adsorption capacity of LiAl-LDHs. Also, previous researches have reported that interlayer anions of LDHs can be precisely regulated via anion exchange, and the species and content of interlayer anions affect the structures and physicochemical properties of LDHs [28,29], which encourages the modification of LiAl-LDHs to hinder the intercalation of SO_4^{2-} and following "SO_4^{2-} poisoning" effect. Therefore, we hypothesize that the rational intralayer and interlayer engineering of LiAl-LDHs can enhance Li^+ adsorption capacity, improve selectivity, and suppress sulfate intercalation,

thereby enabling stable lithium extraction from different types of brines.

1.3. Objectives

1.3.1. General objective

Building on the structural properties of LiAl-LDHs, the study aims to design and develop a series of novel LiAl-LDH-based lithium adsorbents, overcoming the limitations of low adsorption capacity and vulnerability to sulfate poisoning. By bridging fundamental structure-function relationships with practical performance, the study offers theoretical insights and technical support for the development of next-generation high-performance lithium adsorbents. These advances hold significant promise for promoting sustainable lithium extraction from brines and securing the global lithium supply for clean energy technologies.

1.3.2. Goals

(1) Improving the Li^+ adsorption capacity of LiAl-LDHs via doping engineering. By regulating dopant cation species and their dosage, the structural and physicochemical properties of LiAl-LDHs are optimized to comprehensively improve the adsorption capacity, selectivity, stability and reusability of LiAl-LDHs.

(2) Enabling an anti-sulfate poisoning feature of LiAl-LDHs via steering interlayer interaction. By modulating the intercalated anions, the interlayer environments and physicochemical properties of LiAl-LDHs are steered to create a strong electrostatic repulsion region to inhibit the intercalation of SO_4^{2-} for effective and continuous Li extraction from SO_4^{2-}-type brines.

(3) Strengthening anti-sulfate poisoning performance via constructing multiple functional domains in LiAl-LDHs. Leveraging the enriched hydroxyl groups on the interface and ion exchange feature of LiAl-LDHs, SO_4^{2-} barrier domains are created at the interface and within the interlayer by organic modification to increase barrier energies of SO_4^{2-} migration, enabling highly feasible for long-term Li extraction from SO_4^{2-}-type brine.

(4) Achieving high-efficiency lithium recovery from various low-quality brines via polymer side-chain structure design. By tuning the side-chain structure of polymer building blocks, the electric charge and ionophilic properties of LiAl-LDHs are precisely controlled for purpose-driven lithium extraction from low-quality brines with different characteristics, and ultimately producing high-purity Li_2CO_3.

1.4. References

[1] B. Dunn, H. Kamath, J.M. Tarascon, Electrical Energy Storage for the Grid: A Battery of Choices, Science 334 (2011) 928-935.
[2] S. Wang, S. Zheng, Z. Wang, W. Cui, H. Zhang, L. Yang, Y. Zhang, P. Li, Superior lithium adsorption and required magnetic separation behavior of iron-doped lithium ion-sieves, Chem. Eng. J. 332 (2018) 160-168.
[3] M.L. Vera, W.R. Torres, C.I. Galli, A. Chagnes, V. Flexer, Environmental impact of direct lithium extraction from brines, Nat. Rev. Earth Environ. 4 (2023) 149-165.
[4] N. Delaporte, G. Lajoie, A. Darwiche, M.J. Vigeant, S. Collin-Martin, D. Clément, Stabilization of lithium anode with ceramic-rich interlayer for all solid-state batteries, RSC Adv. 12 (2022) 15493-15507.
[5] F. Degen, M. Winter, D. Bendig, J. Tübke, Energy consumption of current and future production of lithium-ion and post lithium-ion battery cells, Nat. Energy 8 (2023) 1284-1295.
[6] C. Liu, Y. Li, D. Lin, P.-C. Hsu, B. Liu, G. Yan, T. Wu, Y. Cui, S. Chu, Lithium Extraction from Seawater through Pulsed Electrochemical Intercalation, Joule 4 (2020) 1459-1469.
[7] Z.H. Foo, J.B. Thomas, S.M. Heath, J.A. Garcia, J.H. Lienhard, Sustainable Lithium Recovery from Hypersaline Salt-Lakes by Selective Electrodialysis: Transport and Thermodynamics, Environ. Sci. Technol. 57 (2023) 14747-14759.
[8] G. Yan, M. Wang, G.T. Hill, S. Zou, C. Liu, Defining the challenges of Li extraction with olivine host: The roles of competitor and spectator ions, Proc. Natl. Acad. Sci. 119 (2022) e2200751119.
[9] T. Kanagasundaram, O. Murphy, M.N. Haji, J.J. Wilson, The recovery and separation of lithium by using solvent extraction methods, Coord. Chem. Rev. 509 (2024) 215727.
[10] V. Balaram, M. Santosh, M. Satyanarayanan, N. Srinivas, H. Gupta, Lithium: A review of applications, occurrence, exploration, extraction, recycling, analysis, and environmental impact, Geosci. Front. 15 (2024) 101868.
[11] B. Tansel, Significance of thermodynamic and physical characteristics on permeation of ions during membrane separation: Hydrated radius, hydration free energy and viscous effects, Sep. Purif. Technol. 86 (2012) 119-126.
[12] T. Zhang, H. Bai, Y. Zhao, B. Ren, T. Wen, L. Chen, S. Song, S. Komarneni, Precise Cation Recognition in Two-Dimensional Nanofluidic Channels of Clay Membranes Imparted from Intrinsic Selectivity of Clays, ACS Nano 16 (2022) 4930-4939.
[13] Y. Orooji, Z. Nezafat, M. Nasrollahzadeh, N. Shafiei, M. Afsari, K. Pakzad, A. Razmjou, Recent advances in nanomaterial development for lithium ion-sieving technologies, Desalination 529 (2022) 115624.
[14] S. Safari, B.G. Lottermoser, D.S. Alessi, Metal oxide sorbents for the sustainable recovery of lithium from unconventional resources, Appl. Mater. Today 19 (2020) 100638.

[15] J.O. Ighalo, J.F. Amaku, C. Olisah, A.O. Adeola, K.O. Iwuozor, K.G. Akpomie, J. Conradie, K.A. Adegoke, K.O. Oyedotun, Utilisation of adsorption as a resource recovery technique for lithium in geothermal water, J. Mol. Liq. 365 (2022) 120107.
[16] A. Gao, Z. Sun, S. Li, X. Hou, H. Li, C. Wang, W. Wu, Self-assembled layered lithium manganese oxide shows ultra-large adsorption capacity and high selectivity for lithium, Chem. Eng. J. 471 (2023) 144287.
[17] R. Chitrakar, Y. Makita, K. Ooi, A. Sonoda, Lithium recovery from salt lake brine by H_2TiO_3, Dalton Trans. 43 (2014) 8933-8939.
[18] X. Li, L. Chen, Y. Chao, L. Zhu, G. Luo, J. Sun, L. Jiang, W. Zhu, Z. Liu, C. Xu, Highly selective separation of lithium with hierarchical porous lithium-ion sieve microsphere derived from MXene, Desalination 537 (2022) 115847.
[19] L. Zhang, T. Zhang, Y. Zhao, G. Dong, S. Lv, S. Ma, S. Song, M. Quintana, Doping engineering of lithium-aluminum layered double hydroxides for high-efficiency lithium extraction from salt lake brines, Nano Res. 17 (2024) 1646–1654.
[20] R. Zhang, S. Liu, C. Lian, J. Yu, S. Lin, Machine Learning-Accelerated Design of High-Efficient Lithium Adsorbents for Salt Lake Brines, Angew. Chem., Int. Ed. 64 (2025) e202503644.
[21] S. Lv, Y. Zhao, L. Zhang, T. Zhang, G. Dong, D. Li, S. Cheng, S. Ma, S. Song, M. Quintana, Anion regulation strategy of lithium-aluminum layered double hydroxides for strengthening resistance to deactivation in lithium recovery from brines, Chem. Eng. J. 472 (2023) 145026.
[22] Y. Zhang, J. Liu, Y. Yang, S. Lin, P. Li, Preparation of granular titanium-type lithium-ion sieves and recyclability assessment for lithium recovery from brines with different pH value, Sep. Purif. Technol. 267 (2021) 118613.
[23] L. Bao, J. Zhang, W. Tang, S. Sun, Synthesis and adsorption properties of metal oxide-coated lithium ion-sieve from salt lake brine, Desalination 546 (2023) 116196.
[24] J. Chen, S. Lin, J. Yu, Instant Interlayer Restoration Strategy for Lithium Adsorption Engineering Enhancement in Sulfate-type Brines, ACS Appl. Mater. Interfaces 16 (2024) 34850-34858.
[25] J. Chen, K. Huang, J. Du, C. Lian, J. Yu, S. Lin, Why is aluminum-based lithium adsorbent ineffective in Li^+ extraction from sulfate-type brines, AIChE J. 69 (2023) e18176.
[26] W. Xiao, X. Jiang, X. Liu, W. Zhou, Z.N. Garba, I. Lawan, L. Wang, Z. Yuan, Adsorption of organic dyes from wastewater by metal-doped porous carbon materials, J. Cleaner Prod. 284 (2021) 124773.
[27] Z. Ma, W. Shi, K. Yan, L. Pan, G. Yu, Doping engineering of conductive polymer hydrogels and their application in advanced sensor technologies, Chem. Sci. 10 (2019) 6232-6244.
[28] H.-M. Liu, X.-J. Zhao, Y.-Q. Zhu, H. Yan, DFT study on MgAl-layered double hydroxides with different interlayer anions: structure, anion exchange, host–guest interaction and basic sites, Phys. Chem. Chem. Phys. 22 (2020) 2521-2529.
[29] Q. Wang, D. O'Hare, Recent Advances in the Synthesis and Application of Layered

Double Hydroxide (LDH) Nanosheets, Chem. Rev. 112 (2012) 4124-4155.

Chapter 2. Background

2.1. Introduction

Lithium (Li) is a critical element for the clean energy transition, for which the global demand is growing exponentially [1]. The demand for Li is expected to grow at over 30% per annum by 2030 [2]. The sustainable supply of Li is, therefore, particularly urgent and challenging [3]. Currently, the main sources of Li are ores (including hard-rock minerals and Li-enriched clays) and brines (including seawater, salt lake brines, geothermal brines, and oilfield brines) (Figure 2.1). Herein, harvesting Li from brines, typically salt lake brines, has attracted increasing interest from the lithium industry due to the abundant reserves (thousands of times greater than the ore reserves), environmentally friendly operation and cost-effectiveness compared to conventional ore mining [4-6]. Therefore, one important way to enable the sustainable supply of lithium is to develop a promising approach for lithium extraction from brines.

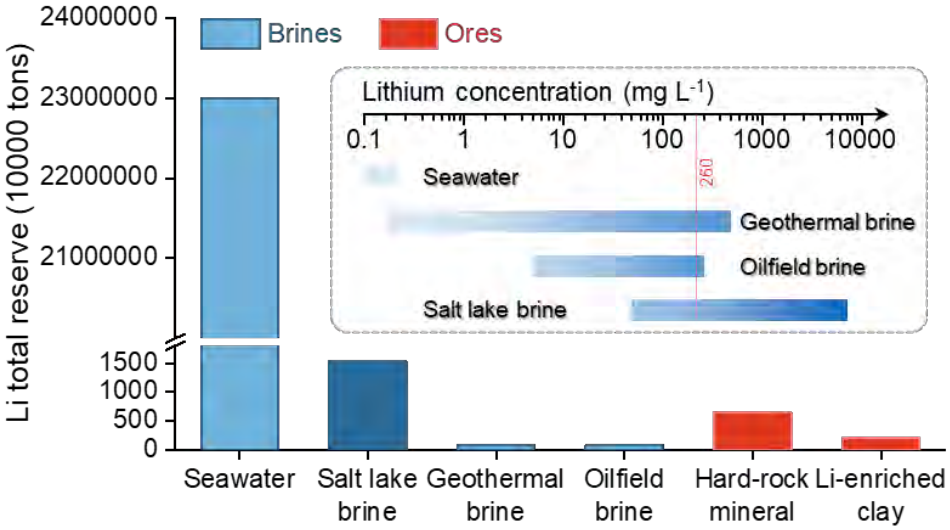

Figure 2.1 Global lithium resource reserve in brines and ores, and the range of Li concentration in different type of brines.

(Note: The statistics are from the Mineral Commodity Summaries 2023 and the Mineral Resources Program by U.S. Geological Survey (USGS).)

Li in brines is normally accompanied by many high concentrations of cations such as Mg^{2+}, Na^{+}, K^{+}, and Ca^{2+}. These cations, especially Mg^{2+}, possess similar ionic radii to Li^{+} in bare or hydrated state [7], which causes it challenging to recover and produce

high purity lithium from brines [8,9]. In such cases, alternative lithium extraction technologies have been proposed, involving adsorption [10], nanofiltration [11], electrodialysis [12], reverse osmosis [13], evaporation concentration [14], and so forth (Figure 2.2).

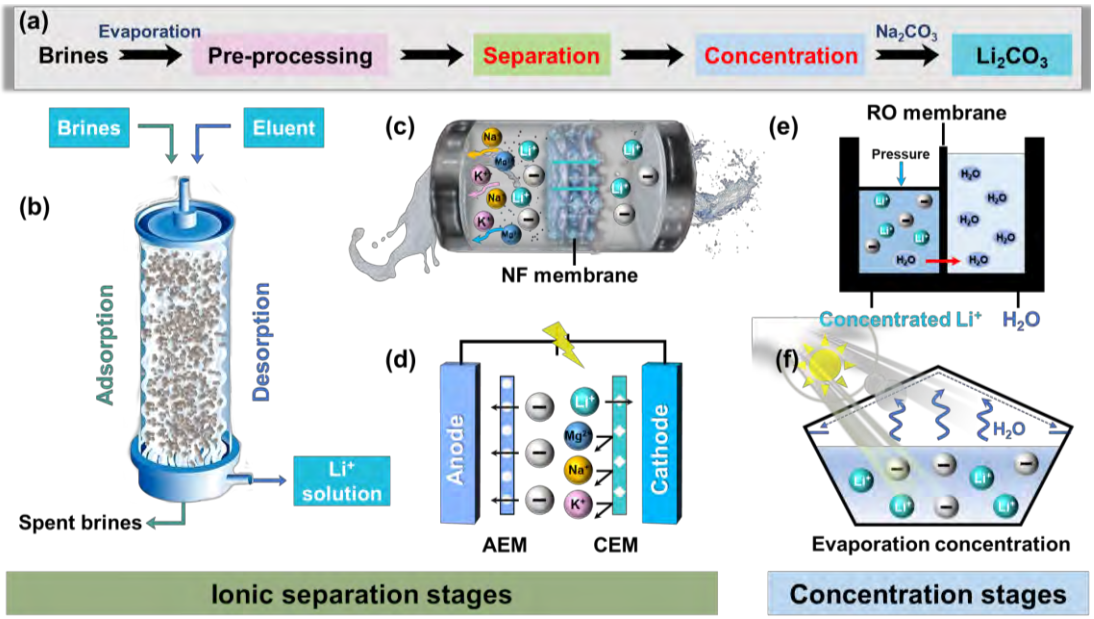

Figure 2.2 Schematic of the technologies for lithium recovery from brines. (a) The general recovery process. Li^+ separation stages include three technologies, (b) adsorption, also known as ion exchange, (c) nanofiltration, NF, and (d) electrodialysis. Li^+ concentration stages include two technologies, (e) reverse osmosis, RO, and (f) evaporation concentration.

(Note: AEM, anion exchange membrane; CEM, cation exchange membrane; RO, reverse osmosis.)

Of the above advanced technologies, adsorption is not only a critical procedure in lithium extraction process, but also is considered to the most versatile technique for direct lithium extraction from salt lake brines, especially those with low grades and high Mg^{2+}/Li^+ ratios, due to the advantages of the minimal pre-processing requirement of the brine, high lithium selectivity and recovery, additional concentration function, cost-effective and environment-friendly advantages [15-17]. Notably, the lithium recovery efficiency significantly depends on the lithium adsorbents. The selection of lithium adsorbents commonly relies on the performance of adsorbents (including adsorption capacity, selectivity, stability, cycle regeneration, etc.), the structures of adsorbents (including macro and microstructure), brine characteristics (including pH,

lithium concentration, temperature, Mg^{2+}/Li^{+} ratio, etc.). Thus, this chapter will focus on various lithium adsorbents and the full adsorption process for the extraction and recovery of Li^{+} from brines.

2.2. Various lithium adsorbents and structure-property relationship

The mainly studied lithium adsorbents involve inorganic metal-based adsorbents and organic adsorbents. The common metal-based adsorbents are lithium-aluminum layered double hydroxides (LiAl-LDHs), lithium titanium oxide type lithium-ion sieves (LTO-LISs), and lithium manganese oxide type lithium-ion sieves (LMO-LISs), in which template Li^{+} are introduced and then eluted from the crystalline structure of aluminum hydroxides or Mn and Ti oxides to generate lithium ion-specific vacancies for selective lithium extraction due to ion sieve and memory effect (Figure 2.3) [18]. Organic adsorbents include ion-imprinted polymers (Li-IIPs) and ion-exchange resins. Among them, heterocyclic compounds, such as crown ethers, attract particular attention by virtue of their ability to bind selectively to Li^{+} [19].

Figure 2.3 Schematic of selective lithium recovery by lithium adsorbents.

2.2.1. LiAl-LDHs

The structure and property: Lithium-aluminum layered double hydroxides were first derived from aluminum hydroxides, which were coated on ion exchange resins in 1978 to recover lithium from brine [20,21], forming crystalline layered double hydroxides upon contact with Li^{+}. The products were then eluted with dilute LiCl solution to recover the adsorbed Li^{+} [15]. Such produced adsorbents were called lithium-aluminum layered double hydroxides (LiAl-LDHs) [22].

The chemical structure model of LiAl-LDHs is presented in Figure 2.4a. Specifically, the structures of LiAl-LDHs, formed by the intercalation of lithium salts into the ordered octahedrons vacancies in the structure of $Al(OH)_3$ layers [23,24], are

hexagonal layered structure, where Al^{3+} occupy two-thirds of the octahedrons vacancies created by close-packed oxygen layers and the Li^+ (~0.68 Å) are inserted in the remaining unoccupied vacancies with radius of approximately 0.70 Å to form $[LiAl_2(OH)_6]^+$ layers by hydrogen bonding, electrostatic interaction, and van der Waals forces [25-27]. During the insertion of Li^+ into the $Al(OH)_3$ layers, the anions (e.g., Cl^-, NO_3^-, CO_3^{2-}) and water molecules are incorporation into the interlayer to keep charge balance [28], and then $[LiAl_2(OH)_6]^+$ layers are separated along the c-axis [23,29].

Lithium intercalation/deintercalation mechanisms: Among the metal-based adsorbents, the lithium intercalation and deintercalation mechanisms of LiAl-LDHs are the clearest, and were studied as early as 1998 [30], which have been checked, supplemented, and improved by recent researches. To extract Li^+ from brines, the obtained LiAl-LDHs have to be desorbed and activated with deionized water or dilute Li^+ solution to release octahedrons vacancies. Li et al. [31] reported that based on the structural memory effect, specific channels are formed during the desorption of LiAl-LDHs, involving specific layer spacing, sorption site sizes and interlayer path networks. Numerous interfacial channels with highly matched geometric configuration of Li^+ are created between the layers. Therefore, the Li^+ is quite easily inserted into the space between LDH layers. At the same time, the radius of Li^+ (~0.68 Å) is slightly smaller than that of octahedrons vacancies (0.70 Å) [25], hence Li^+ tends to migrate from the interlayer space to the vacancies to be adsorbed [30]. Furthermore, for the charge balance, the intercalation of Li^+ is accompanied by the insertion of anions [32]. Intercalation of Li^+ results in weakened hydrogen bonding due to electrostatic repulsion between Li^+ and protons, which provides the feasibility of insertion of anions between the layers [30]. In summary, taking Cl^- as an anion as an example, the intercalation (Equation 2.1) and deintercalation (Equation 2.2) mechanisms of Li^+ can be expressed by the following formulas [24,33].

$$LiCl{\cdot}2Al(OH)_3{\cdot}mH_2O + H_2O \rightarrow xLiCl + (1\text{-}x)LiCl{\cdot}2Al(OH)_3{\cdot}(m+1)H_2O \quad (2.1)$$

$$xLiCl(brines) + (1\text{-}x)LiCl{\cdot}2Al(OH)_3{\cdot}(m+1)H_2O \rightarrow LiCl{\cdot}2Al(OH)_3{\cdot}mH_2O + H_2O \quad (2.2)$$

Limitations and challenges: As mentioned earlier, LiAl-LDHs have been applied as the lithium extraction adsorbents on industrial- and commercial-scale applications. However, LiAl-LDH have inherently limited Li^+ theoretical maximum adsorption capacity (~ 30 mg g^{-1}) [34], which limits the further development of LiAl-LDH. Moreover, the practical adsorption capacity of LiAl-LDH (4 ~ 8 mg g^{-1}) was always far below the theoretical capacity [35]. Additionally, LiAl-LDHs readily suffer from the

'sulfate ion (SO_4^{2-}) poisoning' effect in SO_4^{2-}-type brines, causing the gradual decrease in adsorption capacity. Therefore, improvement in the Li^+ adsorption capacity and anti-sulfate poisoning property of LiAl-LDHs has become major challenges to foster further progress of the Li extraction industry.

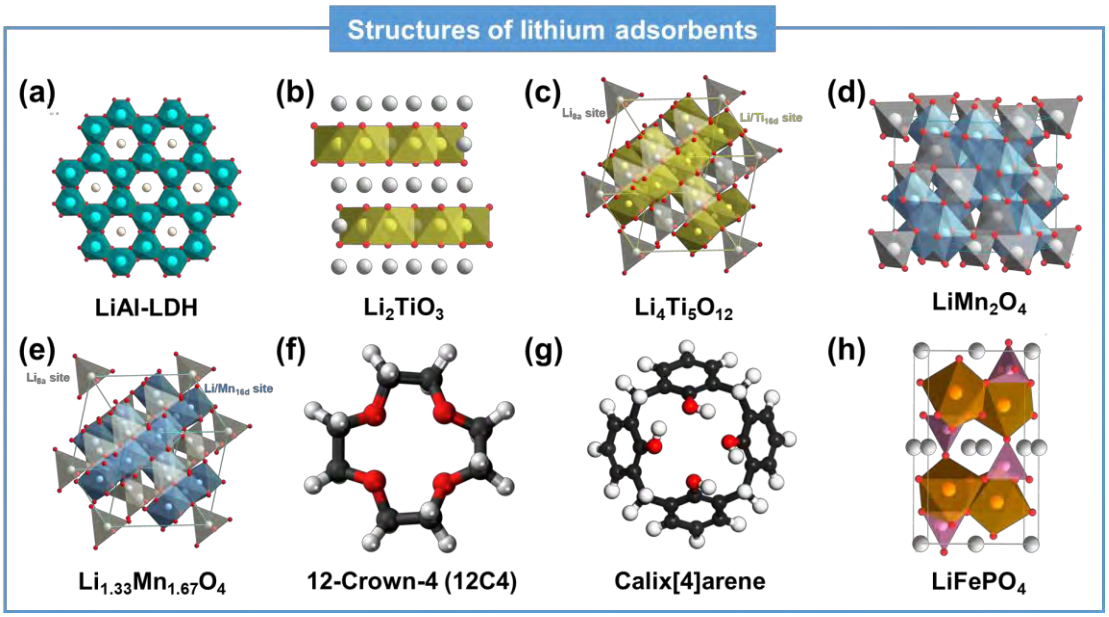

Figure 2.4 Schematic structures of various lithium adsorbents. (a) LiAl-LDH, (b) Li_2TiO_3, (c) $Li_4Ti_5O_{12}$, (d) $LiMn_2O_4$, (e) $Li_{1.33}Mn_{1.67}O_4$, (f) 12-Crown-4, (g) Calix[4]arene, (h) $LiFePO_4$.

(Note: The gray, green, yellow, blue, orange, violet, black, red, and white spheres represent the Li, Al, Ti, Mn, Fe, P, C, O, and H atoms, respectively.)

2.2.2. LTO-LISs

The structure and property: Lithium titanates were earlier used in the lithium battery industry due to excellent cyclability. The first exploration of lithium extraction using lithium titanates occurred in Japan in 1989, when Onodera et al. [36] successfully prepared a new inorganic titanium compound, now known as lithium titanium oxide type lithium-ion sieves (LTO-LISs), with high selectivity for Li^+ via calcining a mixture of Li_2CO_3 and TiO_2 and treating the pyrolysis product with acid. Since then, LTO has been extensively studied.

Currently, LTO-LISs are mainly divided into two types: the layered titanate H_2TiO_3 and spinel phase $H_4Ti_5O_{12}$ [35]. Layered H_2TiO_3 are derived from layered Li_2TiO_3 precursors. To better describe the crystal structure, Li_2TiO_3 precursors can also be expressed as $Li[Li_{1/3}Ti_{2/3}]O_2$, consisting of cubic close packed O, as well as Li and Ti placed in octahedral voids, where Ti and O atoms form a $[TiO_6]$ octahedral structure,

and Li are located in the adjacent two [TiO_6] octahedra, forming alternating ($LiTi_2$) and (Li) layers [37]. The (Li) layers are filled only by Li atoms, while 1/3 of Li and 2/3 of Ti occupy another ($LiTi_2$) layers [38]. Therefore, Li in the (Li) layers account for 75% of the total lithium in the Li_2TiO_3 structure, while the remaining 25% of Li are located in the ($LiTi_2$) layer [39], as shown in Figure 2.4b. Further, layered H_2TiO_3 are obtained by replacing Li^+ in Li_2TiO_3 with H^+ using acid. Spinel phase $Li_4Ti_5O_{12}$, another LTO-LISs, are formed by the interspaced arrangement of [LiO_4] tetrahedral structural units and [TiO_6] octahedral structural units with $Fd\bar{3}m$ space group as well as cubic symmetry, and a lattice constant of 0.836 nm [40]. As displayed in Figure 2.4c, in the crystal structure of $Li_4Ti_5O_{12}$, Li^+ occupy the tetrahedral 8a sites and 1/6 of the octahedral 16d sites, while the remaining octahedral 16d sites are occupied by Ti^{4+} with a Li^+/Ti^{4+} ratio of 1:5 [41]. Besides, the oxygen ions are located at position 32e. Thus, spinel phase $H_4Ti_5O_{12}$ can be represented as $Li_{(8a)}[Li_{1/3}Ti_{5/3}]_{(16d)}O_{4(32e)}$ [42].

Lithium intercalation/deintercalation mechanisms: In general, the major Li^+ intercalation and deintercalation mechanisms of LTO-LIS are deemed to be ion exchange mechanism between Li^+ and H^+, and this exchange happens during the preparation, adsorption, and desorption processes of LTO-LISs, which can be expressed as following:

$$H_2TiO_3 + 2Li^+ \rightleftharpoons Li_2TiO_3 + 2H^+ \quad (2.3)$$

$$H_4Ti_5O_{12} + 4Li^+ \rightleftharpoons Li_4Ti_5O_{12} + 4H^+ \quad (2.4)$$

Limitations and challenges: Although the theoretical Li^+ adsorption capacity is high (127.3 mg g^{-1} for H_2TiO_3 and 60.8 mg g^{-1} for $H_4Ti_5O_{12}$), both the Li^+ adsorption and desorption rates are relatively slow (requiring one day to attain equilibrium at room temperature) [39]. In addition, due to the mechanism of ion-exchange, the adsorption process of LTO-LISs always requires a high-alkaline solution environment, which is difficult to realize in most brines. Other limitation of LTO-LISs applications is the relatively high cost of preparation. Overall, LTO-LIS is also gradually showing industrial promise, especially for alkaline brines. Before that, however, the disadvantages of slow and costly extraction have to be addressed.

2.2.3. LMO-LISs

The structure and property: One of the first lithium manganese oxide type lithium-ion sieves (LMO-LISs) was λ-MnO_2. In 1981, Hunter et al. [43] found that the lithium of $LiMn_2O_4$ could be almost completely desorb and converse to MnO_2 after

acid treatment, while the resultant material reserved the structural framework of the $LiMn_2O_4$, which was called λ-MnO_2. Since this discovery, numerous LMO-LISs have been well developed.

The typical precursors of LMO-LISs present spinel structures. Among them, the most common LMO-LISs precursors include $LiMn_2O_4$, $Li_{1.33}Mn_{1.67}O_4$ (or $Li_4Mn_5O_{12}$), and $Li_{1.6}Mn_{1.6}O_4$ (or $Li_2Mn_2O_5$), which produce the λ-MnO_2, $MnO_2{\cdot}0.31H_2O$, and $MnO_2{\cdot}0.5H_2O$ with Li^+ selective adsorption capacity by acid treatment [44,45]. LMO-LISs can be represent by one general formula $Li_{1+x}Mn_{2-x}O_4$ ($0 \leq x \leq 0.33$) [46]. At x is 0, the $LiMn_2O_4$ is obtained. $LiMn_2O_4$ is the most typical class of spinel (formula AB_2O_4) with a cubic crystal structure belonging to the $Fd\bar{3}m$ space group, and the lattice constant of 0.825 nm [47]. The structure of $LiMn_2O_4$ was shown in Figure 2.4d. The oxygen atoms are densely packed in a face-centered cubic configuration with adjacent oxygen octahedra common-edge connection, the Li^+ occupy the tetrahedral 8a sites, and the Mn^{3+} and Mn^{4+} are randomly located at the octahedral 16d sites in a molar ratio of 1:1, and the oxygen anions occupy the 32e sites of the face-centered cubes [48]. Thus, the $LiMn_2O_4$ spinel can be represented by the formula of $Li_{(8a)}[Mn^{3+}Mn^{4+}]_{(16d)}O_{4(32e)}$ with a mean oxidation state of 3.5+ for Mn [49]. When x is 0.33, the "0.33" of Li implies that some Li^+ occupy the 16d sites and replace part of the Mn ions without changing the whole crystal framework, and the oxidation state of Mn is 4+ [50,51]. It can be seen from Figure 2.4e that $Li_{1.33}Mn_{1.67}O_4$ (or $Li_4Mn_5O_{12}$) has similar chemical structure as $Li_4Ti_5O_{12}$. For $Li_{1.6}Mn_{1.6}O_4$, a new type of spinel-structured LMO-LISs, two models $Li_{(8a)1}Li_{(16c)0.2}Li_{(16d)0.4}Mn_{(16d)1.6}O_{(32e)4}$ and $Li_{(8a)1}Li_{(16d)0.5}Mn_{(16d)1.5}O_{(32e)3.75}$ are favored, where Li^+ mainly occupy the 8a and 16d sites, and Mn^{4+} occupy the 16d sites of a cubic closed-packed oxygen framework [52,53]. According to the formulas of precursors, the theoretical maximum lithium capacities of λ-MnO_2, $MnO_2{\cdot}0.31H_2O$, and $MnO_2{\cdot}0.5H_2O$ are 39.9, 59.5, and 72.8 mg g^{-1}, respectively [54].

Lithium intercalation/deintercalation mechanisms: Compared to the LiAl-LDH and LTO-LISs, the Li^+ intercalation/deintercalation mechanisms of LMO-LISs are more complex and controversial. In recent years, redox and ion exchange mechanisms have been commonly accepted by researchers. For $LiMn_2O_4$, the intercalation and deintercalation of Li^+ were first proposed in research by Hunter as a pair of redox reactions [43], which can be expressed as following Equation 2.5 (where □ represents vacancies for Li^+). Such conclusion was confirmed and elaborated in the work of Gao et al. [51]. They suggested that Li occupying only the 8a site on $LiMn_2O_4$, i.e., $[Li_{(8a)}O_4]$

groups, are decomposed during acid treatment. Meanwhile, due to $[Mn^{3+}O_6]$ octahedrons are not as steady as Mn^{3+}, Mn^{3+} release electrons to become stable Mn^{4+} accompanying by the $[Mn^{3+}O_6]$ accept electrons and then decompose to Mn^{2+}. Finally, the generated O^{2-} react with H^+ to form H_2O. However, the individual redox mechanism hardly explains the phenomenon of the positive effect of the adsorption capacity with solution pH in the adsorption process. Therefore, Ooi et al. [55] and Feng et al. [45] put forward a composite mechanism of redox and ion exchange that Mn^{3+} deliver redox sites and Mn^{4+} supplied ion-exchange sites. Specifically, $LiMn_2O_4$ was firstly treated by HCl. Then, the $[Li_{(8a)}O_4]$ groups decomposed, and $[Mn^{3+}O_6]$ group released electrons into stable $[Mn^{4+}O_6]$, and another $[Mn^{3+}O_6]$ accepted electrons and broke down. Finally, Mn^{2+}, Li^+ and H_2O were produced and went into solution, and only $[Mn^{4+}O_6]$ groups constructed the crystal skeleton of λ-MnO_2.

$$Li_{(8a)}[Mn^{3+}Mn^{4+}]_{(16d)}O_{4(32e)} + 8H^+ \rightarrow 3\square_{(8a)}\left[Mn_2^{4+}\right]O_{4(32e)} + 4Li^+ + 2Mn^{2+} + 4H_2O \quad (2.5)$$

In the cases of $Li_{1.33}Mn_{1.67}O_4$ and $Li_{1.6}Mn_{1.6}O_4$, the ion-exchange is considered as the Li^+ intercalation and deintercalation mechanism based on the stable oxidation state of Mn [56]. For instance, Wang et al. [57] used complexometric titration with EDTA to measure the amount of Mn, and found that the valence of Mn in $Li_{1.6}Mn_{1.6}O_4$ was close to 4+. Furthermore, the change in the Mn valence during adsorption and desorption of Li^+ was feeble, which meant that the redox reaction could be neglected. Therefore, the Li^+ intercalation/deintercalation reaction of $Li_{1.33}Mn_{1.67}O_4$ (Equation 2.6) and $Li_{1.6}Mn_{1.6}O_4$ (Equation 2.7) may be expressed by the following equations:

$$H_4Mn_5O_{12} + 4Li^+ \rightleftharpoons Li_4Mn_5O_{12} + 4H^+ \quad (2.6)$$

$$H_2Mn_2O_5 + 2Li^+ \rightleftharpoons Li_2Mn_2O_5 + 2H^+ \quad (2.7)$$

Limitations and challenges: The Mn loss induced by Jahn-Teller effect ($Mn^{3+} \rightarrow Mn^{3+} + Mn^{2+}$) has been deemed to be the most severe limitation for the practical application of LMO-LISs during the desorption with acid treatment (0.1-0.5 mol L^{-1}) [54]. For $LiMn_2O_4$, the desorption process is accompanied by the disproportionation reaction of Mn^{3+}, resulting in the continues manganese dissolution. Although disproportionation theoretically does not occur in $Li_{1.33}Mn_{1.67}O_4$ and $Li_{1.6}Mn_{1.6}O_4$ owing to Mn valence close to 4+, the strong acid solution can corrode the LMO during acid desorption [58]. As a recent example, Bao et al. [59] prepared $Li_{1.6}Mn_{1.6}O_4$ for recovering Li^+ from salt lake brine. However, the adsorption amount decreased by 44.2% and the Mn loss was more than 15% after 10 adsorption-desorption cycles.

2.2.4. Ion-Imprinted polymers

The structure and property: In 1967, Pedersen successfully synthesized a series of cyclic polyether, and found that most of them were capable of complexing with alkali and alkaline earth metal cations by ion-dipole interaction [60]. Inspired in this work, ion-imprinted technique based on polymers have been rapidly developed.

Recently, the ion-imprinted polymers for lithium extraction (Li-IIPs) mainly include crown ether and calixarene [61,62], which are macrocyclic organic ligands with unique cavity structures matching Li^+ diameter (1.36 Å) [63], especially 12-crown-4-ether (12C4) with the ring diameter of 1.20-1.50 Å and calix[4]arene with the ring diameter of 1.20-1.60 Å [64,65]. The structures were shown in Figure 2.4f-g. Herein, 12C4 is liquid at ambient temperature, making it difficult to be recovered after the adsorption process. Therefore, crown ether needs to be immobilized or grafted onto solid materials. For instance, 12C4 incorporated graphene-in-polyethersulfone (PES) nanofiber membrane owned superior Li^+ uptake of 86.3 mg g^{-1}, and adsorption capacity could still maintain more than 93% of initial value after 10 regeneration cycles [66]. Calix[4]arene and their derivatives have been attracting attention as another types of host compounds with Li^+ discrimination properties. Calix[4]arene exhibit a high adsorption potential, while the relatively slow kinetics for Li^+. A high-efficient recovery of Li^+ from seawater had been realized within 24 h by using ester-functionalized Li^+ imprinted composite membrane adsorbent containing calix[4]arene with poly-dopamine PDA modified [67].

Lithium intercalation/deintercalation mechanisms: The intercalation mechanisms of Li^+ into Li-IIPs can be attributed to two aspects: i) the "macrocyclic effect" from the size and shape of the generated cavities; and i) the "chelating effect" between the four oxygen atoms of ligand and Li^+ [68]. Moreover, in acidic conditions, the oxygen atoms of ligand trend to protonate, inducing the electrostatic repulsion towards Li^+, weakening the complexation of ligand with Li^+ [61]. Hence, the deintercalation of Li-IIPs can be conducted by using acid solution. Taking 12C4 as an example, the intercalation and deintercalation processes of Li^+ can be expressed as following:

$$Li^+ + 12C4 \rightleftharpoons 12C4\text{-}Li^+ \quad (2.8)$$

Limitations and challenges: Although the crown ethers and calixarenes have been recognized as the promising adsorption units for alkali and alkaline earth metal cations, the industrial application still is limited by several practical problems, including high

cost, toxicity, and suboptimal selectivity. Particularly, compared with the inorganic metal-based lithium adsorbents, the preparation procedures of Li-IIPs are complicated and cumbersome, and the raw materials are relatively expensive, which cause the high cost. Moreover, the selectivity of Li-IIPs for Li^+ is remarkable low than inorganic metal-based lithium adsorbent, and typical the separation factor can only reach approximately 10. Apparently, the selectivity of Li-IIPs is rarely sufficient for industrial requirements in brines with high Mg^{2+}/Li^+ ratio.

2.2.5. Other lithium adsorbents

As one of the most sophisticated adsorbents, the researches of ion-exchange resins for lithium extraction are gradually reported as well [69,70]. There are numerous types of Li-exchange resins. According the ionic form of resin, it can be divided into Na^+ type and H^+ type, while depending on the acidity strength, it can also be classified into strongly acidic resin and weakly acidic resin [71,72]. Normally, the capacity and selectivity of ion-exchange resins mainly are determined by the nature of the acidic functional group, the form of the cation, and the density of the structure [72,73]. Lemaire et al. [74] used Amberlite IR 120 resin to adsorb Li^+ from LiCl solution and found that the adsorption capacity of sodium form was higher than that of hydrogen form. Güneysu reported that the adsorption of the carboxylated weakly acidic H^+ type resin (CNP 80) outperformed sulfonated strongly acidic Na^+ type resin (Armfield) [72]. However, the ion-exchange resins show poor selectivity for Li^+, which is ascribed to the low affinity towards Li^+ compared to other cations [74]. The adsorption capacity of commercial strong acid-type cation exchange UBK 10 resin (Na type) in environmental lithium-bearing solution followed the order: $K^+ > Li^+ > Ca^{2+} > Mg^{2+}$ [75]. Therefore, the ion-exchange resins are effective in selective extracting Li^+ only after coupling inorganic metal-based adsorbents. In fact, in the first study on the use of ion-exchange resins to selectively extract and recover lithium from brines in the 1970s, the Li extraction was realized by compounding the resin with $Al(OH)_3$ [21].

In addition to the aforementioned promising adsorbents, several other metal oxides also show certain Li extraction ability, including lithium-iron-phosphates ($LiFePO_4$) [76], Zr-phosphate ($Zr(LiPO_4)_2$) [77], Sb-oxides ($LiSbO_3$) [78], Ta-oxides ($LiTaO_3$) [79], $H_8Nb_{22}O_{59}\cdot 8H_2O$ [80], and so forth. The theoretical maximum Li^+ adsorption capacity of those metal oxide adsorbents ranges from 22 to 53 mg g^{-1}. Nevertheless, their inferior adsorption selectivity for Li^+ and complicated adsorption-desorption

procedures severely hinder their application in lithium extraction from brines. For example, $LiFePO_4$ (Figure 2.4h) with the theoretically possible maximum Li^+ adsorption capacity of 44 mg g^{-1} is capable of recovering monovalent cations, in which the presence of Na^+ and K^+ in brines will compete the adsorption sites [81]. Meanwhile, for the reason that the adsorption process is primarily dominated by redox reactions ($Fe^{3+}PO_4 + e^- + Li^+ \rightarrow LiFe^{2+}PO_4$), oxidizing agents are required [76], which made it has attracted attention in the field of electrochemical lithium extraction [82,83]. Therefore, these materials used as adsorbents have rarely been reported in recent years.

Recently, inspired by the specific coordination of fluorine-containing electrolytes towards Li^+ in lithium-ion batteries, a novel F-rich supramolecular nano-container crosslinked hydrogel with extraordinary Li^+ adsorption capacity (122.3 mg g^{-1}) and $\alpha_{Li/Na}$ (153.72) was prepared, which provides a new insight into the design of lithium adsorbents [84]. In the future, more delicate research as well as practical application evaluation should be carried out.

2.3. Comparison of various lithium adsorbents

After elucidating the structures and performances of various Li extraction adsorbents, it is worth to perform a comprehensive comparison between different adsorbents. For visual comparison, several figures of merit were here proposed, as shown in Figure 2.5.

In the case of maximum adsorption capacity (q_m), LTO-LISs and LMO-LISs possess significantly higher q_m, wherein the average reach 32.79 and 33.65 mg g^{-1}, and medium values are 36.13 and 32.72 mg g^{-1}, respectively (Figure 2.5a). In contrast, LiAl-LDHs exhibited lowest q_m. In general, the order of the actual adsorption capacity followed that of the theoretical maximum adsorption capacity. LiAl-LDHs and resins typically own fast Li^+ adsorption kinetics (Figure 2.5b). In comparison, the Li extraction processes of LTO-LISs and LMO-LISs are remarkable slow, usually lasting 12-24 h. Based on the results of q_m and adsorption equilibrium time, Li-IIPs seem to have relatively balanced adsorption ability. However, the practical applications of Li-IIPs are hinder by their poor selectivity (Figure 2.5c). Considering the high Mg^{2+}/Li^+ ratio of brines, the Li^+ selectivity is a vital indicator for assessing the practical potential of lithium adsorbents. Three common inorganic metal oxides adsorbents (namely LiAl-LDHs, LTO-LISs and LMO-LISs) show considerable lithium-magnesium separation capability with extraordinary $\alpha_{Li/Mg}$, normally greater than 100. Specifically, LTO-LISs

present better Li extraction than others in the brines containing Ca^{2+}, while LMO-LISs are slightly superior to LTO-LISs for Li extraction in alkali metal brines. The resins possess almost no selectivity for lithium extraction, so comparative analyses of their performance are unavailable in this study. The excellent stability and regeneration ability always are expected, and the promising adsorbents need to be in the upper right area of Figure 2.5d. A quick glance at the area will suffice to see that LiAl-LDHs show best reusability, followed by LTO-LISs, while LMO-LISs are less reusable due to the Mn loss induced by Jahn-Teller effect [54]. Notably, LiAl-LDHs require a simple desorption procedure in water without dissolution loss [85], whereas others, including LTO-LISs, LMO-LISs, Li-IIPs and resins, rely on strong acids (such as HCl) to complete the desorption process, which may not only corrode equipment, but also contaminate the brine.

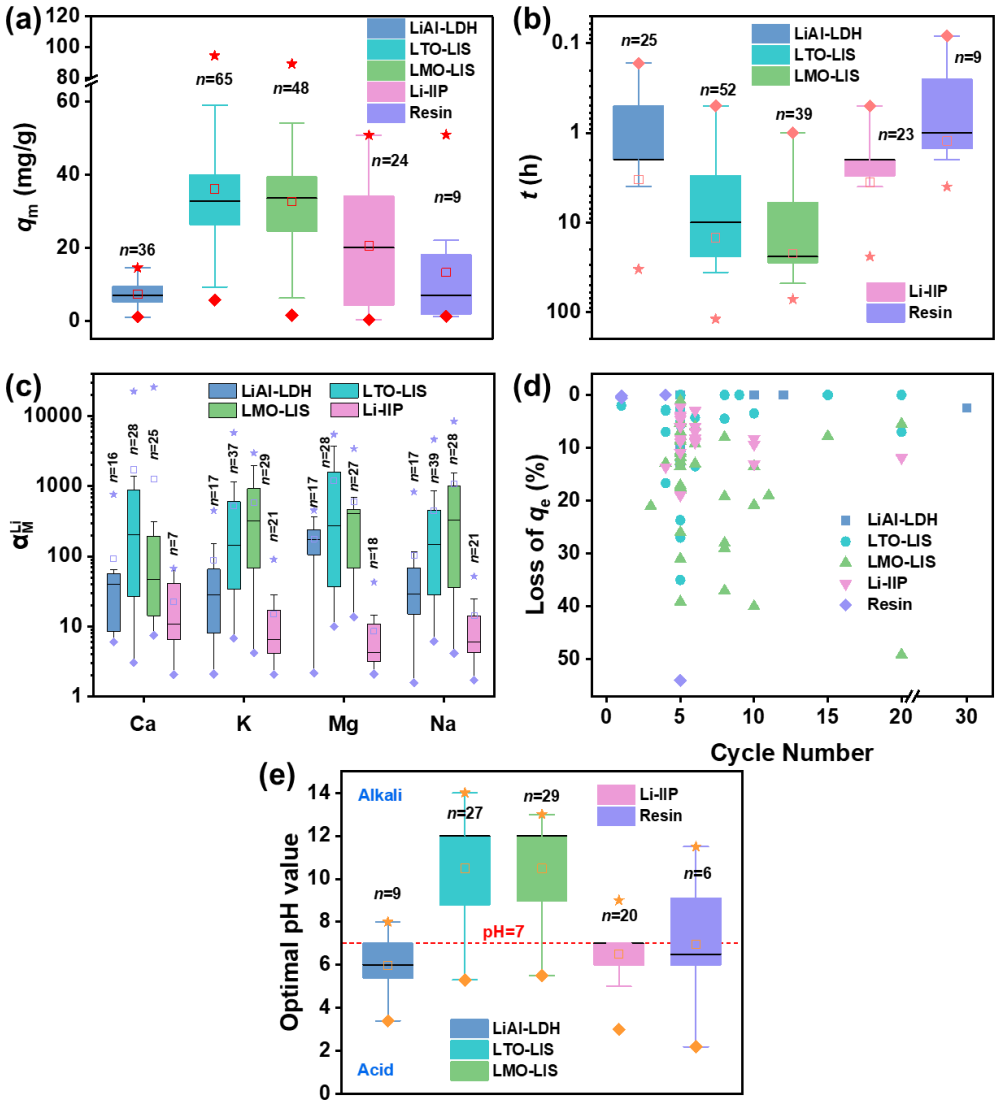

Figure 2.5 Comparison of various lithium adsorbents. (a) Adsorption capacity, (b)

adsorption equilibrium time, (c) Li^+ selectivity for, (d) regeneration stability, and (e) optimal pH value of LiAl-LDHs, LTO-LIS, TMO-LIS, Li-IIPs, and Resins.
(Note: The "★" and "♦" stand for the maximum and minimum values, respectively. The upper and lower edges of the boxes are 75% and 25% of the data, and the cross line in the box refers the median value and the "□" refers the mean value. Data were collected from cited literatures, and n in the legend is the number of obtained data.)

Moreover, pH regulation of brines is impractical before actual applications, thus comparison of effective pH ranges between adsorbents is of major significance. As presented in Figure 2.5e, the LiAl-LDHs, Li-IIPs, and resins exhibit the best Li extraction performance in common neutral brines. Whereas, LTO-LISs and LMO-LISs have the highest Li^+ adsorption capacity in basic conditions owing to the Li^+/H^+ exchange adsorption mechanism. Unfortunately, most brines are normally in a relatively steady neutral environment, suggesting that the additional alkali is necessary to be added to the brines prior to extraction using both LISs, which dramatically increases the cost of lithium extraction.

Based on the above results, performance comparison heatmap was plotted in Figure 2.6. Taking the all levels into account, LiAl-LDHs are currently the most mature lithium adsorbents for industrial applications. The major challenges for LiAl-LDHs remain to enhance the adsorption capacity and prevent SO_4^{2-} poisoning. Therefore, the chapter will subsequently focus on LiAl-LDHs for discussion and synthesis.

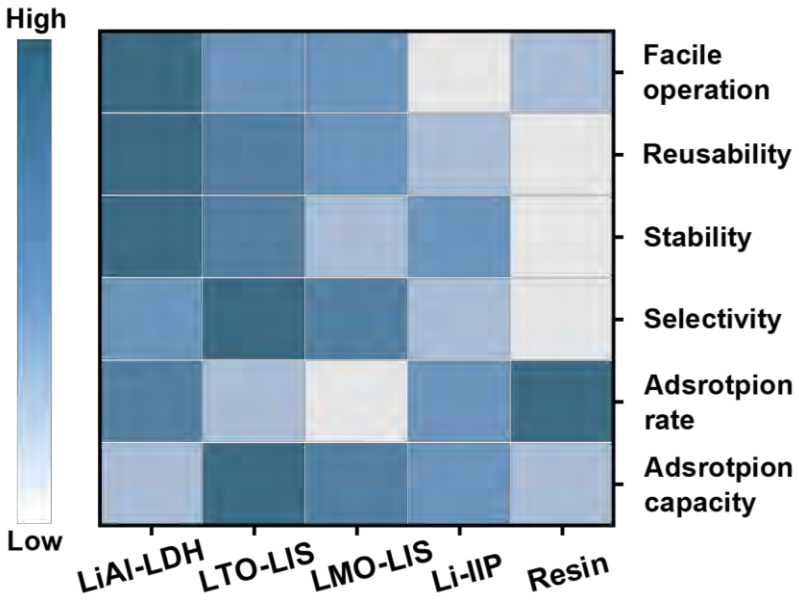

Figure 2.6 Performance heatmap of LiAl-LDHs, LTO-LIS, TMO-LIS, Li-IIPs, and Resins.

2.4. Conclusions and perspectives

As technology advances, especially in lithium-ion batteries, the demand for lithium resources is soaring. Due to the endless lithium resources in the brine, lithium recovery from brines undoubtedly attracts more interest and desires more advanced selective Li extraction processes. Among various advanced techniques, adsorption is considered to the most versatile technique for direct lithium recovery from brines owing to minimal pre-processing requirement, high lithium recovery and selectivity, cost-effective and environment-friendly advantages. Consequently, the researches on lithium adsorbents are significantly growing.

The lithium adsorbents involve inorganic metal-based adsorbents and organic adsorbents, the former comprising LiAl-LDHs, LTO-LISs, and LMO-LISs, while the latter including Li-IIPs and ion-exchange resins. Currently, the inorganic metal-based adsorbents present more promising and applicable in Li extraction, especially LiAl-LDHs. However, this does not mean that these adsorbents are capable of directly working for the Li^+ recovery from brines. For LiAl-LDHs, though they have applied as the lithium extraction adsorbents on industrial- and commercial-scale applications, the relatively low adsorption capacity aspires to improve by structural modification. On the other hand, the long-term cycling stability is attacked by the 'SO_4^{2-} poisoning' effect.

With the development of industrial and commercial Li extraction, emerging challenges for Li extraction by adsorption methods have arisen: i) High grade brines with high Li^+ concentration and low Mg^{2+}/Li^+ ratio are rapidly decreasing, thus the LiAl-LDHs with effective Li extraction performance for low-quality brines should be the focus of future research; ii) To enhance the commercial competitiveness of enterprises, the Li^+ adsorption kinetics of adsorbents should be improved, and LiAl-LDHs with high Li^+ transfer rate and relevant adsorption tower need to be designed.

2.5. References

[1] M. Yong, M. Tang, L. Sun, F. Xiong, L. Xie, G. Zeng, X. Ren, K. Wang, Y. Cheng, Z. Li, E. Li, X. Zhang, H. Wang, Sustainable lithium extraction and magnesium hydroxide co-production from salt-lake brines, Nat. Sustain. 7 (2024) 1662-1671.
[2] F. Degen, M. Winter, D. Bendig, J. Tübke, Energy consumption of current and future production of lithium-ion and post lithium-ion battery cells, Nat. Energy 8 (2023) 1284-1295.
[3] Y. Xiong, J. Zhou, P. Lu, J. Yin, Y. Wang, Z. Fan, Electrochemical lithium extraction from aqueous sources, Matter 5 (2022) 1760-1791.

[4] Z.H. Foo, J.B. Thomas, S.M. Heath, J.A. Garcia, J.H. Lienhard, Sustainable Lithium Recovery from Hypersaline Salt-Lakes by Selective Electrodialysis: Transport and Thermodynamics, Environ. Sci. Technol. 57 (2023) 14747-14759.
[5] T. Kanagasundaram, O. Murphy, M.N. Haji, J.J. Wilson, The recovery and separation of lithium by using solvent extraction methods, Coord. Chem. Rev. 509 (2024) 215727.
[6] V. Balaram, M. Santosh, M. Satyanarayanan, N. Srinivas, H. Gupta, Lithium: A review of applications, occurrence, exploration, extraction, recycling, analysis, and environmental impact, Geosci. Front. 15 (2024) 101868.
[7] B. Tansel, Significance of thermodynamic and physical characteristics on permeation of ions during membrane separation: Hydrated radius, hydration free energy and viscous effects, Sep. Purif. Technol. 86 (2012) 119-126.
[8] T. Zhang, H. Bai, Y. Zhao, B. Ren, T. Wen, L. Chen, S. Song, S. Komarneni, Precise Cation Recognition in Two-Dimensional Nanofluidic Channels of Clay Membranes Imparted from Intrinsic Selectivity of Clays, ACS Nano 16 (2022) 4930-4939.
[9] Y. Orooji, Z. Nezafat, M. Nasrollahzadeh, N. Shafiei, M. Afsari, K. Pakzad, A. Razmjou, Recent advances in nanomaterial development for lithium ion-sieving technologies, Desalination 529 (2022) 115624.
[10] Y. Boroumand, A. Razmjou, Adsorption-type aluminium-based direct lithium extraction: The effect of heat, salinity and lithium content, Desalination 577 (2024) 117406.
[11] S. Zhang, X. Wei, X. Cao, M. Peng, M. Wang, L. Jiang, J. Jin, Solar-driven membrane separation for direct lithium extraction from artificial salt-lake brine, Nat. Commun. 15 (2024) 238.
[12] T. Wen, Y. Zhao, X. Wang, L. Chen, R. Gao, S. Wang, T. Zhang, Efficient and ultrafast separation of Li^+ and Mg^{2+} by the porous two-dimensional nanochannel of perm-selective montmorillonite membrane, Chem. Eng. J. 475 (2023) 146101.
[13] M. Gulied, S. Zavahir, T. Elmakki, H. Park, G.H. Gago, H.K. Shon, D.S. Han, Efficient lithium recovery from simulated brine using a hybrid system: Direct contact membrane distillation (DCMD) and electrically switched ion exchange (ESIX), Desalination 572 (2024) 117127.
[14] J. Zhou, X. Li, W. Xie, Q. Chen, Y. Jiang, X. Wu, L. Yang, Realizing efficient solar evaporation and rapid lithium sorption by the halloysite nanotubes-based hydrogel, J. Cleaner Prod. 437 (2024) 140523.
[15] S. Safari, B.G. Lottermoser, D.S. Alessi, Metal oxide sorbents for the sustainable recovery of lithium from unconventional resources, Appl. Mater. Today 19 (2020) 100638.
[16] J.O. Ighalo, J.F. Amaku, C. Olisah, A.O. Adeola, K.O. Iwuozor, K.G. Akpomie, J. Conradie, K.A. Adegoke, K.O. Oyedotun, Utilisation of adsorption as a resource recovery technique for lithium in geothermal water, J. Mol. Liq. 365 (2022) 120107.
[17] A. Gao, Z. Sun, S. Li, X. Hou, H. Li, C. Wang, W. Wu, Self-assembled layered lithium manganese oxide shows ultra-large adsorption capacity and high selectivity for

lithium, Chem. Eng. J. 471 (2023) 144287.
[18] L. Baudino, C. Santos, C.F. Pirri, F. La Mantia, A. Lamberti, Recent Advances in the Lithium Recovery from Water Resources: From Passive to Electrochemical Methods, Adv. Sci. 9 (2022) 2201380.
[19] Y. Huang, X. Li, L. Chen, G. Luo, D. Tao, J. Sun, Z. Qiu, Y. Chao, W. Zhu, Synthesis of a magnetic crown ether ion imprinted polymer material for the selective adsorption of lithium, New J. Chem. 47 (2023) 3134-3139.
[20] J.M. Lee, W.C. Bauman, Recovery of lithium from brines, US Patent 4159311A, (1979).
[21] J.M. Lee, W.C. Bauman, Recovery of lithium from brines, US Patent 4116856A, (1978).
[22] A.V. Besserguenev, A.M. Fogg, R.J. Francis, S.J. Price, D. O'Hare, V.P. Isupov, B.P. Tolochko, Synthesis and Structure of the Gibbsite Intercalation Compounds $[LiAl_2(OH)_6]X$ {X = Cl, Br, NO_3} and $[LiAl_2(OH)_6]Cl{\cdot}H_2O$ Using Synchrotron X-ray and Neutron Powder Diffraction, Chem. Mater. 9 (1997) 241-247.
[23] A.M. Fogg, A.J. Freij, G.M. Parkinson, Synthesis and Anion Exchange Chemistry of Rhombohedral Li/Al Layered Double Hydroxides, Chem. Mater. 14 (2002) 232-234.
[24] Y. Sun, R. Yun, Y. Zang, M. Pu, X. Xiang, Highly Efficient Lithium Recovery from Pre-Synthesized Chlorine-Ion-Intercalated LiAl-Layered Double Hydroxides via a Mild Solution Chemistry Process, Materials 12 (2019).
[25] T.R. Graham, J.Z. Hu, X. Zhang, M. Dembowski, N.R. Jaegers, C. Wan, M. Bowden, A.S. Lipton, A.R. Felmy, S.B. Clark, K.M. Rosso, C.I. Pearce, Unraveling Gibbsite Transformation Pathways into LiAl-LDH in Concentrated Lithium Hydroxide, Inorg. Chem. 58 (2019) 12385-12394.
[26] S. Wang, C. Lin, Y. Yan, M.K. Wang, Synthesis of Li/Al LDH using aluminum and LiOH, Appl. Clay Sci. 72 (2013) 191-195.
[27] X.-J. Hou, H. Li, P. He, Z. Sun, S. Li, Structural and electronic analysis of Li/Al layered double hydroxides and their adsorption for CO_2, Appl. Surf. Sci. 416 (2017) 411-423.
[28] S.G. Kozlova, S.P. Gabuda, V.P. Isupov, L.É. Chupakhina, Using NMR in Structural Studies of Aluminum Hydroxide Intercalation Compounds with Lithium Salts, J. Struct. Chem. 44 (2003) 198-205.
[29] J.P. Thiel, C.K. Chiang, K.R. Poeppelmeier, Structure of lithium aluminum hydroxide dihydrate ($LiAl_2(OH)_7{\cdot}2H_2O$), Chem. Mater. 5 (1993) 297-304.
[30] V.P. Isupov, N.P. Kotsupalo, A.P. Nemudry, L.T. Menzeres, Aluminium hydroxide as selective sorbent of lithium salts from brines and technical solutions, in: A. Dąbrowski (Ed.) Studies in Surface Science and Catalysis, Elsevier1999, pp. 621-652.
[31] Y. Li, N. Tang, L. Zhang, J. Li, Fabrication of Fe-doped lithium-aluminum-layered hydroxide chloride with enhanced reusable stability inspired by computational theory and its application in lithium extraction, Colloids Surf., A 658 (2023) 130641.
[32] H. Jiang, S. Zhang, Y. Yang, J. Yu, Synergic and competitive adsorption of Li-Na-$MgCl_2$ onto lithium-aluminum hydroxides, Adsorption 26 (2020) 1039-1049.

[33] Y. Kong, X. He, H. Wu, Y. Yang, L. Cao, R. Li, B. Shi, G. He, Y. Liu, Q. Peng, C. Fan, Z. Zhang, Z. Jiang, Tight Covalent Organic Framework Membranes for Efficient Anion Transport via Molecular Precursor Engineering, Angew. Chem., Int. Ed. 60 (2021) 17638-17646.
[34] L. Bao, J. Zhang, W. Tang, S. Sun, Synthesis and adsorption properties of metal oxide-coated lithium ion-sieve from salt lake brine, Desalination 546 (2023) 116196.
[35] Y. Zhang, J. Liu, Y. Yang, S. Lin, P. Li, Preparation of granular titanium-type lithium-ion sieves and recyclability assessment for lithium recovery from brines with different pH value, Sep. Purif. Technol. 267 (2021) 118613.
[36] Y. Onodera, T. Iwasaki, H. Hayashi, K. Torii, A New Inorganic Titanium Compound with High Selective Adsorbability for Li^+, J. Ceram. Soc. Jpn. 97 (1989) 888-894.
[37] R. Marthi, Y.R. Smith, Application and limitations of a H_2TiO_3-Diatomaceous earth composite synthesized from titania slag as a selective lithium adsorbent, Sep. Purif. Technol. 254 (2021) 117580.
[38] Y. Du, X. Niu, W. Li, J. An, Y. Liu, Y. Chen, P. Wang, X. Yang, Q. Feng, Microwave-Assisted Synthesis of High-Energy Faceted TiO_2 Nanocrystals Derived from Exfoliated Porous Metatitanic Acid Nanosheets with Improved Photocatalytic and Photovoltaic Performance, Materials 12 (2019).
[39] R. Chitrakar, Y. Makita, K. Ooi, A. Sonoda, Lithium recovery from salt lake brine by H_2TiO_3, Dalton Trans. 43 (2014) 8933-8939.
[40] X. Sun, P.V. Radovanovic, B. Cui, Advances in spinel $Li_4Ti_5O_{12}$ anode materials for lithium-ion batteries, New J. Chem. 39 (2015) 38-63.
[41] B. Zhao, Y. Qiao, Z. Qian, W. Wei, J. Li, Z. Wu, Z. Liu, Unraveling the Li^+ desorption behavior and mechanism of $Li_4Ti_5O_{12}$ with different facets to enhance lithium extraction, J. Mater. Chem. A 11 (2023) 7094-7104.
[42] W.J.H. Borghols, M. Wagemaker, U. Lafont, E.M. Kelder, F.M. Mulder, Size Effects in the $Li_{4+x}Ti_5O_{12}$ Spinel, J. Am. Chem. Soc. 131 (2009) 17786-17792.
[43] J.C. Hunter, Preparation of a new crystal form of manganese dioxide: λ-MnO_2, J. Solid State Chem. 39 (1981) 142-147.
[44] R. Chitrakar, Y. Makita, K. Ooi, A. Sonoda, Selective Uptake of Lithium Ion from Brine by $H_{1.33}Mn_{1.67}O_4$ and $H_{1.6}Mn_{1.6}O_4$, Chem. Lett. 41 (2012) 1647-1649.
[45] Q. Feng, Y. Miyai, H. Kanoh, K. Ooi, Li^+ extraction/insertion with spinel-type lithium manganese oxides. Characterization of redox-type and ion-exchange-type sites, Langmuir 8 (1992) 1861-1867.
[46] S. Sun, X. Song, Q. Zhang, J. Wang, J. Yu, Lithium extraction/insertion process on cubic Li-Mn-O precursors with different Li/Mn ratio and morphology, Adsorption 17 (2011) 881-887.
[47] Q. Feng, H. Kanoh, K. Ooi, Manganese oxide porous crystals, J. Mater. Chem. 9 (1999) 319-333.
[48] C.M. Julien, Local structure of lithiated manganese oxides, Solid State Ionics 177 (2006) 11-19.

[49] K. Ooi, Y. Miyai, S. Katoh, Lithium-ion sieve property of λ;-type manganese oxide, Solvent Extr. Ion Exch. 5 (1987) 561-572.
[50] Y.S. Kim, H. Kanoh, T. Hirotsu, K. Ooi, Chemical bonding of ion-exchange type sites in spinel-type manganese oxides $Li_{1.33}Mn_{1.67}O_4$, Mater. Res. Bull. 37 (2002) 391-396.
[51] A. Gao, X. Hou, Z. Sun, S. Li, H. Li, J. Zhang, Lithium-desorption mechanism in $LiMn_2O_4$, $Li_{1.33}Mn_{1.67}O_4$, and $Li_{1.6}Mn_{1.6}O_4$ according to precisely controlled acid treatment and density functional theory calculations, J. Mater. Chem. A 7 (2019) 20878-20890.
[52] R. Chitrakar, H. Kanoh, Y. Miyai, K. Ooi, A New Type of Manganese Oxide ($MnO_2 \cdot 0.5H_2O$) Derived from $Li_{1.6}Mn_{1.6}O_4$ and Its Lithium Ion-Sieve Properties, Chem. Mater. 12 (2000) 3151-3157.
[53] A. Gao, Z. Sun, S. Li, X. Hou, H. Li, Q. Wu, X. Xi, The mechanism of manganese dissolution on $Li_{1.6}Mn_{1.6}O_4$ ion sieves with HCl, Dalton Trans. 47 (2018) 3864-3871.
[54] G. Zhang, C. Hai, Y. Zhou, W. Tang, J. Zhang, J. Zeng, Y. Liu, S. Dong, G. Peng, Al and F ions co-modified $Li_{1.6}Mn_{1.6}O_4$ with obviously enhanced Li^+ adsorption performances, Chem. Eng. J. 450 (2022) 137912.
[55] K. Ooi, Y. Miyai, J. Sakakihara, Mechanism of Li^+ insertion in spinel-type manganese oxide. Redox and ion-exchange reactions, Langmuir 7 (1991) 1167-1171.
[56] M.J. Ariza, D.J. Jones, J. Rozière, R. Chitrakar, K. Ooi, Probing the Local Structure and the Role of Protons in Lithium Sorption Processes of a New Lithium-Rich Manganese Oxide, Chem. Mater. 18 (2006) 1885-1890.
[57] L. Wang, L. Wang, J. Wang, X. Wang, Synthesis of zirconium-coated lithium ion sieve with enhanced cycle stability, Sep. Purif. Technol. 303 (2022) 121933.
[58] L. Li, W. Qu, F. Liu, T. Zhao, X. Zhang, R. Chen, F. Wu, Surface modification of spinel λ-MnO_2 and its lithium adsorption properties from spent lithium ion batteries, Appl. Surf. Sci. 315 (2014) 59-65.
[59] L. Bao, J. Zhang, J. Wu, G. Zhang, Y. Yang, W. Tang, M. Xue, Preparation of Mg-doped $Li_{1.6}Mn_{1.6}O_4$ with enhanced Li^+ adsorption performance and anti-dissolution properties of Mn, Hydrometallurgy 209 (2022) 105772.
[60] C.J. Pedersen, Cyclic polyethers and their complexes with metal salts, J. Am. Chem. Soc. 89 (1967) 2495-2496.
[61] J. Cui, Z. Zhou, S. Liu, Y. Zhang, L. Yan, Q. Zhang, S. Zhou, Y. Yan, C. Li, Synthesis of cauliflower-like ion imprinted polymers for selective adsorption and separation of lithium ion, New J. Chem. 42 (2018) 14502-14509.
[62] Y. Steven Kurniawan, R. Rao Sathuluri, K. Ohto, W. Iwasaki, H. Kawakita, S. Morisada, M. Miyazaki, Jumina, A rapid and efficient lithium-ion recovery from seawater with tripropyl-monoacetic acid calix[4]arene derivative employing droplet-based microreactor system, Sep. Purif. Technol. 211 (2019) 925-934.
[63] R.E.C. Torrejos, G.M. Nisola, H.S. Song, L.A. Limjuco, C.P. Lawagon, K.J. Parohinog, S. Koo, J.W. Han, W.J. Chung, Design of lithium selective crown ethers: Synthesis, extraction and theoretical binding studies, Chem. Eng. J. 326 (2017) 921-

933.
[64] L. Mao, R. Chen, J. He, H. Pei, B. He, X. Ma, J. Li, Remarkably High Li^+ Adsorptive Separation Polyamide Membrane by Improving the Crown Ether Concentration and Electron Density, ACS Sustainable Chem. Eng. 10 (2022) 10047-10056.
[65] M.M. Nigra, A.J. Yeh, A. Okrut, A.G. DiPasquale, S.W. Yeh, A. Solovyov, A. Katz, Accessible gold clusters using calix[4]arene N-heterocyclic carbene and phosphine ligands, Dalton Trans. 42 (2013) 12762-12771.
[66] H. Jo, T.H. Le, H. Lee, J. Lee, M. Kim, S. Lee, M. Chang, H. Yoon, Macrocyclic ligand-embedded graphene-in-polymer nanofiber membranes for lithium ion recovery, Chem. Eng. J. 452 (2023) 139274.
[67] C. Yu, J. Lu, J. Dai, Z. Dong, X. Lin, W. Xing, Y. Wu, Z. Ma, Bio-inspired fabrication of Ester-functionalized imprinted composite membrane for rapid and high-efficient recovery of lithium ion from seawater, J. Colloid Interface Sci. 572 (2020) 340-353.
[68] Y. Huang, R. Wang, An efficient lithium ion imprinted adsorbent using multi-wall carbon nanotubes as support to recover lithium from water, J. Cleaner Prod. 205 (2018) 201-209.
[69] Z. Xu, X. Wang, S. Sun, Performance of a synthetic resin for lithium adsorption in waste liquid of extracting aluminum from fly-ash, Chin. J. Chem. Eng. 44 (2022) 115-123.
[70] S. Liu, C. Li, D. Li, S. Zhao, L. Song, G. Kuang, Tri(ethylene glycol) modified HYC-100 resin for lithium ion recovery from aqueous solution, J. Appl. Polym. Sci. 140 (2023) e54251.
[71] F. Arroyo, J. Morillo, J. Usero, D. Rosado, H. El Bakouri, Lithium recovery from desalination brines using specific ion-exchange resins, Desalination 468 (2019) 114073.
[72] S. Güneysu, Lithium sorption from aqueous solution with cationic resins, Desalin. Water Treat. 177 (2020) 102-108.
[73] A. Çiçek, O. Yılmaz, O. Arar, Removal of lithium from water by aminomethylphosphonic acid containing resin, J. Serb. Chem. Soc. 83 (2018) 1059-1069.
[74] J. Lemaire, L. Svecova, F. Lagallarde, R. Laucournet, P.-X. Thivel, Lithium recovery from aqueous solution by sorption/desorption, Hydrometallurgy 143 (2014) 1-11.
[75] S. Aljarrah, A. Alsabbagh, M. Almahasneh, Selective recovery of lithium from Dead Sea end brines using UBK10 ion exchange resin, Can. J. Chem. Eng. 101 (2023) 1185-1194.
[76] N. Intaranont, N. Garcia Araez, A.L. Hector, J.A. Milton, J.R. Owen, Selective lithium extraction from brines by chemical reaction with battery materials, J. Mater. Chem. A 2 (2014) 6374-6377.
[77] A. Clearfield, J. Troup, Mechanism of ion exchange in crystalline zirconium phosphate. II. Lithium ion exchange of .alpha.-zirconium phosphate, J. Phys. Chem. 74

(1970) 314-317.
[78] T. Oi, M. Endoh, M. Narimoto, M. Hosoe, Ion and lithium isotope selectivity of monoclinic antimonic acid, J. Mater. Sci. 35 (2000) 509-513.
[79] Y. Inoue, M. Abe, Synthetic inorganic ion exchange materials. XLIII. Ion exchange mechanism of lithium ions on cubic tantalic acid, Solvent Extr. Ion Exch. 14 (1996) 507-518.
[80] X. Yang, Y. Makita, J. Hosokawa, K. Sakane, K. Ooi, Preparation and Alkali Metal Ion Exchange Properties of Protonated $Rb_8Nb_{22}O_{59}$ Compound, Chem. Mater. 17 (2005) 5420-5427.
[81] Z. Zhao, X. Si, X. Liu, L. He, X. Liang, Li extraction from high Mg/Li ratio brine with $LiFePO_4/FePO_4$ as electrode materials, Hydrometallurgy 133 (2013) 75-83.
[82] W. Xu, D. Liu, X. Liu, D. Wang, L. He, Z. Zhao, Highly selective and efficient lithium extraction from brines by constructing a novel multiple-crack-porous $LiFePO_4/FePO_4$ electrode, Desalination 546 (2023) 116188.
[83] R. Yin, W. Zhu, Z. Zhao, W. Xu, X. Liu, L. He, Lithium recovery from brine by PEG-modified porous $LiFePO_4/FePO_4$ electrode system, Sep. Purif. Technol. 338 (2024) 126375.
[84] L. Yang, Y. Tu, H. Li, W. Zhan, H. Hu, Y. Wei, C. Chen, K. Liu, P. Shao, M. Li, G. Yang, X. Luo, Fluorine-Rich Supramolecular Nano-Container Crosslinked Hydrogel for Lithium Extraction with Super-High Capacity and Extreme Selectivity, Angew. Chem., Int. Ed. 62 (2023) e202308702.
[85] J. Zhong, S. Lin, J. Yu, Lithium recovery from ultrahigh Mg^{2+}/Li^{+} ratio brine using a novel granulated Li/Al-LDHs adsorbent, Sep. Purif. Technol. 256 (2021) 117780.

Chapter 3. Doping engineering of lithium-aluminum layered double hydroxides for high-efficiency lithium extraction from salt lake brines

3.1. Introduction

Lithium (Li), one of the most important strategic resources today, has many industrial applications, such as ceramics and glass, energy storage, nuclear fusion, pharmaceuticals and the well-known lithium-ion batteries (LIBs), which renders a skyrocket in the demand and market price of Li [1,2]. According to the statistics, most of the world's Li resources are found in salt lakes brines [3]. For China, even up to 80% of lithium resources are in salt lake brines [4]. Unfortunately, in addition to Li^+, a variety of competing cations in high concentrations are present in numerous brines, especially Mg^{2+} with similar properties to Li^+ [5,6]. Therefore, it is imperative but challenging to develop efficient Li extraction technologies from the brines.

Hitherto, many extraction technologies for recovering Li^+ from sale lakes brines have been researched, including solar evaporation, electrochemistry, precipitation, membrane separation, adsorption, etc. [7-9] Among them, adsorption method is considered a promising methodology for Li extraction due to easy operation, high selectivity to Li^+, and eco-friendliness, especially for applications in low-grade brines with ultrahigh Mg^{2+}:Li^+ ratio [5,10]. Various types of adsorbents have been reported, in which inorganic metal-based lithium extraction adsorbents, namely manganese-based ion sieve (LMO), titanium-based ion sieve (LTO), and lithium-aluminum layered double hydroxides (LiAl-LDH), are the research hotspot in view of the innate merits [11]. For example, the LMO and LTO possess superior Li^+ adsorption capacity and selectivity, while LiAl-LDH features stable adsorption performance and negligible elution damage with deionized water [12]. In practical application, LMO suffer from large dissolution losses during the desorption process, while the production cost of LTO are expensive [13]. Fortunately, LiAl-LDH are capable of overcoming the issues mentioned above and have become the only adsorbent material that can be used on commercial-scale applications in China [14,15]. However, LiAl-LDH have an innate limited Li^+ theoretical adsorption capacity according to the formula of

[$LiCl·2Al(OH)_3·nH_2O$] [16,17]. Moreover, the actual adsorption capacity of LiAl-LDH (4 ~ 8 mg/g) is always much lower than theoretical capacity [15]. Therefore, improvement in the Li^+ adsorption performance of LiAl-LDH has become the keystone to promote the further development of the Li extraction industry.

To meet this preceding requirement, researchers carried out numerous works on the modification of LiAl-LDH [11,18,19]. Previous work on the interlayer regulation found that although expanding the layer spacing could enhance the Li^+ uptake of LiAl-LDH, it leaded to a decline in the Li^+ selectivity owing to the depressed interlayer confinement effect [19]. Wu and co-workers [20] revealed that the higher interlayer of water, the less the thermodynamic barriers, which facilitated Li^+ adsorption on LiAl-LDH, yet resulted in structural destabilization. Porous LiAl-LDH prepared by surfactants modification exhibited an increasing Li^+ adsorption capacity, but complex preparation process and the unstable material recycling capacity restrict their application [18]. The dopant modification with high electron density metals have also been utilized to retain structural and functional stability, whereas fail to enhance Li^+ adsorption capacity [21]. Apparently, a suitable strategy to improve the performance of LiAl-LDH for Li extraction is eager but unready. On the other hand, the mechanism of Li extraction by LiAl-LDH, i.e., the intercalation of Li^+ into the octahedral vacancies of $Al(OH)_3$ via weak hydrogen bonding and van der Waals forces ($xLiCl + (1-x)LiCl·2Al(OH)_3 + (n+1)H_2O \rightleftharpoons LiCl·2Al(OH)_3·nH_2O$), had been reported [14,22]. However, the whole process and steps of extraction are still unrevealed, whole hinders the further development of LiAl-LDH.

Indeed, doping engineering has been proven to be a simple yet effective strategy for improving physicochemical property of adsorbents, thereby facilitating adsorption [23]. By utilizing different dopants and levels of doping, adsorbents exhibit a highly flexible tunability in terms of surface electronegativity, stability, selectivity, and microstructures [24]. Herein, a low-valent metal doping-engineering strategy were presented to comprehensively improve the Li extraction performance of LiAl-LDH via simple one-pot co-precipitation method. Further, the three-steps process for Li extraction on LiAl-LDH was proposed. The results of experiments and theoretical calculations demonstrated that this doping-engineering strategy not only regulate the surface charge, specific surface area and hydrophilicity of LiAl-LDH, which increased the affinity for Li^+ and facilitated the transfer and insertion of lithium, but also introduced defects and accelerated the diffusion process of Li^+ in the internal bulk of

LiAl-LDH. Furthermore, the systematic investigations were performed to reveal the advance of doping-engineering strategy, where the samples after doping could effectively retain outstanding reusability and stability with significantly improved Li^+ adsorption capacity and selectivity. This work delivered pivotal scientific significance and application value to develop efficient adsorption for the Li extraction from salt lakers brines.

3.2. Experimental section

3.2.1. Material synthesis

Materials: All the analytical reagents used in experiments were obtained from Shanghai Aladdin Biochemical Technology Co., Ltd., including lithium chloride (LiCl), aluminum chloride hexahydrate ($AlCl_3·6H_2O$), zinc chloride ($ZnCl_2$), magnesium chloride hexahydrate ($MgCl_2·6H_2O$), cupric chloride dihydrate ($CuCl2·2H_2O$), nickel chloride hexahydrate ($NiCl_2·6H_2O$), cobalt chloride hexahydrate ($CoCl_2·6H_2O$), stannous chloride pentahydrate ($SnCl_4·5H_2O$), molybdenum chloride ($MoCl_5$), lanthanum chloride heptahydrate ($LaCl_3·7H_2O$), calcium chloride($CaCl_2$), ferric chloride ($FeCl_3$), antimony trichloride ($SbCl_3$), and sodium hydroxide (NaOH).

The brine used in the experiments was the Lop Nor brine, and the compositions were provided in Table 3.1.

Table 3.1 Composition of the Lop Nor brine.

Components	Li^+	Mg^{2+}	Na^+	K^+	Cl^-
Concentration (mg/L)	222	105276	1849	3827	2224000

Synthesis of LiAl-LDHs with metal ions doping (LiMAl-LDHs): LiMAl-LDHs were fabricated by a modified co-precipitation method, in which the reactions of metal ions doping and Li-insertion reaction were coupled. Typically, the aqueous solution with the Al/M/Li molar ratio of 19:1:10 (M represents the common divalent, trivalent, tetravalent, and pentavalent metal cations) was dropped into 8.0 mol/L NaOH solution, stirred at 75 ℃ together with detecting the pH of the mixture with a pH meter (Sartorius PB-10) until the its pH was 5 and then aged for 30 min. Finally, the LiAl-LDHs with metal ions doping (LiMAl-LDHs) were obtained after deionized water washing, filtration, and freeze-drying. In addition, to investigated the effect of metal ions doping amount, LiZnAl-LDHs with various Zn-doping amount were prepared via mixing $AlCl_3$, $ZnCl_2$ and LiCl with different molar ratio [$n_{(Al + M)}$:n_{Li} = (100+0):50, (99+1):50,

(95:5):50, (90:10):50, (80:20):50], and the produced materials were denoted as LiAl-LDH, LiZnAl-LDH-1%, LiZnAl-LDH-5%, LiZnAl-LDH-10%, and LiZnAl-LDH-20%, respectively, where 1-20% represent the molar content of Zn^{2+} in the raw material as a percentage of (Zn^{2+} + Al^{3+}).

3.2.2. Characterizations

The morphologies of samples were characterized using scanning electron microscopy (SEM, Zeiss Gemini 300, Germany) and transmission electron microscopy (TEM, JEM-JEOL-2100, Japan) equipped with energy dispersive spectroscopy (EDS) system. X-ray diffraction patterns were recorded using D/max RBX diffractometer (XRD, D8 ADVANCE X, Germany) with Cu Kαradiation (40 kV, 100 mA). The N_2 adsorption-desorption measurements were measured by ASAP2460 aperture analyzer, and the specific area, porosity and pore size distributions were determined via Brunauer-Emmett-Teller method (BET). Raman spectroscopy was carried out using a Thermo scientific DXR3 Raman microscope with 532 nm laser excitation. Electron spin resonance (EPR) spectrum was obtained on a Bruker ER200-SRC spectrometer. Contact angle (CA) of sample was taken by micro-scopic contact angle meter (Kyowa Interface Science Co. Ltd., Japan). X-ray photoelectron spectroscopy (XPS) was taken with AXIS SUPRA spectrometer.

3.2.3. Lithium-ion extraction performance evaluation

All batch adsorption experiments were performed at room temperature in thermostatic water bath at 150 rpm with adsorbents (20 g/L) suspended in Lop Nor brine. The adsorption kinetics were conducted, and the pseudo-first-order, the pseudo-second-order and the intraparticle diffusion models were employed to fit the experimental data, respectively [25]. The adsorption isotherms were measured for 6 h. The experimental data were analyzed by the Langmuir isotherm and Freundlich isotherm models, respectively [26]. To evaluate the performance of adsorbents, supernatants were filtered at given intervals through 0.22 μm filter membrane, and the concentration of Li^+ before and after adsorption were measured by filtering the atomic absorption spectrum (AAS). The adsorption capacity q_e (mg/g) was calculated by Equation 3.1:

$$q_e = (C_0 - C_e)V/m \tag{3.1}$$

where C_0 (mg/L) and C_e (mg/L) are the initial and equilibrium concentrations of Li^+,

respectively; V (L) represents the solution volume; m (g) is the mass of adsorbent.
The desorption performance was investigated as well. Deionized water was used as eluent, and the liquid-solid ratio was 100 mL/g. The Li^+ desorption capacity was determined by Equation 3.2:

$$q_{dt} = C_{dt}V/m \tag{3.2}$$

where q_{dt} (mg/g) and C_{dt} (mg/L) are the desorption capacity and concentration at time t, respectively.

The adsorption selectivity of samples to different metal cations in the brine was assessed by measuring the initial and equilibrium concentrations of each metal ion. The distribution coefficient K_d (mL/g) and separation coefficient α_M^{Li} were determined according to Equation 3.3 and 3.4:

$$K_d = V(C_0 - C_e)/(mC_e) \tag{3.3}$$

$$\alpha_M^{Li} = K_{d,\,Li}/K_{d,\,M} \tag{3.4}$$

where M represents K^+, Na^+, and Mg^{2+}.

Reusability and stability for Li extraction was also studied for practical applications. After a fast wash with ice water (adsorbent to water ratio of 1 g/10 mL) for removal of residual brine adhering to the separated adsorbent surface, the desorption process of saturated absorbents was performed by shaking with 100 g/mL deionized water at 40 ℃ for 3 h, and then the regenerated absorbents were used in the brine for next adsorption/desorption cycle. Moreover, the stability of absorbents was revealed by monitoring the amounts of doped metal ion in desorption solutions.

3.2.4. Calculation details

All Density functional theory (DFT) calculations were performed with the Cambridge Sequential Total Energy Package (CASTEP) module or Dmol^3 module of the Materials Studio software. The exchange and correlation interactions were established by the Perdew-Burke-Ernzerhof (PBE) formulation with the generalized gradient approximation (GGA). The structure of LiAl-LDH with interlayer spacing of 9.7 Å was obtained from Materials Project (Materials ID: mp-643655). The cut-off energy was set to 430 eV and the k-point mesh with a size of 1 × 1 × 1 grid was used. For all structural optimization, atomic positions were fully relaxed (the convergence thresholds of energy < 2×10^{-5} eV/atom, maximum displacement < 0.002 Å, maximum force < 0.05 eV/Å, respectively) [27]. Then, the adsorption energies (E_{ad}) were

calculated by Equation 3.5:

$$E_{ad}=E_{cluster/adsorbate}-E_{cluster}-E_{adsorbate} \quad (3.5)$$

where $E_{cluster/adsorbate}$ represents the total energy of Li adsorbed on the LiAl-LDH and LiZnAl-LDH; $E_{cluster}$ is the energy of LiAl-LDH and LiZnAl-LDH; $E_{adsorbate}$ stands for the energy of Li.

The density functional perturbation theory (DFPT) as implemented in CASTEP code were employed to calculate the entropies and zero-point energies. Further, the Gibbs free energies (G) of Li-insertion reaction were obtained at 298.15 K and 1 bar using Equation 3.6 [28]:

$$G=E_{DFT}+E_{ZPE}-TS \quad (3.6)$$

where E_{DFT} represents the DFT calculate DFT energy; E_{ZPE} and TS are the zero-point energy and the entropic contribution, respectively.

The energy barrier of Li^+ diffusion within the samples were performed by searching their transition states. The transition state searching calculations were carried out by using linear and quadratic synchronous transit (LST/QST) method nudged elastic band (NEB) tools implemented in $DMol^3$ [29].

3.3. Results and discussion

3.3.1. Optimization of doping strategy

The effect of doping and optimal LiMAl-LDHs were first determined. As displayed in Figure 3.1a, various metal elements with different valence were doped into LiAl-LDH to prepare LiMAl-LDH, whose Li extraction kinetics were carried out as well. One could see that doping of divalent elements was able to improve the Li^+ uptake, whereas the incorporation of higher valence elements had negative effect. The results might be related to the change in surface charge of LiMAl-LDHs. The positions of Al^{3+} are replaced by divalent metal ions can reduce the surface charge of aluminum hydroxide layered plate, facilitating the adsorption of Li^+ [30]. Indeed, the surface charge exhibited a positive correlation with the adsorption capacity of LiMAl-LDHs to certain extent (Figure 3.1b). Value of R^2, however, is less than 0.8, suggesting the presence of other interaction mechanisms derived from doping engineering, which will be discussed below. Considering the best adsorption capacity of Li^+, the LiZnAl-LDHs was chosen the optimal doping element for emphatical investigation.

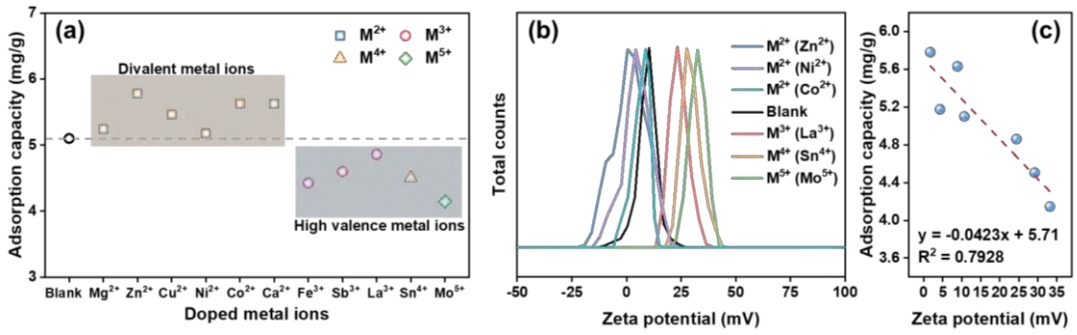

Figure 3.1 (a) The adsorption capacity of Li^+ on LiAl-LDHs doped with various metal cations; (b) The surface zeta potential of LiAl-LDHs doped with various metal cations; (c) The relationship between surface zeta potential and adsorption capacity of Li^+.

3.3.2. Fabrication and characterization of LiZnAl-LDH

The in-situ Zn-doped LiAl-LDHs were synthesized via co-precipitation method (Figure 3.2). During the preparation of LiZnAl-LDH, the Zn-doping and Li-insertion reaction were coupled [31]. At the beginning of the reaction, ZnAl-LDHs were formed rather than $Al(OH)_3$ due to the more stable structure of the former [32,33]. Then, the intercalation reaction of Li^+ proceeded to form adsorbent precursors. Finally, the target LiZnAl-LDHs were prepared by washing and activating with deionized water.

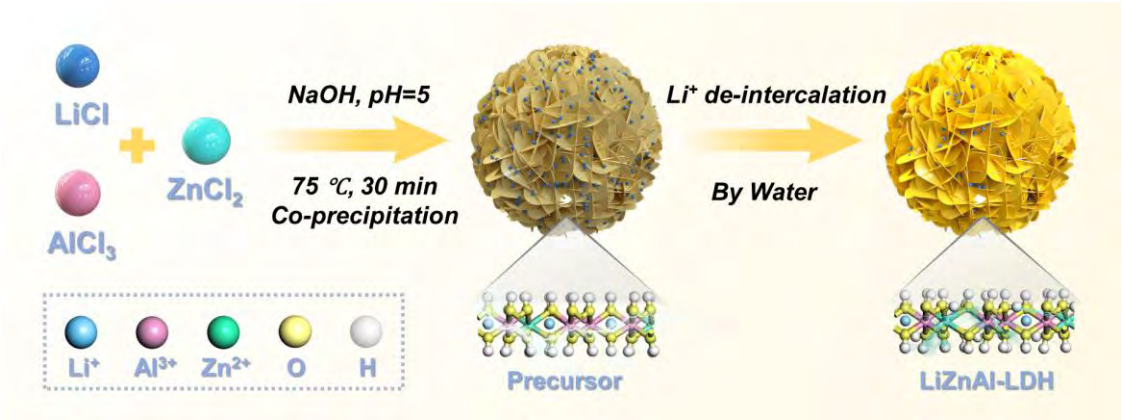

Figure 3.2 The schematic illustration of the fabrication strategy for LiZnAl-LDHs.

The microscopic morphologies LiZnAl-LDHs were observed. TEM images clearly uncovered the two-dimensional hexagonal nanosheet morphology of LiZnAl-LDH-5% with a size of 40-60 nm (Figure 3.3a-b). The high-resolution TEM (HRTEM) image of the LiZnAl-LDH-5% showed continuous lattice fringes and the determined lattice spacing was about 0.398 nm (Figure 3.3c), corresponding to the (006) crystal planes of LiAl-LDH. The four strong diffraction rings in the selected area electron

diffraction (SAED) pattern of LiZnAl-LDH-5% indexed to (006), (112), (118), and (300) crystal planes were observed (Figure 3.3d), confirming the LiAl-LDH crystal phase. Additionally, scanning transmission electron microscopy (STEM) coupled with energy-dispersive X-ray spectroscopy (EDS) elemental mapping of LiZnAl-LDH-5% demonstrated that Al, O, Cl, and Zn elements were homogeneously distributed throughout the whole sample (Figure 3.3e-f), where Zn element presented perfect dispersion with Al element, suggesting that Zn was doped into the octahedral voids of $Al(OH)_3$ [31,34].

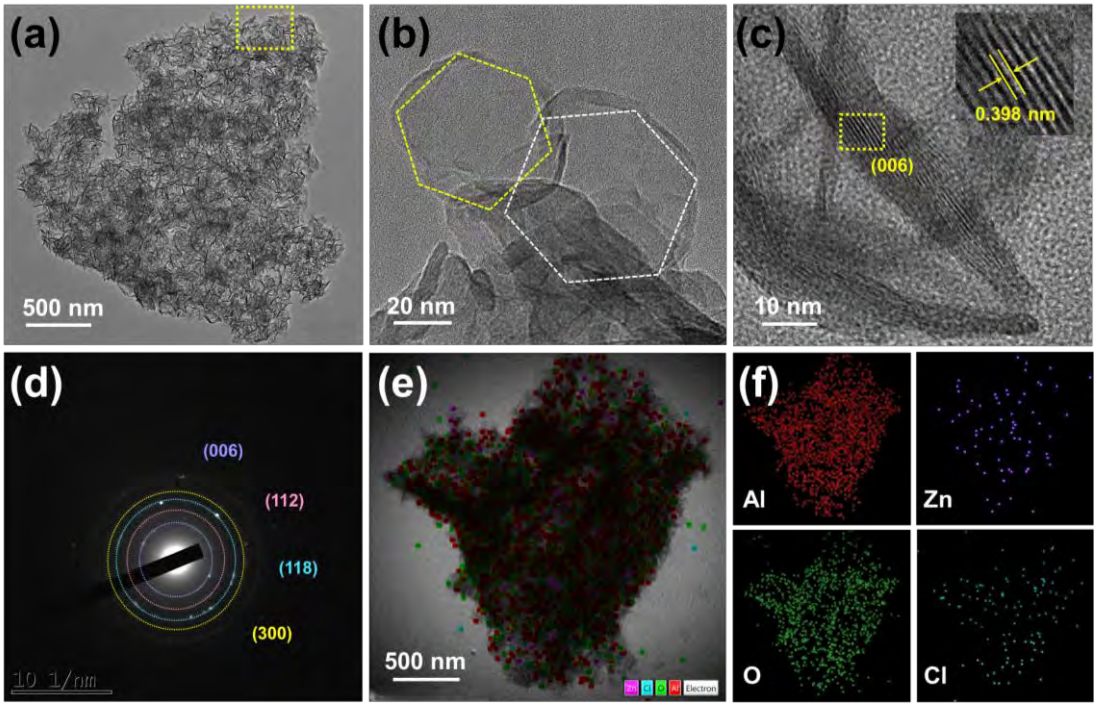

Figure 3.3 (a) TEM images, (b-c) HRTEM image, (d) SAED pattern and (e-f) STEM-EDS of LiZnAl-LDH-5%.

The XRD patterns of prepared adsorbents were shown in Figure 3.4a-c. It was found that the diffraction peaks belonging to $LiCl{\cdot}2Al(OH)_3{\cdot}nH2O$ (JCPDS No. 31-0700) were observed in all samples, indicating that the crystalline products belong to LiAl-LDH (Figure 3.4b). Furthermore, the major crystal planes of (003) and (006) slightly shifted to the lower angle with the content of Zn^{2+} increasing (Figure 3.4a and c), confirming that Zn^{2+} (74 pm) with a larger ion radius than Al^{3+} (54 pm) was doped into the lattice of Al-O octahedrons in LiAl-LDH, resulting in crystal cell expansion according to Bragg's law ($2d\sin\theta = n\lambda$) [35]. Also, these two diffraction peaks broadened with the incorporation of larger radius Zn^{2+} due to lattice distortion [36]. Besides, as the content of Zn^{2+} increased from 0% to 10%, no other impurity phases

were detected. Additional ZnO phase (JCPDS No. 74-0534), however, was determined in the XRD pattern of LiZnAl-LDH-20%. These phenomena illustrated that when the content of Zn^{2+} is less than 10%, the Zn^{2+} could be completely doped into the lattice of LiAl-LDH, while the excess Zn^{2+} could not be incorporated into the LiAl-LDH and existed in the form of oxide.

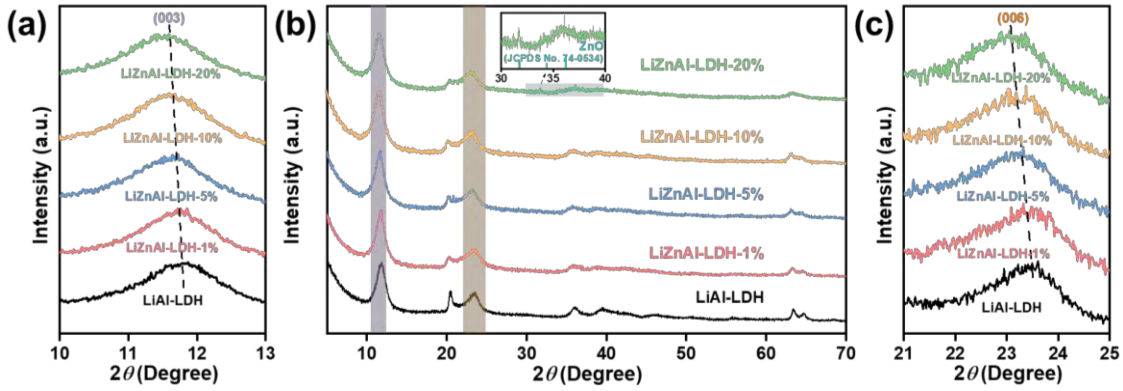

Figure 3.4 XRD patterns of the LiAl-LDH and LiZnAl-LDHs.

Based on the Debye-Scherrer formula, D = $k\lambda$/(FWHM·cosθ) (D is crystal size, λ = 0.1541 nm, k = 0.89, FWHM is the full width half maxima, and θ is Bragg diffraction angle), the crystal sizes of all samples ($D_{(003)}$) were calculated and presented decreasing $D_{(003)}$ after Zn-doping (Figure 3.5), suggesting reduction of particle aggregation derived from doping engineering [2], which is conducive to shorten the transport path of Li^+ within the particles and improve the specific surface area of samples [35,37].

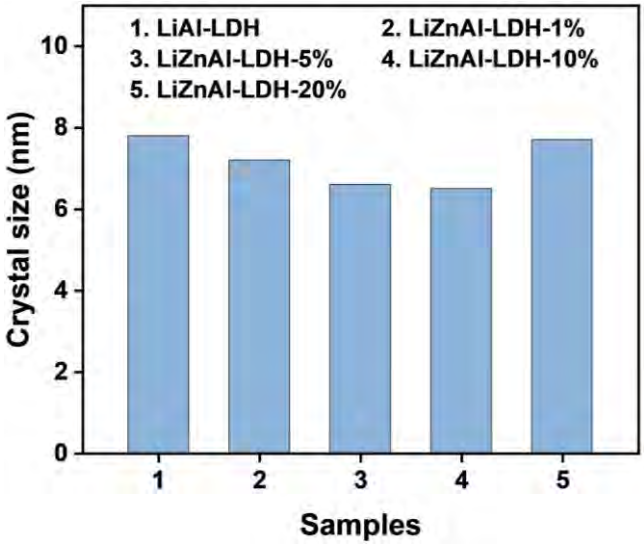

Figure 3.5 Crystal sizes of the LiAl-LDH and LiZnAl-LDHs based on Scherrer equation.

The improvement of LiZnAl-LDHs in textural properties could also be confirmed

by N_2 adsorption-desorption isotherms (Figure 3.6) and pore size analyses (Table 3.2). As observed, all samples showed type IV isotherms with a hysteresis of H3 type, revealing the mesoporous structures [25,38]. More importantly, with the doping of Zn^{2+}, the BET specific surface area and pore volume of LiZnAl-LDHs increased conspicuously, which was conducive to the rapid transfer of Li^+ into the interface.

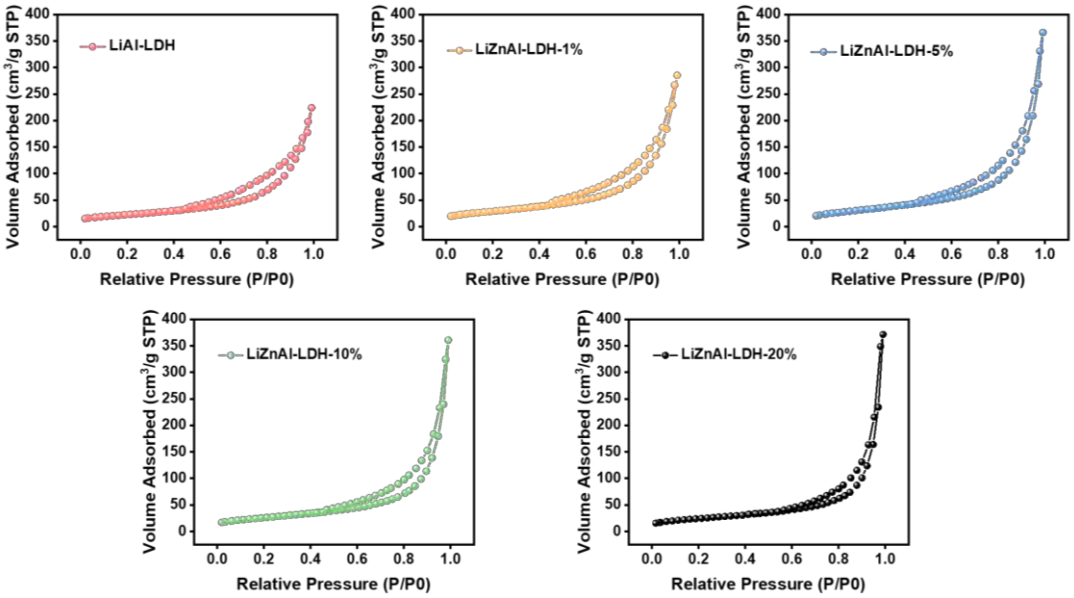

Figure 3.6 N_2 adsorption-desorption isotherms of the LiAl-LDH and LiZnAl-LDHs.

Table 3.2 The textural properties of the LiAl-LDH and LiZnAl-LDHs.

Samples	Specific surface area (m^2/g)	Total pore volume (cm^3/g)	Mean pore diameter (nm)
LiAl-LDH	105.6	0.4568	23.06
LiZnAl-LDH-1%	133.7	0.5075	18.51
LiZnAl-LDH-5%	166.4	0.5757	18.49
LiZnAl-LDH-10%	152.2	0.5765	18.55
LiZnAl-LDH-20%	133.4	0.4611	18.46

Raman spectra were employed to investigated the structural changes of samples (Figure 3.7a). Compared to the LiAl-LDH, several strong peaks assigned to the Al-O and Li-O stretching became broadened and weaker [39], that might be attributed to the effects of crystal distortion and surface defects (*e.g.,* oxygen vacancy) as a result of Zn^{2+} incorporation [40]. The presence of surface oxygen vacancies was proved by EPR analyses (Figure 3.7b), in which the typical signal of oxygen vacancy was observed at g = 2.003 in LiZnAl-LDH-5%.

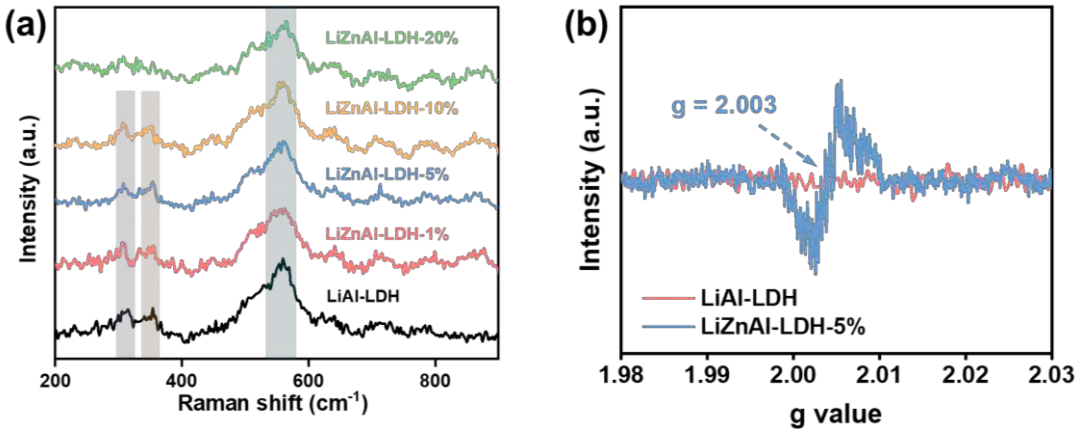

Figure 3.7 (a) Raman spectra and (b) EPR analyses of the LiAl-LDH and LiZnAl-LDHs.

Further, XPS analyses were employed to investigated the effect of doping on surface chemical state of LiZnAl-LDH-5%. It was found that some new peaks assigned to Al-O-Metal bond [41] and Zn^{2+} [34] appeared in Al 2p and Zn 2p spectra after Zn-doping, respectively, implying the presence of the doped Zn^{2+}. The O 1s spectra showed two major peaks at ~532.0 and 531.5 eV (Figure 3.8), corresponding to oxygen vacancy (O_v) and lattice oxygen (O_l) species, respectively [42]. Notably, the content of O_v significantly increased for LiZnAl-LDH-5%, reconfirming the increase in oxygen vacancies, which was consistent with the results of EPR and Raman analyses.

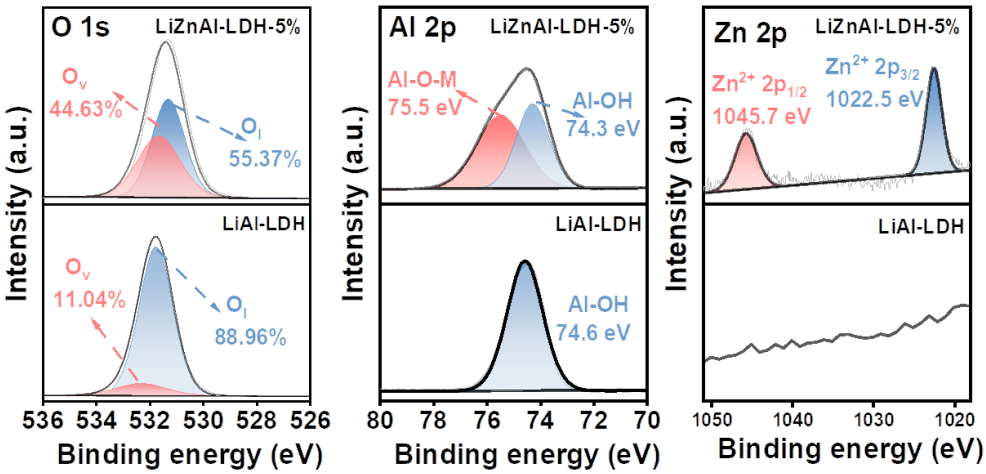

Figure 3.8 XPS spectra of the LiAl-LDH and LiZnAl-LDH-5%.

To better understand the difference in Li extraction before and after doping, the wetting ability was determined by contact angle measurement. As displayed in Figure 3.9, the contact angles of LiZnAl-LDHs decreased from 43° to 18° with the increasing Zn^{2+} dopant amount, indicating the enhanced hydrophilicity. Such feature ensured the easier transportation of Li^+ [43].

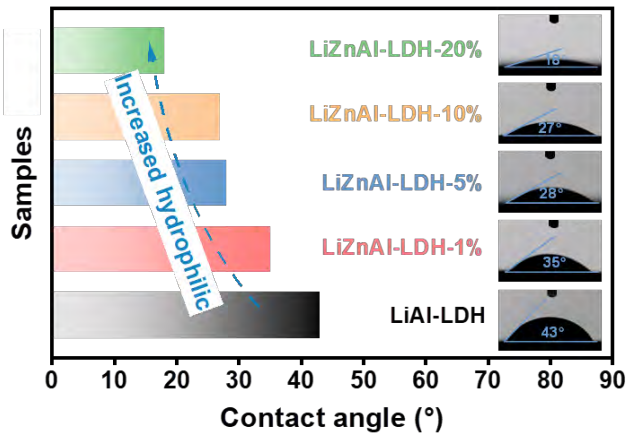

Figure 3.9 Contact angles of the LiAl-LDH and LiZnAl-LDHs.

3.3.3. Lithium-ion extraction performance

To evaluate the Li extraction performance of LiZnAl-LDH, the adsorption behaviors were investigated comprehensively. As shown in Figure 3.10, the Li^+ adsorption capacities on LiZnAl-LDHs were enhanced with the doping of Zn^{2+}, which resulted from the stronger affinity surface and larger specific surface area. Therein, LiZnAl-LDH-5% exhibited the best Li^+ uptake (6.1 mg/g within 1 h) with 18% improvement compared to the LiAl-LDH without Zn-doping. It was worth noting that although the Zn-doping had an obvious positive effect on the Li extraction, excessive amount would cause a sharp decline in Li^+ uptake owing to the generation of ZnO impurities without Li^+-extraction activity in the samples.

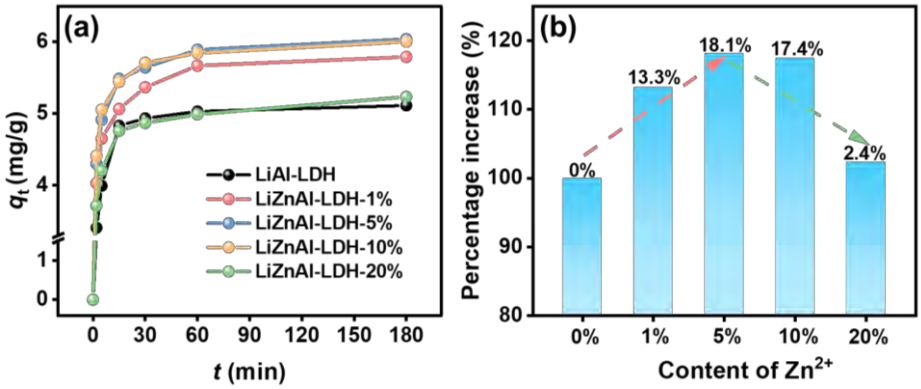

Figure 3.10 (a) The Li^+ adsorption capacity and (b) increase of LiZnAl-LDHs with different Zn^{2+} doping amounts in brine.

Further, the time-adsorption capacity data were analyzed for the kinetic characteristics. The results of the pseudo-first-order and the pseudo-second-order models were displayed in Table 3.3. One could see that the adsorption of Li^+ on all samples was better fitted by the pseudo-second-order model, suggesting that

chemisorption is the control step of LiAl-LDH and LiZnAl-LDHs [44].

Table 3.3 Parameters for the reactive kinetic models of Li^+ on samples.

Samples	Pseudo-first order model			Pseudo-second order model		
	k_1 (min^{-1})	$q_{e,cal}$ (mg/g)	R^2	k_2 (g/(mg·min))	$q_{e,cal}$ (mg/g)	R^2
LiAl-LDH	0.0328	2.28	0.7342	0.1472	5.15	0.9999
LiZnAl-LDH-1%	0.0288	2.10	0.8621	0.1247	5.84	0.9998
LiZnAl-LDH-5%	0.0179	1.85	0.7694	0.1361	6.08	0.9999
LiZnAl-LDH-10%	0.0176	1.64	0.7383	0.1540	6.04	0.9999
LiZnAl-LDH-20%	0.0321	1.71	0.7614	0.1349	5.27	0.9997

Moreover, the intraparticle diffusion model was used to examine the adsorption process. It could be found that all the Li extraction processes could be divided into three major steps (Figure 3.11), corresponding to (i) rapid transfer of Li^+ from the brine solution to the interface of LiAl-LDH; (ii) dehydration of Li^+ and insertion into the octahedral voids of LiAl-LDH; (iii) diffusion of Li^+ into the interior of the LiAl-LDH bulk to release the external active sites [31]. In addition, LiZnAl-LDHs possess faster surface transfer rate and diffusion inside rate with higher diffusion rate constants, reconfirming that doping engineering can enhance the affinity of samples for Li^+.

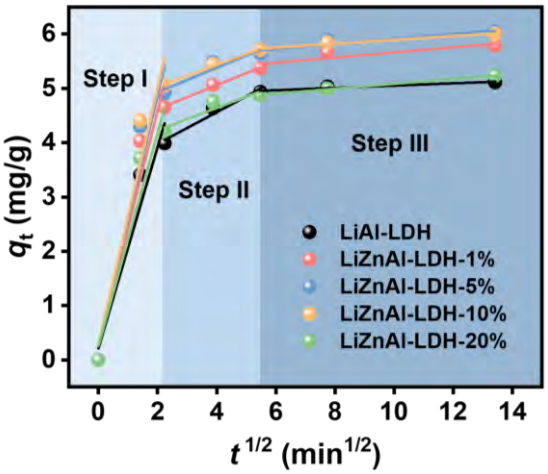

Figure 3.11 The intraparticle diffusion model for Li^+ adsorption process of the LiAl-LDH and LiZnAl-LDHs.

To speak of, the LiZnAl-LDHs presented significantly improved selectivity for Li^+ from Figure 3.12. The main competing metal cations of Lop Nor brine involve K^+, Na^+, and Mg^{2+}. Encouragingly, compared with the LiAl-LDH, the selectivity of Li^+/K^+,

Li^+/Na^+, and Li^+/Mg^{2+} of the LiZnAl-LDH-5% increased to ca. 3.3, ca. 12.3, and ca. 2.3 with separation factors as high as 213, 834, 171, respectively, which are well superior to those of the reported and commercialized lithium-aluminum layered double hydroxides. Such extraordinary selectivity was attributed to the high specific surface area and hydrophilicity of LiZnAl-LDH-5%, which exposed more adsorption sites and increased the number of sites for selective adsorption [45]. Considering the excellent adsorption capacity and selectivity of LiZnAl-LDH-5%, the 5% was chosen the optimal content of Zn^{2+} for the following tests.

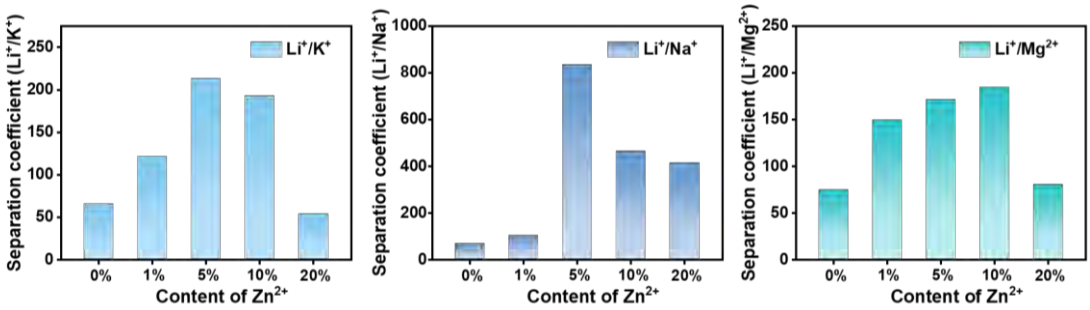

Figure 3.12 The comparison of the selectivity of LiZnAl-LDHs with different content of Zn^{2+} for (a) Li^+/K^+, (b) Li^+/Na^+, and (c) Li^+/Mg^{2+} in the brine.

To better assess the Li^+ adsorption ability of LiZnAl-LDH-5%, the maximum adsorption (q_m), a vital parameter in industrial applications, was determined by adsorption isotherm. As shown in Figure 3.13a, the q_e of adsorbents sharply increased and then reached a plateau (9.45 mg/g for LiAl-LDH, 13.10 mg/g for LiZnAl-LDH-5%) with the Li^+ concentration of 750 mg/L. Furthermore, the Langmuir and Freundlich models were applied to elucidate the adsorption process. From Figure 3.13b-c, the Langmuir model fitted better with LiAl-LDH, whereas the Freundlich model could describe better the adsorption on LiZnAl-LDH-5%, revealing a potential change in the adsorption mechanism from monolayer adsorption to multilayer adsorption after Zn-doping [44].

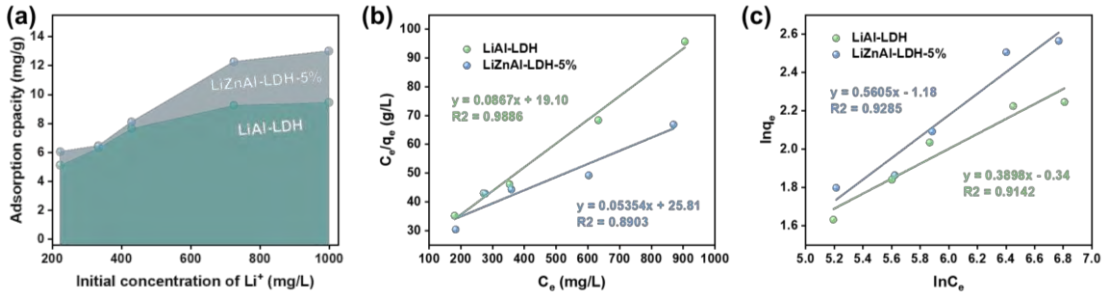

Figure 3.13 (a) The adsorption capacity of Li^+ with different initial concentration on

the LiAl-LDH and LiZnAl-LDH-5%. (b) Langmuir and (c) Freundlich models of Li^+ on pristine LiAl-LDH and LiZnAl-LDH-5%.

Washing process with deionized water was adopted to desorb ions in saturated adsorbents after initial Li extraction procedure. The desorption solution was mainly composed of Li^+ and Mg^{2+} with sporadic amounts of K^+ and Na^+. Importantly, the Mg^{2+}/Li^+ mass ratios sharply decreased from 459.5 in raw brine to 1.1 in desorption solution, which is greatly lower than the 1.8 in that of pristine LiAl-LDH (Table 3.4). Moreover, the desorption kinetics and cation (Li^+, K^+, Na^+ and Mg^{2+}) concentrations of elution solutions were presented in Figure 3.14. It could be seen that LiZnAl-LDH-5% had a fast Li^+ desorption rate with 30 min. Thus, LiZnAl-LDH-5% is a promising adsorbent for Li^+ recovery from brine with ultrahigh Mg^{2+}/Li^+ mass ratios.

Table 3.4 The cation concentrations of adsorbents elution solutions.

Samples	Li^+ (mg/L）	Mg^{2+} (mg/L）	Na^+ (mg/L）	K^+ (mg/L）
LiAl-LDH	79.3	143.885	11.28	6.865
LiZnAl-LDH-5%	66.95	74.905	4.18	3.415

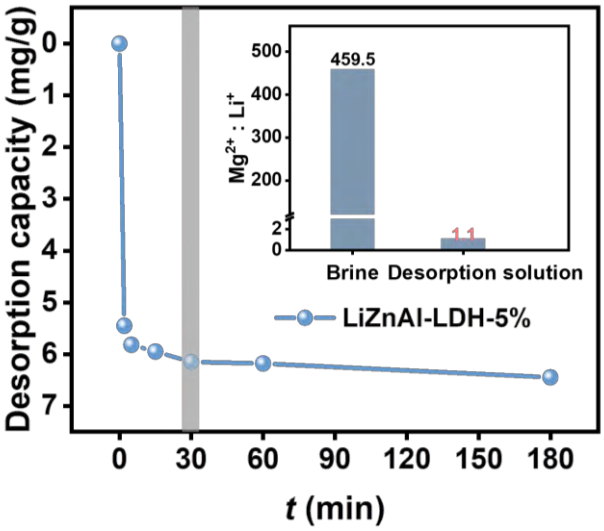

Figure 3.14 The Li^+ desorption capacity of LiZnAl-LDH-5%. Inset is the Mg^{2+}/Li^+ mass ratios in brine and desorption solution.

Also, the LiZnAl-LDH-5% exhibited long-term stability with a neglected Zn^{2+} loss (Figure 3.15a). Specifically, the adsorption capacity of LiZnAl-LDH-5% maintained almost unchanged of 7.0 mg/g in 10 cycles and showed almost no loss of Zn^{2+} in each subsequent cycle. From Figure 3.15b-c, the SEM image and XRD pattern after Li^+

adsorption showed neglected changes as well. These results indicated the good reusability and stability of LiZnAl-LDH-5% when applied in Li extraction from brines.

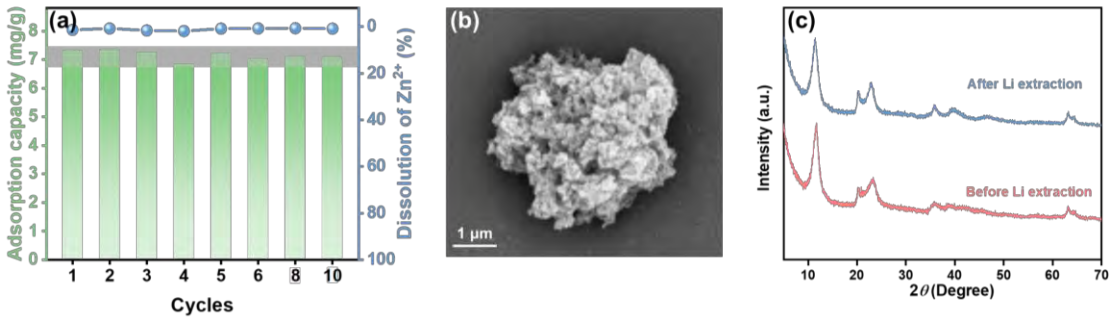

Figure 3.15 (a) The reusability and stability of LiZnAl-LDH-5%. (b) The SEM image of LiZnAl-LDH-5% after lithium extraction. (c) XRD patterns of LiZnAl-LDH-5% before and after lithium extraction.

At the same time, in comparison with previously reported lithium-aluminum layered double hydroxides (Figure 3.16), the Li extraction performance of LiZnAl-LDH-5% from brines, including q_m, adsorption kinetics, the selectivity of Li^+/K^+, Li^+/Na^+ and Li^+/Mg^{2+}, is extraordinarily excellent.

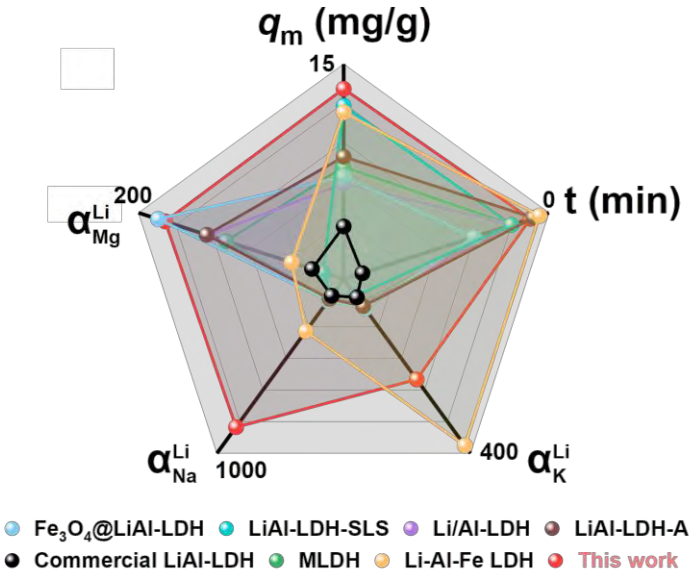

Figure 3.16 Comparison of Li extraction performance of different lithium-aluminum layered double hydroxides.

3.3.4. Mechanisms of enhanced performance for lithium extraction by Zn-doping

The preceding experiments demonstrated that LiZnAl-LDHs have a better Li extraction compared to pristine LiAl-LDH. The role of Zn-doping, however, is still unclear. Computational simulations were conducted to illustrate the mechanisms of

improved adsorption performance of LiZnAl-LDHs for Li^+. Generally, metal ions tend to bind to water molecules to form stable hydrated metal ion structures. For lithium-ion, four-coordinated structure [$Li(H_2O)_4^+$] is deemed to be the favorable hydration clusters in the aqueous phase [31], which was also certified by the results of calculations (Figure 3.17). Thus, the adsorption processes of $Li(H_2O)_4^+$ on samples before and after Zn-doping were researched in detail.

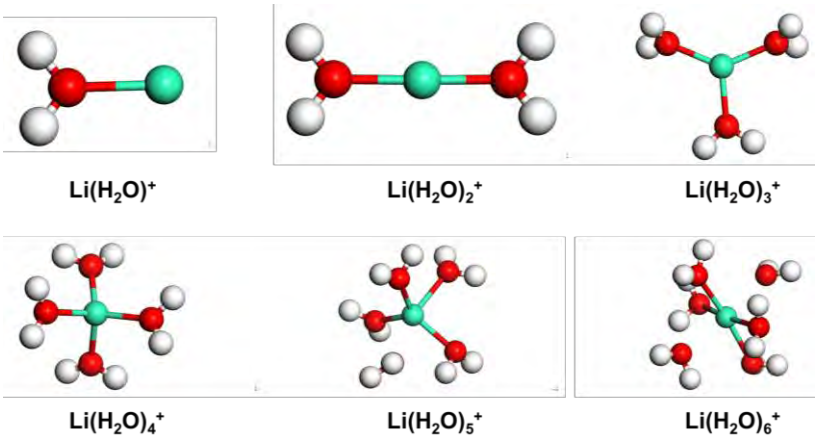

Figure 3.17 Optimal configuration of hydrated lithium ions.

During the transfer step, only the typical adsorption sites at the tip of the octahedral voids were considered owing to the "ion sieve effect" of LiAl-LDHs. Then, the adsorption energys (E_{ad}) of $Li(H_2O)_4^+$ on LiZnAl-LDHs and pristine LiAl-LDH were simulated in Fig (Figure 3.18b), respectively, in which the LiZnAl-LDHs possessed more negative E_{ad} (-22.51 kal/mol) than LiAl-LDH without Zn-doping (-19.90 kal/mol). Meanwhile, the Li-O distance of the former (5.401 Å) was apparently shorter compared with the latter. These results indicated that doping engineering delivered a stronger Li^+ affinity to the LiZnAl-LDHs, enabling easier transfer of $Li(H_2O)_4^+$ from the brine solution to the surface of LiZnAl-LDHs, which was consistent with the results of intraparticle diffusion model analyses [25]. The improvement in transfer might be due to lower surface charge, higher specific surface area and more hydrophilic surface of sample after Zn-doping. Further, the Li^+ transferred and adsorbed on the surface is ready for the following insertion reaction step. With the help of more negative E_{ads}, the $Li(H_2O)_4^+$ was more easily dehydrated and inserted into the lithium vacancies of LiZnAl-LDH, which could be manifested by the lower Gibbs free energy (ΔG) of the insertion reaction (Figure 3.18c). In the final step (diffusion), the Li^+ inserted was ready to diffuse into the bulk of LiAl-LDH to release the external active sites. Thus, the

diffusion pathways of Li^+ between two adjacent octahedral voids were simulated. It could be seen that the diffusion energy barrier for Li^+ within pristine LiAl-LDH was calculated to be 11.53 kcal/mol (Figure 3.18d). After Zn-doping, the Li^+ diffusion process within LiZnAl-LDHs was accelerated with lower diffusion energy, which might result from the presence of defects [46].

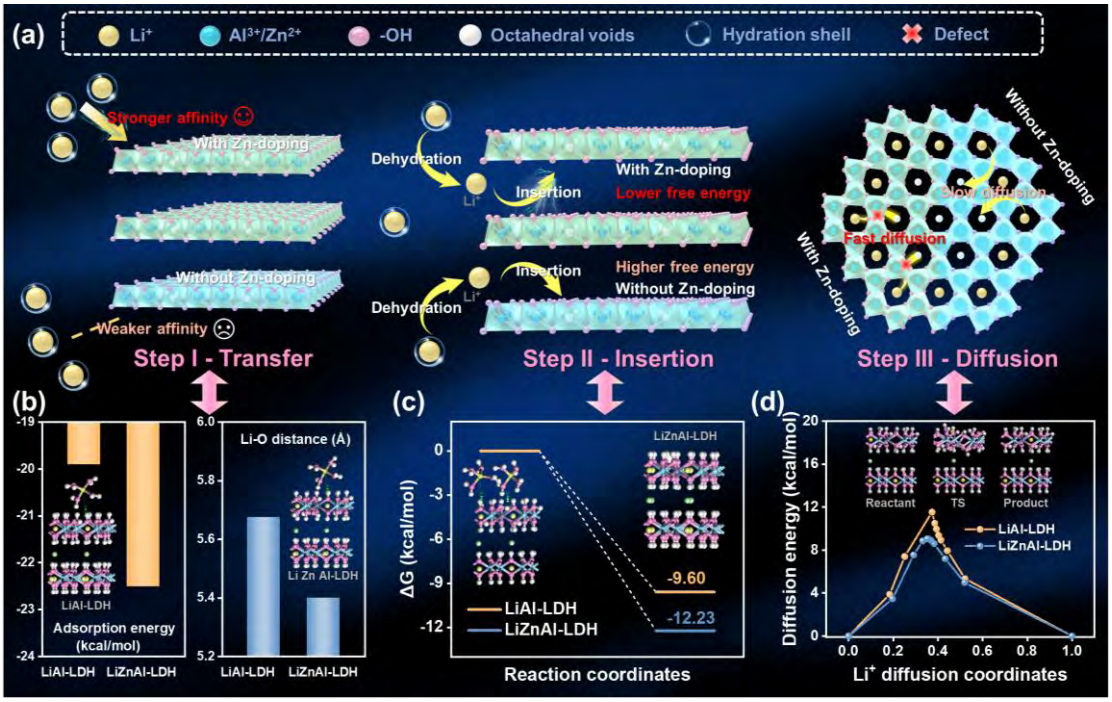

Figure 3.18 (a) Three-steps schematic representation of Li extraction on pristine LiAl-LDH and LiZnAl-LDH. (b) Theoretical calculation analysis: The adsorption energy of $Li(H_2O)_4^+$ on pristine LiAl-LDH and LiZnAl-LDHs surface; (c) The Gibbs free energy of Li-insertion reaction on pristine LiAl-LDH and LiZnAl-LDHs; (d) The diffusion energy barrier of Li^+ within pristine LiAl-LDH and LiZnAl-LDHs.

Based on above analyses, it could be deduced that the doping engineering can deliver a superior Li extraction performance to LiAl-LDH by facilitating the transfer of $Li(H_2O)4^+$, reducing the free energy of Li-insertion reaction, and accelerating the solid-phase diffusion of Li^+. Eventually, the prepared LiZnAl-LDHs presented unprecedented potential as Li^+ adsorbent.

3.4. Conclusions

In summary, the doping engineering of LiZnAl-LDHs were achieved via one-pot co-precipitation method, which can make up the unsatisfactory performance of LiAl-LDHs commercial adsorbents for Li extraction. Benefited from the Zn-doping, the

enhanced specific surface area, hydrophilic as well as surface attraction for Li^+, and the generation of intrinsic defects comprehensively improved the Li extraction performance. That is, q_m is up to 13.10 mg/g, and α_{K+}^{Li+}, α_{Na+}^{Li+} and α_{Mg2+}^{Li+} for Lop Nor brine are as high as 213, 834, 171, respectively, which are far superior to the reported and commercialized LiAl-LDHs. Furthermore, combining experiments and theoretical calculations, a three-steps process for Li extraction on LiAl-LDHs was proposed. Importantly, after the doping engineering, the LiZnAl-LDH exhibits the more favorable three-steps processes with more negative adsorption energy and Gibbs free energy for Li^+ transfer and insertion, and lower Li^+ diffusion energy barrier. Overall, this work provides a prospective strategy for promote the development of the Li extraction industry on a larger scale.

3.5. References

[1] S. Xu, J. Song, Q. Bi, Q. Chen, W. Zhang, Z. Qian, L. Zhang, S. Xu, N. Tang, T. He, Extraction of lithium from Chinese salt-lake brines by membranes: Design and practice, J. Membr. Sci. 635 (2021) 119441.
[2] S. Zhou, X. Guo, X. Yan, Y. Chen, W. Lang, Zr-doped titanium lithium ion sieve and EP-granulated composite: Superb adsorption and recycling performance, Particuology 69 (2022) 100-110.
[3] L. Wu, C. Zhang, S. Kim, T.A. Hatton, H. Mo, T.D. Waite, Lithium recovery using electrochemical technologies: Advances and challenges, Water Res. 221 (2022) 118822.
[4] X. Sun, M. Ouyang, H. Hao, Surging lithium price will not impede the electric vehicle boom, Joule 6 (2022) 1738-1742.
[5] J. Chen, S. Lin, J. Yu, High-selective cyclic adsorption and magnetic recovery performance of magnetic lithium-aluminum layered double hydroxides (MLDHs) in extracting Li^+ from ultrahigh Mg/Li ratio brines, Sep. Purif. Technol. 255 (2021) 117710.
[6] T. Zhang, H. Bai, Y. Zhao, B. Ren, T. Wen, L. Chen, S. Song, S. Komarneni, Precise Cation Recognition in Two-Dimensional Nanofluidic Channels of Clay Membranes Imparted from Intrinsic Selectivity of Clays, ACS Nano 16 (2022) 4930-4939.
[7] X. Zhao, S. Yang, Y. Hou, H. Gao, Y. Wang, D.A. Gribble, V.G. Pol, Recent progress on key materials and technical approaches for electrochemical lithium extraction processes, Desalination 546 (2023) 116189.
[8] L. Baudino, C. Santos, C.F. Pirri, F. La Mantia, A. Lamberti, Recent Advances in the Lithium Recovery from Water Resources: From Passive to Electrochemical Methods, Adv. Sci. 9 (2022) 2201380.
[9] Y. Sun, Q. Wang, Y. Wang, R. Yun, X. Xiang, Recent advances in magnesium/lithium separation and lithium extraction technologies from salt lake brine, Sep. Purif. Technol. 256 (2021) 117807.

[10] J. Miao, K. Zhao, F. Guo, L. Xu, Y. Xie, T. Deng, Novel LIS-doped mixed matrix membrane absorbent with high structural stability for sustainable lithium recovery from geothermal water, Desalination 527 (2022) 115570.
[11] S. Safari, B.G. Lottermoser, D.S. Alessi, Metal oxide sorbents for the sustainable recovery of lithium from unconventional resources, Appl. Mater. Today 19 (2020) 100638.
[12] X. Xu, Y. Chen, P. Wan, K. Gasem, K. Wang, T. He, H. Adidharma, M. Fan, Extraction of lithium with functionalized lithium ion-sieves, Prog. Mater. Sci. 84 (2016) 276-313.
[13] J. Chen, S. Lin, J. Yu, Quantitative effects of Fe_3O_4 nanoparticle content on Li^+ adsorption and magnetic recovery performances of magnetic lithium-aluminum layered double hydroxides in ultrahigh Mg/Li ratio brines, J. Hazard. Mater. 388 (2020) 122101.
[14] H. Yu, G. Naidu, C. Zhang, C. Wang, A. Razmjou, D.S. Han, T. He, H. Shon, Metal-based adsorbents for lithium recovery from aqueous resources, Desalination 539 (2022) 115951.
[15] Y. Zhang, J. Liu, Y. Yang, S. Lin, P. Li, Preparation of granular titanium-type lithium-ion sieves and recyclability assessment for lithium recovery from brines with different pH value, Sep. Purif. Technol. 267 (2021) 118613.
[16] K. Zhao, B. Tong, X. Yu, Y. Guo, Y. Xie, T. Deng, Synthesis of porous fiber-supported lithium ion-sieve adsorbent for lithium recovery from geothermal water, Chem. Eng. J. 430 (2022) 131423.
[17] L.-R. Bao, J.-Z. Zhang, W.-P. Tang, S.-Y. Sun, Synthesis and adsorption properties of metal oxide-coated lithium ion-sieve from salt lake brine, Desalination 546 (2023) 116196.
[18] M. Dong, Q. Luo, J. Li, Z. Wu, Z. Liu, Lithium adsorption properties of porous LiAl-layered double hydroxides synthesized using surfactants, J. Saudi Chem. Soc. 26 (2022) 101535.
[19] S. Lin, Y. Pan, J. Du, Y. Yang, H. Su, J. Yu, Double-edged role of interlayer water on Li^+ extraction from ultrahigh Mg^{2+}/Li^+ ratio brines using Li/Al-LDHs, J. Colloid Interface Sci. 627 (2022) 872-879.
[20] L. Wu, S.F. Evans, Y. Cheng, A. Navrotsky, B.A. Moyer, S. Harrison, M.P. Paranthaman, Neutron Spectroscopic and Thermochemical Characterization of Lithium–Aluminum-Layered Double Hydroxide Chloride: Implications for Lithium Recovery, J. Phys. Chem. C 123 (2019) 20723-20729.
[21] X. Li, L. Chen, Y. Chao, L. Zhu, G. Luo, J. Sun, L. Jiang, W. Zhu, Z. Liu, C. Xu, Highly selective separation of lithium with hierarchical porous lithium-ion sieve microsphere derived from MXene, Desalination 537 (2022) 115847.
[22] M.P. Paranthaman, L. Li, J. Luo, T. Hoke, H. Ucar, B.A. Moyer, S. Harrison, Recovery of Lithium from Geothermal Brine with Lithium–Aluminum Layered Double Hydroxide Chloride Sorbents, Environ. Sci. Technol. 51 (2017) 13481-13486.
[23] W. Xiao, X. Jiang, X. Liu, W. Zhou, Z.N. Garba, I. Lawan, L. Wang, Z. Yuan, Adsorption of organic dyes from wastewater by metal-doped porous carbon materials,

J. Cleaner Prod. 284 (2021) 124773.
[24] Z. Ma, W. Shi, K. Yan, L. Pan, G. Yu, Doping engineering of conductive polymer hydrogels and their application in advanced sensor technologies, Chem. Sci. 10 (2019) 6232-6244.
[25] L. Zhang, Z. Ke, W. Wang, H. Liu, Y. Mao, M. Xiang, P. Zhang, Enhanced removal of multiple metal ions on S-doped graphene-like carbon-supported layered double oxide: Mechanism and DFT study, Sep. Purif. Technol. 288 (2022) 120636.
[26] L. Zhang, S. Zheng, P. Li, Z. Zhu, Y. Zou, P. Zhang, Resource utilization of organic spent adsorbent to prepare three-dimensional sulfate-functionalized layered double oxide for superior removal of azo dye, Environ. Sci. Pollut. Res. 28 (2021) 53021-53033.
[27] J. Wu, B. Yang, S. Song, M. Quintana, F. Jia, X. Tian, The efficient recovery of molybdenite fines using a novel collector: Flotation performances, adsorption mechanism and DFT calculation, Miner. Eng. 188 (2022) 107848.
[28] M. Jiang, Y. Hu, B. Mao, Y. Wang, Z. Yang, T. Meng, X. Wang, M. Cao, Strain-regulated Gibbs free energy enables reversible redox chemistry of chalcogenides for sodium ion batteries, Nat. Commun. 13 (2022) 5588.
[29] D. Sun, D. Ye, P. Liu, Y. Tang, J. Guo, L. Wang, H. Wang, MoS_2/Graphene Nanosheets from Commercial Bulky MoS_2 and Graphite as Anode Materials for High Rate Sodium-Ion Batteries, Adv. Energy Mater. 8 (2018) 1702383.
[30] F. Qian, M. Guo, Z. Qian, B. Zhao, J. Li, Z. Wu, Z. Liu, Enabling highly structure stability and adsorption performances of $Li_{1.6}Mn_{1.6}O_4$ by Al-gradient surface doping, Sep. Purif. Technol. 264 (2021) 118433.
[31] Y. Li, N. Tang, L. Zhang, J. Li, Fabrication of Fe-doped lithium-aluminum-layered hydroxide chloride with enhanced reusable stability inspired by computational theory and its application in lithium extraction, Colloids Surf., A 658 (2023) 130641.
[32] T.R. Graham, J.Z. Hu, X. Zhang, M. Dembowski, N.R. Jaegers, C. Wan, M. Bowden, A.S. Lipton, A.R. Felmy, S.B. Clark, K.M. Rosso, C.I. Pearce, Unraveling Gibbsite Transformation Pathways into LiAl-LDH in Concentrated Lithium Hydroxide, Inorg. Chem. 58 (2019) 12385-12394.
[33] A.I. Khan, D. O'Hare, Intercalation chemistry of layered double hydroxides: recent developments and applications, J. Mater. Chem. 12 (2002) 3191-3198.
[34] X. Zhang, H. Yi, M. Jin, Q. Lian, Y. Huang, Z. Ai, R. Huang, Z. Zuo, C. Tang, A. Amini, F. Jia, S. Song, C. Cheng, In Situ Reconstructed Zn doped $Fe_xNi_{(1-x)}OOH$ Catalyst for Efficient and Ultrastable Oxygen Evolution Reaction at High Current Densities, Small 18 (2022) 2203710.
[35] X. Pu, X. Du, P. Jing, Y. Wei, G. Wang, C. Xian, K. Wu, H. Wu, Q. Wang, X. Ji, Y. Zhang, Interface and defect engineering enable fast and high-efficiency Li extraction of metatitanic acid adsorbent, Chem. Eng. J. 425 (2021) 130550.
[36] R. Keyikoglu, A. Khataee, H. Lin, Y. Orooji, Vanadium (V)-doped ZnFe layered double hydroxide for enhanced sonocatalytic degradation of pymetrozine, Chem. Eng. J. 434 (2022) 134730.

[37] G. Cao, X. Yang, Z. Yin, Y. Lei, H. Wang, J. Li, Synthesis, adsorption properties and stability of Cr-doped lithium ion sieve in salt lake brine, Bull. Chem. Soc. Jpn. 92 (2019) 1205-1210.
[38] L. Hou, B. Xing, W. Kang, H. Zeng, H. Guo, S. Cheng, G. Huang, Y. Cao, Z. Chen, C. Zhang, Aluminothermic reduction synthesis of porous silicon nanosheets from vermiculite as high-performance anode materials for lithium-ion batteries, Appl. Clay Sci. 218 (2022) 106418.
[39] E.S. Zhitova, I.V. Pekov, I.I. Chaikovskiy, E.P. Chirkova, V.O. Yapaskurt, Y.V. Bychkova, D.I. Belakovskiy, N.V. Chukanov, N.V. Zubkova, S.V. Krivovichev, V.N. Bocharov, Dritsite, $Li_2Al_4(OH)_{12}Cl_2 \cdot 3H_2O$, a New Gibbsite-Based Hydrotalcite Supergroup Mineral, Minerals 9 (2019) 492.
[40] D. Luo, B. Yang, Z. Mei, Q. Kang, G. Chen, X. Liu, N. Zhang, Tuning the d-Band States of Ni-Based Serpentine Materials via Fe^{3+} Doping for Efficient Oxygen Evolution Reaction, ACS Appl. Mater. Interfaces 14 (2022) 52857-52867.
[41] Q. Li, W. Liang, F. Liu, G. Wang, J. Wan, W. Zhang, C. Peng, J. Yang, Simultaneous immobilization of arsenic, lead and cadmium by magnesium-aluminum modified biochar in mining soil, J. Environ. Manage. 310 (2022) 114792.
[42] Y. Ding, Z. Wang, Z. Zhang, Y. Zhao, S. Yang, Y. Zhang, S. Yao, S. Wang, T. Huang, Y. Zhang, L. Li, Oxygen vacancy-engineered $BaTiO_3$ nanoparticles for synergistic cancer photothermal, photodynamic, and catalytic therapy, Nano Res. 15 (2022) 7304-7312.
[43] X. Li, Y. Chao, L. Chen, W. Chen, J. Luo, C. Wang, P. Wu, H. Li, W. Zhu, Taming wettability of lithium ion sieve via different TiO_2 precursors for effective Li recovery from aqueous lithium resources, Chem. Eng. J. 392 (2020) 123731.
[44] P. Zhang, L. Zhang, Z. Ke, M. Xiang, Y. Cai, W. Wang, Y. Chen, Z. Zhu, Sulfate-loaded layered double oxide: A bifunctional adsorbent for simultaneous purification of metal ion and anionic dye, Appl. Clay Sci. 216 (2022) 106366.
[45] K. Ding, G. Zhu, C. Song, Q. Wang, L. Wang, Z. Wang, C. Meng, C. Gao, Fabrication of polyacrylonitrile-$Li_{1.6}Mn_{1.6}O_4$ composite nanofiber flat-sheet membranes via electrospinning method as effective adsorbents for Li^+ recovery from salt-lake brine, Sep. Purif. Technol. 284 (2022) 120242.
[46] J. Lin, C. Zeng, X. Lin, C. Xu, X. Xu, Y. Luo, Metal–Organic Framework-Derived Hierarchical MnO/Co with Oxygen Vacancies toward Elevated-Temperature Li-Ion Battery, ACS Nano 15 (2021) 4594-4607.

Chapter 4. Steering interlayer interaction of lithium-aluminum layered double hydroxide beads for stable lithium extraction from sulfate-type brines

4.1. Introduction

Lithium, one of the most valuable energy metals, has been widely applied in numerous areas, particularly in lithium-ion batteries (LIBs) [1-4]. To ensure the sustainable development of LIBs market, it is imperative to extract lithium from brines due to high lithium reserves (60% of the global total) and low environmental impact, yet hampered by competing ions with high concentrations, such as Mg^{2+} [5-7]. Adsorption has a reputation for lithium extraction from brines with ultrahigh Mg^{2+}/Li^{+} ratios owing to low cost, superior Li^{+} selectivity and performance [8-10]. Up to date, lithium-aluminum layered double hydroxide (LiAl-LDH) are the most successful industrialized adsorbents for recovering Li^{+} from brines because of stable adsorption performance and easy elution with deionized water [11,12]. Nevertheless, the applications of LiAl-LDH focus on Cl^{-}-type brines, less on SO_4^{2-}-type brines, another common lithium-bearing brines in nature, as a result of deactivation caused by the abatement of adsorption capacity during long-term process [13-15].

The essential reason for the deactivation of LiAl-LDH in SO_4^{2-}-type brines is the intercalation of SO_4^{2-} into interlayers, which hinders the Li^{+} desorption and reduces subsequent Li^{+} adsorption. The generic formula of LiAl-LDH can be expressed as $LiX{\cdot}mAl(OH)_3{\cdot}nH_2O$, where X represents the interlayer anions, which connect to the laminates by interactions, like electrostatic interactions [16-18]. The Li^{+} adsorption-desorption process of LiAl-LDH can be described by $LiX{\cdot}mAl(OH)_3{\cdot}nH_2O + H_2O \rightleftharpoons xLiX + (1\text{-}x)LiX{\cdot}mAl(OH)_3 + (n+1)\ H_2O$, in which Li^{+} (~0.68 Å) can insert into octahedral cavities of $Al(OH)_3$ (0.70 Å) through size and memory effect [19-21]. Interlayer anions would simultaneously intercalate or deintercalate to maintain the electroneutrality of LiAl-LDH during the Li^{+} adsorption or desorption process [8,22]. Notably, LDHs possess anion exchange property with the order of $PO_4^{3-} > CO_3^{2-} > SO_4^{2-} > OH^{-} > Cl^{-}$, and the species, radius, and content of interlayer anions affect the structures and physiochemical properties of LDHs [23,24]. Tarasov et al. [25] found

that the desorption rate of Li^+ on LiAl-LDH relies on the interlayer anion via in-situ XRD analysis, where Li^+ would spontaneously release in water with Cl^-, and the deintercalation of Li^+ would only complete 40% with SO_4^{2-}, causing the decreasing adsorption sites for Li^+. The stronger stability of LiAl-LDH intercalated with SO_4^{2-} (LiAl-LDH-S) than that with Cl^- (LiAl-LDH-Cl) was also confirmed by electronic analyses [26]. At the atomic level, due to the electrostatic attraction between guest SO_4^{2-} and host laminates is stronger compared with Cl^-, the intercalation of Li_2SO_4 requires lower energy barrier, but higher energy barrier for deintercalation [27]. Hence, SO_4^{2-} in brines tend to replace interlayer Cl^- by ion exchange, obstructing the Li^+ desorption, thus reducing the re-adsorption capacity of LiAl-LDH.

Currently, limited efforts have been carried out by researchers to address this dilemma. For example, the desorption of intercalated Li^+ and SO_4^{2-} on LiAl-LDH would be improved by increasing temperature and eluent consumption [28]. Worryingly, the structures of LiAl-LDH readily collapse and transfer to gibbsite without Li extraction activity under such conditions [13,29,30]. The evasive strategy of removing SO_4^{2-} by nanofiltration and resin ion exchange prior to Li extraction avoided the SO_4^{2-} intercalation in LiAl-LDH, but operational costs and complexity skyrocketed [31]. Moreover, these methods failed to essentially solve dilemma. The efforts to overcome the deactivation of LiAl-LDH in Li extraction from SO_4^{2-}-type brines are still needed.

Compared to monovalent Cl^-, divalent SO_4^{2-} show higher ionic potentials (charge/radius, a critical parameter to describe the electric field intensity) [32], which provides spur for modification of LiAl-LDH. Based on the Coulomb's law, it is reasonable to speculate that the introduction of few negatively charged anions with highly ionic potentials to replace partial Cl^- in the interlayer of LiAl-LDH would induce a higher electrostatic repulsion with SO_4^{2-}, hindering the intercalation of SO_4^{2-}, and thus promising a solution to the feasibility of lithium extraction from SO_4^{2-}-type brines. To speak of, the excessive desorption of LiAl-LDH is also solved by regulating the intercalation amount of highly negatively charged anions to precisely anchor the amount of Li^+ required to maintain structural stability in the host layer, without impacting the deintercalation of LiCl adsorbed in LiAl-LDH, killing two birds with one stone. Herein, a novel strategy of steering interlayer interaction by replacing part of the Cl^- in the interlayer of LiAl-LDH with PO_4^{3-} (LiAl-LDH-P) was proposed to realize long-term recycling of LiAl-LDH in SO_4^{2-}-type brines. As a proof of concept, a mechanically robust LiAl-LDH-P bead (BLDH-P) was constructed to evaluate the

advancement of the resulting adsorbent in static and dynamic Li extraction in Lop Nur salt lake brine, the largest sulfate-type brine in the world. The adsorption, desorption, re-adsorption performance and property for preventing SO_4^{2-} intercalation of BLDH-P were comprehensively performed. Density functional theory (DFT) calculations were used to reveal the mechanisms of the steering interlayer interaction as well. This work provides a solution for sustainable lithium extraction from SO_4^{2-}-type brines and offers insights into the design of promising LDHs.

4.2. Experimental section

4.2.1. Reagents and materials

Lithium chloride (LiCl), aluminum chloride hexahydrate ($AlCl_3 \cdot 6H_2O$), sodium dodecahydrate phosphate ($Na_3PO_4 \cdot 12H_2O$), sodium hydroxide (NaOH), polyvinyl chloride (PVC), N, N-dimethylformamide (DMF), and polyacrylonitrile (PAN) were purchased from Aladdin Co., Ltd. All reagents are analytical grade without further purification.

The brine used in the experiments was obtained from Lop Nor Salt Lake Brine, a typical sulfate-type brine. The detailed compositions were summarized in Table 4.1.

Table 4.1 Properties of Lop Nor brine before and after static extraction.

Li^+ (mg/L)	Mg^{2+} (mg/L)	Na^+ (mg/L)	K^+ (mg/L)	SO_4^{2-} (mg/L)	Cl^- (mg/L)	pH
223.2	106045	3284.8	3725.6	37600	222400	5.04

4.2.2. Preparation of BLDH-P

Lithium-aluminum layered double hydroxide intercalated with phosphate ions (LiAl-LDH-P) were obtained by a modified co-precipitation method with reference to our previous research [19]. Furthermore, the PO_4^{3-} intercalated LiAl-LDH beads (BLDH-P) were prepared via inverse solvent phase conversion method.

Specifically, the solution with the $AlCl_3$:LiCl molar ratio of 2:1 was added into mixture solution of NaOH (8mol/L) and Na_3PO_4, stirred until the pH of mixed solution was 6, and then aged at 80 °C for 30 min to achieve the LiAl-LDH-P powder. Considering the balance between adsorption capacity and desorption ability, an adequate concentration of PO_4^{3-} (0.05 mol/L) was selected. Next, the PO_4^{3-} intercalated LiAl-LDH beads (BLDH-P) was prepared via inverse solvent phase conversion method, in which LiAl-LDH-P powder was mixed with PAN/PVC in wight ratio of 8:2 using

DMF as solvent to product adsorption-binder slurry, and then the slurry was dropped into deionized water using the injector to form adsorbent beads called BLDH-P-x (x represents the weight ratio of PAN in the binder, x = 0, 20%, 40%, 50%, and 60%). For comparison, Cl^- intercalated LiAl-LDH beads (BLDH-Cl) were also prepared by similar procedure except for the preparation of LiAl-LDH-Cl without Na_3PO_4.

4.2.3. Characterizations

The morphological structure and the elemental distribution of materials were observed by scanning electron microscopy (SEM, Phenom-Pro XL, China) equipped with energy distributions (EDS) system. To analyzed the materials phase structure, the X-ray diffraction (XRD) patterns were measured by the powder X-ray diffractometer (D8 ADVANCE X, Germany) with Cu K α radiation (40 kV, 100 mA). The surface functional groups of materials were determined using the Fourier transform infrared spectrometer (FTIR, 6700, Nicolet, USA). The N_2 adsorption-desorption measurements were performed by ASAP2460 aperture analyzer (Micromeritics, USA) to analyze the surface specific area, porosity and pore size of materials. The microscopic contact angle meter (Kyowa Interface Science Co. Ltd., Japan) was employed to obtain the contact angle (CA) of materials. The concentrations of anions and cations were measured by the anion chromatograph (Dionex Aquion, Thermo Scientific, USA) and the atomic absorption spectrum (AAS, G8434A, Japan). The chemical oxygen demand (COD) of dissolution was measured by the dichromate method based on the Standard of the People's Re public of China for Environmental Protection (GB 11914-89).

4.2.4. Lithium-ion extraction

Lithium extraction experiments were all performed in Lop Nor brine. Static experiments were conducted at room temperature in thermostatic water bath at 150 rpm (20 g/L), while dynamic experiments in a fixed bed with an inner diameter of 2.4 cm and a height of 30 cm. Adsorption kinetics were performed, and the pseudo-first-order, pseudo-second-order kinetic model, and the intraparticle diffusion models were used to analyzed experimental data, respectively [33]. Adsorption isotherms were carried out for 36 h, and the Langmuir and Freundlich models were employed to fit experimental data, respectively [19]. The desorption experiments were carried out by using deionized water with the solid/liquid of 1 g/50 mL as the eluent, stirred at 150 rpm for 8 h at 25 ℃. Considering the residual brine adhered to the surface of adsorbents, a rapid washing through ice water (1 g/5 mL) was performed before the desorption procedure. The

adsorption capacity (q_t, mg/g) and desorption capacity (q_d, mg/g) were calculated by Equation 4.1-4.2:

$$q_t = (C_0 - C_t)V/m \quad (4.1)$$

$$q_d = C_d V/m \quad (4.2)$$

where C_0, C_t, and C_d (mg/L) represent initial, residual, and desorption concentration, respectively. V (L) is the volume of brine, and m (g) indicates the mass of adsorbent.

The Li^+ adsorption selectivity was evaluated by the distribution coefficient K_d (mL/g) and separation coefficient αLi M, which were determined by Equation 4.3-4.4:

$$K_d = V(C_0 - C_e)/(mC_e) \quad (4.3)$$

$$\alpha_M^{Li} = K_{d,Li}/K_{d,M} \quad (4.4)$$

where M represents other cations.

4.2.5. Theoretical calculations

The Gaussian 09 software was used to calculate the electrostatic potential (ESP) distributions described using basis set of 6-31+G(d), and the results were analyzed by GaussView 5.0 [34]. The binding energies between anions and energy barriers of anions diffusion were performed by Materials Studio software (MS 8.1, Accelrys, San Diego, CA). The exchange-correlation interactions were established by the generalized gradient approximation of Perdew-Burke-Ernzerhof (GGA-PBE). The structures of LiAl-LDH-P and LiAl-LDH-Cl with interlayer spacing of 7.45 Å and 7.67 Å was constructed by modifying the structure obtained from Materials Project (Materials ID: mp-643655), respectively. The cut-off energy was set to 580 eV and the k-point mesh with a size of 3 × 1 × 1 grid was used. The convergence criteria for displacement, energy, and force were 0.002 Å, 2×10^{-5} eV/atom, and 0.05 eV/Å, respectively. The binding energy (E_b) were calculated by Equation 4.5:

$$E_b = E_{A/B} - E_A - E_B \quad (4.5)$$

where $E_{A/B}$ represents the total energy of A and B bonded system; E_A and E_B were the energies of individual A and B, respectively.

Further, the Gibbs free energies (G) as followed Equation 4.6. The energy barrier of anions diffusion within the LiAl-LDH were carried out via transition states searching, which were conducted by linear and quadratic synchronous transit (LST/QST) method nudged elastic band (NEB) tools implemented in $DMol^3$ [35,36].

$$G=E_{DFT}+E_{ZPE}-TS \quad (4.6)$$

where E_{DFT} indicates the total energy calculated through density functional theory (DFT); E_{ZPE} and TS represent the zero-point energy and the entropic contribution, respectively.

4.3. Results and discussion

4.3.1. Construction and optimization of LiAl-LDH beads

Considering the readily available and high mechanical properties, the polyvinyl chloride (PVC) can be an ideal binder for the large-scale production adsorbent beads [37]. Nevertheless, the diffusion process of Li^+ from brine to adsorbent surface is always impeded due to the hydrophobic instinct of PVC, which might be addressed by combination of hydrophilic polymer blend, such as polyacrylonitrile (PAN). Hence, the phosphate ions intercalated lithium-aluminum layered double hydroxide beads (BLDH-P) were prepared by co-precipitation followed by antisolvent method using PVC and PAN as the hybrid binders (Figure 4.1).

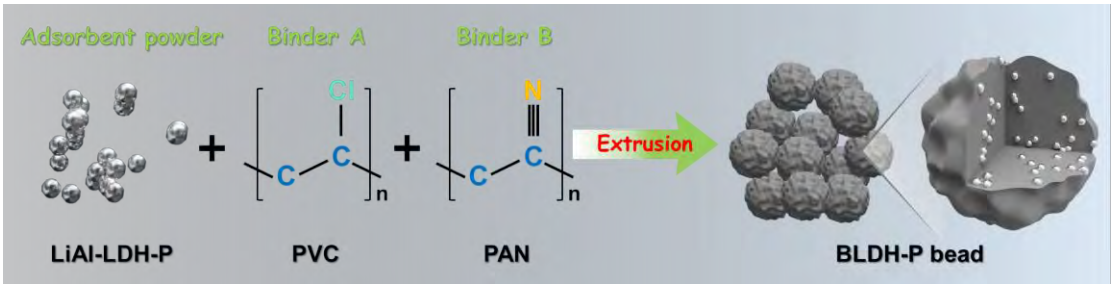

Figure 4.1 Schematic illustration of the fabrication strategy for BLDH-P beads.

The resultant BLDH-P beads appeared while with the diameters of 2.5-4.0 mm. The compatibility of both binders was optimized through determining the lithium extraction performance and stability of BLDH-P with various PVC/PAN ratios. As illustrated in the Figure 4.2, most BLDH-P mixtures were transparent except for the BLDH-P-60% after 24h of vigorous shaking in the brine. Such phenomena suggested that BLDH-P beads with suitable contents (i.e., PAN/PVC=0-50%) presented well stability.

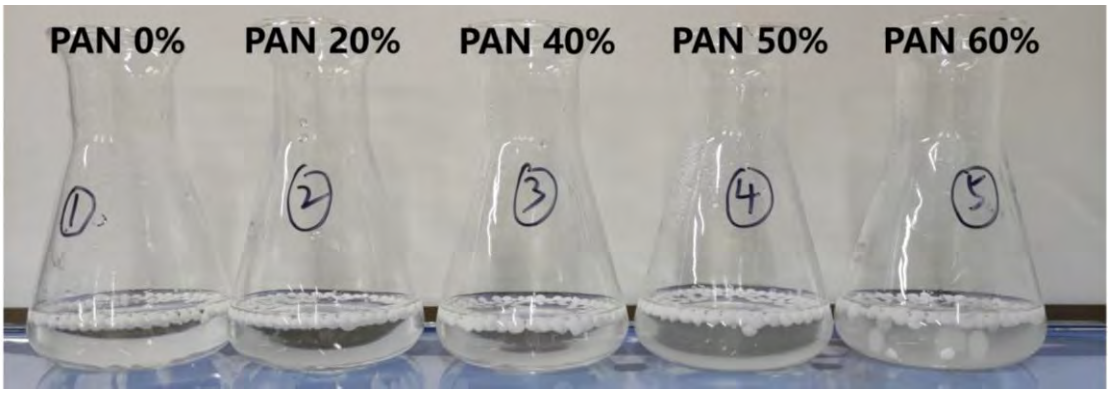

Figure 4.2 Optical photographs of the BLDH-P with various PVC/PAN ratios after 24h of vigorous shaking in brine.

The stability of adsorbents was confirmed by the dissolution results of BLDH-P beads in strong acid (pH=3) and alkali (pH=11) solutions. From Figure 4.3, it can be found that the mass losses, dissolution amounts of Al^{3+} and dissolution COD of BLDH-P were negligible levels except for a few samples with high PAN content.

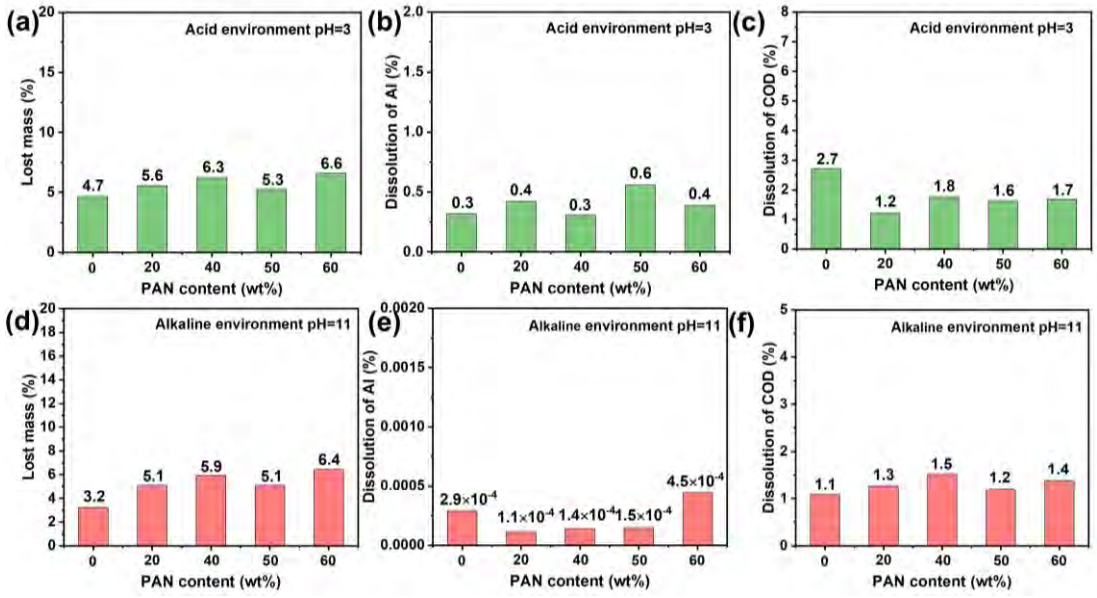

Figure 4.3 Mass losses, dissolution amounts of Al^{3+} and dissolution COD of BLDH-P beads with various PVC/PAN ratios in strong acid and alkali solutions.

Moreover, the effect of PVC/PAN ratios on wettability and surface structures was investigated to reveal the Li extraction potential of BLDH-P. As shown in Figure 4.4a, the contact angles of BLDH-P decreased from 64.25° to 47.75° with the increasing PAN content. Meanwhile, the pore number and roughness of BLDH-P surfaces increased with the addition of PAN (Figure 4.4c). These results indicated the improved water permeability and hydrophilicity, favoring Li^{+} diffusion and transfer on adsorbent beads.

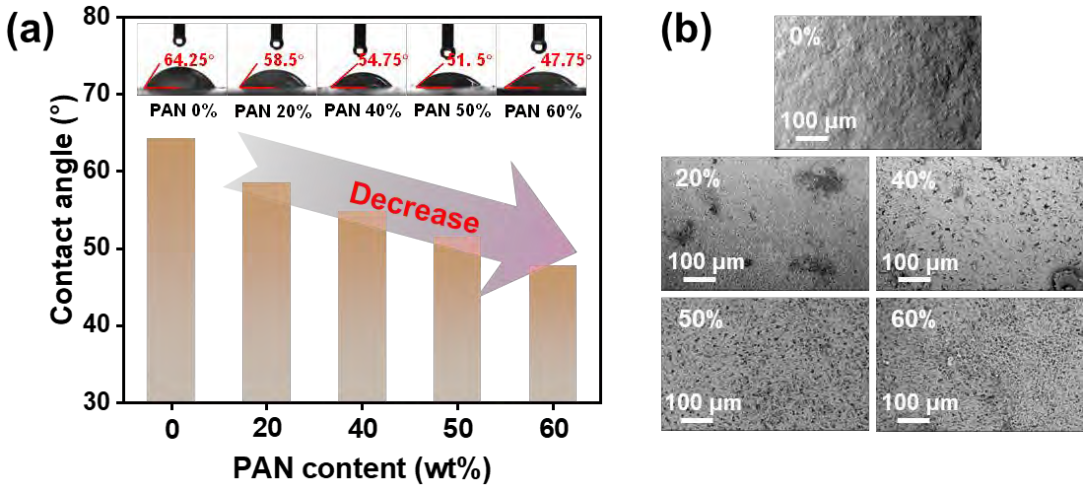

Figure 4.4 (a) Contact angles, and (b) SEM images of BLDH-P beads with various PVC/PAN ratios.

As expected, as the PAN content increased, BLDH-P exhibited a gradual grow in the Li^+ adsorption capacity in Lop Nor brine (Figure 4.5). Notably, the capacity of BLDH-P-50% was similar to that of BLDH-P-60%, which might result from the instable structure at high PAN content.

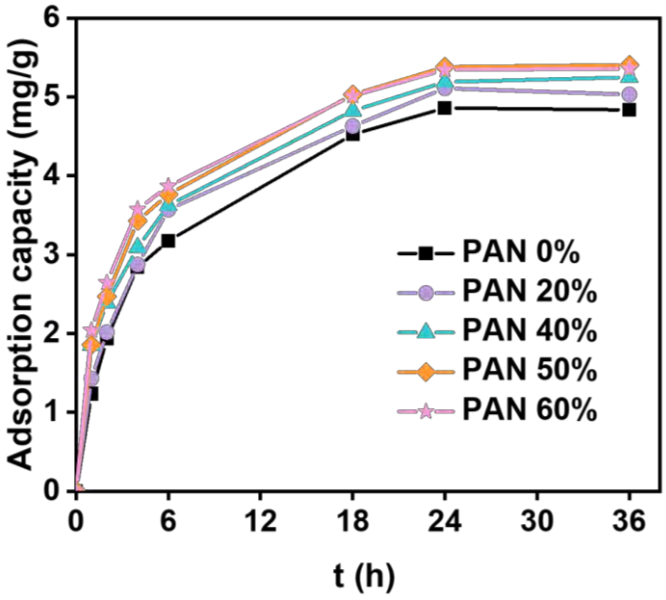

Figure 4.5 Li^+ adsorption capacities of BLDH-P beads with various PVC/PAN ratios.

In light of the above discussions, the full effect of PVC/PAN ratios was unveiled and schematically illustrated in Figure 4.6, where the Li extraction performance enhanced with the increasing PAN content, and the BLDH-P beads were capable of maintaining stable structure at appropriate PAN content, however, were instable at high content. BLDH-P-50% (abbreviated BLDH-P) was selected as the optimal lithium

adsorbent for following investigation as well.

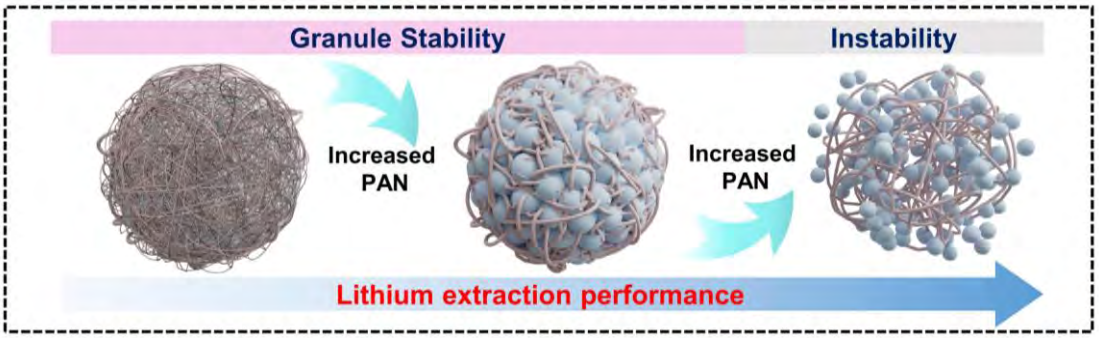

Figure 4.6 Schematic illustration of effect of PVC/PAN ratios on BLDH-P beads.

4.3.2. Characterization of LiAl-LDH beads intercalated with PO_4^{3-}

Micro-characterization and physicochemical properties of BLDH-P beads was systematically carried out. The X-ray diffraction (XRD) patterns in Figure 4.7 showed that all the characteristic diffraction peaks of LiAl-LDH-Cl and LiAl-LDH-P powder were well indexed into the standard card of the $LiCl{\cdot}2Al(OH)_3{\cdot}nH_2O$ (JCPDS No. 31-0700), indicating that crystalline products belong to LiAl-LDH. It was worth noting that compared to the LiAl-LDH-Cl, the crystal plane of (003) of LiAl-LDH-P mildly shifted to the lower angle accompanied by the increased interlayer spacing ($d_{(003)}$), suggesting intercalation of PO_4^{3-} with larger ion radius than Cl^- into the interlayer, resulting in the enlarged interlamellar space [38]. After the granulation process, BLDH-P showed a similar XRD pattern to LiAl-LDH-P powder, indicating that binders were adequately mixed and crystal structure of resultant bead was unaffected.

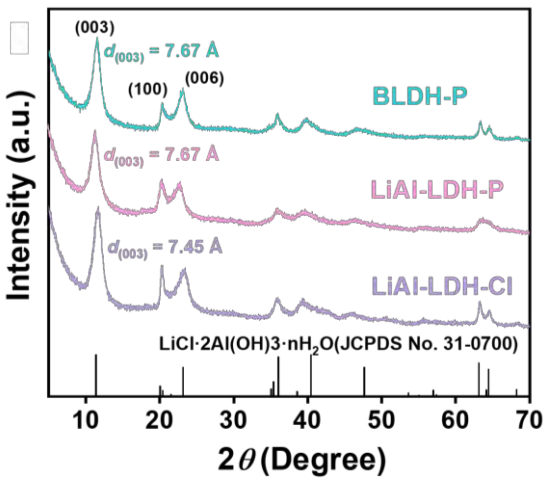

Figure 4.7 XRD patterns of LiAl-LDH-Cl powder, LiAl-LDH-P powder and BLDH-P bead.

Further, the Fourier transform infrared (FT-IR) spectra of samples were exhibited

in Figure 4.8, where beside P=O (1025 cm^{-1}), Al-O (530 and 943 cm^{-1}), and O-H assigned to PO_4^{3-} and LDH [19,39], respectively, BLDH-P showed both PVC- and PAN- (including C≡N, C-H) related functional groups [40], proving the successful preparation of BLDH-P beads.

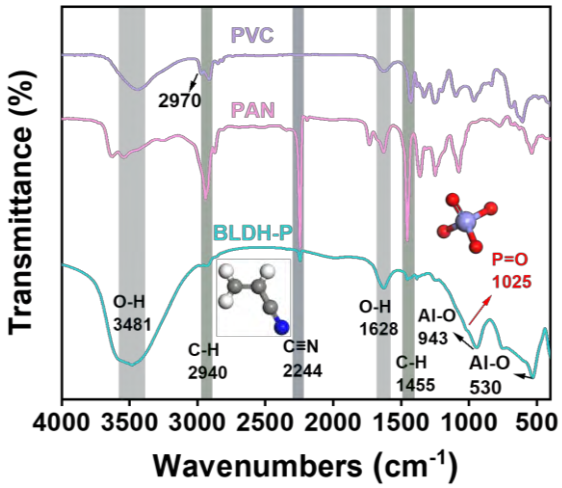

Figure 4.8 FT-IR spectra of PVC, PAN and BLDH-P bead.

Scanning electron microscope (SEM) image and energy dispersive spectroscopy (EDS) mapping images of BLDH-P also confirmed the coexistence of LiAl-LDH-P, PVC and PAN in BLDH-P, in which Al, O, P, C, N, Cl elements homogeneously distributed throughout internal structure of beads (Figure 4.9). From the SEM image, BLDH-P consisted of organic 3D net-framework with numerous mesopores and embedded LiAl-LDH-P powders. Such structure ensured excellent stability and multiple Li^+ diffusion channels, facilitating the Li extraction from brines.

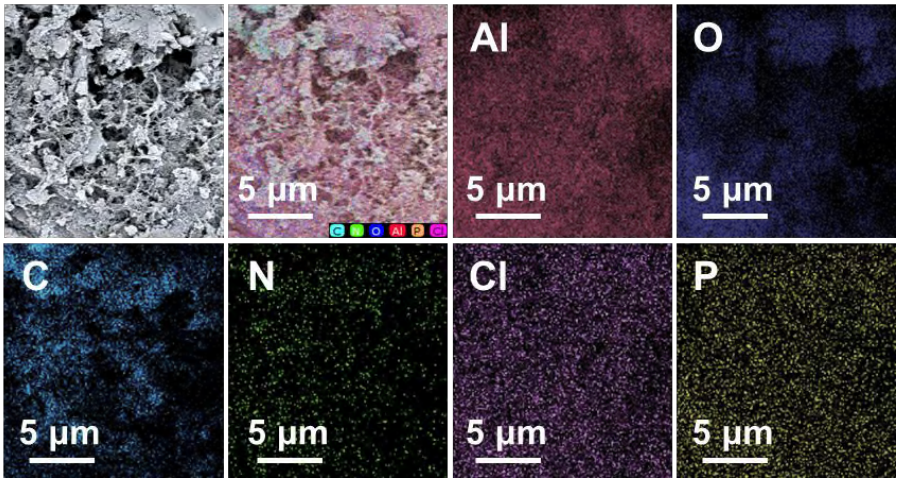

Figure 4.9 SEM images and EDS mapping images of BLDH-P internal.

The textural properties of adsorbents were investigated by N_2 adsorption-

desorption isotherms in detail (Figure 4.10a). Obviously, both BLDH-P and BLDH-Cl showed type IV isotherms with a hysteresis of H3 type, demonstrating the mesoporous structure [41], which was substantiated by the results of pore size analyses (Table 4.2 and Figure 4.10b). Importantly, the BET specific surface area (SSA) and pore volume of BLDH-P were markedly higher than these of BLDH-Cl, being conducive to the Li^+ diffusion and adsorption.

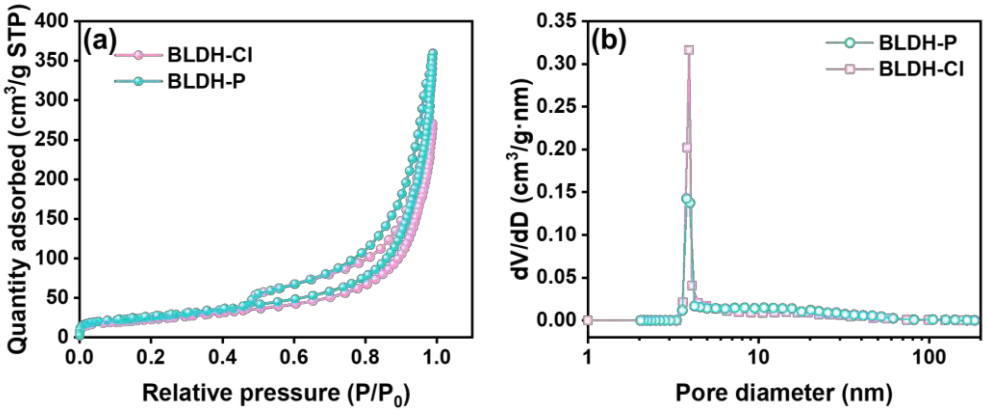

Figure 4.10 (a) Nitrogen adsorption-desorption isotherms, and (b) pore size distributions of BLDH-Cl and BLDH-P bead.

Table 4.2 The textural properties of BLDH-P and BLDH-Cl.

Samples	Specific surface area ($m^2 \cdot g^{-1}$)	Total pore volume ($cm^3 \cdot g^{-1}$)	Mean pore diameter (nm)
BLDH-Cl	105.6	0.4568	18.49
BLDH-P	146.00	1.0487	15.23

To estimate the potential of BLDH-P for preventing intercalation of SO_4^{2-}, the Cl^-, SO_4^{2-} and PO_4^{3-} were employed as models and density functional theory (DFT) calculations of electrostatic potential (ESP) distributions were conducted. As shown in Figure 4.11, the entire frames of all anions presented negative charges, and as the anion charge raised, the region with negative electrostatic potential was more concentrated (redder in color). Specifically, although both Cl^- and PO_4^{3-} had negative ESP, the latter exhibited more negative electrostatic potential, which might induce the stronger electrostatic repulsion between interlayered anions and SO_4^{2-} in brines [42], thus hindering the intercalation of SO_4^{2-}, and facilitating the long-term extraction of Li^+ from sulfate-type brines by LiAl-LDH.

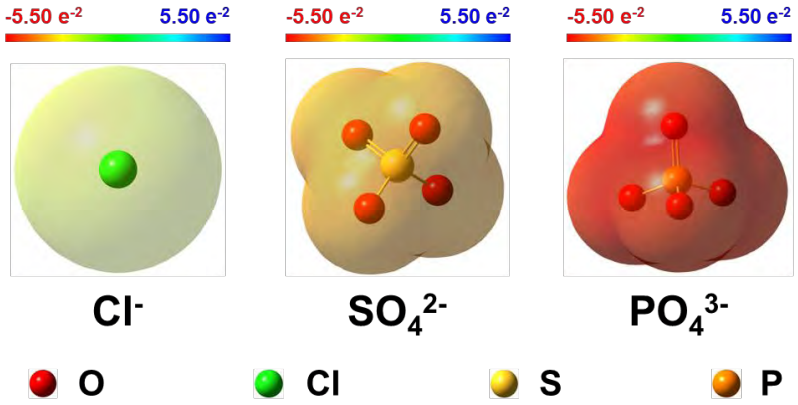

Figure 4.11 ESP distributions of Cl^-, SO_4^{2-}, PO_4^{3-} and their solvation energies.

4.3.3. Lithium extraction performance in sulfate-type brines

Static lithium extraction: To determine the suitability of BLDH-P in sulfate-type brines, the multiple cycle static Li extraction experiments with adsorption, desorption and re-adsorption were carried out in Lop Nor brine. As shown in Figure 4.12a, the adsorption capacities of both BLDH-P and BLDH-Cl rapidly increased in the first 8 h, then followed by slow adsorption rates until reaching equilibrium within 36 h. It was worth noting that BLDH-P exhibited a higher Li^+ adsorption capacity (5.26 mg/g) than BLDH-Cl (4.72 mg/g), which might be attributed to the higher SSA and interlayer spacing, promoting the Li^+ transfer and diffusion in adsorbent bead [43]. Moreover, the kinetic characteristics of extraction processes were investigated (Figure 4.12b-c and Table 4.3), where both adsorption kinetics fitted well the pseudo-second-order kinetic model according to the analysis of correlation coefficient (R^2), indicating that the chemical adsorption was the dominated during extraction processes [44,45]. In addition, the higher rate constant (k_2) proved the stronger driven force of BLDH-P for Li extraction than BLDH-Cl.

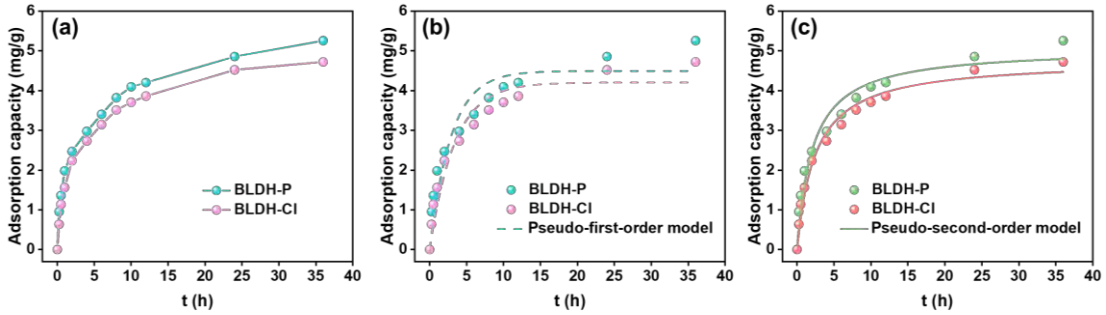

Figure 4.12 (a) Adsorption kinetics of Li^+ on BLDH-P and BLDH-Cl during the adsorption process. (b) The pseudo-first-order and (c) pseudo-second-order kinetic models of the BLDH-P and BLDH-Cl.

Table 4.3 Kinetic model parameters of BLDH-P and BLDH-Cl.

Samples	Pseudo-first-order			Pseudo-second-order		
	q_e (mg/g)	k_1 (min^{-1})	R^2	q_e (mg/g)	k_2 (g/(mg·min))	R^2
BLDH-P	4.49	0.35	0.9088	5.07	0.094	0.9658
BLDH-Cl	4.20	0.30	0.9415	4.77	0.084	0.9831

The intraparticle diffusion model were further used to analyzed the adsorption process (Figure 4.13). The Li extraction on adsorbents could be divided into three major steps, involving fast Li^+ surface adsorption from brine to the adsorbents interface, Li^+ transfer into octahedral voids of LiAl-LDH, and Li^+ internal diffusion [46]. To speak of, all three steps of BLDH-P showed faster rates than these of BLDH-Cl (Table 4.4), in consistence with the results of kinetics.

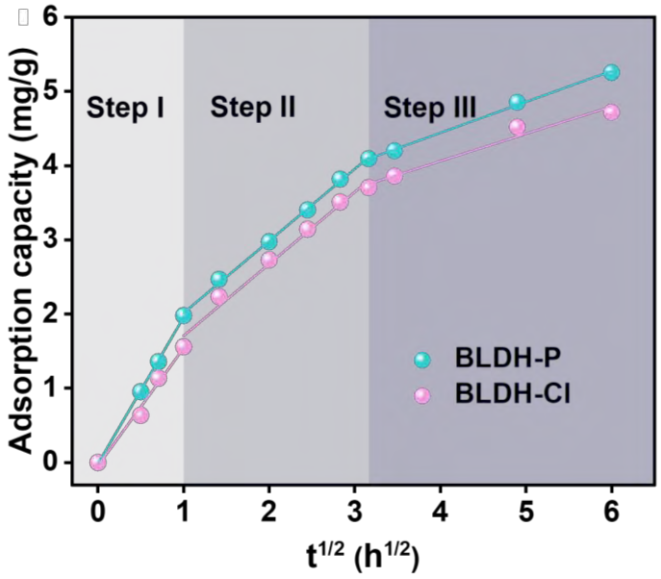

Figure 4.13 The intraparticle diffusion model of Li^+ on BLDH-P and BLDH-Cl during the adsorption process.

Table 4.4 The intraparticle diffusion model calculated parameters for the adsorption of Li^+ on samples.

Samples	k_{p1}	C_1	R^2_1	k_{p2}	C_2	R^2_2	k_{p3}	C_3	R^2_3
BLDH-P	1.97	-0.01	0.9990	0.97	1.05	0.9978	0.42	2.77	0.9963
BLDH-Cl	1.58	-0.04	0.9794	0.96	0.74	0.9803	0.37	2.59	0.9496

To in-depth investigate the Li extraction performance, adsorption isotherms were also estimated (Figure 4.14 and Table 4.5). One can see that adsorption processes of

both adsorbents agree better with the Langmuir model, suggesting that Li extraction was close to monolayer adsorption [47]. The theoretical maximum uptake from Langmuir model was as high as 8.46 mg/g.

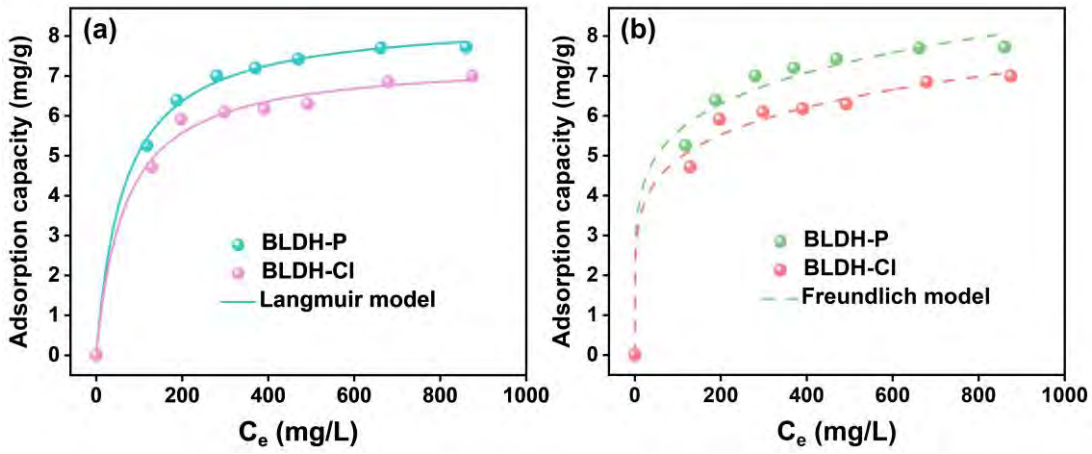

Figure 4.14 (a) Langmuir and (b) Freundlich isotherm models of BLDH-P and BLDH-Cl.

Table 4.5 Adsorption isotherm models parameters of BLDH-P and BLDH-Cl.

Samples	Langmuir			Freundlich		
	q_m (mg/g)	K_L (L/mg)	R^2	K_F (mg/g) (L/mg)$^{1/n}$	n_F	R^2
BLDH-P	8.46	0.0152	0.9926	2.58	5.93	0.9878
BLDH-Cl	7,42	0.0150	0.9913	2.25	5.91	0.9890

Next, the continuous desorption procedure was performed. Encouragingly, the desorption capacity of BLDH-P maintained stable level throughout ten desorption times (Figure 4.15a), revealing that the desorption is relatively easy for BLDH-P. In contrast, BLDH-Cl presented a gradual decrease in the desorption capacity. Based on previous research, such phenomena might derive from the accumulation of SO_4^{2-}, which had a strong electrostatic attraction with positively charged laminates in interlayer of LiAl-LDH, causing the difficulty of SO_4^{2-} and Li^+ desorption [13]. The accumulation of SO_4^{2-} was proved by the results of XRD patterns (Figure 4.15b), where the $d_{(003)}$ of BLDH-Cl enlarged from 7.45 Å to 7.65 Å after ten adsorption-desorption cycles, indicating the intercalation of SO_4^{2-} from the brine into BLDH-Cl [27]. While the structure of BLDH-P remained virtually unchanged for ten cycles, in agreement with the results of desorption capacity, suggesting that BLDH-P might repel SO_4^{2-} via interlayered PO_4^{3-}.

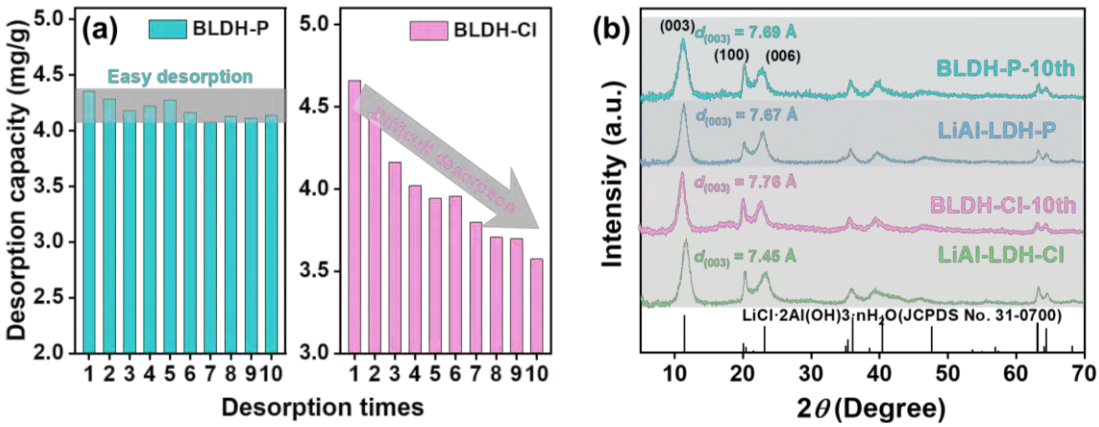

Figure 4.15 (a) Desorption capacities of BLDH-P and BLDH-Cl during ten desorption cycles. (b) The XRD patterns of LiAl-LDH-Cl powder, BLDH-Cl and BLDH-P after ten adsorption-desorption cycles.

In order to evaluate the long-term suitability of BLDH-P, the continuous re-adsorption procedure was also conducted in Lop Nor brine (Figure 4.16). As expected, the uptake of desorbed BLDH-P still maintained a high level (~4.1 mg/g) in ten re-adsorption cycles, while the re-adsorption capacity of BLDH-Cl showed a reduced Li extraction performance, which was in line with the results of desorption process. Owing to the strong interaction between SO_4^{2-} and LiAl-LDH laminates, Li^+ can be anchored into the octahedral voids during the desorption process, leading that the limited adsorption sites were released, hindering the Li^+ re-adsorption. Intriguingly, intercalated PO_4^{3-} can inhibit the intercalation of SO_4^{2-} into interlayer of LiAl-LDH, endowing BLDH-P with stable capacity.

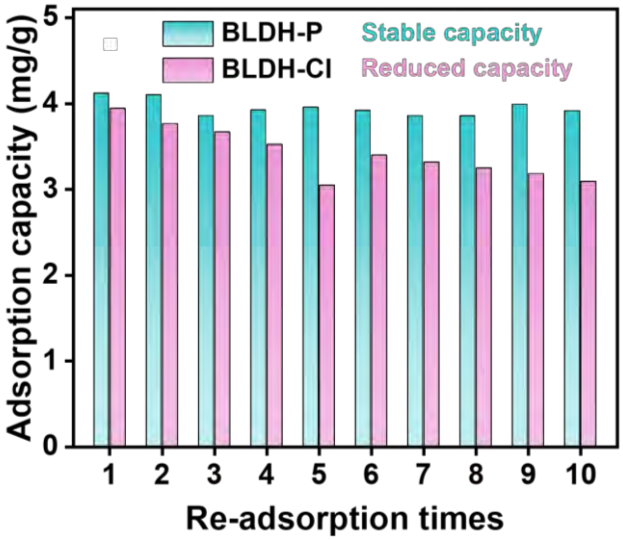

Figure 4.16 Adsorption capacities of BLDH-P and BLDH-Cl during ten cycles.

The selectivity of lithium adsorbent is crucial for Li extraction and recovery from salt lake brines, consisting of ultrahigh concentration K^+, Na^+, and Mg^{2+}. Figure 4.17 showed that BLDH-P realized the higher Li^+ selectivity compared with BLDH-Cl, and the separation factors of Li^+/K^+, Li^+/Na^+, and Li^+/Mg^{2+} reached 39.84, 48.14, and 144.87, demonstrating the extraordinary practical applicability of BLDH-P.

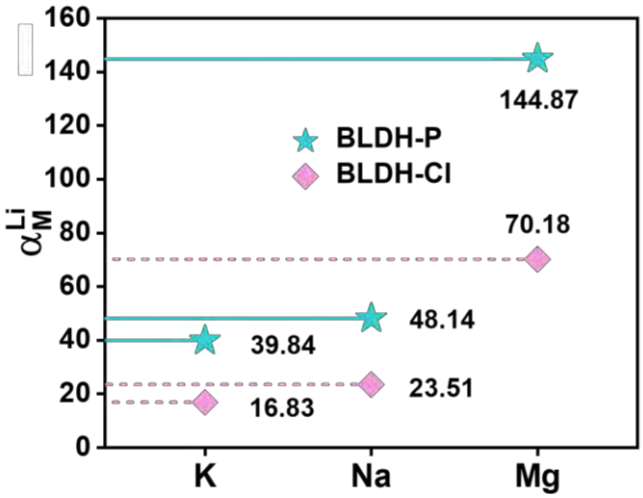

Figure 4.17 The selectivity of BLDH-P and BLDH-Cl.

Continuous column extraction: To assess the application prospect of BLDH-P in SO_4^{2-}-type brine, a facile fixed bed column adsorption device was developed. A continuous flow of Lop Nor brine through a column packed with BLDH-Cl or BLDH-P beads, as shown in Figure 4.18a. The results of Li^+ breakthrough curves presented a stable and long-term process of 12.4 bed volume (BV) for BLDH-P, which was well superior than that of BLDH-Cl (9.0 BV) (Figure 4.18b). At the same time, the total Li^+ adsorption capacity of BLDH-P was as high as 3.96 mg/g (Figure 4.18c).

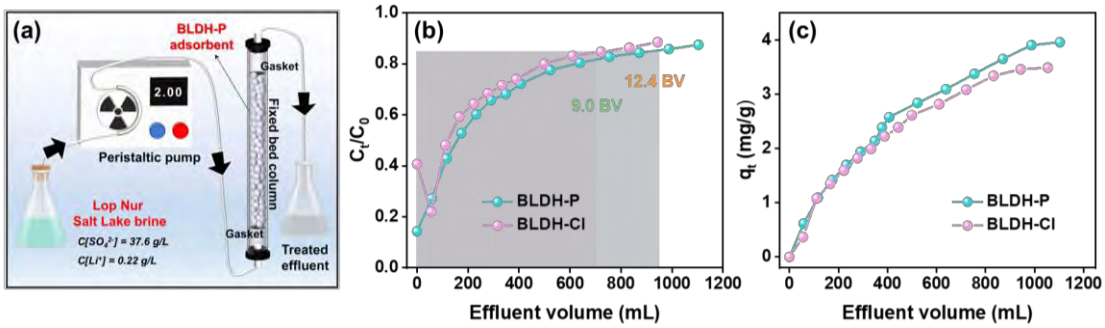

Figure 4.18 (a) Schematic illustration of the fixed bed column device. (b) The Li^+ breakthrough curves and (c) the Li^+ adsorption curves of BLDH-Cl and BLDH-P.

Such exceptional dynamic uptake in brine with low Li^+ concentration exceeded

most of the granulated LiAl-LDH adsorbents previously reported (Figure 4.19), demonstrating the extraordinary lithium extraction performance and strong adsorption drive.

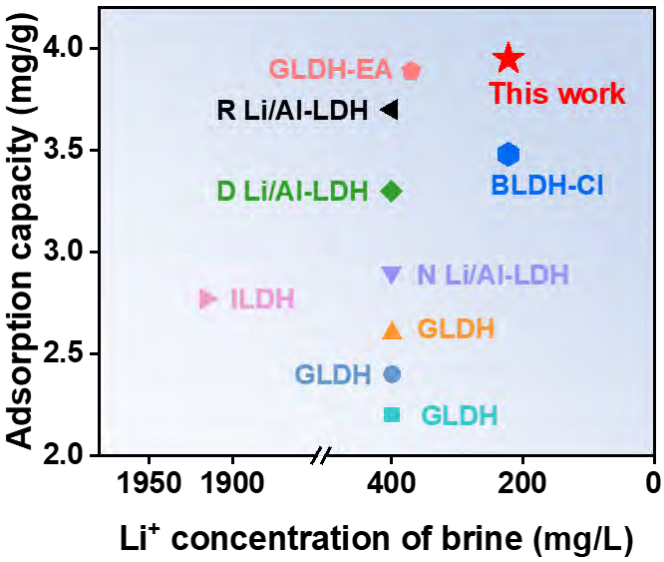

Figure 4.19 Comparison of Li^+ dynamic extraction properties of different LiAl-LDHs.

Moreover, considering the crucial significance of the adsorbents' reusability for large-scale application in practical Li extraction from brines, the consecutive dynamic Li^+ adsorption and desorption cycles were performed. Based on the results of dynamic adsorption (Figure 4.18b) and desorption (Figure 4.20), the volume of pumped brine was set to 1200 mL, and the volume of deionized water was set to 300 mL.

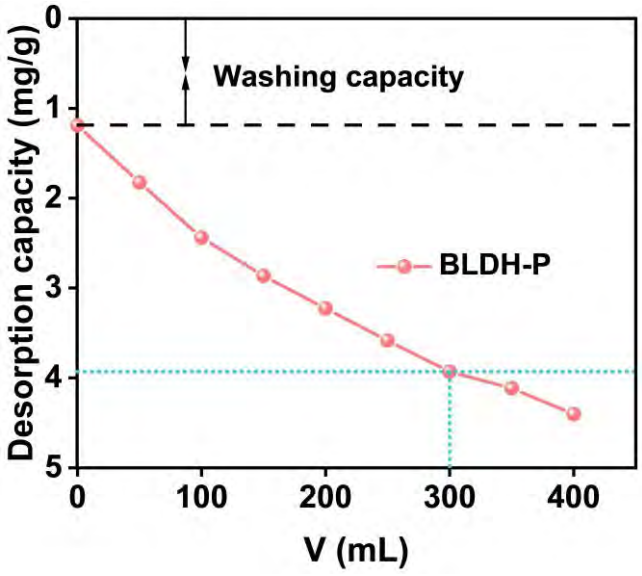

Figure 4.20 The dynamic desorption capacity of BLDH-P in fixed bed.

As exhibited in Figure 4.21a, the both dynamic adsorption capacity and desorption capacity maintained stable levels during 12 cycling process. Meanwhile, the surface of BLDH-P exhibited no cracks and the structure remained unchanged during the entire continuous extraction process (Figure 4.21b-c), suggesting the excellent reusability and advancement of BLDH-P.

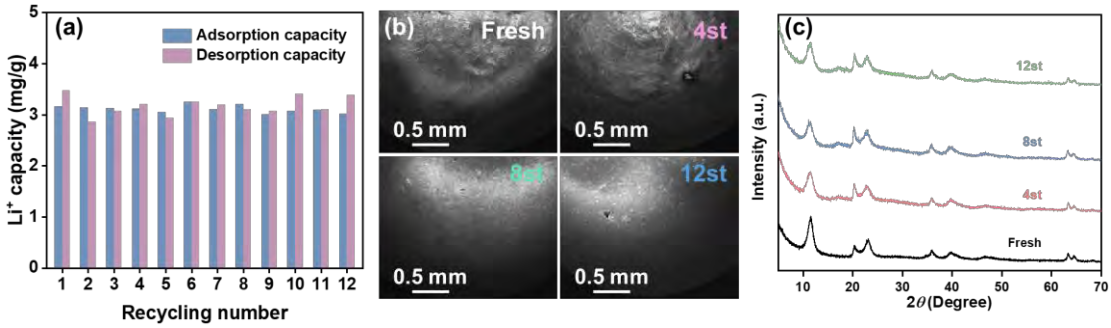

Figure 4.21 (a) The dynamic adsorption-desorption cycling adsorption performance of BLDH-P. (b) SEM images and (c) XRD patterns of BLDH-P after different cycling numbers

4.3.4. Mechanisms of stable extraction in sulfate-type brines

The preceding experiments have stated that BLDH-P bead possesses the property for preventing intercalation of SO_4^{2-} into LiAl-LDH interlayer, which results from the stronger electrostatic repulsion between PO_4^{3-} and SO_4^{2-}. The insights into the interaction mechanisms, however, still remain unclear. To this end, the DFT calculations were carried out to simulate the ions specific interactions and the processes of LiCl and Li_2SO_4 capture by LiAl-LDH intercalated with PO_4^{3-} or Cl^-. The electrostatic interaction might obviously affect the interaction between interlayered anions (i.e., PO_4^{3-} or Cl^-) and SO_4^{2-} in brines, further impacting the intercalation behaviors of SO_4^{2-}. Herein, the binding energy (E_b) was used to evaluate the insertion resistance of SO_4^{2-} into the interlayer of LiAl-LDH, where the higher E_b, the stronger interaction, the easier insertion of anion in brines [48]. As shown in the Figure 4.22, the E_b between Cl^- and SO_4^{2-} ($E_{Cl/S}$) was as high as -76.62 kcal/mol, while the E_b between PO_4^{3-} and SO_4^{2-} ($E_{P/S}$) was only -1.22 kcal/mol. Such calculation results indicated that common Cl^- tends to combine with SO_4^{2-}, inducing more SO_4^{2-} inserting into the interlayer of LiAl-LDH-Cl. Nevertheless, it is difficult for SO_4^{2-} to bind with PO_4^{3-} according to the low $E_{P/S}$. At the same time, it can be found that the E_b between PO_4^{3-} and Cl^- ($E_{P/Cl}$) increased to -76.51 kcal/mol, which suggested that Li extraction by LiAl-LDH-P favors being accompanied by the intercalation of Cl^- to balance the charge

instead of SO_4^{2-} in sulfate-type brine.

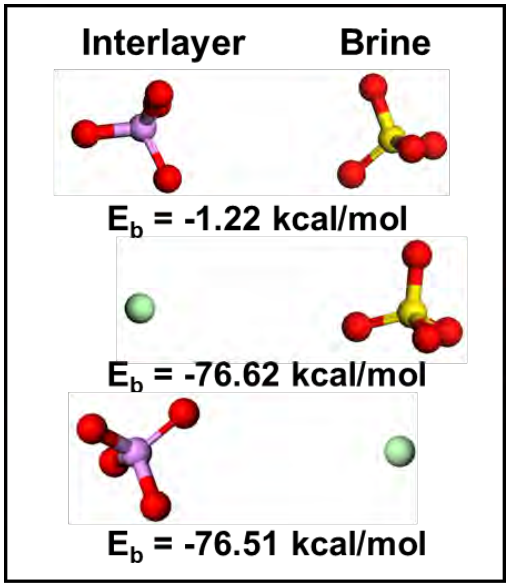

Figure 4.22 The optimized anion structure and binding energy between anions.

Although the highly negative electric field of PO_4^{3-} could induce electrostatic repulsion for both Cl^- and SO_4^{2-}, the former presented the smaller ionic potential (1.81) than that of the latter (2.40) (Figure 4.23a), demonstrating the lower electrostatic repulsion [49]. Additionally, the interlayer of LiAl-LDH-P consisted of PO_4^{3-} and Cl^-, that is, the adsorbent had a specific affinity for Cl^- due to memory effect [3]. Thus, LiAl-LDH-P featured a selective electrostatic interaction, allowing the Cl^- to overcome the electrostatic repulsion to achieve a smooth intercalation process. To better visualize the intercalation disparity, a normalized parameter of NP = E_b / $E_{p/s}$ was defined. The results of the $E_{Cl/S}$ NP indicated that the selectivity of SO_4^{2-}/Cl^- insertion into LiAl-LDH-P was the 62.57 (Figure 4.23b).

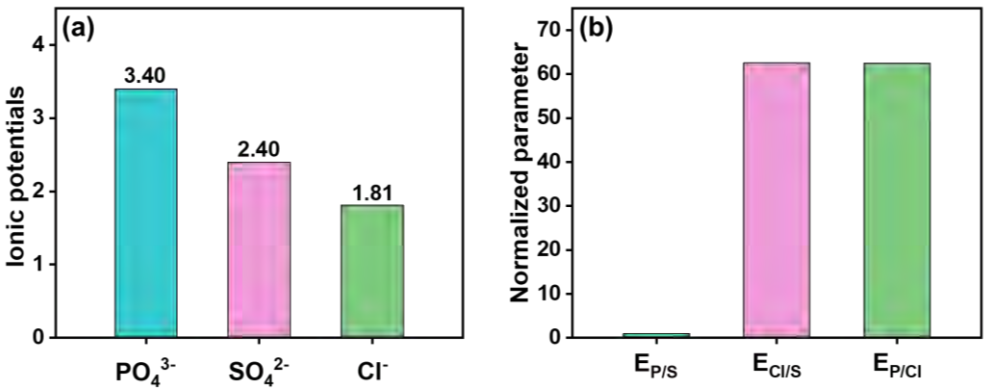

Figure 4.23 (a) Ionic potentials of different anions. (b) Quantitative diagram of anion interaction disparity.

Furthermore, interlayer SO_4^{2-} contents of BLDH-P and BLDH-Cl were determined as well (Figure 4.24). There was an upward trend in amount of interlayer SO_4^{2-} within BLDH-Cl after successive adsorption-desorption cycles. Whereas, the interlayer SO_4^{2-} amount of BLDH-P retained a low plateau, which might be due to the residual brine adhering to the bead, proving that PO_4^{3-} were capable of repelling SO_4^{2-} via stronger electrostatic repulsion.

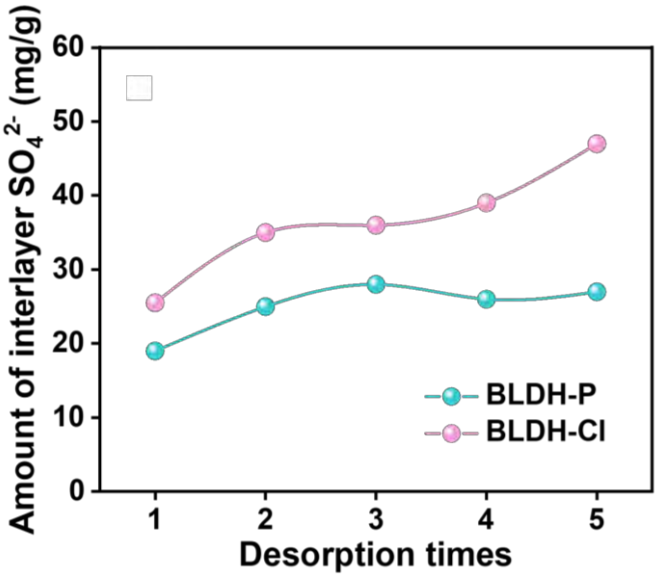

Figure 4.24 Amounts of interlayer SO_4^{2-} of BLDH-P and BLDH-Cl during five desorption cycles.

The EDS spectra of adsorbents after various desorption times realized similar trend in SO_4^{2-} amount as well (Figure 4.25). The facts that the low and stable SO_4^{2-} amount of BLDH-P provided solid proof for function of steering interlayer interaction strategy, i.e., prevention of SO_4^{2-} intercalation, in favor of the Li^+ and Cl^- re-adsorption in sulfate-type brines.

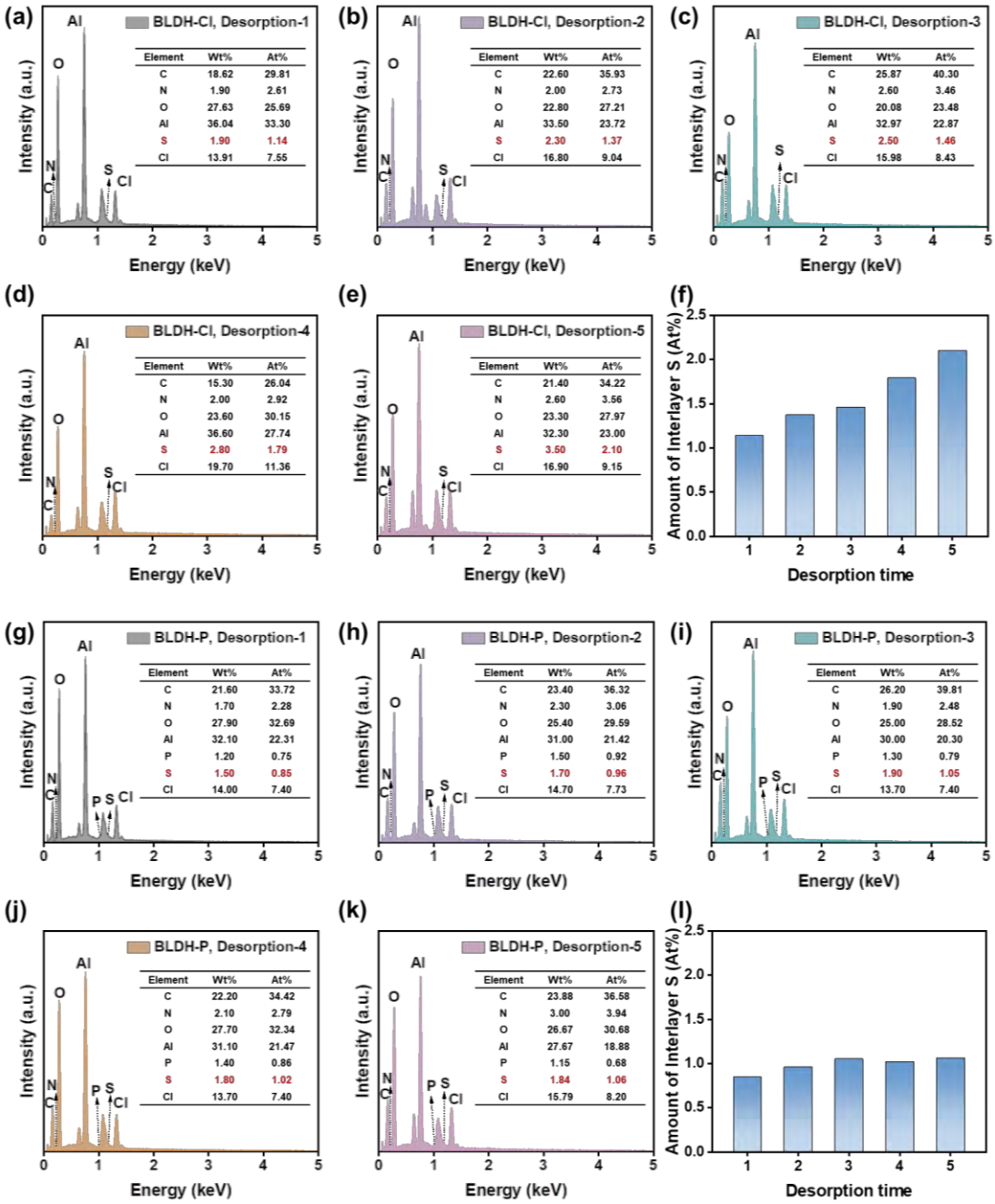

Figure 4.25 (a-e) The EDS spectra of BLDH-Cl after various desorption times. (f) The amount of S element in BLDH-Cl from the results of EDS spectra. (g-k) The EDS spectra of BLDH-P after various desorption times. (l) The amount of S element in BLDH-P from the results of EDS spectra.

Considering that the insertion of brine anions and their diffusion into LiAl-LDH are not only affected by the interaction between ions, but also by the diffusion paths and the spatial confinement of interlayer nanostructures, the calculation of diffusion energy barriers of Cl^- and SO_4^{2-} within LiAl-LDH-P or LiAl-LDH-Cl (Figure 4.26) was performed. It can be found that the energy barrier of SO_4^{2-} within common LiAl-LDH-

Cl was only 0.20 eV, indicating that there is low resistance for SO_4^{2-} diffusion, in consistence with the result of previous research [27]. Encouragingly, such energy barrier in LiAl-LDH-P intercalated with phosphate ions increased to 0.78 eV, corroborating the difficult diffusion of SO_4^{2-} within LiAl-LDH-P [36]. Comparing with SO_4^{2-}, the diffusion activation energy of Cl^- within LiAl-LDH-P was 0.45 eV, suggesting that for LiAl-LDH-P in brine with high concentration SO_4^{2-} and Cl^-, the Cl^- readily inserts into the interlayer and diffusion instead of SO_4^{2-}, preventing the reduction of Li^+ adsorption capacity derived from the tough desorption. Figure 4.27 exhibited the structures of initial state (IS), transition state (TS) and final state (FS) configurations for anion diffusion reaction within adsorbents.

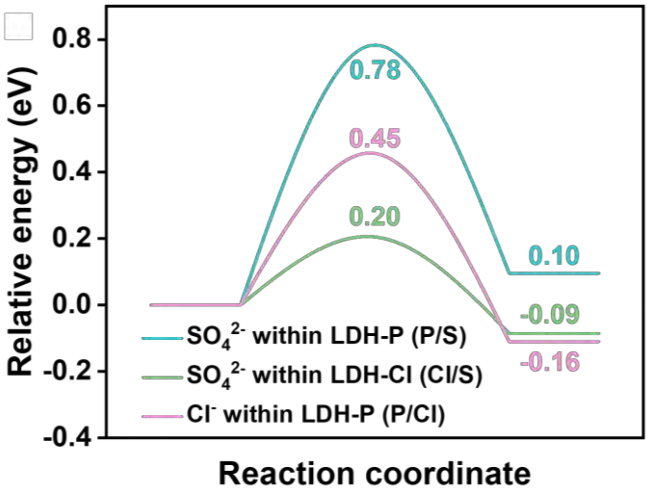

Figure 4.26 Relative energies for the diffusion of SO_4^{2-} and Cl^- within LiAl-LDH-P or LiAl-LDH-Cl.

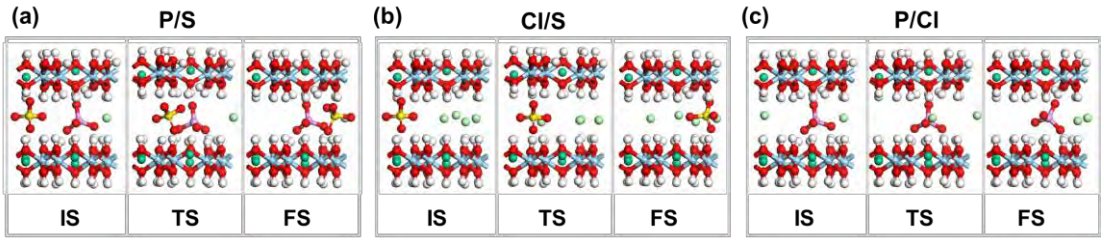

Figure 4.27 Optimized structures of initial state, transition state and final state configurations for SO_4^{2-}/Cl^- diffusion reaction within LiAl-LDH-P or LiAl-LDH-Cl.

Based on the above data and discussion, the functional mechanisms of PO_4^{3-} intercalation steering interlayer interaction strategy were schematically illustrated in Figure 4.28. Benefiting from the expansion of the interlayer spacing and the inhibition of SO_4^{2-} intercalation due to enhanced electrostatic repulsion as well as raised the

diffusion energy barrier within interlayers, BLDH-P was imparted with long-lasting excellent Li^+ adsorption capacity and selectivity in brines with ultrahigh concentrations of impurity cations and SO_4^{2-}.

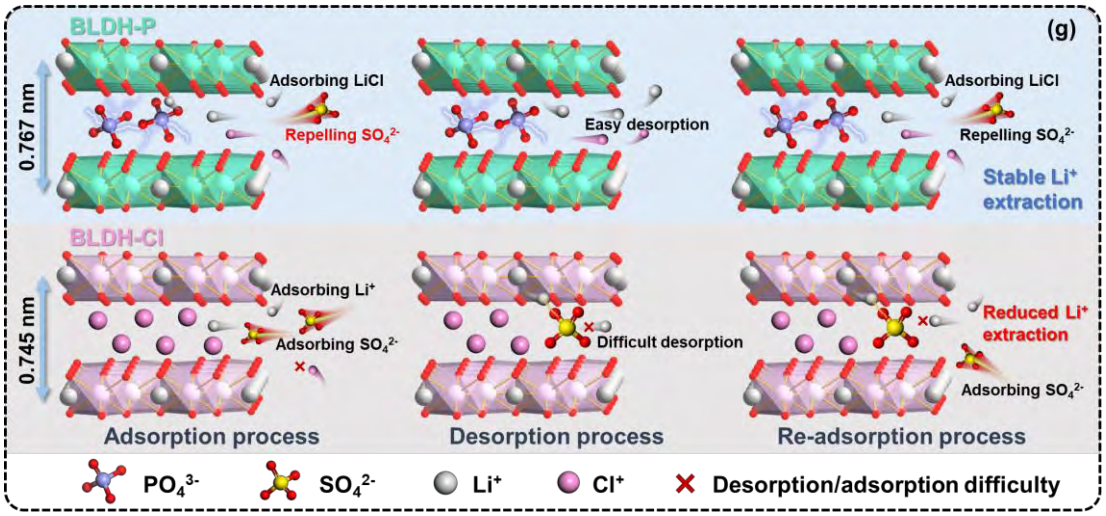

Figure 4.28 Schematic illustration of adsorption, desorption and re-adsorption processes of BLDH-P and BLDH-Cl.

4.4. Conclusions

In summary, a steering interlayer interaction strategy was proposed to improve the feasibility of LiAl-LDH-Cl in lithium extraction from SO_4^{2-}-type brines. The prepared BLDH-P beads intercalated with phosphate ions showed well mechanical properties and outstanding Li extraction performance. Specifically, the static and dynamic Li^+ adsorption capacity of BLDH-P reached 5.26 mg/g and 3.96 mg/g in Lop Nor brine, with high separation factors of 39.84, 48.14, and 144.87 for Li^+/K^+, Li^+/Na^+, and Li^+/Mg^{2+}, respectively, outperforming the reported and commercialized LiAl-LDH. Moreover, BLDH-P were endowed with property for preventing SO_4^{2-} intercalation through strong electrostatic repulsion between interlayer PO_4^{3-} and SO_4^{2-} in brine, which was proved by DFT calculation. Unlike BLDH-Cl, BLDH-P therefore presented the stable desorption and re-adsorption ability and low amount of interlayer SO_4^{2-} in continuous desorption and re-adsorption procedure. As expected, BLDH-P demonstrated the excellent stability and reusability during 12 cycles of column extraction, revealing the application prospect. Overall, this work not only provides an efficient strategy for solving the actual dilemma of LiAl-LDH in long-term Li extraction from SO_4^{2-}-type brines, but also inspires the development and design of state-of-the-art LDHs.

4.5. References

[1] B. Dunn, H. Kamath, J.-M. Tarascon, Electrical energy storage for the grid: A battery of choices, Science 334 (2011) 928-935.
[2] L. Wu, C. Zhang, S. Kim, T.A. Hatton, H. Mo, T.D. Waite, Lithium recovery using electrochemical technologies: Advances and challenges, Water Res. 221 (2022) 118822.
[3] X. Wu, H. Zhang, X. Zhang, Q. Guan, X. Tang, H. Wu, M. Feng, H. Wang, R. Ou, Sustainable lithium extraction enabled by responsive metal-organic frameworks with ion-sieving adsorption effects, Proc. Natl. Acad. Sci. 121 (2024) e2309852121.
[4] T. Zhang, H. Bai, Y. Zhao, B. Ren, T. Wen, L. Chen, S. Song, S. Komarneni, Precise Cation Recognition in Two-Dimensional Nanofluidic Channels of Clay Membranes Imparted from Intrinsic Selectivity of Clays, ACS Nano 16 (2022) 4930-4939.
[5] S. Zhang, X. Wei, X. Cao, M. Peng, M. Wang, L. Jiang, J. Jin, Solar-driven membrane separation for direct lithium extraction from artificial salt-lake brine, Nat. Commun. 15 (2024) 238.
[6] C. Chen, C.A. Lee, M. Tang, K. Biddle, W. Sun, Lithium systematics in global arc magmas and the importance of crustal thickening for lithium enrichment, Nat. Commun. 11 (2020) 5313.
[7] T. Wen, Y. Zhao, B. Kuang, Y. Sun, Y. Li, H. Wang, L. Chen, R. Gao, L. Zhang, T. Zhang, Enhanced Li^+/Mg^{2+} selectivity of two-dimensional montmorillonite membranes by end-face and interfacial layer constraint for nanosheets, Sep. Purif. Technol. 339 (2024) 126707.
[8] L. Zhang, T. Zhang, S. Lv, S. Song, H.J.O. Galván, M. Quintana, Y. Zhao, Adsorbents for lithium extraction from salt lake brine with high magnesium/lithium ratio: From structure-performance relationship to industrial applications, Desalination 579 (2024) 117480.
[9] L. Yang, Y. Tu, H. Li, W. Zhan, H. Hu, Y. Wei, C. Chen, K. Liu, P. Shao, M. Li, G. Yang, X. Luo, Fluorine-Rich Supramolecular Nano-Container Crosslinked Hydrogel for Lithium Extraction with Super-High Capacity and Extreme Selectivity, Angew. Chem., Int. Ed. 62 (2023) e202308702.
[10] X. Xu, Y. Chen, P. Wan, K. Gasem, K. Wang, T. He, H. Adidharma, M. Fan, Extraction of lithium with functionalized lithium ion-sieves, Prog. Mater. Sci. 84 (2016) 276-313.
[11] J. Chen, C. Lian, J. Yu, S. Lin, A directional growth strategy for high layer charge Li/Al-LDHs to reinforce Li^+ extraction in low-grade salt lake brines, AIChE J. 70 (2024) e18280.
[12] X. Li, L. Chen, Y. Chao, L. Zhu, G. Luo, J. Sun, L. Jiang, W. Zhu, Z. Liu, C. Xu, Highly selective separation of lithium with hierarchical porous lithium-ion sieve microsphere derived from MXene, Desalination 537 (2022) 115847.
[13] H. Zhou, J. Li, L. Xu, C. Li, X. Lai, P. Zhang, Y. Huang, Efficient regeneration of the crystal structure and Li^+ adsorption capacity of Li/Al layered double hydroxides, Mater. Lett. 340 (2023) 134159.

[14] J. Chen, J. Du, J. Yu, S. Lin, A one-step regeneration method in-situ for deactivated aluminum-based lithium adsorbent used in high Mg^{2+}/Li^{+} brines, Desalination 554 (2023) 116491.
[15] R. Zhang, Y. Guo, J. Yu, S. Lin, Interlayer confinement imprinting to enhance the feasibility of Li/Al-LDHs in lithium extraction from sulfate-type brines, Appl. Surf. Sci. 639 (2023) 158241.
[16] L. Wu, S.F. Evans, Y. Cheng, A. Navrotsky, B.A. Moyer, S. Harrison, M.P. Paranthaman, Neutron Spectroscopic and Thermochemical Characterization of Lithium–Aluminum-Layered Double Hydroxide Chloride: Implications for Lithium Recovery, J. Phys. Chem. C 123 (2019) 20723-20729.
[17] H. Yi, S. Liu, C. Lai, G. Zeng, M. Li, X. Liu, B. Li, X. Huo, L. Qin, L. Li, M. Zhang, Y. Fu, Z. An, L. Chen, Recent advance of transition-metal-based layered double hydroxide nanosheets: Synthesis, properties, modification, and electrocatalytic applications, Adv. Energy Mater. 11 (2021) 2002863.
[18] H. Yu, G. Naidu, C. Zhang, C. Wang, A. Razmjou, D.S. Han, T. He, H. Shon, Metal-based adsorbents for lithium recovery from aqueous resources, Desalination 539 (2022) 115951.
[19] S. Lv, Y. Zhao, L. Zhang, T. Zhang, G. Dong, D. Li, S. Cheng, S. Ma, S. Song, M. Quintana, Anion regulation strategy of lithium-aluminum layered double hydroxides for strengthening resistance to deactivation in lithium recovery from brines, Chem. Eng. J. 472 (2023) 145026.
[20] L. Baudino, C. Santos, C.F. Pirri, F. La Mantia, A. Lamberti, Recent Advances in the Lithium Recovery from Water Resources: From Passive to Electrochemical Methods, Adv. Sci. 9 (2022) 2201380.
[21] M.P. Paranthaman, L. Li, J. Luo, T. Hoke, H. Ucar, B.A. Moyer, S. Harrison, Recovery of Lithium from Geothermal Brine with Lithium-Aluminum Layered Double Hydroxide Chloride Sorbents, Environ. Sci. Technol. 51 (2017) 13481-13486.
[22] Y. Kong, X. He, H. Wu, Y. Yang, L. Cao, R. Li, B. Shi, G. He, Y. Liu, Q. Peng, C. Fan, Z. Zhang, Z. Jiang, Tight Covalent Organic Framework Membranes for Efficient Anion Transport via Molecular Precursor Engineering, Angew. Chem., Int. Ed. 60 (2021) 17638-17646.
[23] Q. Wang, D. O'Hare, Recent Advances in the Synthesis and Application of Layered Double Hydroxide (LDH) Nanosheets, Chem. Rev. 112 (2012) 4124-4155.
[24] H. Liu, X. Zhao, Y. Zhu, H. Yan, DFT study on MgAl-layered double hydroxides with different interlayer anions: structure, anion exchange, host-guest interaction and basic sites, Phys. Chem. Chem. Phys. 22 (2020) 2521-2529.
[25] K.A. Tarasov, V.P. Isupov, L.E. Chupakhina, D. O'Hare, A time resolved, in-situ X-ray diffraction study of the de-intercalation of anions and lithium cations from $[LiAl_2(OH)_6]nX{\cdot}qH_2O$ ($X = Cl^{-}$, Br^{-}, NO_3^{-}, SO_4^{2-}), J. Mater. Chem. 14 (2004) 1443-1447.
[26] X. Hou, H. Li, P. He, Z. Sun, S. Li, Structural and electronic analysis of Li/Al layered double hydroxides and their adsorption for CO_2, Appl. Surf. Sci. 416 (2017)

411-423.
[27] J. Chen, K. Huang, J. Du, C. Lian, J. Yu, S. Lin, Why is aluminum-based lithium adsorbent ineffective in Li^+ extraction from sulfate-type brines, AIChE J. 69 (2023) e18176.
[28] Y. Guo, J. Yu, H. Su, S. Lin, Desorption enhancement of aluminum-based adsorbent in lithium extraction from sulfate-type salt lakes, Desalination 571 (2024) 117113.
[29] F. Hu, S. Lin, P. Li, J. Yu, Quantitative Effects of Desorption Intensity on Structural Stability and Readsorption Performance of Lithium/Aluminum Layered Double Hydroxides in Cyclic Li^+ Extraction from Brines with Ultrahigh Mg/Li Ratio, Ind. Eng. Chem. Res. 59 (2020) 13539-13548.
[30] J. Zhong, S. Lin, J. Yu, Effects of excessive lithium deintercalation on Li^+ adsorption performance and structural stability of lithium/aluminum layered double hydroxides, J. Colloid Interface Sci. 572 (2020) 107-113.
[31] J. Sun, X. Li, Y. Huang, G. Luo, D. Tao, J. Yu, L. Chen, Y. Chao, W. Zhu, Preparation of high hydrophilic H_2TiO_3 ion sieve for lithium recovery from liquid lithium resources, Chem. Eng. J. 453 (2023) 139485.
[32] Y. Chen, H. Tao, J. Cheng, S. Lin, C. Lian, H. Liu, A molecular model for understanding the membrane separation of Li^+/Mg^{2+}, Ind. Eng. Chem. Res. 62 (2023) 8433-8443.
[33] B. Liu, L. Zhang, K. Ning, W. Yang, Biochar with nanoparticle incorporation and pore engineering enables enhanced heavy metals removal, J. Environ. Chem. Eng. 11 (2023) 111056.
[34] Y. Zhang, L. Wang, R. Zhang, C. He, L. Jia, X. Wang, X. Feng, T. Jiang, B. Xie, X. Ma, J. Cao, Y. Ma, X. Tan, T. Yu, Steering Electron Density of Zr Sites Using Ligand Effect in Bio-Beads for Efficient Defluoridation, Adv. Funct. Mater. 33 (2023) 2213999.
[35] M. Jiang, Y. Hu, B. Mao, Y. Wang, Z. Yang, T. Meng, X. Wang, M. Cao, Strain-regulated Gibbs free energy enables reversible redox chemistry of chalcogenides for sodium ion batteries, Nat. Commun. 13 (2022) 5588.
[36] D. Wang, H. Liu, Z. Shan, D. Xia, R. Na, H. Liu, B. Wang, J. Tian, Nitrogen, sulfur Co-doped porous graphene boosting $Li_4Ti_5O_{12}$ anode performance for high-rate and long-life lithium ion batteries, Energy Storage Mater. 27 (2020) 387-395.
[37] G. Xiao, K. Tong, L. Zhou, J. Xiao, S. Sun, P. Li, J. Yu, Adsorption and desorption behavior of lithium ion in spherical PVC-MnO_2 ion sieve, Ind. Eng. Chem. Res. 51 (2012) 10921-10929.
[38] M. Luo, Z. Cai, C. Wang, Y. Bi, L. Qian, Y. Hao, L. Li, Y. Kuang, Y. Li, X. Lei, Z. Huo, W. Liu, H. Wang, X. Sun, X. Duan, Phosphorus oxoanion-intercalated layered double hydroxides for high-performance oxygen evolution, Nano Res. 10 (2017) 1732-1739.
[39] P. Zhou, Y. Shen, S. Zhao, G. Li, B. Cui, D. Wei, Y. Shen, Synthesis of clinoptilolite-supported BiOCl/TiO_2 heterojunction nanocomposites with highly-enhanced photocatalytic activity for the complete degradation of xanthates under

visible light, Chem. Eng. J. 407 (2021) 126697.
[40] G. Zhang, C. Hai, Y. Zhou, J. Zhang, Y. Liu, J. Zeng, Y. Shen, X. Li, Y. Sun, Z. Wu, W. Tang, Synthesis and performance estimation of a granulated PVC/PAN-lithium ion-sieve for Li^+ recovery from brine, Sep. Purif. Technol. 305 (2023) 122431.
[41] L. Zhang, T. Zhang, Y. Cai, Y. Zhao, S. Song, M. Quintana, Engineering sulfuric acid-pretreated biochar supporting MnO_2 for efficient toxic organic pollutants removal from aqueous solution in a wide pH range, J. Clean. Prod. 416 (2023) 137968.
[42] P. Zhang, Z. Wang, S. Wang, J. Wang, J. Liu, T. Wang, Y. Chen, P. Cheng, Z. Zhang, Fabricating industry-compatible olefin-linked COF resins for oxoanion pollutant scavenging, Angew. Chem., Int. Ed. 61 (2022) e202213247.
[43] S. Lin, Y. Pan, J. Du, Y. Yang, H. Su, J. Yu, Double-edged role of interlayer water on Li^+ extraction from ultrahigh Mg^{2+}/Li^+ ratio brines using Li/Al-LDHs, J. Colloid Interface Sci. 627 (2022) 872-879.
[44] P. Zhang, M. Xiang, H. Liu, C. Yang, S. Deng, Novel two-dimensional magnetic titanium carbide for methylene blue removal over a wide pH range: Insight into removal performance and mechanism, ACS Appl. Mater. Interfaces 11 (2019) 24027-24036.
[45] T. Zhang, M. Li, L. Chen, H. Bai, W. Wang, Y. Zhao, Novel montmorillonite nanosheets-based hydrogel beads with high adsorption performance and structural strength for removal of dyes and heavy metals, Chem. Phys. Lett. 813 (2023) 140322.
[46] L. Zhang, T. Zhang, Y. Zhao, G. Dong, S. Lv, S. Ma, S. Song, M. Quintana, Doping engineering of lithium-aluminum layered double hydroxides for high-efficiency lithium extraction from salt lake brines, Nano Res. 17 (2024) 1650-1658.
[47] L. Zhang, Z. Ke, W. Wang, H. Liu, Y. Mao, M. Xiang, P. Zhang, Enhanced removal of multiple metal ions on S-doped graphene-like carbon-supported layered double oxide: Mechanism and DFT study, Sep. Purif. Technol. 288 (2022) 120636.
[48] Z. Lu, Y. Wu, L. Ding, Y. Wei, H. Wang, A lamellar MXene ($Ti_3C_2T_x$)/PSS composite membrane for fast and selective lithium-ion separation, Angew. Chem., Int. Ed. 60 (2021) 22265-22269.
[49] L. Lv, J. He, M. Wei, D.G. Evans, X. Duan, Factors influencing the removal of fluoride from aqueous solution by calcined Mg-Al-CO_3 layered double hydroxides, J. Hazard. Mater. 133 (2006) 119-128.

Chapter 5. Constructing multiple functional domains of lithium aluminum layered double hydroxides for sustainable lithium extraction in sulfate-type brines

5.1. Introduction

Lithium (Li) is a critical element for the clean energy transition, for which the global demand is growing exponentially [1-3]. The sustainable supply of Li is, therefore, particularly urgent [4,5]. Currently, commercial Li is exclusively from high-grade Li ores and continental brines, with the latter being more abundant than the former [6,7]. The conventional evaporitic process used to concentrate and extract Li from continental brines is time-consuming, land-intensive, and negatively impacts local ecosystems [6,8-11]. What's more, the entrainment loss of Li readily occurs with the precipitation of co-dissolved elements (such as Na and K) during the evaporation process, causing Li yield of less than 40% of the overall, which entails a great waste of resources [12,13]. Moreover, the dramatic competing effects originated from the numerous impurity ions (especially Mg^{2+}) usually requires to be surmounted to extract Li even from concentrated brines [14,15]. Thus, to secure the Li supply, it is required to explore more efficient avenues and expand accessible brine resources for lithium extraction.

Adsorption has widely applied to perform direct lithium extraction (DLE) from brines due to simple process and low energy consumption [16,17]. In particular, lithium-aluminum layered double hydroxides (LiAl-LDHs) are the most successful adsorbents for industrialized Li extraction owing to their unique octahedral cavity structure (~1.4 Å) matching the Li^+ diameter and desorption without dissolution loss [18,19]. LiAl-LDHs are a class of two-dimensional laminated materials whose chemical formula is $LiX{\cdot}2Al(OH)_3{\cdot}nH_2O$ [20]. During the Li extraction procedure, Li^+ selectively intercalates into octahedral vacancies of $Al(OH)_3$ to form positively charged host layers, accompanied by the charge-balancing anions (*i.e.,* X) and water molecules entering the interlayer [21,22]. In the case of Li recovery, the Li^+ in the octahedral units and interlayer anions are readily deintercalated using water [18,23]. To date, LiAl-LDHs are only used in Cl^--type brines, which are limited in number. The industrialized Li extraction of LiAl-LDHs in SO_4^{2-}-type brines that are the second most significant

type of brines in the world, remains to be achieved, which suffers from the 'SO_4^{2-} poisoning' effect. Specifically, SO_4^{2-} readily intercalates into the interlayer of LiAl-LDHs, while it is challenging to be desorbed to release Li^+ adsorption sites due to the strong interlayer binding interaction, inducing the gradually reduced Li^+ adsorption capacity of LiAl-LDHs [24,25]. Such poisoning effect seriously hampers application diversification of LiAl-LDHs. To this end, the innovation and design of state-of-art LiAl-LDHs for sustainable Li extraction from SO_4^{2-}-type brines are imperative.

The strategy of steering interlayer interaction by PO_4^{3-} has been proposed to realize lithium extraction of LiAl-LDHs from SO_4^{2-}-type brines, while PO_4^{3-} may be gradually replaced by other anions during long-term cycling. What's more, it is also difficult to avoid progressive poisoning due to gradual diffusion of SO_4^{2-} into the LiAl-LDHs by regulating only the interlayer interactions. Herein, a novel organic modification strategy of constructing multiple functional domains of LiAl-LDHs using polyacrylamide (PAM) was proposed for sustainable lithium extraction in SO_4^{2-}-type brines. Leveraging the enriched hydroxyl groups on the interface and ion exchange feature of LiAl-LDHs, part of the PAM was connected to the surface by hydrogen bonds, and the rest was intercalated into the LiAl-LDH interlayer to form multiple SO_4^{2-} repelling domains. Benefiting from the rational design, the LiAl-LDHs modified with PAM (LiAl-LDH/PAM) offered excellent Li^+ selectivity, extraordinary anti-sulfate poisoning property, and the adsorption capacity of up to 13.25 mg g^{-1} in the real SO_4^{2-}-type brine. The strategy significantly enables the feasibility of long-term Li extraction by LiAl-LDHs from SO_4^{2-}-type brines, significantly expanding the availability of Li resources.

5.2. Experimental section

5.2.1. Reagents and materials

Lithium chloride (LiCl), aluminum chloride hexahydrate ($AlCl_3 \cdot 6H_2O$), sodium hydroxide (NaOH), and polyacrylamide (PAM) were purchased from Shanghai Aladdin Biochemical Technology Co., Ltd. All reagents are analytical grade.

The brine used in the experiments is the real Lop Nor Salt-Lake brine, the largest SO_4^{2-}-type brine in the world. The detailed compositions were summarized in Table 5.1.

Table 5.1 Properties of Lop Nor brine before and after static extraction.

Li^+ (g/L)	Mg^{2+} (g/L)	K^+ (g/L)	Na^+ (g/L)	Cl^- (g/L)	SO_4^{2-} (g/L)
0.2222	97.015	2.549	2.899	222.400	37.600

5.2.2. Preparation of LiAl-LDH-PAM

A two-step co-precipitation-activation modification method to ensure the negligible influence on the structure of LiAl-LDHs from the PAM introduction. First, LiAl-LDH precursors were prepared using the common co-precipitation method. Briefly, a mixed solution containing LiCl and $AlCl_3 \cdot 6H_2O$ was dropped into a NaOH solution (8 mol L^{-1}) until the pH of the mixture was below 5. The resultant precipitates were dried and collected to obtain LiAl-LDH precursors. For inserting PAM without structural damage, a one-step activation-modification method was proposed. Specifically, the PAM solution with 0.1% concentration were prepared, and LiAl-LDH precursors were added to the above solutions (liquid-solid ratio of 100 mL g^{-1}). After shaking in an air bath at 40 °C for 2 h, centrifugation and freeze-drying were performed to complete the desorption-activation and organic modification processes simultaneously. The as-obtained samples were abbreviated as LiAl-LDH/PAM.

For comparison, the pristine LiAl-LDH were also prepared using the same method but with deionized water for desorption-activation.

5.2.3. Characterizations

Transmission electron microscope (TEM, JEM-JEOL-2100) equipped with energy dispersive spectroscopy (EDS) system was used to characterize the morphological structures of the samples. X-ray diffraction patterns were recorded using a Bruker diffractometer (XRD, Empyrean) with Cu Kα irradiation (40 kV, 100 mA). The surface potentials of the samples were tested using a zeta potential analyzer (Malvern Zetasizer Nano ZS90 zeta). Raman spectra were performed using a LabRAM Odyssey Raman microscope in 532 nm laser excitation. X-ray photoelectron spectra (XPS) were determined by a Thermo Scientific K-Alpha spectrometer.

5.2.4. Lithium-ion extraction

All batch adsorption experiments carried out in a water temperature-controlled shaker at room temperature. To determine the Li^+ uptake, LiAl-LDHs were added into various real brines for 3 h, in which the liquid-solid ratio was 50 mL g^{-1}. The adsorption capacity q (mg g^{-1}) was calculated by the Equation 5.1:

$$q = (C_0\text{-}C_t)V/m \tag{5.1}$$

where C_0 (mg L^{-1}) and C_t (mg L^{-1}) are the initial and residual ion concentrations, respectively; V (L) is the solution volume; m (g) refers the mass of LiAl-LDHs.

The desorption procedure involved two processes, that is, the rapid washing using a little ice deionized water for removing the residual brine on the sample surface and Li^+ deintercalation using deionized water with a liquid-solid ratio of 100 mL g^{-1} at 40 ^oC for 2h. The desorption capacity was determined by the Equation 5.2:

$$q = {}^{C_{dt}V}\!/_{m} \tag{5.2}$$

where q (mg g^{-1}) and C_{dt} (mg L^{-1}) represent the desorption capacity and concentration.

The distribution coefficient K_d (mL g^{-1}) and separation coefficient α_M^{Li} were determined to assess the adsorption selectivity of samples to different cations in brines according to the Equation 5.3-5.4:

$$K_d = {}^{V(C_0\text{-}C_e)}\!/_{(mC_e)} \tag{5.3}$$

$$\alpha_M^{Li} = {}^{K_{d,\,Li}}\!/_{K_{d,\,M}} \tag{5.4}$$

where M represents cations in brines, involving K^+, Na^+, and Mg^{2+}.

The adsorption-desorption cycling experiments were conducted in Lop Nur Salt-Lake brine, where the liquid-solid ratio remained consistent with those in batch adsorption and desorption experiments.

5.2.5. Theoretical calculations

All density functional theory (DFT) calculations were performed through the Materials Studio 8.0 software. The exchange-correlation interactions were described by the generalized gradient approximation of Perdew-Burke-Ernzerhof (GGA-PBE) for structural optimization to minimize the energy. The cut-off energy was set to 570.0 eV, and the convergence criteria for displacement, energy, and force were 0.001 Å, 1×10^{-5} eV/atom, and 0.03 eV/Å, respectively. Considering to the actual system, the transport pathway of SO_4^{2-} was divided into migration over interface and diffusion over interlayer of LiAl-LDHs. The relative energy barrier of SO_4^{2-} transport was calculated from the difference between the energy at the optimal adsorption site and the energy at specified position. Similarly, binding energies (E_b) between ions and PAM were calculated by:

$$E_b=E_{A/B}\text{-}E_A\text{-}E_B \tag{5.5}$$

where $E_{A/B}$ is the total energy of A and B bonded system; E_A and E_B indicate the energies of individual A and B, respectively.

5.2.6. Numerical simulation

Numerical simulation was performed by using finite element package COMSOL

(version 5.6) Multiphysics. A simplified two-dimensional model was constructed to carried out the calculations (Figure 5.1), where the top represents the bulk phase of Li_2SO_4 solution, and the bottom rectangle with a length of 5 μm and a width of 1 μm represents the layered LiAl-LDH adsorbent.

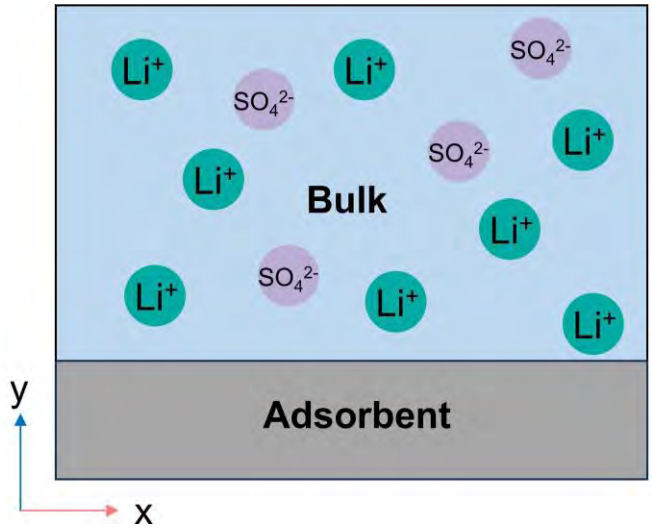

Figure 5.1 Two-dimension model of LiAl-LDHs and bulk phase of Li_2SO_4.

"Transport of Diluted Species (tds)" and "Static Electricity (es)" modules were used to simulate the ions diffusion on the LiAl-LDH interface, and the mesh is controlled by the physical field to ensure accuracy. The Poisson-Nernst-Planck (PNP) model is consisted of the Poisson equation and a set of convective diffusion equations, the former determining the electrostatic potential caused by the moving ions and fixed charges, while the latter represents the ion diffusion induced by the solution concentration gradient and the electric field, as shown in Equations 5.6-5.8:

$$\nabla^2\varphi = -\frac{F}{\varepsilon}\sum_i z_i c_i \tag{5.6}$$

$$J_i = D_i(\nabla c_i + \frac{z_i F c_i}{RT}\nabla\varphi) \tag{5.7}$$

$$\nabla \cdot J_i = 0 \tag{5.8}$$

where, φ (V) is the potential of the adsorbent; ε (F/m) refers dielectric constant; c_i (mol m^{-3}), z_i, and D_i (m^2 s^{-1}) are the ion concentration, valence number, and diffusion coefficient of ion *i*, respectively; J_i (mol m^{-2} s^{-1}) is the ionic flux; F (C mol^{-1}) represents Faraday constant; R (J·mol^{-1} K^{-1}) and T (K) are the gas constant and absolute temperature, respectively. The φ is obtained as:

$$\nabla \cdot (-\varepsilon\nabla\varphi) = \sigma \tag{5.9}$$

where σ (C m^{-2}) is the surface charge density, which be calculated based on the equation:

$$\sigma = \frac{\varepsilon\varepsilon_0\xi}{\lambda_D} \quad (5.10)$$

$$\lambda_D = \sqrt{\frac{(\varepsilon\varepsilon_0 RT)}{(2n_{bulk}z^2F^2)}} \quad (5.11)$$

where ε_0 (F/m) is vacuum dielectric constant and ξ (mV) is the zeta potential; λ_D represents the Debye length; n_{bulk} (mol m^{-3}) indicates the concentration of bulk solution. Based on the determined results of zeta potential, the calculated values of pristine LiAl-LDH and LiAl-LDH/PAM are 6.50×10^{-3} C m^{-2} and -4.17×10^{-3} C m^{-2}, respectively.

5.3. Results and discussion

5.3.1. Synthesis and characterization

First, LiAl-LDH/PAM was prepare to evaluate the effects of the PAM on continuous Li recovery from sulfate-type brines. To speak of, the standard one-step co-precipitation method was not employed, based on the understanding of the properties of the structure of LiAl-LDHs, to shield that PAM impact the polarity and ionic concentration of the precursor slurry, which in turn affects the crystalline nucleation of Li/Al salts [18]. In contrast, a two-step co-precipitation-activation modification method was proposed to ensure the negligible influence on the structure of LiAl-LDHs from the PAM introduction, allowing a solid assessment on the feasibility of the strategy of constructing multiple functional domains. Specifically, the typical LiAl-LDH precursor was first prepared by co-precipitation of Li/Al salts, and then the precursor was mixed with the solution containing modifiers for simultaneous activation and modification to obtain LiAl-LDH/PAM (Figure 2a).

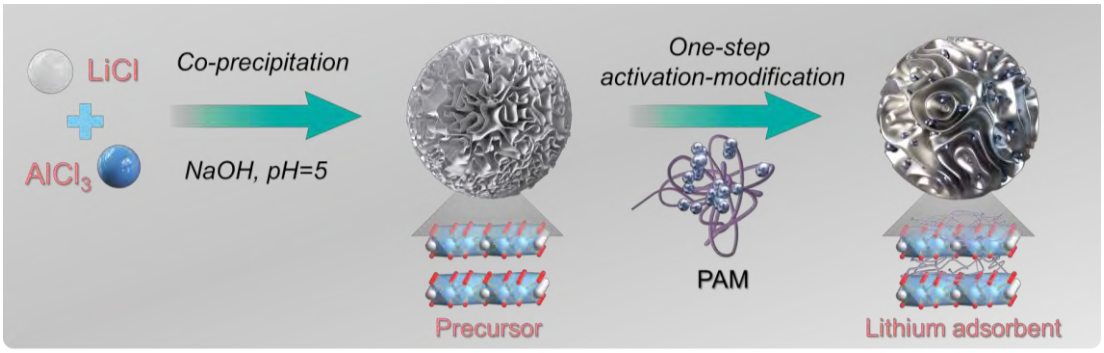

Figure 5.2 Schematic illustration of the LiAl-LDH modified with PAM.

Transmission electron microscopy (TEM) images presented the hexagonal morphologies of LiAl-LDH nanosheets with diameters of ~80 nm (Figure 5.3a,d). The high-solution TEM (HRTEM) image and corresponding selected area electron

diffraction (SAED) pattern indicated that the single crystal nature of the pristine LiAl-LDH. The lattice fringes measured 0.74 nm, consistent with the (003) plane of the LiAl-LDH (JCPDS No. 31-0700) (Figure 5.3b). The SAED pattern exhibited hexagonally arranged diffraction spots, which revealed a hydrotalcite-like crystal structure (Figure 5.3c)[26]. In contrast to the pristine LiAl-LDH, the modified LiAl-LDH/PAM exhibited an interaggregate and densely curled structure owing to the introducing flexible polymers (Figure 5.3d). The distinguishable amorphous regions in the HRTEM image of LiAl-LDH/PAM demonstrated the tight bonding of the PAM to the LiAl-LDH (Figure 5.3e). SAED patterns presented diffuse halo electron diffraction rings indexed to the (009), (006), and (118) planes of the LiAl-LDH, revealing that partial polymer bonded to the adsorbent surfaces, reducing the phase crystallinity (Figure 5.3f)[27]. Notably, the layered structure of LiAl-LDH is retained after PAM modification but increase from original 0.734 nm to 0.776 nm according to the atom distance profiles in Figure 5.3g-h. Moreover, the elemental mapping images reveal the homogeneity of the LiAl-LDH/PAM structures (Figure 5.3i).

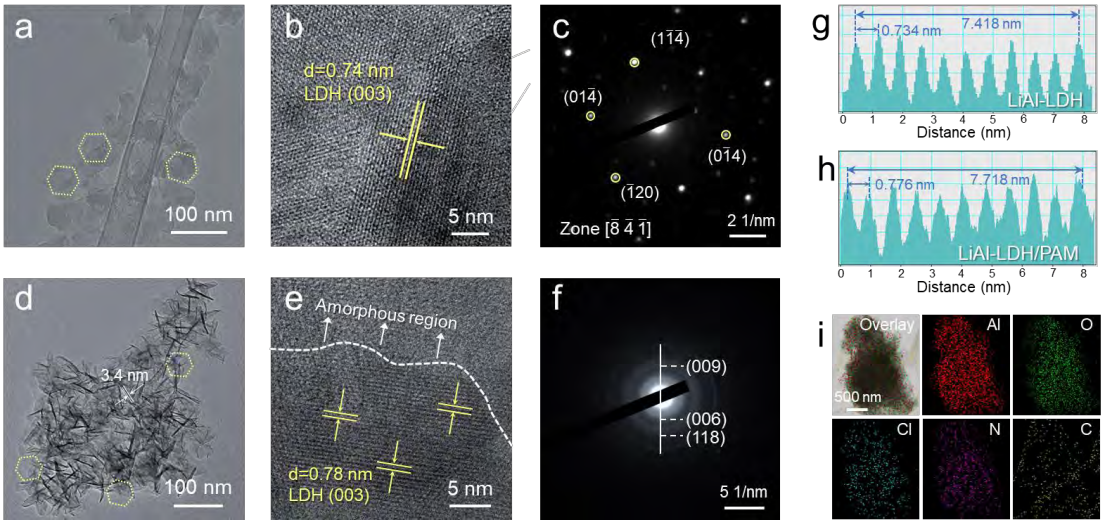

Figure 5.3 (a) TEM image, (b) HRTEM image, (c) SAED pattern of the pristine LiAl-LDH (d) TEM image, (e) HRTEM image, (f) SAED pattern of the LiAl-LDH/PAM. tom distance profiles from lattice fringes of (003) plane of (g) the pristine LiAl-LDH and (h) the LiAl-LDH/PAM. (i) Mapping images of the LiAl-LDH/PAM.

X-ray diffraction (XRD) patterns further demonstrated the successful preparation of LiAl-LDH/PAM with decreased crystallinity and expanded interlayer spacing from 7.45 Å to 7.71 Å (Figure 5.4), in well agreement with the TEM analysis, where the diffraction peak of (003) plane (JCPDS#31-0700) became border and lower accompanying with a shift toward low 2θ after modification.

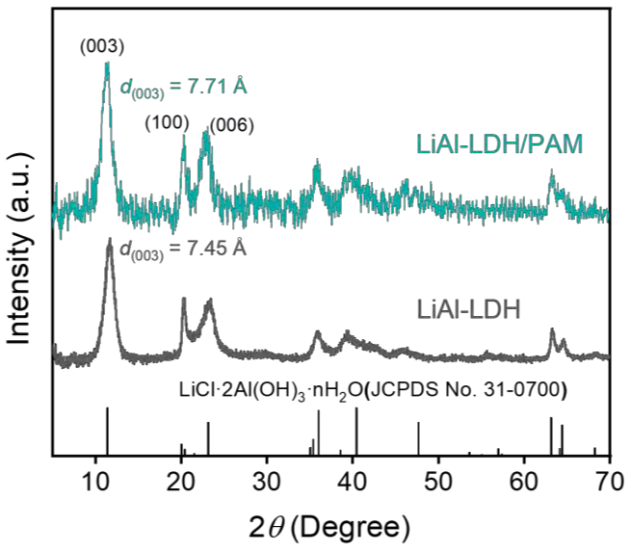

Figure 5.4 XRD patterns of the pristine LiAl-LDH and LiAl-LDH/PAM.

Such modification tuned the zeta potential of LiAl-LDH/PAM from positive to negative due to the polar functional groups with rich lone pair electrons in the PAM, indicating the presence of PAM on the surface of LiAl-LDH/PAM, which can yield a strong attraction for Li^+ while repulsion for SO_4^{2-} (Figure 5.5).

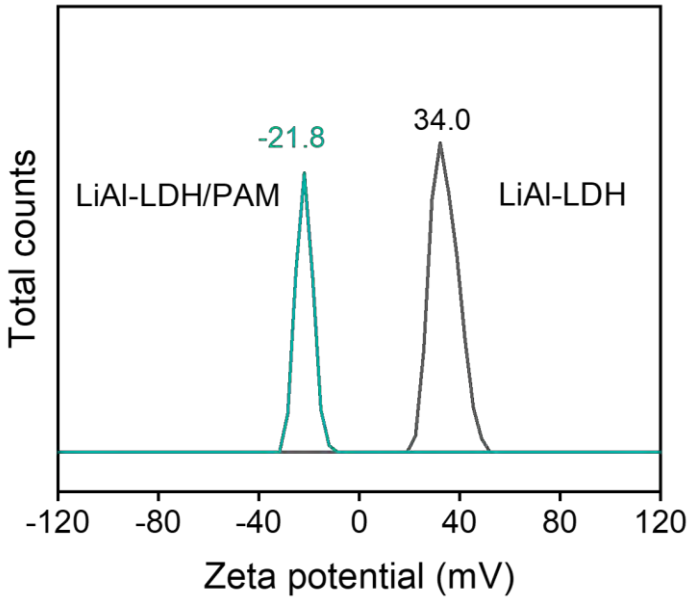

Figure 5.5 Zeta potentials of the pristine LiAl-LDH and LiAl-LDH/PAM.

Moreover, X-ray photoelectron spectroscopy (XPS) of LiAl-LDH/PAM after modification appeared new N 1s peak (Figure 5.6a). XPS spectrum for the characteristic elemental N 1s core level indicated the existence of PAM with groups of -$CONH_2$ on the surface of the LiAl-LDH/PAM (Figure 5.6b).

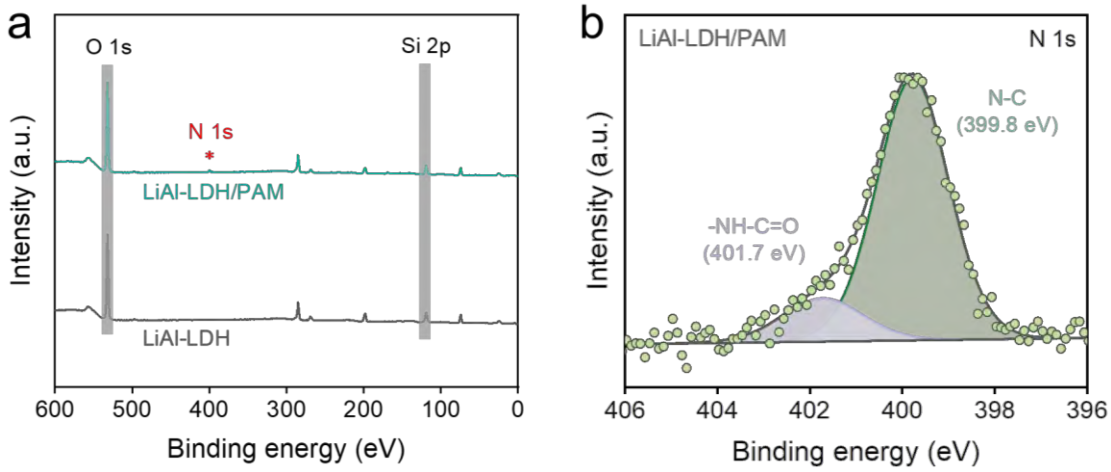

Figure 5.6 (a) XPS survey spectra of the pristine LiAl-LDH and LiAl-LDH/PAM. (b) XPS spectrum for the N 1s core level of the LiAl-LDH/PAM.

Furthermore, as for the XPS spectrum of O 1s core level of the LiAl-LDH/PAM, the peak of Al-OH occurred a significant blue shift (). This implied that the electrons around O atoms on Al-OH transferred to the H atoms on -$CONH_2$ groups of the PAM, and hydrogen bonds were formed between the PAM and the LiAl-LDH [28].

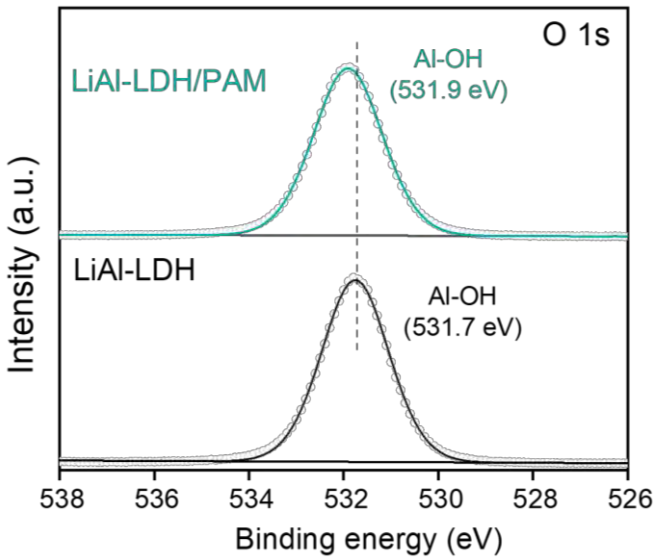

Figure 5.7 XPS spectra of O 1s core level of the pristine LiAl-LDH and LiAl-LDH/PAM.

Briefly, LiAl-LDH/PAM were successfully prepared by two-step co-precipitation-activation modification method, in which part of the PAM was connected to the surface by hydrogen bonds to create, and the rest was intercalated into the LiAl-LDH interlayer via ion exchange to form multiple SO_4^{2-} repelling domains, which facilitate sustainable lithium extraction from SO_4^{2-}-type brines (Figure 3g).

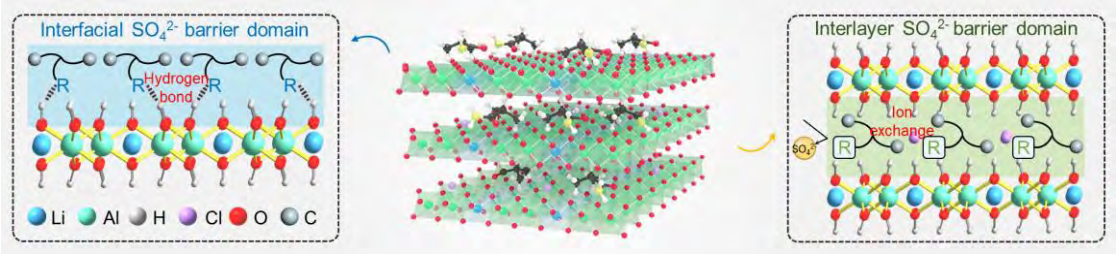

Figure 5.8 Schematic of multiple functional domains of LiAl-LDH/PAM and interactions between LiAl-LDH and polymer building blocks.

5.3.2. Lithium extraction performance

The as-obtained LiAl-LDH/PAM were used in real Lop Nor Salt-Lake brine, the largest SO_4^{2-}-type brine in the world, to evaluate the practical feasibility of the proposed strategy. The kinetics experiments displayed that the pristine LiAl-LDH reached equilibrium in 60 min, while LiAl-LDH/PAM could extract lithium faster within 30 min (Figure 5.9). Moreover, the LiAl-LDH/PAM showed a significantly increased Li^+ adsorption capacity (6.71 mg g^{-1}) compared to the pristine LiAl-LDH (5.57 mg g^{-1}). The improved extraction performance might be attributed to the higher lithium affinity of LiAl-LDH/PAM due to the positive surface potential (Figure 5.5). Further, the adsorption kinetic modeling analysis revealed the chemisorption-dominated Li extraction processes of the pristine LiAl-LDH and LiAl-LDH/PAM (Figure 5.10 and Table 5.2) [20].

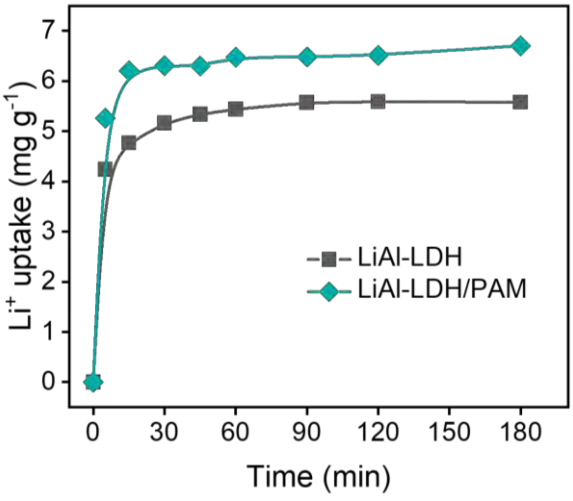

Figure 5.9 Li^+ adsorption kinetics of the pristine LiAl-LDH and LiAl-LDH/PAM in Lop Nor brine.

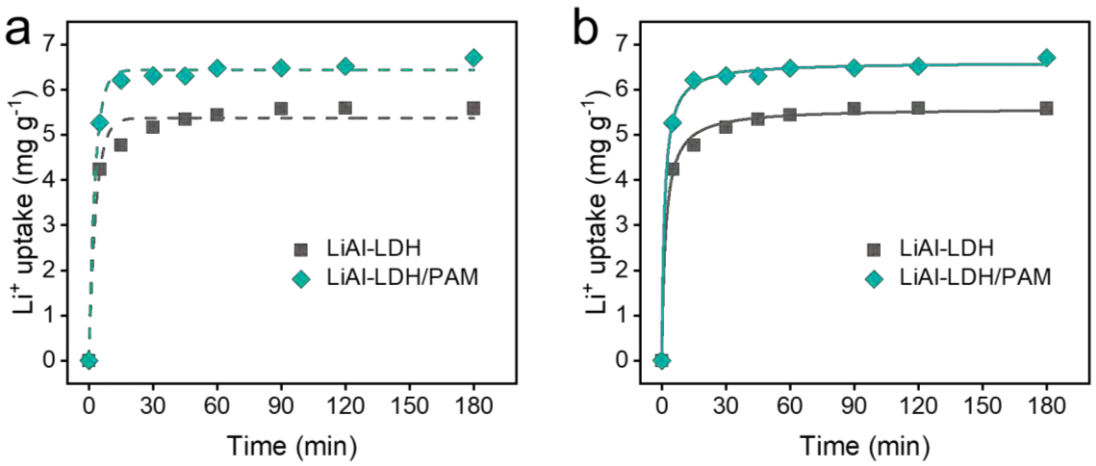

Figure 5.10 (a) Pseudo-first-order and (b) pseudo-second-order kinetic models of Li^+ adsorption on the pristine LiAl-LDH and LiAl-LDH/PAM in Lop Nor brine.

Table 5.2 Adsorption kinetic model parameters of the pristine LiAl-LDH and LiAl-LDH/PAM.

Samples	Pseudo-first-order			Pseudo-second-order		
	q_e (mg/g)	k_1 (min^{-1})	R^2	q_e (mg/g)	k_2 (g/(mg·min))	R^2
LiAl-LDH	5.37	0.2974	0.9787	5.58	0.0792	0.9957
LiAl-LDH/PAM	6.43	0.3368	0.9951	6.61	0.1201	0.9984

Furthermore, the isotherm experiments provided solid support for the strategy, as the Li^+ adsorption capacity of the LiAl-LDH/PAM exceeded that of pristine LiAl-LDH at the full range of Li^+ concentration tested (Figure 5.11a). The analysis of isotherm models presented that Li^+ uptake was a homogeneous adsorption process, suggesting the uniform distribution of PAM on the LiAl-LDH/PAM (Figure 5.11b-c) [29].

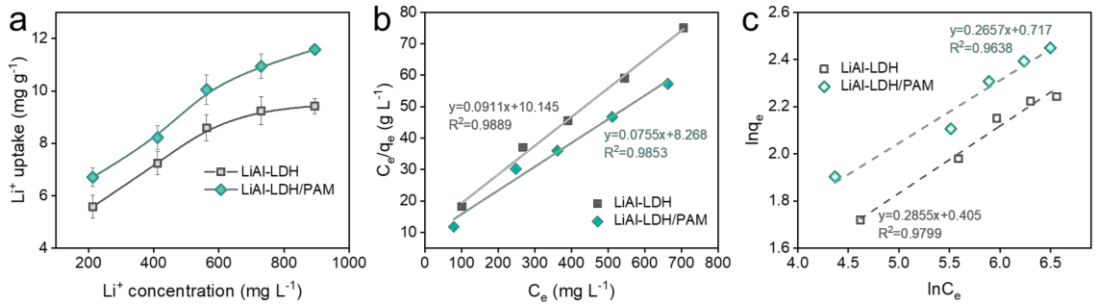

Figure 5.11 (a) The adsorption capacity of Li^+ on the pristine LiAl-LDH and LiAl-LDH/PAM in Lop Nor brine with different Li^+ concentration. (b) Langmuir and (c) Freundlich models of Li^+ on the pristine LiAl-LDH and LiAl-LDH/PAM.

As well, the selectivity was investigated in detail. As shown in Figure 5.12, the dispersion coefficient (K_d) values of the pristine LiAl-LDH and LiAl-LDH/PAM for Li^+ were larger than 50, while those for the other main coexisting metal ions below 1, indicating the well selectivity, which originated from the memory effect and size screening effect [21]. Further, the separation factors (α) of Li^+/Mg^{2+}, Li^+/Na^+ and Li^+/K^+ were determined. The LiAl-LDH/PAM (104.65) presented significant higher $\alpha_{Li/Mg}$ than pristine LiAl-LDH (72.99). The selectivity of LiAl-LDH/PAM for Li^+/Na^+ and Li^+/K^+, on the other hand, was higher than that for Li^+/Mg^{2+}, because of the weaker binding of functional groups to Na^+ and K^+ than Mg^{2+}, as well as the apparently larger ionic sizes of Na^+ (2.76 Å) and K^+ (2.04 Å) [30].

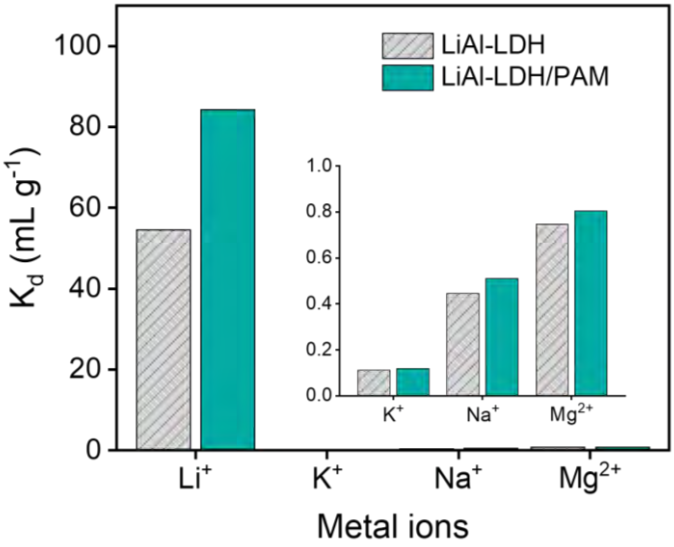

Figure 5.12 Dispersion coefficient (K_d) values of the pristine LiAl-LDH and LiAl-LDH/PAM in Lop Nor brine.

Overall, benefited from the proposed strategy of constructing multiple functional domains, the LiAl-LDH/PAM modified with the PAM presented excellent lithium extraction performance from SO_4^{2-}-type brines, including the adsorption rate, adsorption capacity, and Li^+ selectivity, unveiling the sophistication of the strategy.

5.3.3. Anti-sulfate ion poisoning performance

To evaluate the effect of the proposed strategy on the anti-sulfate ion poisoning performance that is considered as the 'Achilles heel' of the LiAl-LDHs, the SO_4^{2-} exchange capacity during the Li extraction procedure in Lop Nor brine was carried out. As shown in Figure 5.13, the exchange capacity of the pristine LiAl-LDH was 0.33 mmol g^{-1}, indicating that its susceptibility to sulfate ion poisoning. Encouragingly, the

exchange capacities of LiAl-LDH/PAM greatly decreased, which revealed the advancement of the proposed strategy against sulfate ion poisoning.

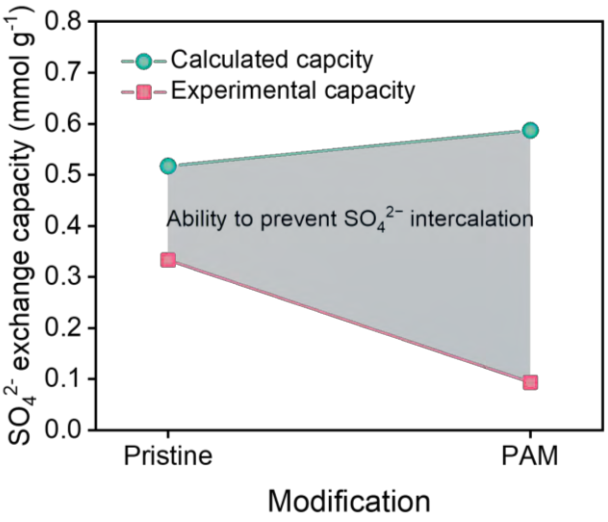

Figure 5.13 The SO_4^{2-} exchange capacities of the pristine LiAl-LDH and LiAl-LDH/PAM.

Further, the re-adsorption experiments were conducted, and the Li^+ re-adsorption capacities slightly reduced or constant (Figure 5.14). It is declared that the single re-adsorption capacity of LiAl-LDHs in certain SO_4^{2-}-type brines with sufficient ionic strength might be high, during long-term desorption-adsorption cycles, however, the replacement of interlayer Cl^- by SO_4^{2-} accumulates and gradually suppresses the desorption and re-adsorption of Li^+, leading to the unsatisfactory long-term Li extraction of from SO_4^{2-}-type brines by LiAl-LDHs. To this end, 10 desorption-adsorption cycle experiments were performed.

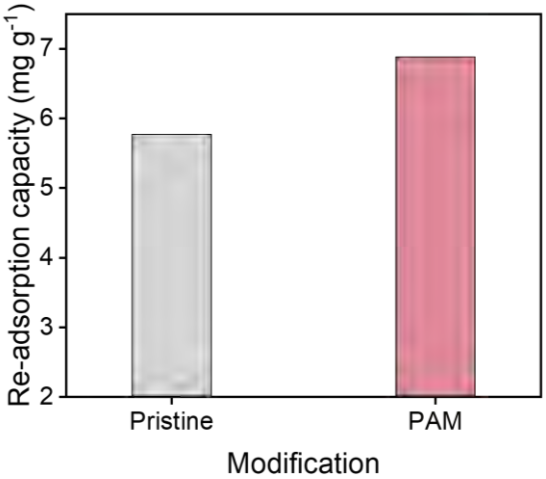

Figure 5.14 Li^+ re-adsorption capacity of the pristine LiAl-LDH and LiAl-LDH/PAM in Lop Nor brine.

To trail the accumulation of SO_4^{2-} in the interlayer, 10 desorption-adsorption cycle experiments were carried out (Figure 5.15). The reduction in uptake was remarkably different. As for the pristine LiAl-LDH, the adsorption and desorption capacity reduced by over 40%, demonstrating severe poisoning. In contrast, these for LiAl-LDH/PAM were reduced from ~6.7 mg/g to ~6.3 mg/g, proving the enhanced anti-sulfate ion poisoning performance.

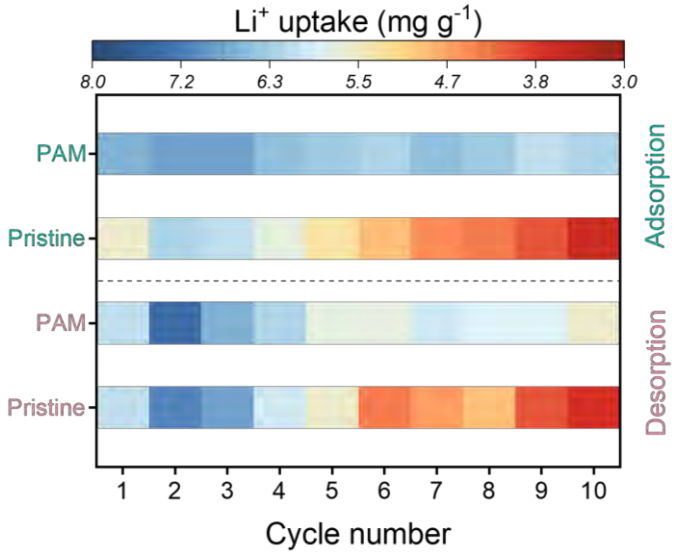

Figure 5.15 Li^+ uptakes of the pristine LiAl-LDH and LiAl-LDH/PAM during the adsorption-desorption cycling experiments.

After ten adsorption-desorption cycles, the XRD measurements of all the pristine LiAl-LDH and LiAl-LDH/PAM were carried out. Compared to the XRD peaks before extraction, peaks of pristine LiAl-LDH were broadened and weakened after 10 cycles, suggesting decreased crystallinity and poor stability in SO_4^{2-}-type brines (Figure 5.16).

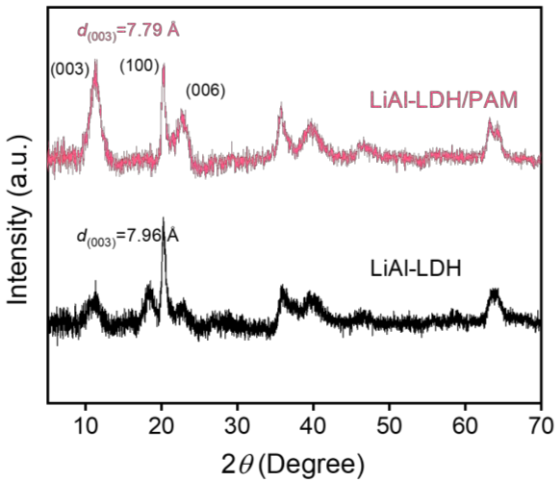

Figure 5.16 XRD patterns of pristine LiAl-LDH and LiAl-LDH/PAM after ten adsorption-desorption cycles.

Moreover, statistical analysis of the (003) plane unveiled the level of SO_4^{2-} intercalation into LiAl-LDH adsorbents (Figure 5.17). The interlayer spacing of pristine LiAl-LDH increased from 7.45 Å to 7.96 Å with an increase of 0.51 Å during cycling, indicating the severe intercalation of SO_4^{2-}. While the (003) plane spacing of LiAl-LDH/PAM were below 7.8 Å with an increase of 0.08 Å, validating the significant improvement in the anti-sulfate ion poisoning property of LiAl-LDH/PAM.

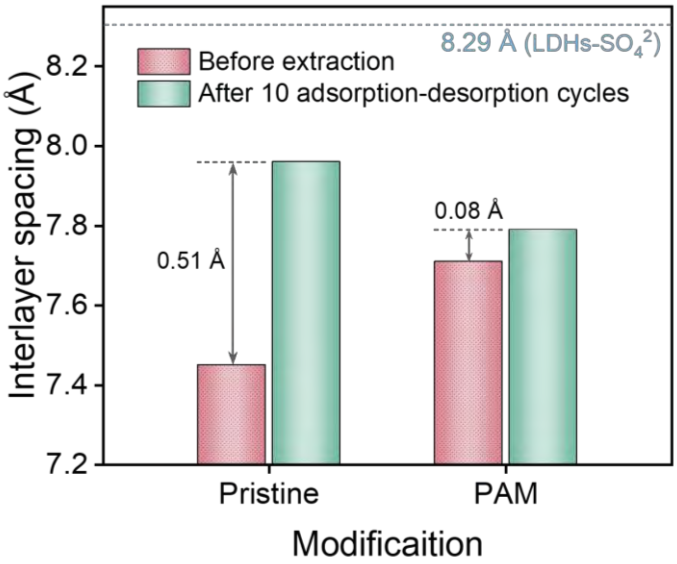

Figure 5.17 The interlayer spacing of LiAl-LDHs before and after 10 adsorption-desorption cycling experiments.

Furthermore, Raman spectroscopy was also applied to track the structural evolution of pristine LiAl-LDH and LiAl-LDH/PAM (Figure 5.18). As for pristine sample, two peaks corresponding to the typical LiAl-LDHs vibration were observed at around 348 and 392 cm^{-1} during the whole desorption-adsorption cycle process (Figure 5.18a) [31]. With the continuous cycle, the Al-O vibration peak corresponding to $Al(OH)_3$ generated at ~320 cm^{-1}, suggesting that certain LiAl-LDH sites had been poisoned, resulting in their inability to trap Li^+ to form a layered double hydroxide structure [23]. At the same time, a new mode corresponding to SO_4^{2-} (near 252 cm^{-1}) was found in the structure [32], demonstrating that the pristine LiAl-LDH was poisoned with sulfate ions at the early stage of the continuous Li extraction cycle. On the contrary, LiAl-LDH/PAM gradually presented low-intensity sulfate ion signals only at the final stage of the cycling process (Figure 5.18b), which reconfirmed its excellent resistance to sulfate poisoning.

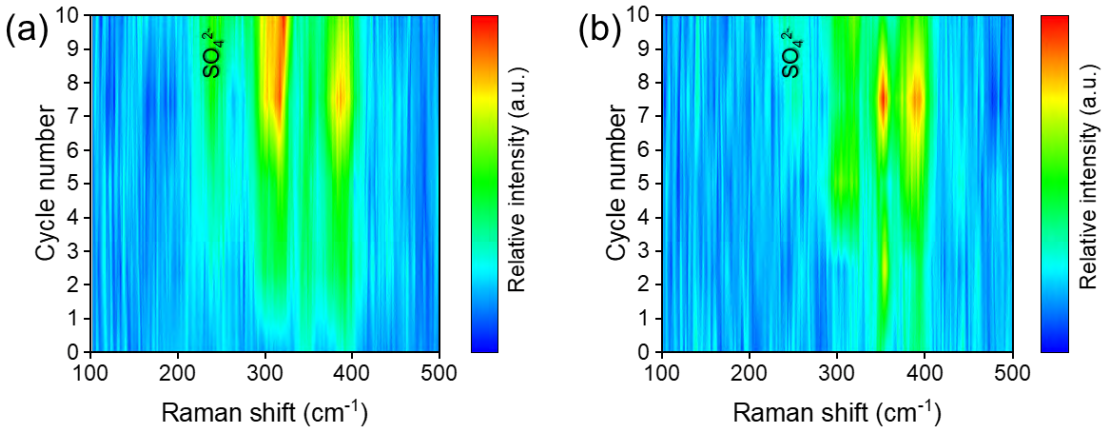

Figure 5.18 Contour plots of Raman spectra of (a) pristine LiAl-LDH and (b) LiAl-LDH/PAM during 10 adsorption-desorption cycling experiments.

Encouraged by the above results, the anti-sulfate poisoning properties of the prepared LiAl-LDH/PAM was compared with the reported LiAl-LDH-based adsorbents. The excellent stability and regeneration ability of the adsorbents are always desired, and thus the promising LiAl-LDHs are required to have larger bubble diameters and be in the upper right region of Figure 5.19. A brief glance at this region revealed that LiAl-LDH/PAM exhibits the best anti-sulfate poisoning performance, namely, the long-term stable Li extraction at higher sulfate ion concentrations with only a slight decrease in uptake. Apparently, the proposed strategy enabled the LiAl-LDH to be highly feasible for continuous Li extraction from SO_4^{2-}-type brines.

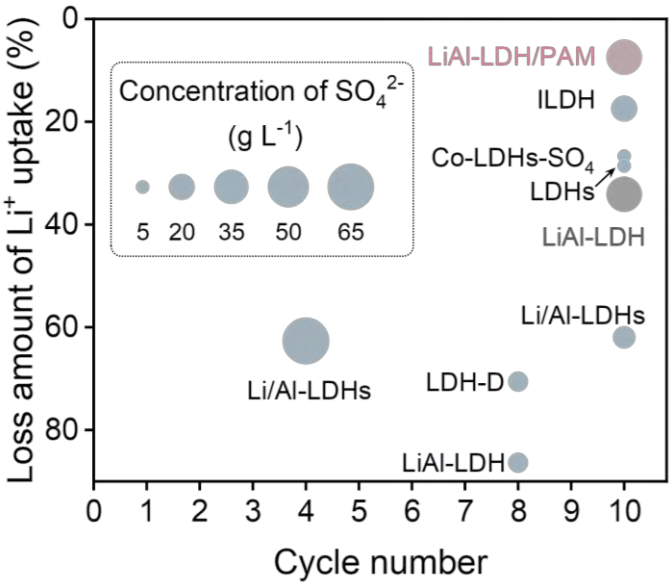

Figure 5.19 Comparison of the anti-sulfate ion poisoning performance between proposed LiAl-LDHs and reported LiAl-LDH-based adsorbents in SO_4^{2-}-type brines.

5.3.4. Mechanisms of anti-sulfate ion poisoning

To demonstrate the mechanisms of anti-sulfate ion poisoning of the LiAl-LDH/PAM, density functional theory (DFT) calculations were performed. Due to the polar functional groups with rich lone pair electrons, the positive binding energy of the PAM (0.93 eV) for SO_4^{2-} were observed, which confirmed the repulsion interaction, favoring to prevent the decline of Li^+ uptake induced by the SO_4^{2-} intercalation into LiAl-LDH (Figure 5.20).

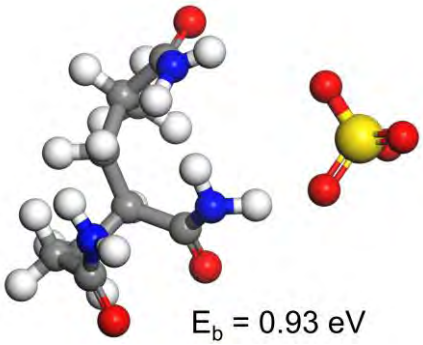

Figure 5.20 The binding energy between SO_4^{2-} and PAA.

Further, the migration of SO_4^{2-} over intralayer and interlayer of LiAl-LDHs was simulated, and the diffusion barrier energies were calculated. As shown in Figure 5.21, the barrier energies either from the intralayer or interlayer of LiAl-LDH/PAM are much higher than that from pristine LiAl-LDH. The results demonstrated that the intercalation of polymer modifiers not only inhibit SO_4^{2-} accessing the intralayer, but also increases the diffusion energy of SO_4^{2-} in LiAl-LDH interlayer, which resulted from the electrostatic repulsion of side groups and steric hindrance effect of polypropylene (PP) backbone (Figure 5.22).

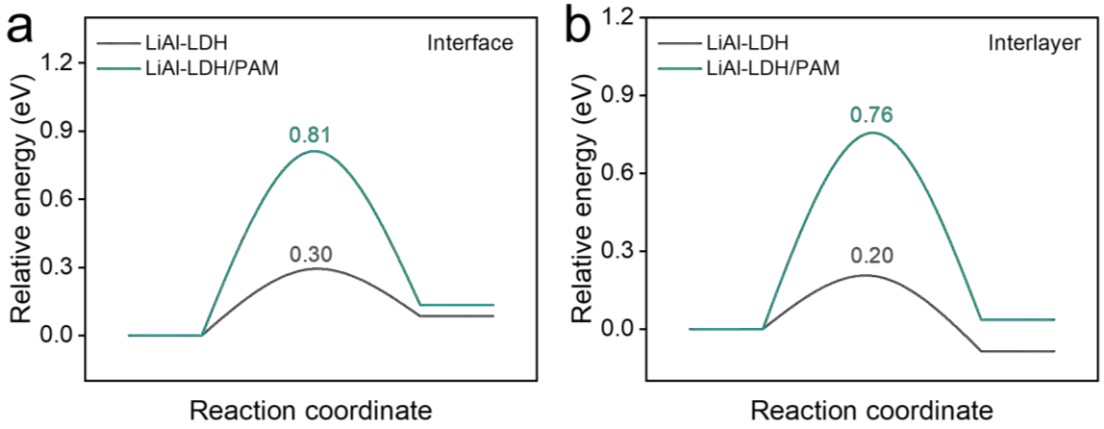

Figure 5.21 Energy barrier for (a) SO_4^{2-} migration over interface and (b) interlayer of the pristine LiAl-LDH and LiAl-LDH/PAM.

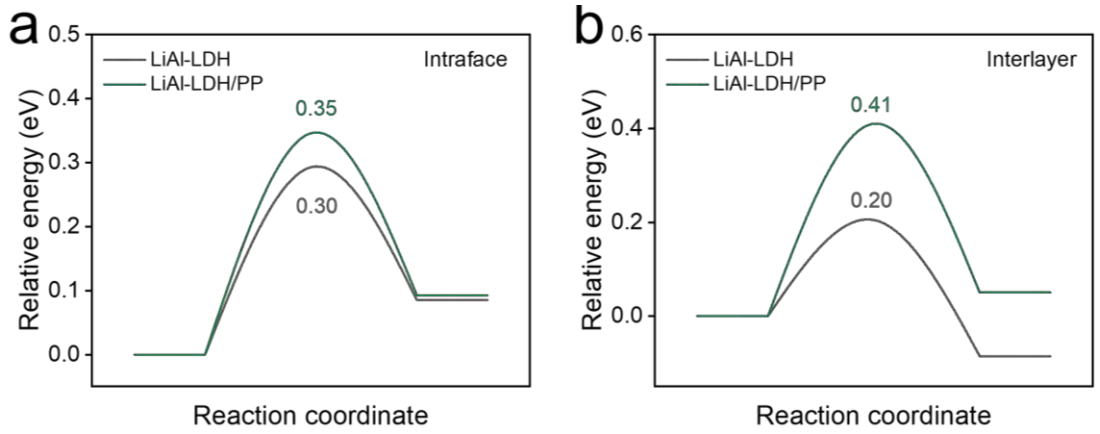

Figure 5.22 Energy barrier for (a) SO_4^{2-} migration over interface and (b) interlayer of the pristine LiAl-LDH and LiAl-LDH/PP.

The advancement of the PAM modification against sulfate ion poisoning were re-confirmed by the numerical simulations. As shown in Figure 5.23, whereby a SO_4^{2-} enrichment region was observed on the pristine LiAl-LDH surface while a depletion region of SO_4^{2-} was found on the LiAl-LDH/PSS surface (Figure 5.24).

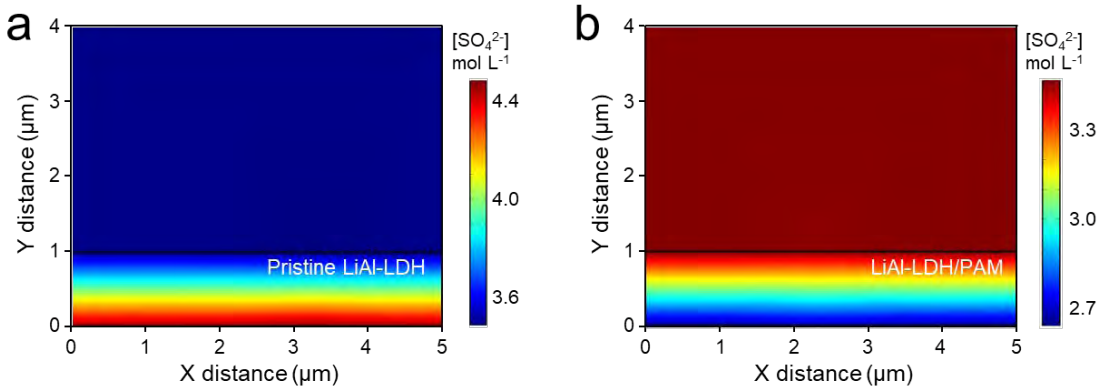

Figure 5.23 Numerical simulation of SO_4^{2-} diffusion in (a) pristine LiAl-LDH, and (b) LiAl-LDH/PAM.

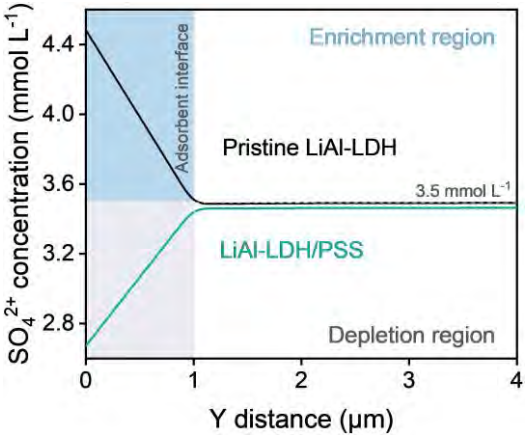

Figure 5.24 The SO_4^{2-} concentration as a function of Y distance from the results of Numerical simulations.

5.4. Conclusions

In summary, based on the instinct properties of LiAl-LDHs, a strategy of constructing multiple SO_4^{2-} repelling domains in the interface and interlayer using the organic modification with the PAM was proposed for sustainable lithium extraction from SO_4^{2-}-type brines. Characterizations and simulations revealed that the electrostatic repulsion induced by negatively charged side-chain groups of the PAM and the steric hindrance effect of polypropylene (PP) backbone delivered the repulsion interaction towards SO_4^{2-} and the increased energy barrier for SO_4^{2-} migration over interface and interlayer of the LiAl-LDH/PAM. Consequently, the intercalation of SO_4^{2-} was greatly hindered to prevent adsorption site blocking, which endowed the LiAl-LDH/PAM excellent anti-sulfate poisoning property for robust lithium extraction from Lop Nor brine, the largest SO_4^{2-}-type in the world. Additionally, negatively charged surface enhanced the affinity between the LiAl-LDH/PAM and Li^+, enabling the excellent Li^+ selectivity and the maximum adsorption capacity (13.25 mg g^{-1}) in the real SO_4^{2-}-type brine. This work provides a feasible strategy for sustainable lithium extraction from SO_4^{2-}-type brines, and can be extended to other kinds of brines, like CO_3^{2-}-type brines.

5.5. References

[1] M. Yong, M. Tang, L. Sun, F. Xiong, L. Xie, G. Zeng, X. Ren, K. Wang, Y. Cheng, Z. Li, E. Li, X. Zhang, H. Wang, Sustainable lithium extraction and magnesium hydroxide co-production from salt-lake brines, Nat. Sustain. 7 (2024) 1662-1671.
[2] P. Greim, A.A. Solomon, C. Breyer, Assessment of lithium criticality in the global energy transition and addressing policy gaps in transportation, Nat. Commun. 11 (2020) 4570.
[3] X. Sun, Z. Liu, F. Zhao, H. Hao, Global Competition in the Lithium-Ion Battery Supply Chain: A Novel Perspective for Criticality Analysis, Environ. Sci. Technol. 55 (2021) 12180-12190.
[4] Raw materials for a truly green future, Nat. Rev. Mater. 6 (2021) 455-455.
[5] Y. Xiong, J. Zhou, P. Lu, J. Yin, Y. Wang, Z. Fan, Electrochemical lithium extraction from aqueous sources, Matter 5 (2022) 1760-1791.
[6] M.L. Vera, W.R. Torres, C.I. Galli, A. Chagnes, V. Flexer, Environmental impact of direct lithium extraction from brines, Nat. Rev. Earth Environ. 4 (2023) 149-165.
[7] G. Yan, M. Wang, G.T. Hill, S. Zou, C. Liu, Defining the challenges of Li extraction with olivine host: The roles of competitor and spectator ions, Proc. Natl. Acad. Sci. 119 (2022) e2200751119.
[8] X. Chen, M. Yang, S. Zheng, F. Temprano-Coleto, Q. Dong, G. Cheng, N. Yao, H.A. Stone, L. Hu, Z.J. Ren, Spatially separated crystallization for selective lithium

extraction from saline water, Nat. Water 1 (2023) 808-817.
[9] É. Lèbre, M. Stringer, K. Svobodova, J.R. Owen, D. Kemp, C. Côte, A. Arratia-Solar, R.K. Valenta, The social and environmental complexities of extracting energy transition metals, Nat. Commun. 11 (2020) 4823.
[10] A.Z. Haddad, L. Hackl, B. Akuzum, G. Pohlman, J.F. Magnan, R. Kostecki, How to make lithium extraction cleaner, faster and cheaper—in six steps, Nature 616 (2023) 245-248.
[11] S.B. Darling, The brine of the times, Science 385 (2024) 1421-1422.
[12] S. Yang, Y. Wang, H. Pan, P. He, H. Zhou, Lithium extraction from low-quality brines, Nature 636 (2024) 309-321.
[13] Y. Bao, Z. Ji, H. Zhou, C. Zhang, S. Song, F. Jia, J. Li, M. Quintana, Li-Ions Pre-intercalation Strategy of Manganese Oxides for Capacitive Deionization-Based Selective Lithium Extraction From Low-grade Brine, Small n/a (2024) 2406951.
[14] Y. Han, J. Ma, D. Liu, Y. Yang, T. Zhang, M. Wang, D. Liang, L. Wen, J. Ma, W. Wang, Microenvironment-Modulating Adsorption Enables Highly Efficient Lithium Extraction under Natural pH Conditions, ACS Nano 18 (2024) 9071-9081.
[15] X. Jiang, L. Zhang, Y. Miao, L. Chen, J. Liu, T. Zhang, S. Cheng, Y. Song, Y. Zhao, Intrinsic roles of nanosheet characteristics in two-dimensional montmorillonite membranes for efficient Li^{+}/Mg^{2+} separation, Water Res. 276 (2025) 123291.
[16] X. Wu, H. Zhang, X. Zhang, Q. Guan, X. Tang, H. Wu, M. Feng, H. Wang, R. Ou, Sustainable lithium extraction enabled by responsive metal-organic frameworks with ion-sieving adsorption effects, Proc. Natl. Acad. Sci. 121 (2024) e2309852121.
[17] Y. Yuan, D. Cao, F. Cui, Y. Yang, C. Zhang, Y. Song, Y. Zheng, J. Cao, S. Chen, Y. Song, F. Wang, G. Zhu, High-capacity uranium extraction from seawater through constructing synergistic multiple dynamic bonds, Nat. Water 3 (2025) 89–98.
[18] J. Chen, C. Lian, J. Yu, S. Lin, A directional growth strategy for high layer charge Li/Al-LDHs to reinforce Li extraction in low-grade salt lake brines, AIChE J. 70 (2024) e18280.
[19] T.R. Graham, J.Z. Hu, X. Zhang, M. Dembowski, N.R. Jaegers, C. Wan, M. Bowden, A.S. Lipton, A.R. Felmy, S.B. Clark, K.M. Rosso, C.I. Pearce, Unraveling Gibbsite Transformation Pathways into LiAl-LDH in Concentrated Lithium Hydroxide, Inorg. Chem. 58 (2019) 12385-12394.
[20] L. Zhang, T. Zhang, Y. Zhao, G. Dong, S. Lv, S. Ma, S. Song, M. Quintana, Doping engineering of lithium-aluminum layered double hydroxides for high-efficiency lithium extraction from salt lake brines, Nano Res. 17 (2024) 1646-1654.
[21] L. Zhang, T. Zhang, S. Lv, S. Song, H.J.O. Galván, M. Quintana, Y. Zhao, Adsorbents for lithium extraction from salt lake brine with high magnesium/lithium ratio: From structure-performance relationship to industrial applications, Desalination 579 (2024) 117480.
[22] L. Zhang, T. Zhang, S. Lv, S. Cheng, G. Dong, M. Quintana, S. Song, Y. Zhao, Steering interlayer interaction of lithium-aluminum layered double hydroxide beads for stable lithium extraction from sulfate-type brines, Desalination 592 (2024) 118130.

[23] S. Lv, Y. Zhao, L. Zhang, T. Zhang, G. Dong, D. Li, S. Cheng, S. Ma, S. Song, M. Quintana, Anion regulation strategy of lithium-aluminum layered double hydroxides for strengthening resistance to deactivation in lithium recovery from brines, Chem. Eng. J. 472 (2023) 145026.
[24] J. Chen, S. Lin, J. Yu, Instant Interlayer Restoration Strategy for Lithium Adsorption Engineering Enhancement in Sulfate-type Brines, ACS Appl. Mater. Interfaces 16 (2024) 34850-34858.
[25] J. Chen, K. Huang, J. Du, C. Lian, J. Yu, S. Lin, Why is aluminum-based lithium adsorbent ineffective in Li^+ extraction from sulfate-type brines, AIChE J. 69 (2023) e18176.
[26] F. Wang, P. Zou, Y. Zhang, W. Pan, Y. Li, L. Liang, C. Chen, H. Liu, S. Zheng, Activating lattice oxygen in high-entropy LDH for robust and durable water oxidation, Nat. Commun. 14 (2023) 6019.
[27] Z. Cai, P. Wang, J. Zhang, A. Chen, J. Zhang, Y. Yan, X. Wang, Reinforced Layered Double Hydroxide Oxygen-Evolution Electrocatalysts: A Polyoxometallic Acid Wet-Etching Approach and Synergistic Mechanism, Adv. Mater. 34 (2022) 2110696.
[28] Y. Pan, Y. Zhang, C. Thompson, G. Liu, W. Zhang, Electrospun Lithium Porous Nanosorbent Fibers for Enhanced Lithium Adsorption and Sustainable Applications, ACS Appl. Mater. Interfaces 16 (2024) 54259-54271.
[29] X. Chen, W. Yu, Y. Zhang, C. Huang, L. Nie, J. Yu, Y. Zhang, C. Zhang, W. Zhai, X. Zhang, Y. Yu, W. Liu, Solar-Driven Lithium Extraction by a Floating Felt, Adv. Funct. Mater. 34 (2024) 2316178.
[30] X. Zhang, X. Wu, J. Gan, X. Yu, H. Wang, R. Ou, Building block design of thermally regenerable metal–organic framework composites for highly selective lithium adsorption, Chem. Eng. J. 499 (2024) 156352.
[31] J. Twu, P.K. Dutta, Structure and reactivity of oxovanadate anions in layered lithium aluminate materials, J. Phys. Chem. 93 (1989) 7863-7868.
[32] K. Yu, H. Yang, H. Zhang, H. Huang, Z. Wang, Z. Kang, Y. Liu, P.W. Menezes, Z. Chen, Immobilization of Oxyanions on the Reconstructed Heterostructure Evolved from a Bimetallic Oxysulfide for the Promotion of Oxygen Evolution Reaction, Nano-Micro Lett. 15 (2023) 186.

Chapter 6. Molecular tailoring engineering of lithium aluminum layered double hydroxides for lithium extraction from low-quality brines

6.1. Introduction

Lithium (Li), a critical metal resource in current global electrification and decarbonization strategies, has become pivotal in powering the novel electric vehicles, consumer electronics and energy storage systems [1-4]. These technological evolution drives exponentially growing global demand, making the sustainable supply of Li particularly urgent [5,6]. Currently, commercial Li is exclusively dependent on high-grade Li ores and continental brines, which are geologically constrained in very few countries [7,8]. Low-quality brines, including salt lakes, geothermal brines, oilfield brines, gas-produced water, and seawater, contain massive untapped Li resources and are distributed throughout the world [9]. Such resources can diversify the Li supplies and offer significant environmental and economic benefits for sustainable lithium extraction. However, Li extraction from brines remains technically and economically feasible only when the Li concentrations exceed 500 mg L^{-1} [9-11]. The low concentration of Li^+ (< 260 mg L^{-1}) and high concentration of competing Mg^{2+} (Mg^{2+}/Li^+ ratio, MLR > 6.15) of low-quality brines are main issues in hindering effective Li extraction [12-14].

Conventional evaporation-based Li extraction from low-quality brines is time-consuming and suffers from lithium entrainment losses potentially exceeding 60% during concentrating [7,8,15-18]. The concentrated brines require further purification to remove competing ions (especially Mg^{2+}), challenging the sustainable production of Li [19,20]. Adsorption has been a prominent industrial solution for direct lithium extraction from brines due to simple process and low energy consumption [21,22]. In particular, lithium-aluminum layered double hydroxides (LiAl-LDHs) are one of the most successful adsorbents due to their tailored octahedral cavity structure (~1.4 Å) for selective coordination by matching the Li^+ diameters and desorption without dissolution loss [23-25]. As presented in the Figure 6.1, LiAl-LDHs has a brucite-like $[LiAl_2(OH)_6]^+$ layered structure with Li^+ embedded in intralayer octahedral sites, while

the interlayer is filled with anions (typically Cl^-) and water molecules [26,27]. The reversible Li^+ intercalation and deintercalation mechanism enables selective lithium extraction from brines and regeneration of LiAl-LDHs adsorbents [24,28]. Current applications of LiAl-LDHs are still restricted in continental brines, while crucial concerns remain regarding lithium extraction from low-quality brines: i) the limited extraction rate and efficiency caused by the low Li^+ concentration. Although external energy-driven methods (e.g. electric field and photothermal energy) can concentrate Li^+ [29,30], they require complex operation, energy consumption, and large-scale supporting equipment, making them unsuitable for industrial-scale integration with LiAl-LDHs; ii) the poor universality of even advanced LiAl-LDHs due to the markedly complex components. Low-quality brines are abundant and widely distributed, and their composition is very complicated, and the differences in components, especially the MLR, are very large, which make even advanced LDH difficult to realize efficient lithium extraction from different low-quality brines. Therefore, purpose-driven design and innovation in LiAl-LDHs adsorbents aiming on high-efficiency and versatile Li extraction is important for sustainable Li extraction from low-quality brines.

Polymer side-chain engineering enables manipulation of the local spatial microstructure and chemical microenvironment of architectures through altering the molecular structure of side chains, which is well recognized as an effective and feasible regulation strategy for ion transport [31-33]. The water transport and ion separation of laminate membranes, for example, could be precisely modulated by introducing porphyrin-based aromatic macrocycle with different side chains [34]. In the previous chapter, we have found that polymer-modified LiAl-LDHs not only exhibits excellent anti-sulfate poisoning properties, but also offers enhanced lithium extraction performance. Inspired by these, the unique layered structure of LiAl-LDHs serves as an ideal platform for intralayer engineering with functional polymers. The diversity of the side chains offers great possibility in effectively addressing poor lithium extraction efficiency in low-quality brine. By rational design, the side-chain modified LiAl-LDH integrates the interdisciplinary theoretical prediction with practical implementation, which allows for scalable lithium recovery that demand high selectivity, capacity, and adaptability to different types low-quality brines.

In this work, a polymer side-chain structure design (SCSD) strategy is reported to engineer LiAl-LDHs with a Li^+-enriched intralayer domains via hydrogen bond interaction (Figure 6.1). Here, LiAl-LDHs was modified by a polypropylene (PP)

backbone, and the common polar functional groups with rich lone pair electrons involving carboxyl groups (polyacrylic acid, PAA), sulfonic acid groups (polystyrene sulfonate, PSS), and amide groups (polyacrylamide, PAM), are adapted as lithium-philic side chains to modulate the properties of intralayer environment. Based on the SCSD strategy, LiAl-LDHs modified by polymers (LiAl-LDH/PR) presented excellent Li^+ selectivity and extraordinary Li^+ enrichment property, enabling Li^+ recovery of over 90% from the oilfield brine with ultra-low Li concentration (19.7 mg L^{-1}). Employing Lop Nor brine (one of the largest low-quality brines in the world), SCSD strategy delivered a robust Li extraction repetition achieving ppb-level residual concentration and produced high-purity Li_2CO_3. The strategy significantly develops the feasibility of LiAl-LDHs, can easily tune the lithium extraction procedure, which holds promise for the scalability.

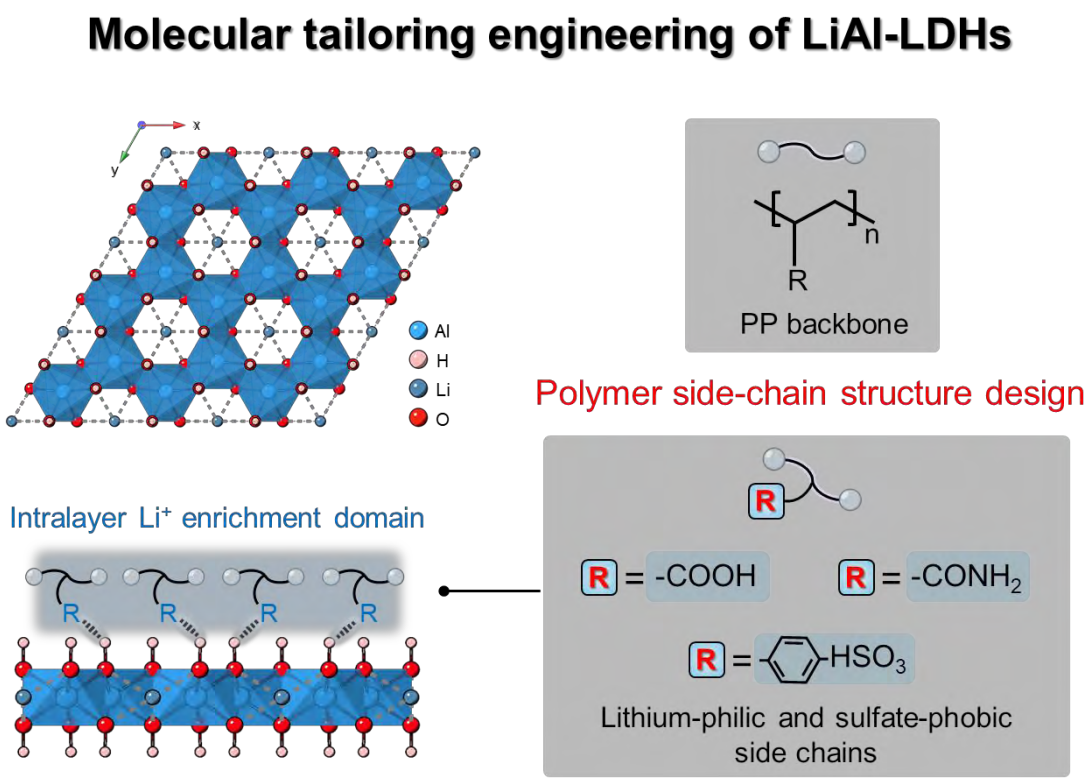

Figure 6.1 Schematic of the LiAl-LDH structure and the effects of polymer side-chain structure design strategy on Li extraction of LiAl-LDHs.

6.2. Experimental section

6.2.1. Reagents and materials

Lithium chloride (LiCl), aluminum chloride hexahydrate ($AlCl_3 \cdot 6H_2O$), sodium hydroxide (NaOH), polyacrylic acid (PAA), polyacrylamide (PAM) and polystyrene

sulfonic acid (PSS) were purchased from Shanghai Aladdin Biochemical Technology Co., Ltd. All chemical reagents were of analytical grade. The brines used in the experiments are all real brines, see Table 6.1 for details.

Table 6.1 Composition of brines used in the experiments.

Salt lake brine	Composition (g L^{-1})					
	Li^+	Mg^{2+}	K^+	Na^+	Cl^-	SO_4^{2-}
Lop Nur [a]	0.2222	97.015	2.549	2.899	222.400	37.600
East Taijinar	2.8190	117.573	0.593	0.185	157.200	13.830
Diluted East Taijinar	0.2819	11.757	0.059	0.019	15.720	1.383
Qianjiang Oilfield	0.0197	0.2101	0.8415	89.76	142.014	3.043

[a]: The brine after potassium extraction

6.2.2. Preparation of LiAl-LDH/PR

The preparation procedure is similar to that in chapter V. Briefly, the two-step co-precipitation-activation modification method instead of the standard one-step co-precipitation method was employed for LiAl-LDHs synthesis. The LiAl-LDH precursor was first prepared by co-precipitation of Li/Al salts, and then the precursor was mixed with the solution containing modifiers (PAA, PAM, and PSS) for simultaneous activation and modification to obtain engineering adsorbents (LiAl-LDH/PR).

6.2.3. Characterizations

The morphological structures of the samples were characterized using a scanning electron microscope (SEM, Zeiss Gemini 300) and transmission electron microscope (TEM, JEM-JEOL-2100) equipped with energy dispersive spectroscopy (EDS) system. X-ray diffraction patterns were recorded using a Bruker diffractometer (XRD, Empyrean) with Cu Kα irradiation (40 kV, 100 mA). The surface potentials of the samples were tested using a zeta potential analyzer (Malvern Zetasizer Nano ZS90 zeta). N_2 adsorption-desorption of the samples was carried out using an ASAP2460 pore analyzer, where the specific area, porosity and pore size distributions were determined by the Brunner-Emmett-Taylor method (BET). The contact angles (CA) of the samples were determined by a microscopic contact angle meter. X-ray photoelectron spectra (XPS) were determined by a Thermo Scientific K-Alpha spectrometer. The inductively coupled plasma optical emission spectrometry (ICP-OES, Prodigy 7) measurement was employed to analyze the proportion of metal species in the sample.

6.2.4. Lithium-ion extraction and Li_2CO_3 production

Lithium extraction: The Li extraction experiments, including adsorption, desorption, selectivity experiments, are consistent with those in Chapter V except for the brines used.

Sequential lithium recovery*:* 3 g LiAl-LDH/PAM were added to Lop Nur brine of 300 mL, shaken for 3h and centrifuged to separate, where the supernatant was retained for the following Li^+ adsorption, and the bottom precipitates were desorbed by adding 150 mL of deionized water at 40 ºC for 2 h. At the end of desorption, centrifugal separation was performed to retain the desorbed solution, and the precipitates (*i.e.*, regenerated LiAl-LDH/PAM) were dried and used for the next adsorption-desorption until the Li^+ in the brine were completely recovery.

Precipitation of Li_2CO_3*:* To ensure Li_2CO_3 production, the collected desorption solution (~1.1 L) was further purified with LiAl-LDH/PAM through reabsorption-desorption to increase the Li/Mg ratio. Further, the collected purified Li^+ solution was heated and concentrated 100 times to prepare the Li^+-rich solution. Finally, the excess sodium carbonate (Na_2CO_3) was added to the Li^+-rich solution, inducing lithium carbonate (Li_2CO_3) precipitation. In order to improve the grade of the precipitated composites, the composites were added to HCl to dissolve and reprecipitation by NaOH to generate insoluble magnesium hydroxide. After filtration to eliminate $Mg(OH)_2$, Na_2CO_3 was added again to precipitate Li^+, and high purity Li_2CO_3 was obtained.

6.2.5. Theoretical calculations

The electrostatic potential (ESP) distributions of various polymers were calculated by the Gaussian 09 software. The hybridization exchange-correlation generalized Becke-Lee-Yang-Parr (B3LYP) was used to optimize all structures, and described by basis set of 6-31+G(d), and the results were analyzed by GaussView 5.0.

All density functional theory (DFT) calculations were performed through the Materials Studio 8.0 software. The exchange-correlation interactions were described by the generalized gradient approximation of Perdew-Burke-Ernzerhof (GGA-PBE) for structural optimization to minimize the energy. The cut-off energy was set to 570.0 eV, and the convergence criteria for displacement, energy, and force were 0.001 Å, 1×10^{-5} eV/atom, and 0.03 eV/Å, respectively. The binding energies (E_b) between ions and polymers were also calculated by Equation 6.1:

$$E_b=E_{A/B}-E_A-E_B \quad (6.1)$$

where $E_{A/B}$ is the total energy of A and B bonded system; E_A and E_B indicate the energies of individual A and B, respectively.

6.2.6. Numerical simulation

The numerical simulations are consistent with those in Chapter V except for the key parameters, which are summarized in Table 6.2.

Table 6.2 Key parameters of multiphysics simulations.

Symbol	Parameter	Value	Unit
D_{Li}	Li^+ diffusion coefficient	1.029×10^{-9}	$m^2\ s^{-1}$
D_S	SO_4^{2-} diffusion coefficient	1.07×10^{-9}	$m^2\ s^{-1}$
C_{Li}	Initial Li^+ concentration	7	mol m^{-3}
C_S	Initial SO_4^{2-} concentration	3.5	mol m^{-3}
z_{Li}	Number of Li^+ charge	1	Dimensionless
z_S	Number of SO_4^{2-} charge	-2	Dimensionless
ε	Permittivity of water	78.4	F/m
ε_0	Permittivity of a vacuum	8.854×10^{-12}	F/m
T	System temperature	298	K

6.3. Results and discussion

6.3.1. Intralayer/interlayer engineering design

First, the theoretical feasibility of the chosen side chains modifiers (PAA, PSS, PAM) in coordinating with Li^+ and SO_4^{2-} is evaluated. The electrostatic potential (ESP) distribution of these polymer modifiers was calculated and shown in Figure 1b. The region with electrostatic potential is mainly distributed on the side chains, where van der Waals surface presents different ESP owing to the distinct electron donor and acceptor properties of side groups [35]. The negative electrostatic potential (red area) originates from the ionization of side groups and is primarily around C=O or S=O, with the minimum ESP following the order: PSS < PAM < PAA.

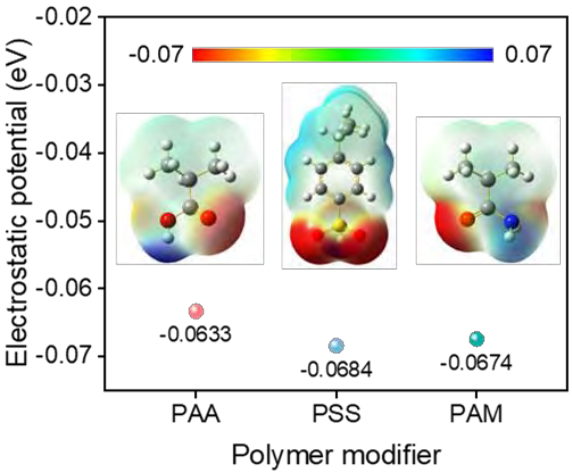

Figure 6.2 Electrostatic potential and the minimum electrostatic potential value of PAA, PSS, PAM.

Then, density functional theory (DFT) calculations were performed to illustrate how the side-chain structure of each polymer modifier affects the extraction and transport of Li^+ (Figure 6.3a). According to the binding energy (E_b), all three modifiers exhibited a favorable binding towards Li^+. It is found that PSS (-5.73 eV) and PAM (-4.42 eV) showed more negative E_b than PAA (-3.38 eV) demonstrating the more powerful coordination of sulfonic acid and amide side groups with Li^+ compared to the carboxyl groups. Despite the higher binding energy to Mg^{2+} , Na^+, and K^+ was found (Figure 6.3b-c), it might have a limited effect on the Li extraction process due to the size screening effect of LiAl-LDHs (Figure 6.4) [19,26].

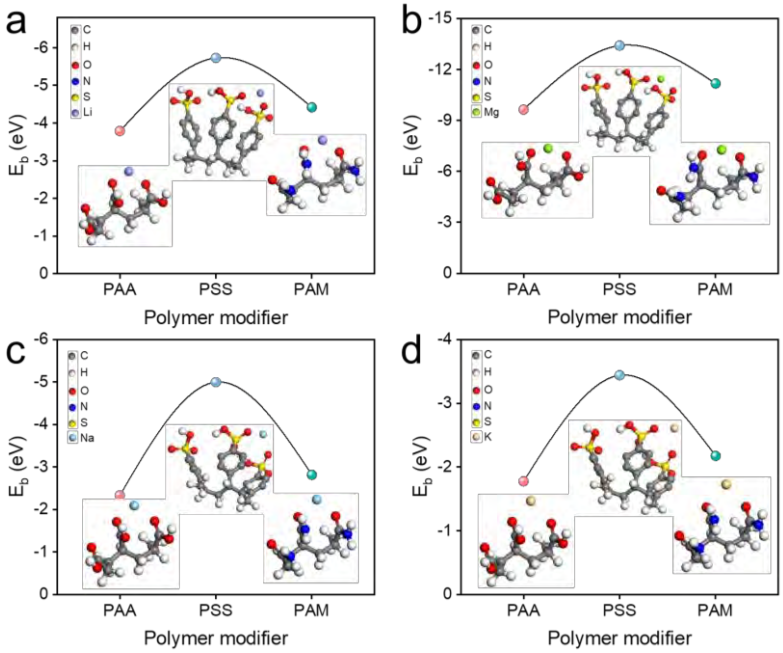

Figure 6.3 Binding energies between (a) Li^+, (b) Mg^{2+}, (c) Na^+, (d) K^+ and PAA, PSS,

PAM, respectively.

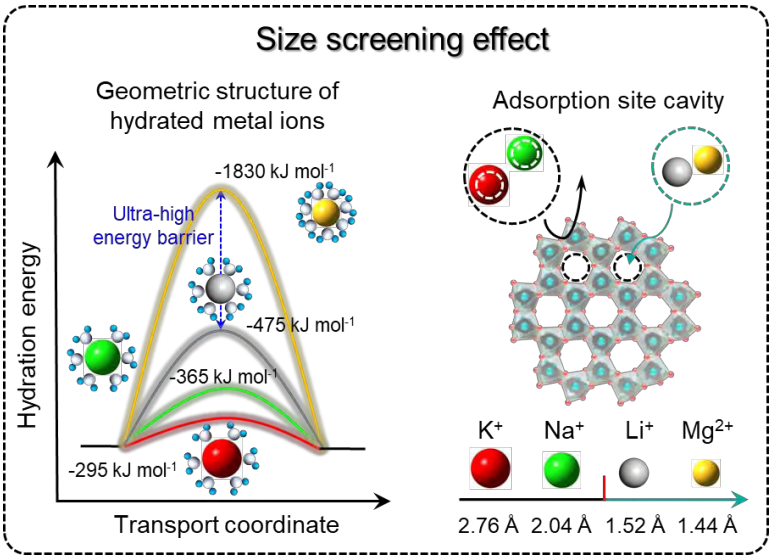

Figure 6.4 Schematic of size screening effect of LiAl-LDHs on Li^+.

To determine the influence of modifiers on the electric charge properties, theoretical models of LiAl-LDHs modified by polymer building blocks (LiAl-LDH/PR) were constructed, as shown in Figure 6.5.

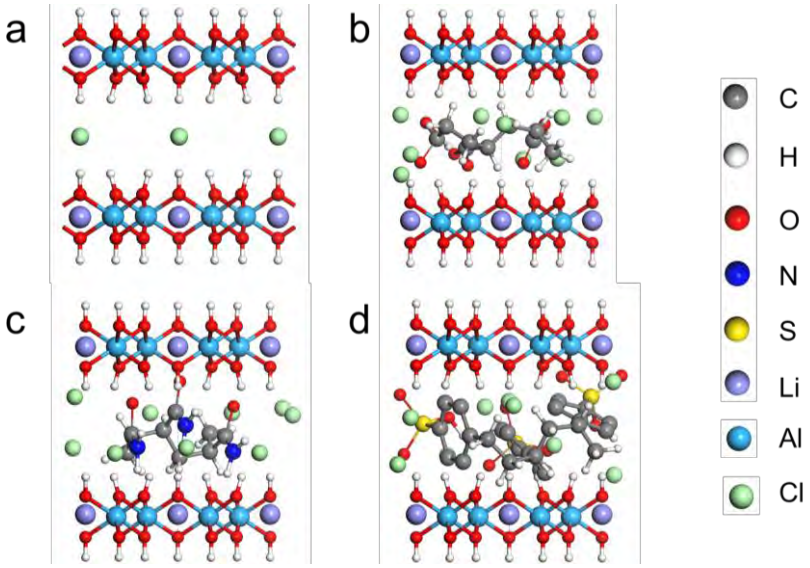

Figure 6.5 Optimized structures of (a) LiAl-LDH, (b) LiAl-LDH/PAA, (c) LiAl-LDH/PAM, and (d) LiAl-LDH/PSS.

Further, the projected density of states (PDOS) of Li and Al atoms in LiAl-LDH/PR were calculated (Figure 6.6). It can be found that compared to the pristine LiAl-LDH, the overlapping bands of Li 1s and Al 2p in LiAl-LDH/PR are significantly broadened and strengthened, accompanied by a shift to the higher energy, unveiling that the introduction of polymer building blocks enhances Li^+ adhesion to the laminae and

promotes Li^+ intercalation into the cavities of $Al(OH)_3$ octahedral framework.

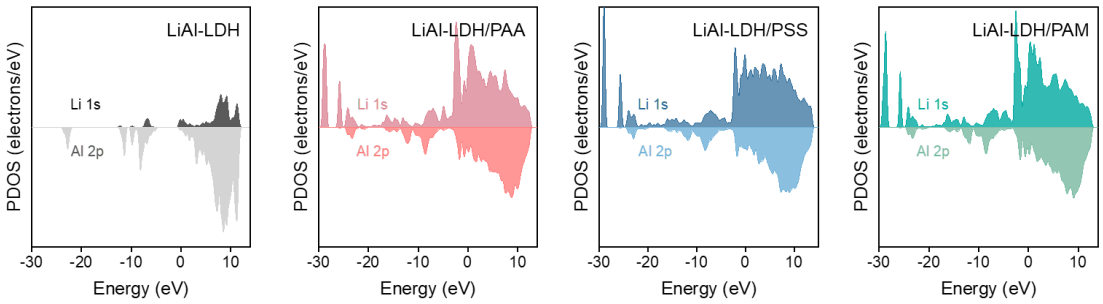

Figure 6.6 Projected density of states (PDOS) of Li and Al atoms of LiAl-LDH, LiAl-LDH/PAA, LiAl-LDH/PSS, and LiAl-LDH/PAM.

Furthermore, the enrichment effect of polymer modifiers on Li^+ was analyzed via finite element method, in which the simplified 2D models of ultra-low Li^+ solutions (7 mol m^{-3}) containing LiAl-LDHs with different surface charges were constructed. The pristine LiAl-LDH exhibited a significant lower Li^+ concentration distribution in the adsorbent than that in bulk solution (Figure 6.7a). Such concentration polarization resulted from the repulsion effect of positively charged surface towards Li^+. In contrast, the LiAl-LDH/PSS, with a negatively charged surface and strong Li^+ affinity, could compress the concentration polarization and self-enrich Li^+ in the adsorbent (Figure 6.7b). These results proved that SCSD strategy develops Li^+ enrichment domains on the intralayer, facilitating LiAl-LDHs to overcome the diffusion-limited Li extraction in Li^+-low brines.

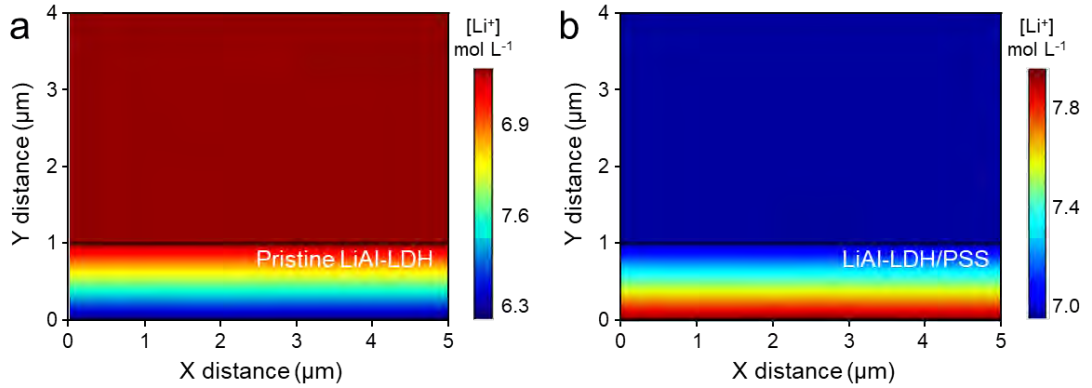

Figure 6.7 Numerical simulation of Li^+ diffusion in (a) pristine LiAl-LDH and (b) LiAl-LDH/PSS.

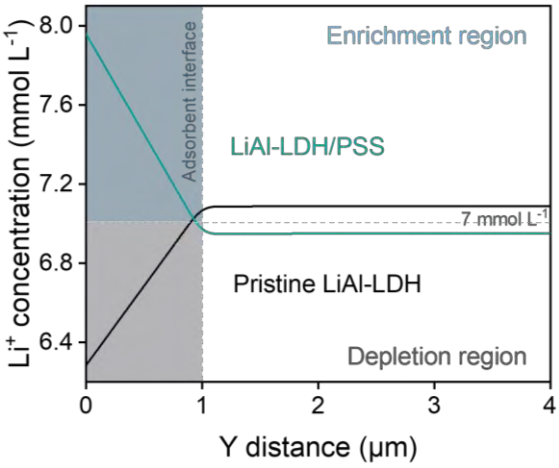

Figure 6.8 The Li^+ concentration as a function of Y distance from the results of numerical simulations.

The results of simulation calculations demonstrated that the SCSD strategy is able to develop Li^+ enrichment domains on the interface, facilitating LiAl-LDHs to overcome the diffusion-limited Li extraction in low-quality brine with Li^+-low concentration. Notably, the chemical microenvironment of these functional domains and spatial microstructure of LiAl-LDHs could be fine-tuned by controlling the side chains of polymers.

6.3.2. Synthesis and characterization

To test the SCSD strategy, three types of polymer-modified LiAl-LDHs (denoted as LiAl-LDH/PR, where R refers to side chain structures) were prepared to evaluate the effects of the three side chain modifiers on continuous Li recovery from sulfate-type brines. Scanning electron microscope (SEM) images showed that due to the high surface energy, all samples exhibited a typical lamellar stacking structure consisting of irregular hexagonal nanosheets with a lateral size of 80 nm (Figure 6.9). In particular, LiAl-LDH/PR were more tightly stacked after modification due to the bridging of polymers with the positively charged nanosheets.

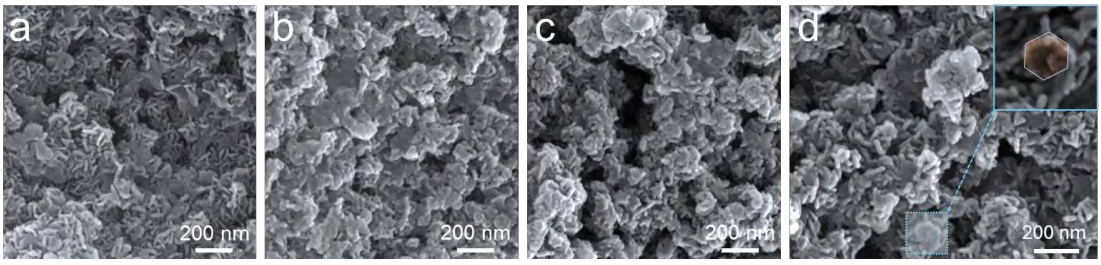

Figure 6.9 SEM images of (a) LiAl-LDH, (b) LiAl-LDH/PAA, (c) LiAl-LDH/PAM, and (d) LiAl-LDH/PSS.

X-ray diffraction (XRD) patterns further demonstrated the successful preparation of LiAl-LDH/PR with expanded interlayer spacing (Figure 6.10a). And the modification tuned the originally positive zeta potential of pristine LiAl-LDH to negative values, indicating polymer availability on the surface, thereby enabling the electrostatic attraction towards Li^+ (Figure 6.10b).

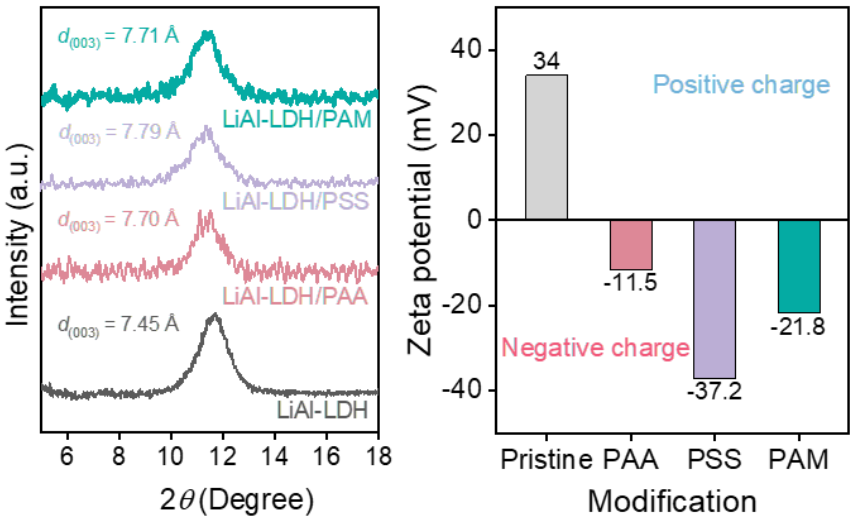

Figure 6.10 (a) XRD patterns and (b) zeta potentials of the pristine LiAl-LDH and LiAl-LDH/PR.

X-ray photoelectron spectroscopy (XPS) spectra for the characteristic elemental C 1s, S 2p, and N 1s core levels indicated the existence of polymer modifiers with side chains of -COOH, $-SO_3H$, and $-CONH_2$ on the surface of the LiAl-LDH (Figure 6.11), which was proved by Fourier transform infrared (FT-IR) spectra (Figure 6.12b) [36-38].

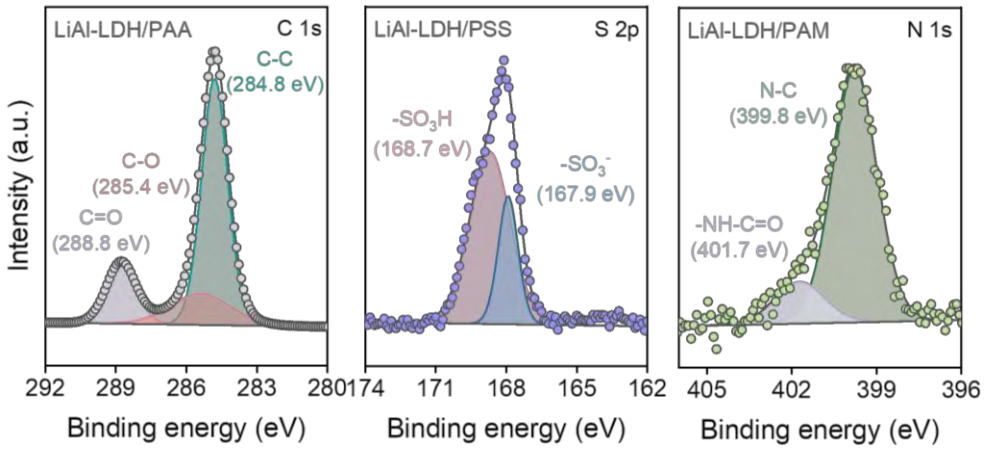

Figure 6.11 XPS spectra for the C 1s, S 2p, and N 1s core level of the pristine LiAl-LDH and LiAl-LDH/PR.

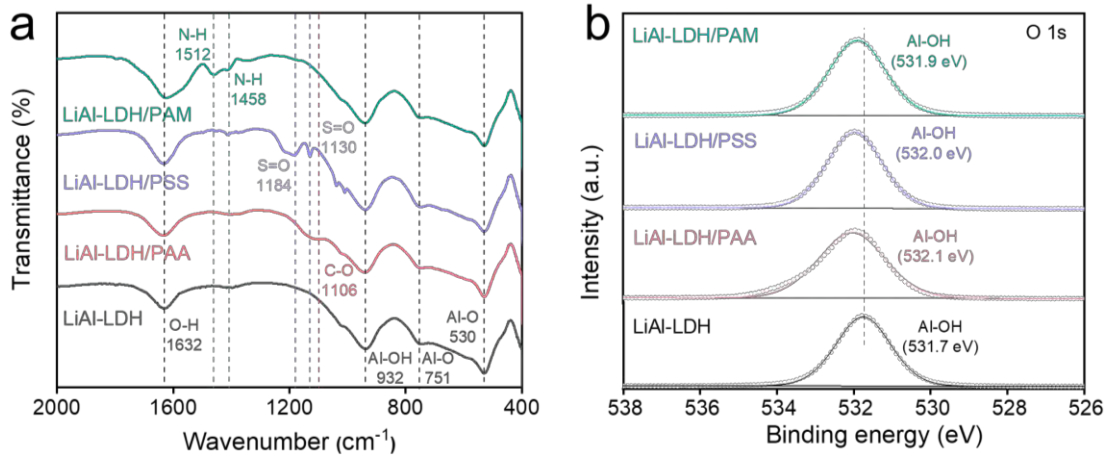

Figure 6.12 (a) FT-IR spectra and (b) XPS spectra for O 1s core levels of the pristine LiAl-LDH and LiAl-LDH/PR.

Furthermore, the shift of O 1s core level toward higher binding energy demonstrated the hydrogen bond interaction between the polymer modifiers and the LiAl-LDH (Figure 6.12b), where the electrons around O atoms in Al-OH were transferred to the H atoms on the polymer side chain, consistent with the ESP results [39].

Moreover, N_2 adsorption-desorption isotherms showed type IV reversible isotherms with H4 hysteresis loops for all LiAl-LDHs, indicating their microporous and mesoporous characteristics, which favored to eliminate concentration polarization (Figure 6.13) [14]. Brunner-Emmet-Teller specific surface areas (SSA) of LiAl-LDH/PR decreased after introducing polymers, reconfirming that polymer chains partially occupied the original surfaces and interlayer channels of LiAl-LDHs (Table 6.3) [40].

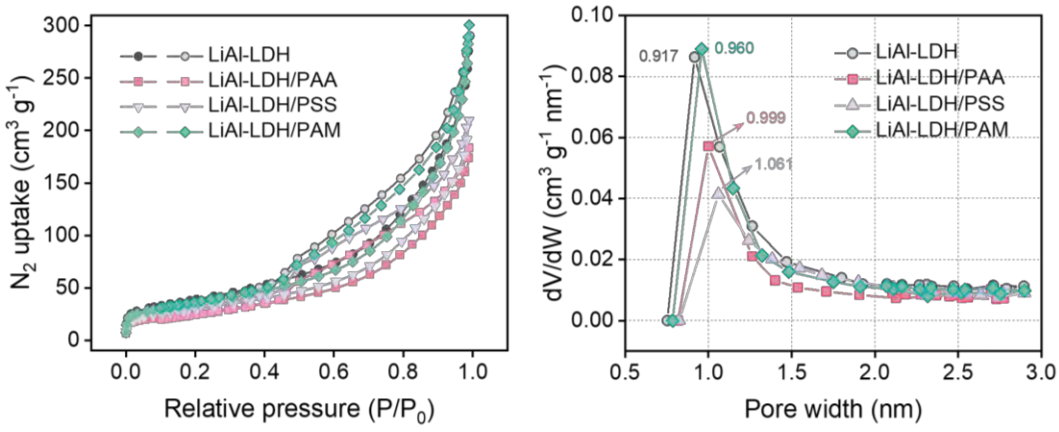

Figure 6.13 (a) N_2 adsorption-desorption isotherms and (b) pore size distributions of the pristine LiAl-LDH and LiAl-LDH/PR.

Table 6.3 The textural properties of pristine LiAl-LDH, LiAl-LDH/PAA, LiAl-LDH/PSS and LiAl-LDH/PAM.

Samples	Specific surface area (m^2 g^{-1})	Total pore volume (cm^3 g^{-1})	Mean pore diameter (nm)
LiAl-LDH	139.63	0.4491	12.87
LiAl-LDH/PAA	93.19	0.2836	12.17
LiAl-LDH/PSS	108.63	0.3245	11.95
LiAl-LDH/PAM	123.10	0.4654	15.12

Also, polymer modification reduced the hydrophilicity of pristine LiAl-LDH, with the resulting hydrophobicity varying depending on the side chain groups (Figure 6.14). The phenomena were attributed to the hydrogen bonds between the side chain groups and the LiAl-LDH, preventing the formation of hydrogen bonds between water molecules and these groups on the LiAl-LDH surface, thus resulting in a decrease in hydrophilicity [41]. In particular, the stronger hydrogen bond connection between PAA and LDH led to the enhanced hydrophobicity of LiAl-LDH/PAA compared to the modifications with PAM and PSS.

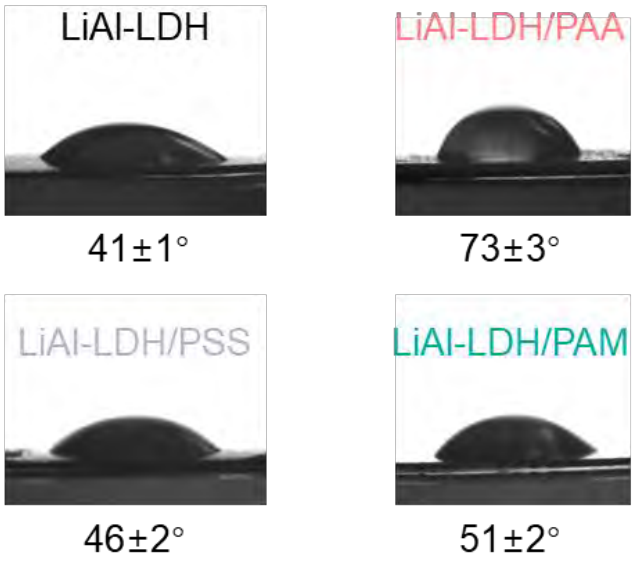

Figure 6.14 Contact angle images of the pristine LiAl-LDH and LiAl-LDH/PR.

6.3.3. Lithium extraction performance

To evaluate the practical feasibility of the proposed strategy, the SCSD-designed LiAl-LDH/PR was first applied to extract lithium from Lop Nor brine that is a typical

low-quality SO_4^{2-}-type brine, occurring low Li^+ concentration (0.222 g L^{-1}) and ultrahigh Mg^{2+}/Li^+ ratio (MLR, 437). As shown in Figure 6.15a, the LiAl-LDH/PR showed improved viability for lithium extraction from such low-quality brine with significantly increased Li^+ uptake (> 6 mg g^{-1}) compared to the pristine LiAl-LDH, which was attributed to the strong attraction of polymer modifiers towards Li^+. Kinetics experiments demonstrated the chemisorption-dominated Li extraction for four adsorbents (Figure 6.15b-d).

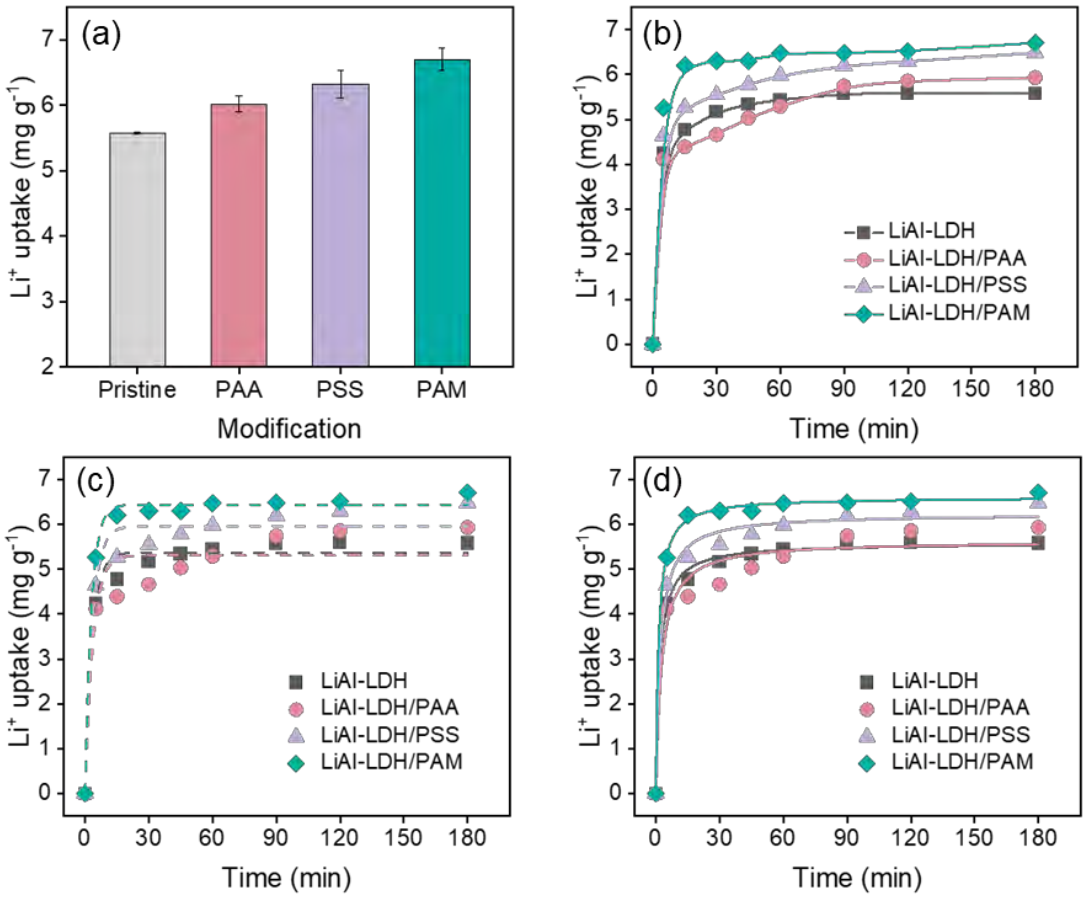

Figure 6.15 (a) Li^+ uptake and (b) uptake kinetics of the pristine LiAl-LDH and LiAl-LDH/PR in Lop Nor brine. (c) Pseudo-first-order and (d) pseudo-second-order kinetic models of Li^+ uptake on the pristine LiAl-LDH and LiAl-LDH/PR.

Such extraction process fitted with three major stages of intraparticle diffusion model in our previous study[23], including rapid transfer to the intralayer, intercalation into octahedral voids, and interior diffusion to release the external active sites (Figure 6.16).

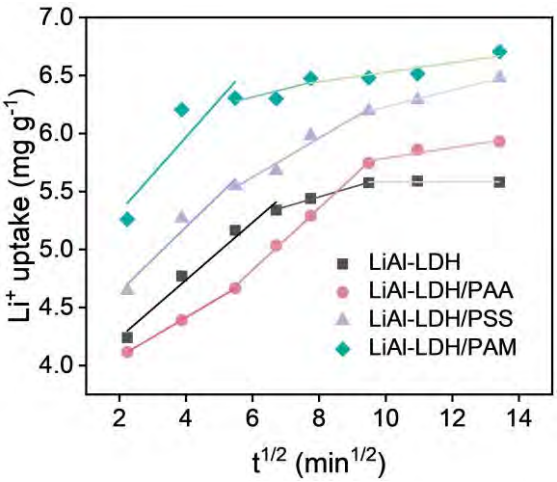

Figure 6.16 The intraparticle diffusion model for Li^+ adsorption process of the pristine LiAl-LDH and LiAl-LDH/PR in Lop Nor brine.

The desorption of LiAl-LDH/PR was slightly slowed due to the attraction between polymers and Li^+, whereas the complete desorption was still finished within 60 min (Figure 6.17a). Even the MLR of desorption solution of LiAl-LDH/PR dropped below 2, a reduction of more than 240 times compared to the original solution, which facilitated the subsequent Li^+ recovery (Figure 6.17b).

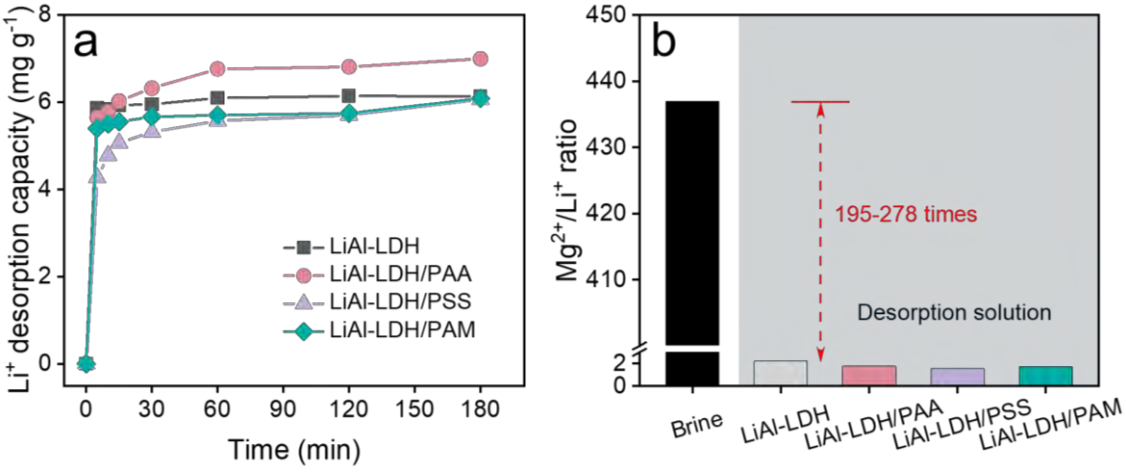

Figure 6.17 (a) Li^+ desorption kinetics of the pristine LiAl-LDH and LiAl-LDH/PR. (b) Mg^{2+}/Li^+ ratios before and after extraction by the pristine LiAl-LDH and LiAl-LDH/PR.

As well, the selectivity was investigated in detail. As shown in Figure 6.18, the distribution coefficient (K_d) values of all LiAl-LDHs for Li^+ were larger than 50, while those for the other main coexisting metal ions below 1, indicating the well selectivity. Further, the separation factors (α) of Li^+/Mg^{2+}, Li^+/Na^+ and Li^+/K^+ were determined. The LiAl-LDH/PR presented significant higher $\alpha_{Li/Mg}$ than pristine LiAl-LDH,

following the order: LiAl-LDH/PAM (104.65) > LiAl-LDH/PSS (94.13) > LiAl-LDH/PAA (81.37) > LiAl-LDH (72.99). Notably, sulfonate groups in the side chains of PSS offered the highest Li^+ affinity according to the DFT calculation results, but both Li^+ uptake and selectivity of LiAl-LDH/PSS were lower than these of LiAl-LDH/PAM. This could be explained by the fact that PSS bonded more strongly with Mg^{2+} as well, yielding the greater competition in Lop Nor brine with ultrahigh MLR. The selectivity of LiAl-LDH/PR for Li^+/Na^+ and Li^+/K^+ was higher than that for Li^+/Mg^{2+} due to the weaker binding of functional groups to Na^+ and K^+ than Mg^{2+}, and the apparently larger ionic sizes of Na^+ (2.76 Å) and K^+ (2.04 Å) [42].

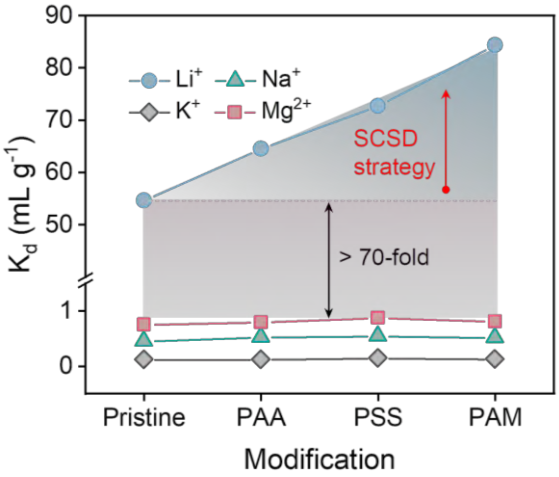

Figure 6.18 Dispersion coefficient (K_d) values of the pristine LiAl-LDH and LiAl-LDH/PR in Lop Nor brine.

Furthermore, the performance of LiAl-LDHs was comprehensively compared by radar chart (Figure 6.19). Generally, the Li^+ uptake, adsorption efficiency and selectivity of LiAl-LDH/PR were enhanced to some extent, unveiling the sophistication of the proposed strategy for lithium extraction from low-quality brines.

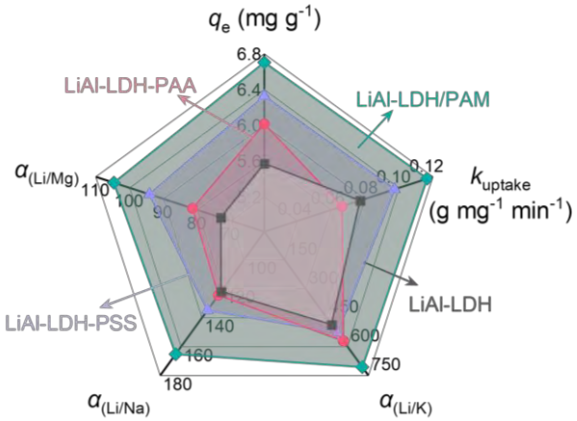

Figure 6.19 The radar chart for performance comparison analysis of LiAl-LDHs.

The universality of the SCSD strategy was evaluated in East Taijinar Salt-Lake brine (Figure 6.20). Due to the high Li^+ concentration (2.82 g L^{-1}) and relatively low MLR (41.69) of East Taijinar brine, the Li^+ uptake of pristine LiAl-LDH increased to 8.25 mg g^{-1}. After modification, uptake was improved to 11.15, 13.90, and 13.65 mg g^{-1} for LiAl-LDH/PAA, LiAl-LDH/PSS, and LiAl-LDH/PAM with the 35.15%, 68.48% and 65.45% higher than the pristine one, respectively (Figure 3c). Among them, LiAl-LDH/PSS demonstrated the highest uptake of 13.90 mg g^{-1}, exceeding previously reported LiAl-LDH-based adsorbents. To reveal the Li extraction performance from the brine with low Li^+ concentration, East Taijinar brine was diluted (V_{H2O}/V_{brine} = 9:1). The similar results of enhanced Li^+ uptake were observed in diluted brine, showing the availability of this strategy (Figure 6.20). To speak of, the performance of LiAl-LDH/PSS surpassed that of LiAl-LDH/PAM in East Taijinar brine before and after dilution, counter to the results in Lop Nor brine. The phenomenon resulted from the lower MLR of the former and thereby weaker competitive effect from Mg^{2+}.

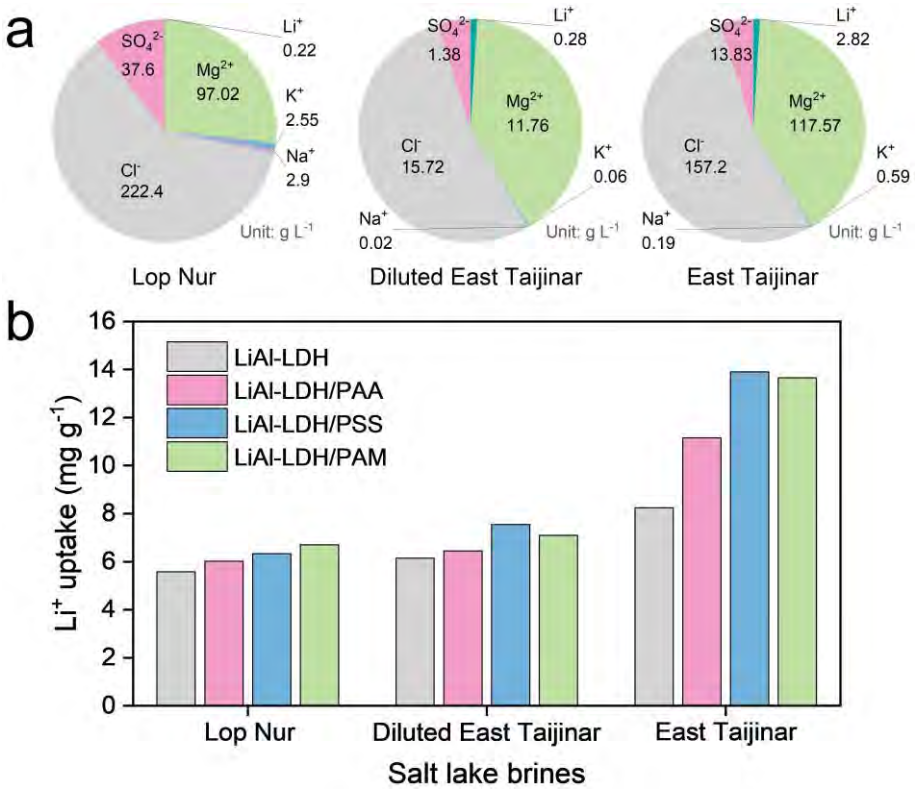

Figure 6.20 (a) Comparative analysis of brine composition (pie charts) and (b) Li uptake (bar plots) for Lop Nur brine, Diluted East Taijinar brine, and East Taijinar brine.

For directly exposing the advancement of the proposed strategy for lithium

extraction in low-quality brines, LiAl-LDH/PR was used for Li extraction from Qianjiang Oilfield brine with ultra-low Li^+ concentration (19.7 mg L^{-1}). Encouragingly, LiAl-LDH/PR presented markedly improved lithium extraction efficiency in such Li^+-low brine, where Li^+ recoveries were all higher than 75%, while that of pristine LiAl-LDH was less than 50%, offering the solid proof for the attraction and enrichment effects of polymer building blocks on Li^+ (Figure 6.21a). Moreover, LiAl-LDH/PSS also exhibited the highest Li^+ uptake in Qianjiang Oilfield brine with relatively low MLR (10.66) Compared to reported state-of-the-art LiAl-LDH-based adsorbents, the LiAl-LDH/PR demonstrates superior lithium extraction from brines with ultra-low Li^+ concentration as well (Figure 6.21b).

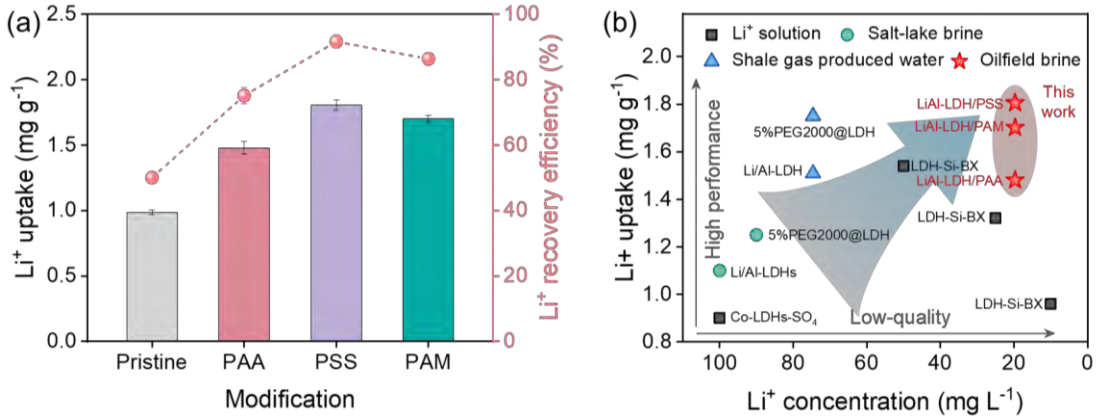

Figure 6.21 (a) Li^+ uptake of LiAl-LDHs in Qianjiang Oilfield brine. (b) Comparison of lithium extraction of LiAl-LDH/PR to other LiAl-LDH-based adsorbents in Li^+-low aqueous with concentrations below 100 mg L^{-1}.

Based on above results, the lithium extraction property heatmap and application scope chart of LiAl-LDH/PR in low-quality brine were plotted (Figure 6.22). Specifically, LiAl-LDH/PSS is more suitable for brines with lower MLR, especially Li^+-low brines, due to slightly reduced SSA and hydrophilicity, and the highest Li^+ enrichment effect but the strongest Mg^{2+} competitive effect. Whereas LiAl-LDH/PAM is more appropriate for brines with higher MLR than LiAl-LDH/PSS due to the high Li^+ enrichment and unsignificant Mg^{2+} competition, but desires higher Li^+ concentration as well. Overall, the SCSD strategy enables optimized and efficient lithium extraction from a wide range of brine resources.

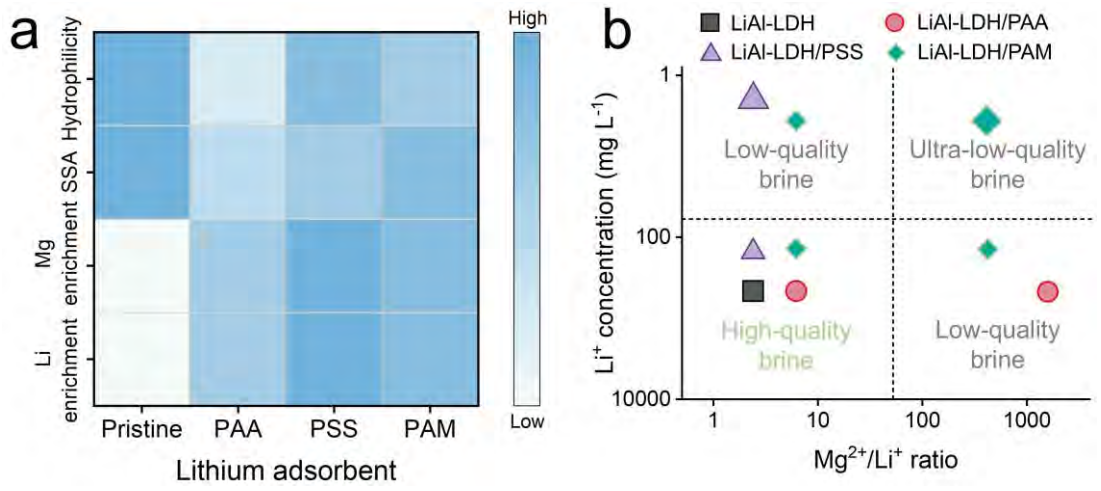

Figure 6.22 (a) The lithium extraction property heatmap and (b) application scope chart of LiAl-LDH/PR in low-quality brine.

6.3.4. Lithium recovery and precipitation of Li_2CO_3

Motivated by distinctive performance of LiAl-LDH/PAM on lithium extraction and reusability in Lop Nor brine, the repeated Li^+ recovery from this brine was explored. As expected, LiAl-LDH/PAM displayed excellent stability during seven adsorption-desorption repetitions with a high Li^+ recovery efficiency of 99.72% (Figure 6.23). Notably, the Li^+ concentration in the brine was only 79.8 mg L^{-1} after three repetitions, while the adsorption capacity of LiAl-LDH/PAM could reach up 4.18 mg g^{-1}. These phenomena confirmed the effect of polymer modifiers in Li^+ enrichment in low-quality brines with Li^+-low concentration.

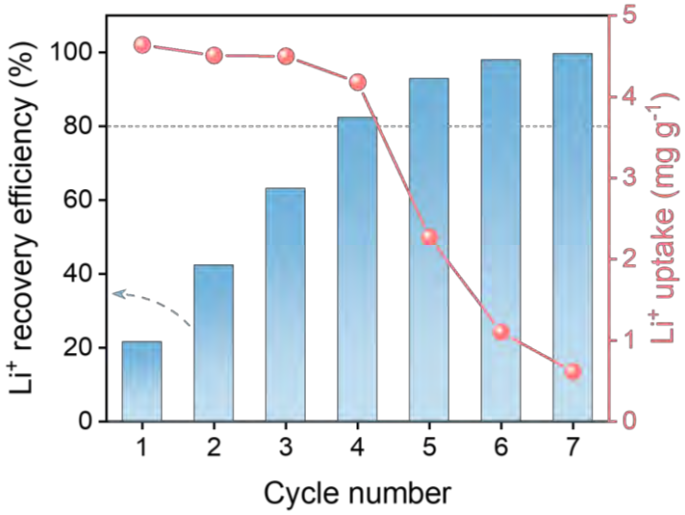

Figure 6.23 Repeated Li^+ uptake and accumulated Li^+ recovery efficiency in Lop Nor brine.

Meanwhile, the Li^+ concentration of the residual brine was only 0.63 mg L^{-1} after repeat extraction, indicating that LiAl-LDH/PAM is able to extract Li^+ down to the ppb-level (< 1000 part per billion). In contrast, the concentration of competing metal ions remained almost constant, demonstrating the ultra-stable selectivity during the repeated procedures (Figure 6.24).

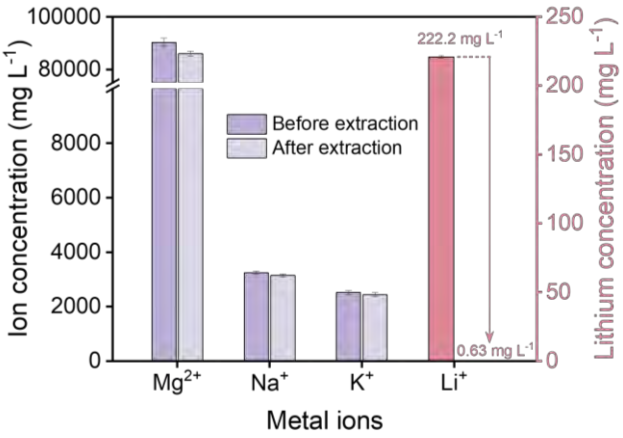

Figure 6.24 The Li extraction efficiency in Lop Nor brine.

The total organic carbon (TOC) throughout the process were also detected to investigate the dissolution of the polymer modifier. The results indicated that the TOC of the residual liquid was lower than that of the original brine, and the summation of the TOC of the desorption solution coupled with the TOC of residual liquid was close to that of the original brine, which suggested almost no dissolution of PAM, revealing excellent stability (Figure 6.25).

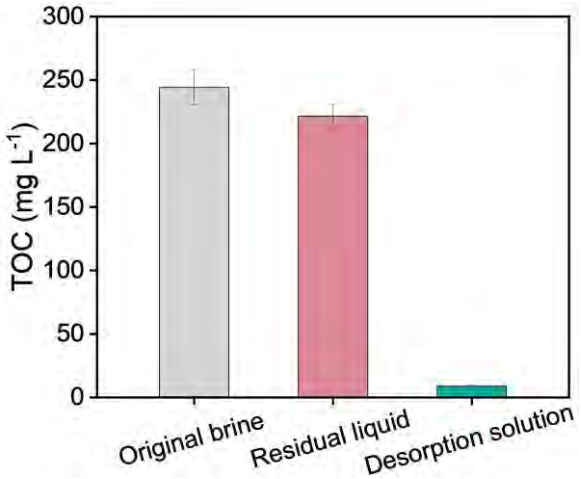

Figure 6.25 TOC values of original brine, residual liquid and desorption solution during the adsorption-desorption process.

In parallel, the Li^+ was recovered through repeated desorption using deionized water after each Li extraction. The total lithium production at the end of the recovery

process reached 23.92 mg g^{-1} (Figure 6.26a). The concentration of all metal species in the original desorption solution was summarized in Figure 6.26b.

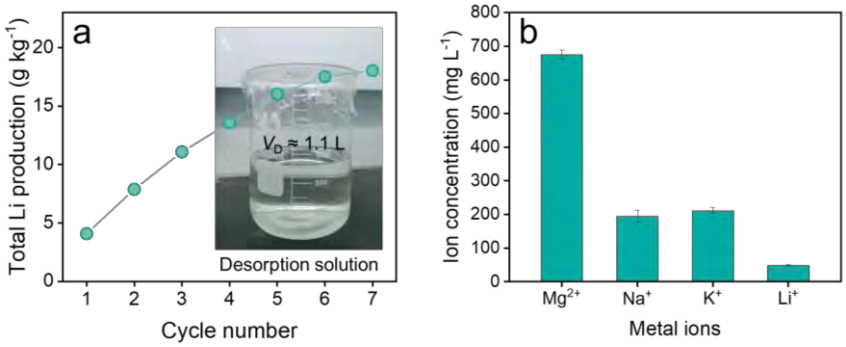

Figure 6.26 (a) The accumulated Li^+ recovery amount in the eluent. (b) The metal ion concentration of desorption solution.

Considering the unsatisfied Li^+/Mg^{2+} ratio (LMR) after only one whole adsorption-desorption repetition, another extraction-recovery using LiAl-LDH/PAM was proceeded to obtain purified Li^+ solution with the LMR to 7.1 (Table 6.4). Then, a Li^+-rich solution (8.112 g L^{-1}) was attained by evaporation-concentration (Figure 6.27), following which excess Na_2CO_3 was added into Li^+-rich solution at 80 °C to induce lithium precipitation.

Table 6.4 Composition variation during the re-adsorption-desorption purification of desorption solution.

Solution	Composition (mg L^{-1})			
	Li^+	Mg^{2+}	K^+	Na^+
Original desorption solution	49.5	675.66	211.41	195.11
Residual solution	3.7	624.53	176.57	206.83
Purified solution	80.6	11.3	5.05	4.13

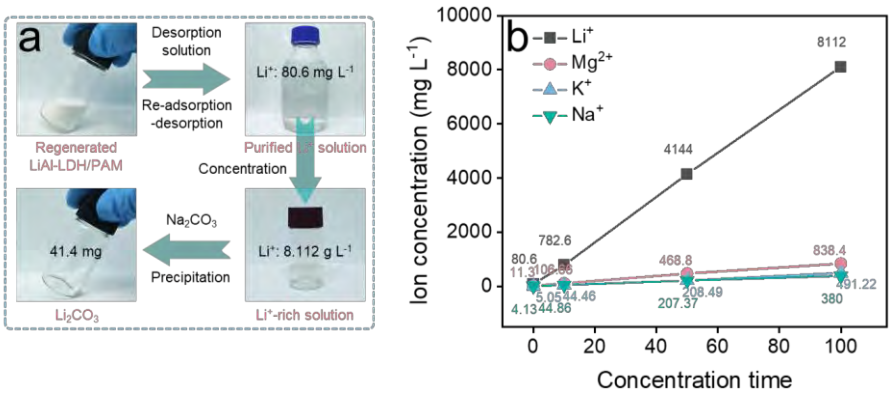

Figure 6.27 (a) Schematic diagram of the purification-concentration-precipitation

process for Li_2CO_3 production. (b) Change curves of metal ion concentration during the concentration stage of desorption solution.

The proportion of metal species in the precipitation was analyzed by ICP optical emission spectrometer (ICP-OES) test (Figure 6.28a). The proportion of Li was 78.65% among the metal elements. Further, a dissolution-reprecipitation process was conducted to purify lithium product. The resulting Li_2CO_3 showed a purity of 97.85% (Figure 6.28b), approaching the battery-grade standard, and was characterized by SEM and XRD.

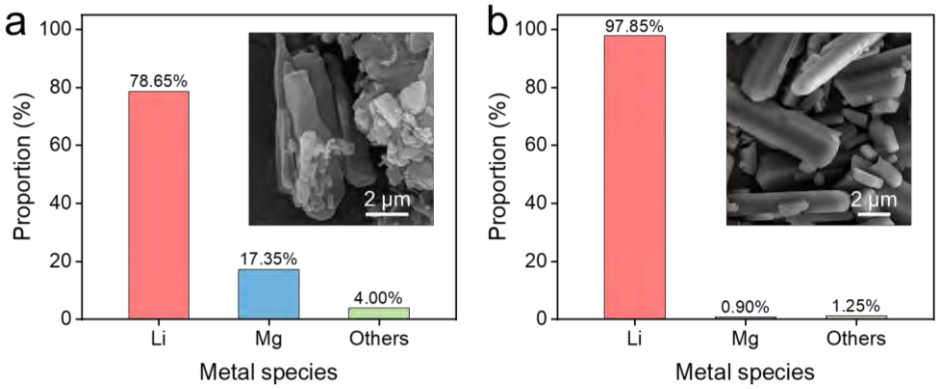

Figure 6.28 The proportion of lithium among the metal species in (a) the precipitation powder and (b) the purification powder. Inset is SEM images of the corresponding powder.

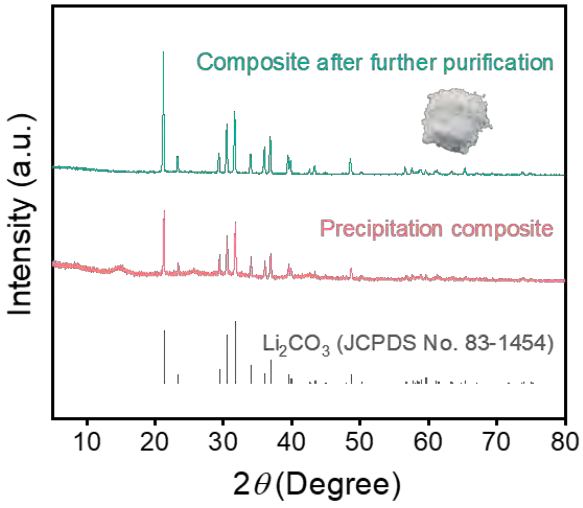

Figure 6.29 XRD patterns of precipitated Li_2CO_3 before and after purification. Insert picture is the obtained Li_2CO_3 product.

The lithium extraction and recovery using LiAl-LDH/PAM was unable to generate battery-grade Li_2CO_3 directly, however, the near 98% purity achieved by adsorption alone suggested that the vast majority of impurity ions had been removed from the brine,

which was clearly conducive to the subsequent membrane and resin treatment processes.

6.3.5. Practical application assessment

To explore the industrial application potential of SCSD-engineered LiAl-LDHs, LiAl-LDH/PAM beads were prepared based on the method presented in Section 4.2.2. In brief, the high mechanical polyvinyl chloride (PVC) and hydrophilic polyacrylonitrile (PAN) were selected as the hybrid binders. LiAl-LDH/PAM powders were mixed with PAN/PVC in wight ratio of 8:2 using DMF as solvent to product adsorption-binder slurry, and then the slurry was dropped into deionized water using the injector to form adsorbent beads. As shown in Figure 6.30, the resultant LiAl-LDH/PAM beads appeared while with the diameters of ~3 mm.

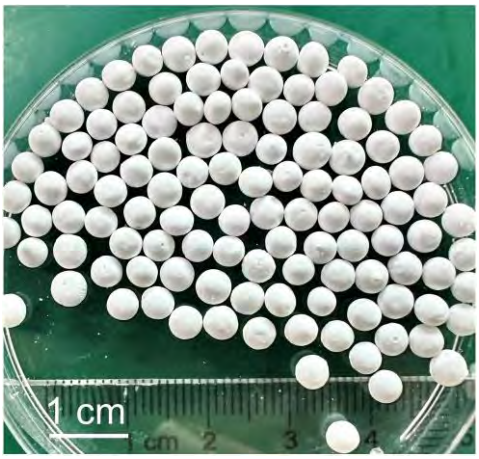

Figure 6.30 The optical photograph of the LiAl-LDH/PAM beads.

Further, to evaluate the dynamic lithium extraction performance of SCSD-engineered LiAl-LDHs, LiAl-LDH/PAM beads were loaded into a fixed bed with an inner diameter of 2.5 cm and a bed height of 30 cm for the dynamic lithium extraction (Figure 6.31a). In a typical dynamic adsorption process, Lop Nor brine was pumped from the bottom at 2.4 BV/h for 8h, with C_t/C_0 = 0.9 as the adsorption breakthrough point. Then, ice water of 20 mL was quickly pumped from the top for a washing process. Next, the desorption process was performed using deionized water from the bottom at 1.2 BV/h for 2 h. After treating 19.2 bed volumes (BV) of Lop Nor brine, the beads achieved a high total Li^+ adsorption capacity of 3.24 mg g^{-1} (Figure 6.31b). The Li^+ breakthrough curve of LiAl-LDH/PAM beads showed a breakthrough point of up to 12.4 BV, highlighting the excellent dynamic lithium extraction performance (Figure 6.31c). Moreover, beads maintained stable performance over five adsorption-desorption cycles, demonstrating the strong practical applicability (Figure 6.31d).

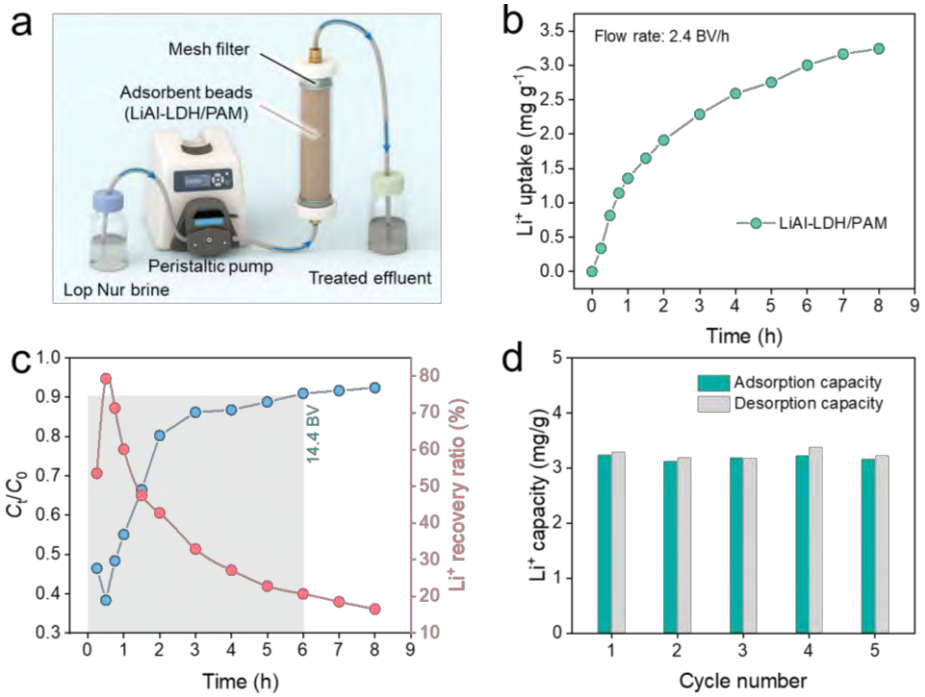

Figure 6.31 (a) Schematic of the fixed bed column device, (b) Li^+ adsorption capacity curves, (c) Li^+ breakthrough and recovery ratio curves in dynamic lithium extraction process, and (d) the dynamic adsorption-desorption cycling adsorption performance of LiAl-LDH/PAM beads.

Finally, the economic viability of the SCSD-engineered LiAl-LDH/PAM was evaluated. The economic process for practical production conditions was simulated using the latest prices of each raw material (Table 6.5). The Sankey diagram presented the major expenses involved in the production of LiAl-LDH/PAM. LiCl accounts for 36.78% of the material cost, whereas PAM contributes only 0.39%, indicating an almost negligible increase in cost from polymer modifier (Figure 6.32). According to the production economic analysis, the production cost of LiAl-LDH/PAM is estimated at \$5.28 per kilogram, demonstrating its strong practical competitiveness.

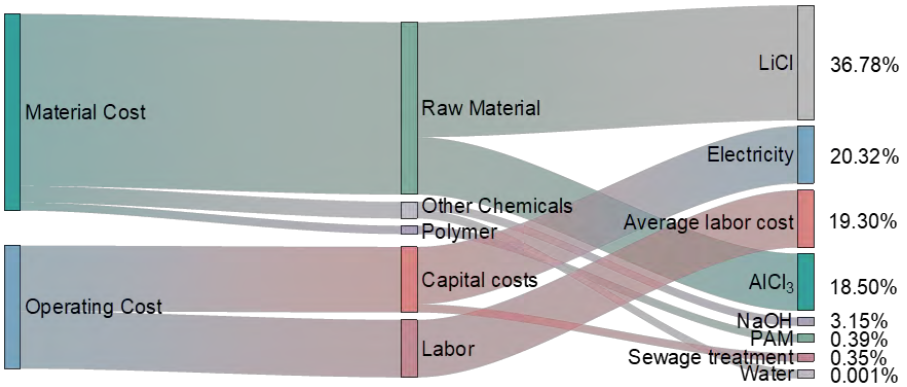

Figure 6.32 Inputs and shares of the preparation of the LiAl-LDH/PAM.

Table 6.5 Prices of substances required to synthesize materials.

	Item	Market price	Unit	Update date	Date source
1	LiCl	67	￥/kg	15-August-25	100PPI
2	$AlCl_3$	5.35	￥/kg	15-August-25	100PPI
3	PAM (anionic, 18 million molecular weight)	3.4	￥/kg	15-August-25	100PPI
4	NaOH	0.859	￥/kg	15-August-25	100PPI
5	Water	0.005	￥/kg	15-August-25	100PPI
6	Electricity	0.67	￥Kw/h	15-August-25	BDB
7	Average labor cost	7000	￥/month	15-August-25	JOBUI
8	Sewage treatment	3.00	￥/t	15-August-25	BDB

Note: a. Chemical raw materials are industrial grade.

b. 1 $ = 7.18 ￥(Update time: 2025/08/15).

c. Data Sources: 100PPl (http://www.100ppi.com/ppi), BDB (http://sz.bendibao.com/), and JOBUI (https://www.jobui.com/).

6.4. Conclusions

In conclusion, to tackle issues of low efficiency of lithium extraction of LiAl-LDHs in low-quality brines, a proof-of-concept polymer side-chain structure design (SCSD) strategy was developed for construction of a Li^+ enrichment domain on the intralayer of the LiAl-LDHs. Such functional domain enabled LiAl-LDH/PR to overcome the diffusion-limited Li^+ uptake caused by the Li^+-low concentration, which delivered an 83.1% increase in Li^+ uptake over pristine LiAl-LDH and an ultrahigh recovery efficiency of 91.62% from genuine oilfield brine with ultra-low Li^+ concentration. The maximum uptake was as high as 13.9 mg g^{-1}, exceeding most of the reported LiAl-LDH-based adsorbents. Additionally, the LiAl-LDH/PR exhibited robust lithium extraction from Lop Nor brine, the one of the largest low-quality brines in the world, by the continuous extraction procedure, enabling residual concentrations down to ppb level. On the basis of these merits, high-purity (97.85%) Li_2CO_3 was produced from the brine using LiAl-LDH/PR. The concept of SCSD can modulate local microenvironment and spatial microstructure of LiAl-LDHs by tuning side-chain groups, that provides a versatile strategy for sustainable lithium extraction from low-quality brines, and can be extended to other kinds of brines or for the extraction of other

critical resources.

6.5. References

[1] M. Yong, M. Tang, L. Sun, F. Xiong, L. Xie, G. Zeng, X. Ren, K. Wang, Y. Cheng, Z. Li, E. Li, X. Zhang, H. Wang, Sustainable lithium extraction and magnesium hydroxide co-production from salt-lake brines, Nat. Sustain. 7 (2024) 1662-1671.
[2] P. Greim, A.A. Solomon, C. Breyer, Assessment of lithium criticality in the global energy transition and addressing policy gaps in transportation, Nat. Commun. 11 (2020) 4570.
[3] X. Sun, Z. Liu, F. Zhao, H. Hao, Global Competition in the Lithium-Ion Battery Supply Chain: A Novel Perspective for Criticality Analysis, Environ. Sci. Technol. 55 (2021) 12180-12190.
[4] D. Yang, Y. Yang, T. Wong, S. Iguodala, A. Wang, L. Lovell, F. Foglia, P. Fouquet, C. Breakwell, Z. Fan, Y. Wang, M.M. Britton, D.R. Williams, N. Shah, T. Xu, N.B. McKeown, M.-M. Titirici, K.E. Jelfs, Q. Song, Solution-processable polymer membranes with hydrophilic subnanometre pores for sustainable lithium extraction, Nat. Water 3 (2025) 319-333.
[5] Raw materials for a truly green future, Nat. Rev. Mater. 6 (2021) 455-455.
[6] Y. Xiong, J. Zhou, P. Lu, J. Yin, Y. Wang, Z. Fan, Electrochemical lithium extraction from aqueous sources, Matter 5 (2022) 1760-1791.
[7] X. Chen, M. Yang, S. Zheng, F. Temprano-Coleto, Q. Dong, G. Cheng, N. Yao, H.A. Stone, L. Hu, Z.J. Ren, Spatially separated crystallization for selective lithium extraction from saline water, Nat. Water 1 (2023) 808-817.
[8] M.L. Vera, W.R. Torres, C.I. Galli, A. Chagnes, V. Flexer, Environmental impact of direct lithium extraction from brines, Nat. Rev. Earth Environ. 4 (2023) 149-165.
[9] G. Yan, M. Wang, G.T. Hill, S. Zou, C. Liu, Defining the challenges of Li extraction with olivine host: The roles of competitor and spectator ions, Proc. Natl. Acad. Sci. 119 (2022) e2200751119.
[10] K. Sun, M. Tebyetekerwa, X. Zeng, Z. Wang, T.T. Duignan, X. Zhang, Understanding the Electrochemical Extraction of Lithium from Ultradilute Solutions, Environ. Sci. Technol. 58 (2024) 3997-4007.
[11] Y. Song, S. Fang, N. Xu, M. Wang, S. Chen, J. Chen, B. Mi, J. Zhu, Solar transpiration–powered lithium extraction and storage, Science 385 (2024) 1444-1449.
[12] S. Yang, Y. Wang, H. Pan, P. He, H. Zhou, Lithium extraction from low-quality brines, Nature 636 (2024) 309-321.
[13] S. Wang, S. Zheng, Z. Wang, W. Cui, H. Zhang, L. Yang, Y. Zhang, P. Li, Superior lithium adsorption and required magnetic separation behavior of iron-doped lithium ion-sieves, Chem. Eng. J. 332 (2018) 160-168.
[14] X. Chen, W. Yu, Y. Zhang, C. Huang, L. Nie, J. Yu, Y. Zhang, C. Zhang, W. Zhai, X. Zhang, Y. Yu, W. Liu, Solar-Driven Lithium Extraction by a Floating Felt, Adv. Funct. Mater. 34 (2024) 2316178.
[15] É. Lèbre, M. Stringer, K. Svobodova, J.R. Owen, D. Kemp, C. Côte, A. Arratia-

Solar, R.K. Valenta, The social and environmental complexities of extracting energy transition metals, Nat. Commun. 11 (2020) 4823.
[16] A.Z. Haddad, L. Hackl, B. Akuzum, G. Pohlman, J.F. Magnan, R. Kostecki, How to make lithium extraction cleaner, faster and cheaper—in six steps, Nature 616 (2023) 245-248.
[17] S.B. Darling, The brine of the times, Science 385 (2024) 1421-1422.
[18] Y. Bao, Z. Ji, H. Zhou, C. Zhang, S. Song, F. Jia, J. Li, M. Quintana, Li-Ions Pre-intercalation Strategy of Manganese Oxides for Capacitive Deionization-Based Selective Lithium Extraction From Low-grade Brine, Small n/a (2024) 2406951.
[19] Y. Han, J. Ma, D. Liu, Y. Yang, T. Zhang, M. Wang, D. Liang, L. Wen, J. Ma, W. Wang, Microenvironment-Modulating Adsorption Enables Highly Efficient Lithium Extraction under Natural pH Conditions, ACS Nano 18 (2024) 9071-9081.
[20] X. Jiang, L. Zhang, Y. Miao, L. Chen, J. Liu, T. Zhang, S. Cheng, Y. Song, Y. Zhao, Intrinsic roles of nanosheet characteristics in two-dimensional montmorillonite membranes for efficient Li^{+}/Mg^{2+} separation, Water Res. 276 (2025) 123291.
[21] X. Wu, H. Zhang, X. Zhang, Q. Guan, X. Tang, H. Wu, M. Feng, H. Wang, R. Ou, Sustainable lithium extraction enabled by responsive metal-organic frameworks with ion-sieving adsorption effects, Proc. Natl. Acad. Sci. 121 (2024) e2309852121.
[22] Y. Yuan, D. Cao, F. Cui, Y. Yang, C. Zhang, Y. Song, Y. Zheng, J. Cao, S. Chen, Y. Song, F. Wang, G. Zhu, High-capacity uranium extraction from seawater through constructing synergistic multiple dynamic bonds, Nat. Water 3 (2025) 89–98.
[23] L. Zhang, T. Zhang, Y. Zhao, G. Dong, S. Lv, S. Ma, S. Song, M. Quintana, Doping engineering of lithium-aluminum layered double hydroxides for high-efficiency lithium extraction from salt lake brines, Nano Res. 17 (2024) 1646-1654.
[24] J. Chen, C. Lian, J. Yu, S. Lin, A directional growth strategy for high layer charge Li/Al-LDHs to reinforce Li extraction in low-grade salt lake brines, AIChE J. 70 (2024) e18280.
[25] T.R. Graham, J.Z. Hu, X. Zhang, M. Dembowski, N.R. Jaegers, C. Wan, M. Bowden, A.S. Lipton, A.R. Felmy, S.B. Clark, K.M. Rosso, C.I. Pearce, Unraveling Gibbsite Transformation Pathways into LiAl-LDH in Concentrated Lithium Hydroxide, Inorg. Chem. 58 (2019) 12385-12394.
[26] L. Zhang, T. Zhang, S. Lv, S. Song, H.J.O. Galván, M. Quintana, Y. Zhao, Adsorbents for lithium extraction from salt lake brine with high magnesium/lithium ratio: From structure-performance relationship to industrial applications, Desalination 579 (2024) 117480.
[27] L. Zhang, T. Zhang, S. Lv, S. Cheng, G. Dong, M. Quintana, S. Song, Y. Zhao, Steering interlayer interaction of lithium-aluminum layered double hydroxide beads for stable lithium extraction from sulfate-type brines, Desalination 592 (2024) 118130.
[28] S. Lv, Y. Zhao, L. Zhang, T. Zhang, G. Dong, D. Li, S. Cheng, S. Ma, S. Song, M. Quintana, Anion regulation strategy of lithium-aluminum layered double hydroxides for strengthening resistance to deactivation in lithium recovery from brines, Chem. Eng. J. 472 (2023) 145026.

[29] H. Zhan, Z. Qian, Y. Qiao, B. Lv, R. Liu, H. Chen, Z. Liu, Triggering Ion Diffusion and Electron Transport Dual Pathways for High Efficiency Electrochemical Li^+ Extraction, ACS Nano 18 (2024) 31204-31214.
[30] H. Li, C. Zhang, J. Xin, Y. Liu, H. Yang, C. Zhu, C. Liu, Z. Xu, Design of Photothermal "Ion Pumps" for Achieving Energy-Efficient, Augmented, and Durable Lithium Extraction from Seawater, ACS Nano 18 (2024) 2434-2445.
[31] B. Shi, X. Pang, B. Lyu, H. Wu, J. Shen, J. Guan, X. Wang, C. Fan, L. Cao, T. Zhu, Y. Kong, Y. Liu, Z. Jiang, Spacer-Engineered Ionic Channels in Covalent Organic Framework Membranes toward Ultrafast Proton Transport, Adv. Mater. 35 (2023) 2211004.
[32] C.E. Pelkowski, A. Natraj, C.D. Malliakas, D.W. Burke, M.I. Bardot, Z. Wang, H. Li, W.R. Dichtel, Tuning Crystallinity and Stacking of Two-Dimensional Covalent Organic Frameworks through Side-Chain Interactions, Journal of the American Chemical Society 145 (2023) 21798-21806.
[33] W. Meng, S. Chen, Z. Guo, F. Gao, J. Wang, J. Lu, Y. Hou, Q. He, X. Zhan, M. Qiu, Q. Zhang, Three-dimensional cationic covalent organic framework membranes for rapid and selective lithium extraction from saline water, Nat. Water 3 (2025) 191-200.
[34] K. Guan, Z. Mai, S. Zhou, S. Fang, Z. Li, P. Xu, Y.-H. Chiao, M. Hu, P. Zhang, G. Xu, K. Nakagawa, H. Matsuyama, Side-Chain-Dependent Functional Intercalations in Graphene Oxide Membranes for Selective Water and Ion Transport, Nano Letters 23 (2023) 6095-6101.
[35] Y. Zhang, L. Wang, R. Zhang, C. He, L. Jia, X. Wang, X. Feng, T. Jiang, B. Xie, X. Ma, J. Cao, Y. Ma, X. Tan, T. Yu, Steering Electron Density of Zr Sites Using Ligand Effect in Bio-Beads for Efficient Defluoridation, Adv. Funct. Mater. 33 (2023) 2213999.
[36] X. Xin, Y. Zhang, R. Wang, Y. Wang, P. Guo, X. Li, Hydrovoltaic effect-enhanced photocatalysis by polyacrylic acid/cobaltous oxide–nitrogen doped carbon system for efficient photocatalytic water splitting, Nat. Commun. 14 (2023) 1759.
[37] M. Xu, R. Cao, B. Hao, D. Wang, D. Luo, H. Dou, Z. Chen, Single-Anion Conductive Solid-State Electrolytes with Hierarchical Ionic Highways for Flexible Zinc-Air Battery, Angew. Chem., Int. Ed. 136 (2024) e202407380.
[38] X. Tong, S. Liu, Y. Zhao, L. Huang, J. Crittenden, Y. Chen, MXene Composite Membranes with Enhanced Ion Transport and Regulated Ion Selectivity, Environ. Sci. Technol. 56 (2022) 8964-8974.
[39] Y. Pan, Y. Zhang, C. Thompson, G. Liu, W. Zhang, Electrospun Lithium Porous Nanosorbent Fibers for Enhanced Lithium Adsorption and Sustainable Applications, ACS Appl. Mater. Interfaces 16 (2024) 54259-54271.
[40] D. Cao, F. Cui, C. Zhang, Y. Song, Y. Zheng, J. Cao, Y. Yuan, Y. Yang, In Situ Synthesis of Polyamidoxime Chains Inside the Negative-Charged Confining Fields for Efficient Adsorption of Uranyl Ions, Adv. Funct. Mater. n/a (2024) 2413729.
[41] Y. Kong, X. He, H. Wu, Y. Yang, L. Cao, R. Li, B. Shi, G. He, Y. Liu, Q. Peng, C. Fan, Z. Zhang, Z. Jiang, Tight Covalent Organic Framework Membranes for Efficient Anion Transport via Molecular Precursor Engineering, Angew. Chem., Int. Ed. 60

(2021) 17638-17646.
[42] X. Zhang, X. Wu, J. Gan, X. Yu, H. Wang, R. Ou, Building block design of thermally regenerable metal–organic framework composites for highly selective lithium adsorption, Chem. Eng. J. 499 (2024) 156352.

Chapter 7. Conclusions

Global electrification and decarbonization drive exponentially growing lithium (Li) demand. While brines offer a virtually abundant lithium source for the sustainable supply of Li, the efficient and stable Li extraction from brines are challenging, even for the industrialized lithium-aluminum layered double hydroxides (LiAl-LDHs) lithium ion-sieves. Several crucial concerns remain regarding lithium extraction by LiAl-LDHs: i) low Li^+ adsorption capacity; ii) 'SO_4^{2-}-poisoning' effect in sulfate-type brines; iii) poor efficiency in low-quality brines. In this thesis, a series of state-of-art LiAl-LDH-based adsorbents have been innovated and designed to address the bottlenecks of current LiAl-LDHs based on their intrinsic structures and properties. The findings are of sufficient impact to ion-sieve development and Li extraction from brines communities. The general conclusions are summarized as follows:

1. The doping engineering strategy was developed to fabricate novel Zn^{2+}-doped LiAl-LDHs (LiZnAl-LDH) with superior Li extraction performance. This strategy endowed tunable surface properties and favorable nanostructures, which enabled the stronger adsorption energy (E_{ad}) towards Li^+, reduced Gibbs free energy (ΔG) for Li^+ transfer and insertion lithium, and depressed diffusion energy barrier of Li^+. Accordingly, the maximum adsorption capacity for Li^+ was raised by about 39% than without doping, while the Li^+/K^+, Li^+/Na^+, and Li^+/Mg^{2+} selectivity in Lop Nor brine is as high as 213, 834, and 171, respectively.

2. The steering interlayer interaction strategy was developed to introduce PO_4^{3-} into the interlayer of beaded LiAl-LDHs (BLDH-P) prevents the intercalation of SO_4^{2-} by selective electrostatic repulsion and enhanced diffusion energy barrier. Based on the rational design, the adsorption and desorption capacity of LiAl-LDHs remained almost identical during the cycling extraction in Lop Nor brine, the largest SO_4^{2-}-type brine in the world. Besides, the static and dynamic Li^+ uptake reached 5.26 mg/g and 3.96 mg/g with a minimum 105% higher selectivity, superior to those of reported and commercialized adsorbents.

3. The organic modification strategy was developed to construct multiple functional domains of LiAl-LDHs (LiAl-LDH/PAM) using polyacrylamide (PAM) for sustainable lithium extraction in SO_4^{2-}-type brines. Through creating multiple SO_4^{2-} repelling domains in the interface and interlayer of the LiAl-LDH/PAM, the energy

barrier for SO_4^{2-} migration over interface and interlayer was increased, which offered extraordinary anti-sulfate poisoning during long-term Li cycling extraction in Lop Nor brine. The anti-sulfate poisoning properties exceeded all previously reported LiAl-LDHs.

4. The proof-of-concept polymer side-chain structure design (SCSD) strategy was developed that delivers intralayer engineering of LiAl-LDHs (LiAl-LDH/PR) with functional polymers for efficient and highly selective Li extraction from low-quality brines. The SCSD strategy engineered LiAl-LDH/PR with a Li^+-enriched intralayer domain that can be readily tuned through rational designs of side-chains of polymer to accommodate lithium extraction from different brines. Accordingly, LiAl-LDH/PR realized an ultrahigh recovery efficiency of 91.62% from genuine oilfield brine with ultra-low Li^+ concentration. Moreover, sustainable Li extraction enables ppb-level Li^+ residual concentration and high-purity Li_2CO_3 production from the world's largest low-quality salt lake brine.

Chapter 8. Perspectives

In this thesis, several promising strategies were developed for improving the efficiency, stability, and feasibility of LiAl-LDHs. Despite considerable progresses, high-efficiency lithium extraction using LiAl-LDHs remains difficulties and challenges in terms of discovery of new materials with various cation-doping and/or anion intercalation, and availability in lithium resources with lower Li^+ concentration (*e.g.*, seawater). The following two perspectives can provide promising views.

Interpretable machine learning (ML) for rapid determination of high-performance modification strategies.

While the feasibility of the Zn^{2+}-doping and PO_4^{3-}-intercalation strategies has been verified, it does not represent that they are the most optimal solutions. Obviously, the workload associated with the preparation and performance verification for the doping and intercalation of LiAl-LDHs is complicated, time-consuming and costly.

With the coming of the era of artificial intelligence, machine learning (ML) methods have shown great potential in reducing experimental costs and accelerating the discovery of new materials. These methods established a link between the raw structure or experimental conditions and the target performance, enabling rapid prediction of properties of modified LiAl-LDHs and increasing screening efficiency greatly.

Solar-driven direct lithium extraction and water harvesting from seawater

Seawater is a vast treasure trove of lithium resources, with over 230 billion tons. However, efficient lithium extraction from seawater by current evaporation and the direct lithium extraction techniques (e.g., LiAl-LDHs ion-sieving) suffers from inefficiency and energy-intensity due to the low concentration of lithium ions (Li^+) ($\sim$0.2 mg L^{-1}) and high concentration of interfering ions (500-10000 mg L^{-1}) in seawater.

Solar-driven direct lithium extraction (SDLE) systems combining conventional evaporation and DLE techniques can overcome the present challenges of Li extraction, allow for spontaneous, continuous Li^+ transport and enrichment under sunlight, achieving efficient and durable lithium extraction from seawater, and promise to advance the exploitation of low-quality brines while simultaneously producing fresh water.

It is convinced for me that ML and SDLE techniques, through continuous evolution, offers a unique perspective on the sustainable development of lithium resources and an important avenue for solving global energy and water issues.

Appendix I. Articles published during the Ph. D studies

(*indicates corresponding author.)

[1] **Lingjie Zhang**, Yunjia Ling, Jianglin Yan, Zhenlei Wang, Yanhui Miao, Haoyu Bai, Tingting Zhang, Shaoxian Song, Mildred Quintana, Yunliang Zhao. Charged two-dimensional nanochannels with high ion density enabling ultrafast monovalent and multivalent ion conductivity. ***Chem. Sci.***, 2026, 17, 1735-1744. (JCR Q1, **Nature Index**)

[2] **Lingjie Zhang**, Jianglin Yan, Zhenlei Wang, Tingting Zhang, Shaoxian Song, Mildred Quintana, Yunliang Zhao. Solar-Driven Direct Lithium Extraction from Low-Quality Brines. ***Adv. Mater.***, 2026, 38, e12998. (JCR Q1, **IF 26.8, Nature Index**)

[3] **Lingjie Zhang**, Jianglin Yan, Shichang Kang, Zhenlei Wang, Yanhui Miao, Renbo Gao, Tingting Zhang, Hiram Joazet Ojeda-Galván, Mildred Quintana, Haoyu Bai, Shaoxian Song, Yunliang Zhao. Tailoring Multiple Functional Domains of Lithium-Ion Sieves for Sustainable Lithium Extraction from Low-Quality Brines. ***ACS NANO***, 2025, 19, 33620-33631. (JCR Q1, **IF 16.1, Nature Index**)

[4] **Lingjie Zhang**, Zhenlei Wang, Tingting Zhang, Xiongrui Jiang, Licai Chen, Hiram Joazet Ojeda Galván, Mildred Quintana, Shaoxian Song, Sridhar Komarneni, Yunliang Zhao. Bioinspired Tunable Subnanochannels in Two-Dimensional Montmorillonite Membranes for Fast and Stable Proton Transport. ***ACS Materials Lett.***, 2025, 7, 2835-2843. (JCR Q1, **Highlighted as Front Cover Paper**)

[5] **Lingjie Zhang**, Tingting Zhang, Shuaike Lv, Shaoxian Song, Hiram Joazet Ojeda Galván, Mildred Quintana, Yunliang Zhao. Adsorbents for lithium extraction from salt lake brine with high magnesium/lithium ratio: from structure-performance relationship to industrial applications. ***Desalination***, 2024, 579, 117480. (JCR Q1, **ESI Highly Cited Paper**)

[6] **Lingjie Zhang**, Tingting Zhang, Yunliang Zhao, Guangfeng Dong, Shuaike Lv, Songliang Ma, Shaoxian Song, Mildred Quintana. Doping engineering of lithium-aluminum layered double hydroxides for high-efficiency lithium extraction from salt lake brines. ***Nano Res.***, 2024, 17(3): 1650-1658. (JCR Q1, **ESI Hot Paper**, **ESI Highly Cited Paper**, **Top Papers Award 2025**)

[7] **Lingjie Zhang**, Tingting Zhang, Shuaike Lv, Shuai Cheng, Guangfeng Dong, Mildred Quintana, Shaoxian Song, Yunliang Zhao. Steering interlayer interaction of lithium-aluminum layered double hydroxide beads for stable lithium extraction from sulfate-type brines. ***Desalination***, 2024, 592, 118130. (JCR Q1)

[8] **Lingjie Zhang**, Tingting Zhang, Yue Cai, Yunliang Zhao, Shaoxian Song, Mildred Quintana. Engineering sulfuric acid-pretreated biochar supporting MnO_2 for efficient toxic organic pollutants removal from aqueous solution in a wide pH range. ***J. Clean. Prod.,*** 2023, 416, 137968. (JCR Q1)

[9] Ying Li, **Lingjie Zhang***, Licai Chen, Yanhui Miao, Jierui Wang, Bowen Kuang, Tingting Zhang, Yunliang Zhao. Interlocking nanoconfined two-dimensional montmorillonite membranes for precise and sustainable antibiotic desalination. ***J. Environ. Chem. Eng.***, 2026, 14, 121132. (JCR Q1)

[10] Xiongrui Jiang, **Lingjie Zhang***, Yanhui Miao, Licai Chen, Jiaoyan Liu, Tingting Zhang, Shuai Cheng, Yuhan Song, Yunliang Zhao. Intrinsic roles of nanosheet characteristics in two-dimensional montmorillonite membranes for efficient Li^+/Mg^{2+} separation, ***Water Res.***, 2025, 276, 123291. (JCR Q1, **ESI Highly Cited Paper, Nature Index**)

[11] Zhenlei Wang, Lianqiu Huang, **Lingjie Zhang***, Tingting Zhang, Jianglin Yan, Licai Chen, Xiongrui Jiang, Damiano Sarocchi, Shaoxian Song, Viridiana García Meza, Mildred Quintana, Yunliang Zhao. A dual-constrained assembly strategy of highly aligned two-dimensional montmorillonite membranes for efficient proton transport, ***J. Mater. Chem. A***, 2025, 13, 25489-25497. (JCR Q1)

[12] Shuaike Lv, Yunliang Zhao, **Lingjie Zhang***, Tingting Zhang, Guangfeng Dong, Dongxing Li, Shuai Cheng, Songliang Ma, **S**haoxian Song, Mildred Quintana. Anion regulation strategy of lithium-aluminum layered double hydroxides for strengthening resistance to deactivation in lithium recovery from brines, ***Chem. Eng. J.***, 2023, 472, 145026. (JCR Q1)

[13] Yanhui Miao, Yunliang Zhao, **Lingjie Zhang***, Licai Chen, Renbo Gao, Xiongrui Jiang, Shaoxian Song, Tingting Zhang. Dewatering behavior and regulation mechanism of montmorillonite nanosheet in aqueous solution, ***J. Colloid Interface Sci.***, 2023, 652, 1620-1630. (JCR Q1, **Highlighted as Front Cover Paper**)

[14] Tingting Zhang, Yinxing Zhao, **Lingjie Zhang***, Qiwu Zhang, Guangsen Song, Guozhi Fan, Yunliang Zhao. Efficient removal of para arsanilic acid with Ca-Al-Fe composite: Performances and mechanisms, ***J. Mol. Liq.*** 2023, 388, 122773. (JCR Q1)

Appendix II. Experimental data

Table II.1 The Li^+ adsorption capacity of LiZnAl-LDH with different Zn^{2+} doping amounts in brine.

Time (min)	Adsorption capacity (mg/g)				
	LiAl-LDH	LiZnAl-LDH-1%	LiZnAl-LDH-5%	LiZnAl-LDH-10%	LiZnAl-LDH-20%
0	0	0	0	0	0
2	3.408	4.032	4.3	4.41	3.715
5	3.993	4.651	4.915	5.055	4.205
15	4.831	5.065	5.485	5.445	4.76
30	4.934	5.367	5.645	5.71	4.87
60	5.031	5.670	5.89	5.845	4.99
180	5.114	5.792	6.04	6.005	5.235

Table II.2 The selectivity of LiZnAl-LDH with different content of Zn^{2+} for Li^+/K^+, Li^+/Na^+, Li^+/Mg^{2+} in brine.

Li^+/M	Selectivity				
	LiAl-LDH	LiZnAl-LDH-1%	LiZnAl-LDH-5%	LiZnAl-LDH-10%	LiZnAl-LDH-20%
K^+	65.75	121.31	213.07	193.03	53.82
Na^+	68.07	104.31	834.16	465.30	414.19
Mg^{2+}	75.09	149.36	171.32	184.49	80.52

Table II.3 The mass losses, dissolution amounts of Al^{3+} and dissolution COD of BLDH-P beads with various PVC/PAN ratios in strong acid and alkali solutions

Time (min)	Dissolution of material									
	PAN-0%		PAN-20%		PAN-40%		PAN-50%		PAN-60%	
	pH=3	pH=11	pH=3	pH=11	pH=3	pH=11	pH=3	pH=11	pH=3	pH=11
Mass	4.86	3.57	5.28	5.41	5.75	5.74	5.67	5.90	6.61	6.46
Al^{3+}	0.31	0.00	0.42	0.00	0.30	0.00	0.55	0.00	0.38	0.00
COD	1.09	1.16	1.27	1.26	1.52	1.50	1.20	1.17	1.38	1.36

Table II.4 The Li^+ adsorption capacity of BLDH-P beads with various PVC/PAN ratios.

Time (h)	Adsorption capacity (mg/g)				
	PAN-0%	PAN-20%	PAN-40%	PAN-50%	PAN-60%
0	0	0	0	0	0
1	1.235	1.43	1.85	1.855	2.04
2	1.935	2.015	2.39	2.47	2.645
4	2.84	2.875	3.09	3.43	3.575
6	3.175	3.57	3.625	3.765	3.87
18	4.525	4.63	4.825	5.03	5.015
24	4.86	5.11	5.19	5.38	5.345

Table II.5 Adsorption kinetics l of Li^+ on BLDH-P and BLDH-Cl during the adsorption process.

Time (h)	Adsorption capacity (mg/g)	
	BLDH-P	BLDH-Cl
0	0	0
0.25	0.955	0.635
0.5	1.36	1.135
1	1.98	1.56
2	2.47	2.235
4	2.975	2.73
6	3.405	3.145
8	3.82	3.51
10	4.095	3.705
12	4.2	3.86
24	4.855	4.52

Table II.6 The Li^+ breakthrough curves and the Li^+ dynamic adsorption curves of BLDH-Cl and BLDH-P.

Effluent volume (mL)	BLDH-P		Effluent volume (mL)	BLDH-Cl	
	$C_t/C0$	q_t (mg/g)		$C_t/C0$	q_t (mg/g)
0.00	0.14	0.00	0.00	0.41	0.00
58.08	0.27	0.62	55.50	0.22	0.37
116.17	0.43	1.09	111.00	0.48	1.08
174.25	0.53	1.42	166.50	0.59	1.35
232.33	0.60	1.70	222.00	0.64	1.59
290.42	0.66	1.94	277.50	0.68	1.82
348.50	0.68	2.14	333.00	0.72	1.99
406.58	0.72	2.58	388.50	0.74	2.22
522.75	0.78	2.84	444.00	0.77	2.39
638.92	0.80	3.09	499.50	0.80	2.61
755.09	0.83	3.38	610.50	0.83	2.82
871.25	0.84	3.65	721.50	0.85	3.08
987.42	0.86	3.90	832.50	0.86	3.34
1103.59	0.87	3.96	943.50	0.89	3.46

Table II.7 The Li^+ adsorption kinetics of LiAl-LDH, LiAl-LDH/PAA, LiAl-LDH/PSS, and LiAl-LDH/PAM.

Time (min)	Adsorption capacity (mg/g)			
	LiAl-LDH	LiAl-LDH/PAA	LiAl-LDH/PSS	LiAl-LDH/PAM
5	4.24	4.115	4.645	5.26
15	4.77	4.39	5.27	6.205
30	5.165	4.665	5.55	6.305
45	5.34	5.035	5.68	6.3
60	5.44	5.29	5.98	6.475
90	5.575	5.745	6.195	6.48
120	5.59	5.86	6.29	6.515
180	5.58	5.93	6.48	6.705

Table II.8 Li^+ uptakes of LiAl-LDHs during the adsorption-desorption cycling experiments.

Cycle number	Adsorption (Ads.)/Desorption (Des.) capacity (mg/g)							
	LiAl-LDH		LiAl-LDH/PAA		LiAl-LDH/PSS		LiAl-LDH/PAM	
	Ads.	Des.	Ads.	Des.	Ads.	Des.	Ads.	Des.
1	6.135	6.995	6.085	6.060	5.580	5.930	6.480	6.705
2	7.137	6.650	6.745	7.328	6.233	5.930	6.058	6.885
3	6.750	6.682	6.248	6.681	6.148	5.325	6.080	6.805
4	5.943	5.474	5.173	6.257	5.698	5.723	5.943	6.525
5	5.570	4.794	4.959	5.669	5.238	5.108	5.648	6.463
6	4.251	4.541	5.245	5.759	4.905	5.493	5.790	6.300
7	4.559	4.346	4.209	5.975	4.435	5.593	5.900	6.503
8	4.891	4.481	4.911	5.911	4.340	5.070	5.603	6.420
9	4.042	4.658	4.806	5.898	4.003	4.790	5.250	6.153
10	3.779	4.469	4.980	5.588	3.678	4.748	5.438	6.208

Table II.9 The Li^+ adsorption isotherms of LiAl-LDH, LiAl-LDH/PAA, LiAl-LDH/PSS, and LiAl-LDH/PAM.

Li^+ concentration (mg/L)	Adsorption capacity (mg/g)			
	LiAl-LDH	LiAl-LDH/PAA	LiAl-LDH/PSS	LiAl-LDH/PAM
213	5.58	5.93	6.48	6.705
412.4	7.24	7.16	7.78	8.22
562.6	8.59	8.89	9.53	10.05
730	9.24	9.34	9.76	10.94
894.8	9.42	9.7	10.08	11.58

Table II.10 The selectivity of LiAl-LDH, LiAl-LDH/PAA, LiAl-LDH/PSS, and LiAl-LDH/PAM for Li^+/K^+, Li^+/Na^+, Li^+/Mg^{2+} in brine.

Li^+/M	Selectivity			
	LiAl-LDH	LiAl-LDH/PAA	LiAl-LDH/PSS	LiAl-LDH/PAM
K^+	483.74	569.61	526.44	705.52
Na^+	122.08	124.65	134.96	165.24
Mg^{2+}	73.00	81.37	94.13	104.64